FEASIBILITY STUDY OF A STELLAR
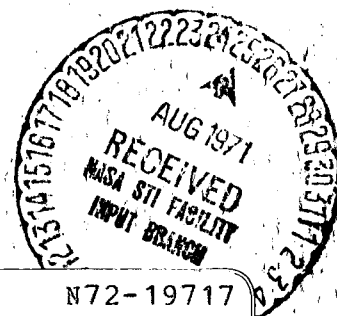
TRACKING ATTITUDE REFERENCE SYSTEM

Final Report

●

NASA Contract NAS 5-21508

B. KLESTADT

Hughes Aircraft Company
Space and Communications Group
1950 East Imperial Highway
El Segundo, California 90009

June 1971

Prepared for

GODDARD SPACE FLIGHT CENTER
Greenbelt, Maryland 20771

TECHNICAL REPORT STANDARD TITLE PAGE

1. Report No.	2. Government Accession No.	3. Recipient's Catalog No.
4. Title and Subtitle A STELLAR TRACKING REFERENCE SYSTEM		5. Report Date June 1971
		6. Performing Organization Code
7. Author(s) B. Klestadt		8. Performing Organization Report No.
9. Performing Organization Name and Address Hughes Aircraft Company Space and Communications Group El Segundo, California		10. Work Unit No.
		11. Contract or Grant No. NAS 5-21508
		13. Type of Report and Period Covered
12. Sponsoring Agency Name and Address Goddard Space Flight Center National Aeronautics and Space Admin. Greenbelt, Maryland 20771 H. Paul Scherer		Final Report 15 Jun 70 - 15 Jun 71
		14. Sponsoring Agency Code
15. Supplementary Notes		

16. Abstract   A Stellar Attitude Reference System (STARS) concept for satellites was studied which promises to permit continuous precision pointing of payloads with accuracies of 0.001 degree without the use of gyroscopes. It is accomplished with the use of a single, clustered star tracker assembly mounted on a non-orthogonal, two gimbal mechanism, driven so as to unwind satellite orbital and orbit precession rates. A set of eight stars was found which assures the presence of an adequate inertial reference on a continuous basis in an arbitrary orbit. Acquisition and operational considerations were investigated and inherent reference redundancy/reliability was established. Preliminary designs for the gimbal mechanism, its servo drive, and the star tracker cluster with its associated signal processing were developed for a baseline sun-synchronous, noon-midnight orbit. The functions required of the onboard computer were determined and the equations to be solved were found. In addition detailed error analyses were carried out, based on structural, thermal and other operational considerations. A brief assessment of laboratory and in orbit calibration techniques was also performed. The reference scheme investigated was found to be a feasible approach, requiring only a detailed development program for its implementation.

17. Key Words (Selected by Author(s)) Stellar Reference Gimbal System Precision Pointing Precision Attitude Reference Gimbal Attitude Control Satellite Star Tracker Control	18. Distribution Statement		
19. Security Classif. (of this report) Unclassified	20. Security Classif. (of this page) Unclassified	21. No. of Pages	22. Price*

*For sale by the Clearinghouse for Federal Scientific and Technical Information, Springfield, Virginia 22151.

PRECEDING PAGE BLANK

FOREWORD

The study described in this report was performed by the
Guidance and Control Systems Laboratory, Technology Division,
Space and Communications Group, Hughes Aircraft Company,
El Segundo, California. The work was done under NASA Contract
NAS 5-21508, with Mr. H. Paul Scherer, Guidance and Control Branch,
Systems Division, Goddard Space Flight Center, Greenbelt, Maryland,
as Technical Officer. The principal members of the project team
were as follows:

        B. Klestadt -   Project Manager and Principal Investigator

        R. B. Clark

        W. L. Townsend

        W. C. Wey

In addition, significant contributions to the feasibility
study were made by the following:

        E. A. Anzivino

        L. E. Ault

        W. F. Hummel

        R. J. McGrath

        B. H. Mueller

        G. R. Noyes

        D. M. Solheim

        G. R. Telle

        R. E. Tweedt

        D. O. Wise

Preface

This final report documents the detailed results of a feasibility study of a Stellar Attitude Reference System (STARS) concept for satellites which promises to permit continuous precision pointing of payloads with accuracies of 0.001 degree without the use of gyroscopes. This is accomplished with the use of a single, clustered star tracker assembly mounted on a non-orthogonal, two-gimbal mechanism, driven so as to unwind satellite orbital and orbit precession rates.

All significant aspects of the STARS concept which could affect its feasibility were investigated. Included were studies/analyses of star visibility, acquisition, and failure/redundancy considerations. Preliminary designs of the gimbal mechanism and star tracker cluster were generated, thus verifying the general feasibility and providing the basis for specific development recommendations. In addition, detailed error analyses were carried out, based on structural, thermal, and external influence factors.

The overall conclusion of the feasibility study is that 0.001 degree precision pointing by means of the STARS concept is achievable and no major technical stumbling blocks should be encountered in the development. Recommended further effort in developing the STARS can be divided into two major portions. The first, a subsystem development activity, should concentrate on development of the polar axis gimbal mechanism and its servo drive, in addition to an engineering model development of the star tracker and its associated signal processing circuits. The second is a combined analysis/laboratory effort to concentrate on sunshade analyses and tests, elastic friction analyses and tests, computer/electronics mechanization and analysis, control system analysis/design/simulation, and assembly, test, and calibration methods. For maximum cross-fertilization benefits and minimum development time, both portions can and should be performed concurrently.

TABLE OF CONTENTS

ILLUSTRATIONS

1. Introduction

In considering the requirements of future scientific and commercial satellites, one of the performance requirements which stands out is the need for a high precision (0.001 degree) earth-pointing capability from circular orbits of various altitudes and inclination. Investigations prior to this study showed that the basic technology for such pointing capability appears to be available at this time if stars are used to establish a precisely known coordinate reference. Since disturbance torques on typical satellites (4000 dyne-cm on 200 slug-ft^2) could produce a 0.001-degree attitude error in 5 seconds, a nearly continuous precision reference is required.

The solution to the above precision pointing requirements, investigated in this study, involves a unique Stellar Tracking Attitude Reference System (STARS) concept which avoids many of the problems associated with other precision pointing schemes by the use of a compact multistar tracker and a simple, unconventional two-gimbal assembly. The advantages of this approach are as follows:

1) The stellar reference is a single, clustered star tracker assembly on a single gimbal mount, thus providing a uniform thermal environment for its components, minimum distortion, and involving minimum interaction with other spacecraft components.

2) The STARS concept is not dependent upon high precision gyros, with their attendant reliability and cost disadvantages.

3) The star tracker concept provides a high level of redundancy in its basic design, being able to track more than the minimum required number of stars most of the time. In addition, it provides gradual degradation of performance in case of failure of one or more individual trackers.

4) The star tracker design and the particular scanning technique used avoid the usual requirements for critical alignment of the scanning device to the boresight axis.

5) The STARS concept operates with essentially constant rates about both gimbal axes, thereby avoiding many of the more significant sources of angular error normally associated with gimbal systems and their drives.

6) The STARS concept minimizes the amount of computational capability required of the on-board computer.

7) The STARS concept can operate with no on-board star cataloging whatsoever, although the baseline approach does involve use of a small amount of star position information.

The baseline design configuration adopted for the study - for low-altitude sun-synchronous orbit application - utilizes a clustered set of eight star trackers mounted on the inner gimbal of a nonorthogonal two-axis gimbal system. The inner gimbal is held essentially parallel to the earth's polar axis, while the outer gimbal is parallel to the satellite pitch axis. Under ideal conditions, the satellite may rotate about its pitch axis while keeping the yaw axis pointed precisely vertical, and the star trackers continue to point at their assigned stars while the orbit precesses about the polar axis. The star trackers are arranged and their signals processed so that two are tracking stars at any one time regardless of earth and satellite body occultation directions. Physical motion of the star trackers in inertial space to permit the tracking function is accomplished by controlling vehicle attitude. Precision pointing of the satellite vertical is achieved by commanding the proper pitch and polar axis gimbal angles, based on ground-determined and regularly updated ephemeris data. An on-board digital computer keeps track of local satellite time, calculates and sets proper gimbal angles, and performs the attitude control signal processing and command functions to enable star tracking as required.

To facilitate management of the feasibility study and permit logical identification and resolution of all significant feasibility questions, the study was divided into four principal task areas, System Analysis, Gimbal System, Star Trackers, and Error Analysis.

System Analysis covered the operational feasibility of the STARS approach, the requirements for reference stars, their characteristics and visibility with changes in orbital conditions, redundancy and reliability questions, and the techniques for and problems associated with initial acquisition of the stellar reference. In addition, the functions required of and equations to be solved by the on-board electronics unit/computer were investigated under this task.

Gimbal system investigations covered the determination of suitable gimbal system components such as structural materials, drive motors, angular position transducers, bearings and lubrication techniques. Further activities under this task included overall gimbal system configuration tradeoffs and selection of a baseline configuration, in addition to investigation of the closed loop precision drive characteristics required for each gimbal axis.

Star tracker investigations consisted initially of conceptual efforts and system level tradeoffs to establish gross characteristics such as multiplexing configuration, aperture number, F number, field of view, off-axis tracking requirements, shuttering and system bandwidth requirements. The optical design problems were then tackled with emphasis on telescope and sunshade feasibility. Extensive use was made of previous experience in star sensor optics and sunshade design analysis and test confirmation to lend credence to the feasibility conclusions reached and the preliminary design parameters adopted. The mechanical design of a typical star tracker cluster - to the extent required to assure overall feasibility - proceeded simultaneously, with appropriate attention paid to the practicality of initial alignment and maintenance of such alignment during launch and orbital environment periods. Additionally, the feasibility of appropriate signal processing techniques was investigated and the appropriate design parameters and a preliminary signal processing system were developed.

The error analysis task consisted principally of identification of all contributors to total system pointing error and generation of an error model, the assessment/evaluation of probable error magnitudes and their variation with changes in environmental conditions and the overall evaluation/ solution of the error model. A separate portion of this task was the assessment of existing laboratory measurement techniques and the problems in achieving an adequate calibration of the STARS mechanism in the laboratory and in orbit, so that the full .001 degree pointing accuracy may be realized.

2.   System Analysis

2.1   System Operation

The system configuration studied applies to the 500 mile sun-synchronous circular orbit selected by NASA as the baseline orbit since such an orbit is a prime candidate for a precision pointing mission. The approach is straightforward in conceptual mechanization. If a platform that is stabilized in inertial space is to be mounted on an earth pointing vehicle in an inclined orbit, there are, excluding perturbations, two essentially independent motions (rotations) of the satellite that must be allowed for (or unwound) by a gimbal system between satellite body and inertial platform. These are the once-per-orbit pitch rotation caused by earth pointing and the longer period precession of the orbit caused by the earth's oblateness. Thus, for a fixed inclination orbit, one gimbal axis may be the satellite pitch axis, while the other gimbal axis is oriented parallel to the earth's pole (the axis about which the orbital precession takes place). As shown diagrammatically in Figure 2-1 for the sun-synchronous orbit, such a set of two nonorthogonal gimbals, with the included angle determined by the orbital inclination, will suffice to unwind both of the principal motions of the satellite. Since the pitch axis rotates once per year in inertial space the pitch gimbal must be the outer gimbal. The basic system concept here is as follows:

1)   Use a stellar reference to establish an inertially fixed coordinate system.

2)   Calculate the correct gimbal angles for the nonorthogonal set described above, based on ground determined and regularly updated ephemeris data and using an on-board computer.

3)   Set and maintain the gimbal angles as continuously computed in item 2.

4)   Obtain error signals from the stellar reference, transform them in the on-board computer into body coordinates, and use these transformed error signals as inputs to the body attitude control system.

At this point, only the system in its idealized form has been described. Clearly, there are a number of perturbing effects and error sources which must be accommodated in any realistic system mechanization. Since the gimbal angle (angle between pitch and polar gimbal axes) is built into the mechanism, as determined by the selected orbit inclination, any actual deviations from this inclination can produce pointing errors in the absence of corrective measures. If the polar gimbal axis is maintained by the stellar reference unit parallel to the earth's pole, even 0.001 degree deviation from the prescribed inclination will produce 0.001 degree pointing error twice per orbit. Apart from the difficulty of placing a satellite in orbit with such precision, there are a number of disturbing forces (as discussed in subsection 2.2.3) which cause inclination errors and resultant pointing errors many times larger than can be tolerated. Another significant effect which affects the satellite's reference system is the precession of the earth's pole around the ecliptic pole. Although the period of that precession is over 28,000 years, a pointing system which depends on an inertially fixed earth's polar axis would be in error by over 20 arcsec in 1 year. Therefore, some means must be provided to compensate for the various deviations from an ideal orbit that will be encountered.

Although frequent orbit corrections could solve these problems the fuel penalty associated with such a scheme makes it extremely unattractive since it is proportionately very expensive to change orbital inclination. The selected approach, one that still retains the fixed angle between pitch and polar axis, is to offset the electrical center of the star trackers by the amount of the instantaneous inclination error, as calculated by the computer, thereby maintaining the pitch and roll axes horizontal as required. This approach will permit star tracking using the attitude control system, while the vehicle yaw axis is held vertical by keeping the proper computer angular relationship between vehicle and stellar reference. An additional benefit of this offset tracking capability is to facilitate the initial acquisition of the stellar reference under realistic spacecraft dynamic conditions.

The stellar reference consists of a cluster of eight star trackers, all of which are mounted solidly to the same platform so that they cannot move with respect to each other.

The cluster can move only as a unit in the previously described gimbal system. Each star tracker is assigned to a particular star, the stars being selected so that at least two of the eight trackers can see their assigned stars at any specific time, regardless of the particular orbital geometry existing at that time. Since the star tracker cluster ideally stays rotationally fixed in inertial space while the satellite and earth rotate around it, the ideal star locations are uniformly distributed through the celestial sphere. Further, since the earth at any one time occults essentially a hemisphere (depending on orbit altitude), a set of six stars, located at the corners of an octahedron, inscribed in the celestial sphere would ideally be sufficient for attitude determination. With such a star set, it would always be possible to find two stars, 90 degrees apart, in any arbitrary hemisphere. However, with a real earth, a real horizon, and sun-, moon-, and earthshine interference problems, six stars are not sufficient. The use of seven stars does not significantly improve the situation; it takes at least eight stars, ideally located at the vertices of a "square antiprism," (see Figure 2-2) to permit adequate visibility of at least two of the eight with any arbitrary spacecraft attitude. In actuality, a real set of stars must be found whose positions come close to the desired positions. Additional constraints that should be placed on the particular stars used are that they not be near the ecliptic plane. The latter constraint will prevent temporary blinding and loss of attitude information as a result of appearance of the sun or moon in the field of view. The factors considered in the search for a satisfactory set of eight reference stars, some of the candidate sets examined, and the evolution of the set selected as the baseline set for the feasibility study, are discussed in the following section.
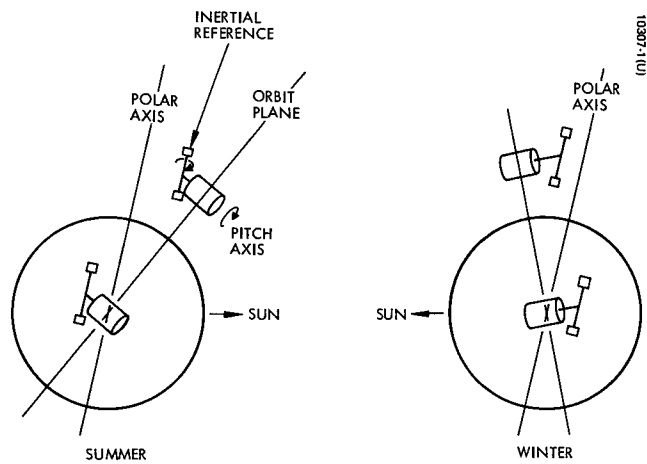
Figure 2-1. Gimbal System Function in Sun-synchronous Orbit
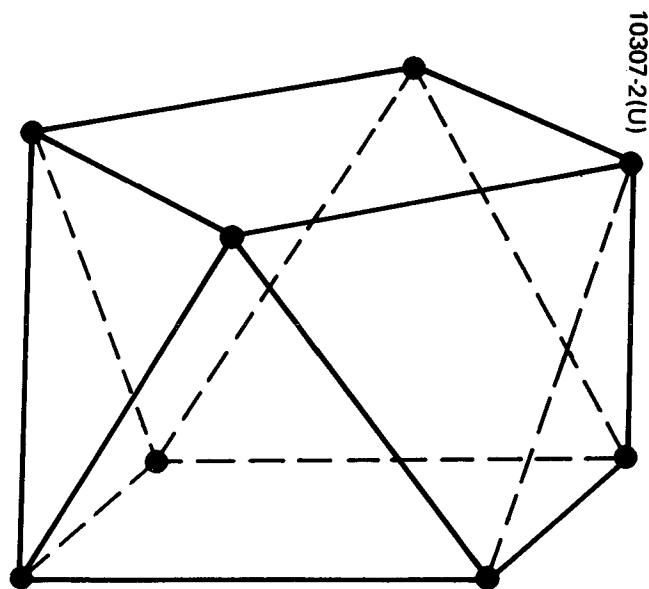
Figure 2-2. Square Antiprism

2.2 Star Visibility

It was recognized from the beginning of the STARS study that the selection of a satisfactory set of reference stars was a corner stone to the entire feasibility study. The original STARS proposal listed a set of eight stars (Table 2-1) which appeared to be satisfactory based on purely analytical considerations. However, the realities of star tracker optical systems and practical sunshades must be considered. It then becomes clear that the use of stars - even bright stars - that can lie much less than 30 degrees away from the sun at any time during a satellite's lifetime, makes the design of the corresponding star trackers extremely difficult. A basic measure of a stars' acceptability, apart from its brightness, is therefore its declination in ecliptic coordinates.

TABLE 2-1. ORIGINAL STAR SET

No.	NAME	EQUATORIAL COORDINATES		ECLIPTIC
		R. A. (deg)	Dec. (deg.)	DECLINATION (Deg.)
1	Sirius	100.93	-16.67	-39.65
5	Achernar	24.13	-57.40	-59.27
9	Capella	78.58	45.97	22.75
50	θ Scorpio	263.75	-42.98	-19.53
51	Mizar	200.66	55.09	56.27
70	Markab	345.79	15.03	19.41
74	Rasalhague	263.36	12.58	35.90
86	Gienah	183.54	-17.36	-14.47

A review of this original star set indicates that four out of the eight stars have ecliptic declinations less than 30 degrees. And in particular, two of the weakest stars, Markab and Gienah, are in this category. In fact Gienah, the weakest of the eight, lies only 14.5 degrees away from the ecliptic. It is obvious therefore that this set of stars is an impractical one in terms of sensor design. Table 2-2 is a computer printout on the 100 brightest stars, giving the details required to permit a better directed search for a suitable reference star set.

TABLE 2-2. STAR LIST

		IRRAD.	EQUATØRIAL CØØRD.		ECLIPTIC CØØRD.	
			R.A.	DEC.	R.A.	DEC.
1	SIRIUS	49.00	100.93	-16.67	103.65	-39.65
2	CANØPUS	20.00	95.81	-52.68	104.60	-75.73
3	VEGA	10.50	278.96	38.75	284.88	61.73
4	RIGEL	9.00	78.25	-8.24	76.36	-31.19
5	ACHERNAR	8.00	24.13	-57.40	344.72	-59.27
6	HADAR	6.80	210.39	-60.22	233.37	-44.01
7	RIGIL KENTAURUS	6.60	219.35	-60.70	239.09	-42.46
8	ACRUX	6.10	186.20	-62.92	221.48	-52.75
9	CAPELLA	5.60	78.58	45.97	81.41	22.75
10	ARCTURUS	5.30	213.55	19.35	203.70	30.76
11	PRØCYØN	5.10	114.41	5.31	115.36	-16.08
12	SPICA	5.00	200.88	-11.00	203.37	-2.02
13	ALTAIR	4.30	297.31	8.78	301.35	29.36
14	MIMØSA	4.00	191.46	-59.51	221.25	-48.52
15	REGULUS	3.80	151.67	12.12	149.40	.41
16	ADHARA	3.50	104.34	-28.93	110.36	-51.40
17	DENEB	3.30	310.08	45.17	335.02	59.88
18	ALNILAM	3.30	83.65	-1.22	83.01	-24.58
19	SHAULA	3.30	262.86	-37.08	264.13	-13.68
20	BELLATRIX	3.20	80.85	6.32	80.48	-16.90
21	FØRMALHAUT	3.10	343.97	-29.79	333.37	-21.06
22	CASTØR	2.60	113.14	31.96	109.79	9.99
23	ALKAID	2.50	206.57	49.47	176.35	54.31
24	ALNITAK	2.50	84.79	-1.96	84.23	-25.37
25	ELNATH	2.40	81.07	28.58	82.13	5.28
26	ALIØTH	2.40	193.16	56.13	158.37	54.21
27	MURZIM	2.40	95.32	-17.94	96.74	-41.31
28	ALDEBARAN	2.30	68.52	16.45	69.32	-5.55
29	PØLLUX	2.30	115.84	28.11	112.77	6.59
30	MIAPLACIDUS	2.20	138.21	-69.59	211.76	-72.04
31	GAMMA VELA	2.20	122.14	-47.24	147.08	-64.42
32	CIH	2.20	13.69	60.54	43.53	48.69
33	BETELGEUSE	2.10	88.36	7.40	88.31	-16.12
34	SAIPH	2.10	86.56	-9.68	85.94	-33.14
35	NUNKI	2.10	283.32	-26.34	281.92	-3.35
36	KAUS AUSTRALIS	2.00	275.51	-34.40	274.61	-10.94
37	ALHENA	2.00	98.97	16.43	98.66	-6.83
38	PEACØCK	2.00	305.78	-56.84	293.34	-36.14
39	NAØS	1.90	120.61	-39.91	138.22	-58.34
40	AL NAIR	1.80	331.56	-47.12	315.42	-32.81
41	DELTA VELA	1.80	130.96	-54.59	168.72	-67.10
42	ANTARES	1.70	246.86	-26.36	249.29	-4.47
43	ALPHERATZ	1.70	1.68	28.91	13.89	25.63
44	MENKALINAN	1.60	89.30	44.95	89.47	21.39
45	MINTAKA	1.60	82.59	.32	81.94	-22.99
46	DZUBA	1.60	239.61	-22.53	242.09	-1.90
47	KAPPA SCØRPIØ	1.50	265.07	-39.02	266.01	-15.54
48	ALUDRA	1.50	110.71	-29.24	119.16	-50.64
49	MIRFAK	1.40	50.51	49.75	61.64	30.01
50	THETA SCØRPIØ	1.40	263.75	-42.98	265.14	-19.53

Table 2-2 (continued)

		IRRAD.	EQUATØRIAL CØØRD.		ECLIPTIC CØØRD.	
			R.A.	DEC.	R.A.	DEC.
51	MIZAR	1.40	200.66	55.09	165.12	56.27
52	E CENTAURUS	1.40	204.46	-53.30	225.13	-39.48
53	H CENTAURUS	1.40	218.37	-42.02	229.80	-25.42
54	KAPPA VELA	1.40	140.28	-54.87	178.62	-63.63
55	AVIØR	1.30	125.46	-59.41	172.99	-72.54
56	DENEBØLA	1.30	176.86	14.75	171.15	12.24
57	MUHLIFAIN	1.30	189.94	-48.78	211.91	-40.07
58	ALPHECCA	1.30	233.33	26.82	221.73	44.34
59	Z ØPHIUCHUS	1.30	248.85	-10.50	248.75	11.48
60	GACRUX	1.20	187.34	-56.93	216.34	-47.72
61	WEZEN	1.20	106.77	-26.34	112.99	-48.49
62	MERAK	1.20	164.98	56.55	138.93	45.01
63	ACRAB	1.20	240.89	-19.72	242.71	1.09
64	DUBHE	1.10	165.44	61.92	134.69	49.55
65	ATRIA	1.10	251.32	-68.97	260.45	-46.00
66	PØLARIS	1.10	30.43	89.12	88.12	65.90
67	SCUTULUM	1.10	137.64	-62.19	190.66	-69.34
68	ALPHA LUPUS	1.10	219.95	-47.25	233.06	-29.92
69	PHECDA	1.10	178.04	53.87	149.95	47.03
70	MARKAB	1.10	345.79	15.03	353.05	19.41
71	BETA LUPUS	1.10	224.11	-43.01	234.58	-24.95
72	U SCØRPIØ	1.10	262.15	-37.27	263.56	-13.90
73	TAU SCØRPIØ	1.10	248.47	-28.15	250.99	-6.02
74	RASALHAGUE	1.00	263.36	12.58	261.96	35.90
75	DELTA CENTAURUS	1.00	181.67	-50.54	207.08	-44.42
76	ZUBENESCH	1.00	228.82	-9.27	228.88	8.56
77	THETA AURIGA	1.00	89.38	37.21	89.49	13.66
78	ZETA PERSEUS	1.00	58.03	31.79	62.67	11.24
79	ALGENIB	1.00	2.90	15.01	8.73	12.58
80	SABIK	.98	257.14	-15.69	257.50	7.28
81	THETA CARINA	.97	160.45	-64.23	208.88	-62.01
82	EPSILØN PERSEUS	.97	58.93	39.92	65.23	19.01
83	PHI SCØRPIØ	.97	239.23	-26.02	242.47	-5.38
84	ZETA TAURUS	.96	83.93	21.12	84.33	-2.30
85	CAPH	.95	1.86	58.97	34.73	51.10
86	GEINAH	.95	183.54	-17.36	190.28	-14.47
87	GAMMA LUPUS	.95	233.25	-41.06	241.04	-21.14
88	Z SAGITTARIUS	.94	285.14	-29.93	283.17	-7.08
89	PHACT	.93	84.62	-34.09	81.69	-57.40
90	ZØSCA	.92	168.10	20.70	160.85	14.28
91	ALPHA ARA	.92	262.34	-49.85	264.48	-26.43
92	SIGMA SCØRPIØ	.90	244.81	-25.52	247.33	-3.95
93	ZETA CENTAURUS	.89	208.38	-47.13	224.51	-32.85
94	SADIR	.88	305.27	40.15	324.51	57.11
95	ALDERAMIN	.88	319.45	62.45	12.54	68.78
96	MU SCØRPIØ	.88	252.42	-37.99	255.69	-15.31
97	DELTA CRUX	.85	183.36	-58.57	215.28	-50.31
98	Z CANIS MAJØR	.85	94.77	-30.05	96.94	-53.41
99	DIPHDA	.83	10.50	-18.16	2.10	-20.77
100	A CN VN CARØLI	.82	193.63	38.49	174.03	40.06

This list gives, in addition to the conventional (equatorial) location coordinates of each star, the same location in ecliptic coordinates and the brightness (irradiance) of each star with respect to the spectral sensitivity of an S-20 photocathode. Based on the above mentioned considerations a new set of reference stars was found as listed in Table 2-3.

TABLE 2-3. IMPROVED SET OF EIGHT STARS

No.	Name	Equatorial Coordinates		Ecliptic Declination
		R.A.	Dec.	
10	Arcturus	213.55	19.35	30.76
13	Altair	297.31	8.78	29.36
32	Cih	13.69	60.54	48.69
62	Merak	164.98	56.55	45.01
4	Rigel	78.25	-8.24	-31.19
7	Rigil Kentaurus	218.35	-60.70	-42.46
31	Gamma Vela	122.14	-47.24	-64.42
40	Al Nair	331.56	-47.12	-32.81

Of these only Altair, a bright star, lies slightly below 30 degrees ecliptic declination (at 29.36 degrees). However, a rather dim star, Al Nair, lying at -32.81 degrees ecliptic declination, is used as one of the eight stars. Since the design of a tracker and sunshade for this star does entail difficulties because it is both dim and not very far from the sun, a search for a better star set is still indicated.

STAR ACCEPTABILITY CRITERION

To obtain a more realistic means of star selection, a star acceptability criterion was established which specified the minimum allowable star irradiance versus the star's ecliptic declination. The criterion used is based on experimental star tracker and sunshade performance for a scanning star sensor and on the assumption that the STARS sensors should be able to achieve at least a factor of two better performance.

The rationale for this conclusion is that the STARS tracker data rate is much higher than that of the other sensor since the STARS is a continuously tracking system whereas the other sensor uses a scanning technique. Figure 2-3 shows the STARS acceptability criterion and its relation to the experimental scanning sensor values.

The acceptability criterion of Figure 2-3 was applied to the list of 100 brightest stars (for an S-20 photocathode), using the GE-265 timesharing program *LISTB, described in the appendix. This program uses a seven straight line segment approximation to the actual acceptability curve. The resulting "filtered" list of stars is given in Table 2-4. It will be noted that AL NAIR, the one questionable star of Table 2-3, is not on this list. However, the fact that only one star of this last set is not acceptable indicates that this star set is not far from being satisfactory. Thus a search for a better set ought to use this set as a point of departure.

SELECTION OF BASELINE SET OF EIGHT REFERENCE STARS

As long as the reference star set is selected from the stars in Table 2-4, and the selected acceptability criterion is held to be valid, then sun, moon, or planet interference has been eliminated as a consideration in star selection. The selection need then be based only on 1) adequate star visibility during the entire satellite lifetime, considering other interference effects, and 2) reliability/redundancy considerations.

The other interference effects of concern here are due to satellite shine, i.e. reflection of sun or moon-light from portions of the satellite body or appendages into the star trackers. The many variables associated with sunshade design have so far prevented the development of a curve similar to that of Figure 2-3, but for reflected light. However, in its absence, experience dictates that the weakest of the eight stars should be at least 15 degrees above the local horizontal when it is used as one of the two reference stars.
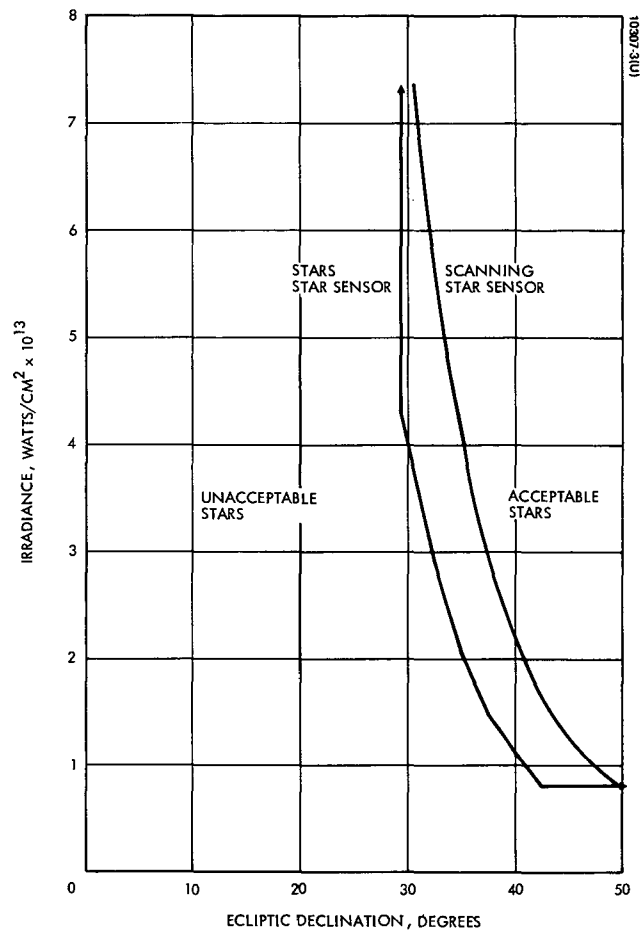
Figure 2-3. Star Acceptability Criterion

TABLE 2-4.

*LISTB   13:36   MON.   06/15/70

		IRRAD.	EQUATORIAL COORD. R.A.	DEC.	ECLIPTIC COORD. R.A.	DEC.
1	SIRIUS	49.00	100.93	-16.67	103.65	-39.65
2	CANOPUS	20.00	95.81	-52.68	104.60	-75.73
3	VEGA	10.50	278.96	38.75	284.88	61.73
4	RIGEL	9.00	78.25	-8.24	76.36	-31.19
5	ACHERNAR	8.00	24.13	-57.40	344.72	-59.27
6	HADAR	6.80	210.39	-60.22	233.37	-44.01
7	RIGIL KENTAURUS	6.60	219.35	-60.70	239.09	-42.46
8	ACRUX	6.10	186.20	-62.92	221.48	-52.75
10	ARCTURUS	5.30	213.55	19.35	203.70	30.76
13	ALTAIR	4.30	297.31	8.78	301.35	29.36
14	MIMOSA	4.00	191.46	-59.51	221.25	-48.52
16	ADHARA	3.50	104.34	-28.93	110.36	-51.40
17	DENEB	3.30	310.08	45.17	335.02	59.88
23	ALKAID	2.50	206.57	49.47	176.35	54.31
26	ALIOTH	2.40	193.16	56.13	158.37	54.21
27	MURZIM	2.40	95.32	-17.94	96.74	-41.31
30	MIAPLACIDUS	2.20	138.21	-69.59	211.76	-72.04
31	GAMMA VELA	2.20	122.14	-47.24	147.08	-64.42
32	CIH	2.20	13.69	60.54	43.53	48.69
38	PEACOCK	2.00	305.78	-56.84	293.34	-36.14
39	NAOS	1.90	120.61	-39.91	138.22	-58.34
41	DELTA VELA	1.80	130.96	-54.59	168.72	-67.10
48	ALUDRA	1.50	110.71	-29.24	119.16	-50.64
51	MIZAR	1.40	200.66	55.09	165.12	56.27
52	E CENTAURUS	1.40	204.46	-53.30	225.13	-39.48
54	KAPPA VELA	1.40	140.28	-54.87	178.62	-63.63
55	AVIOR	1.30	125.46	-59.41	172.99	-72.54
57	MUHLIFAIN	1.30	189.94	-48.78	211.91	-40.07
58	ALPHECCA	1.30	233.33	26.82	221.73	44.34
60	GACRUX	1.20	187.34	-56.93	216.34	-47.72
61	WEZEN	1.20	106.77	-26.34	112.99	-48.49
62	MERAK	1.20	164.98	56.55	138.93	45.01
64	DUBHE	1.10	165.44	61.92	134.69	49.55
65	ATRIA	1.10	251.32	-68.97	260.45	-46.00
66	POLARIS	1.10	30.43	89.12	88.12	65.90
67	SCUTULUM	1.10	137.64	-62.19	190.66	-69.34
69	PHECDA	1.10	178.04	53.87	149.95	47.03
75	DELTA CENTAURUS	1.00	181.67	-50.54	207.08	-44.42
81	THETA CARINA	.97	160.45	-64.23	208.88	-62.01
85	CAPH	.95	1.86	58.97	34.73	51.10
89	PHACT	.93	84.62	-34.09	81.69	-57.40
94	SADIR	.88	305.27	40.15	324.51	57.11
95	ALDERAMIN	.88	319.45	62.45	12.54	68.78
97	DELTA CRUX	.85	183.36	-58.57	215.28	-50.31
98	Z CANIS MAJOR	.85	94.77	-30.05	96.94	-53.41

THE ABOVE LISTED STARS SATISFY THE IRRADIANCE VS. ECLIPTIC
DECLINATION CRITERION DEFINED BY THE FOLLOWING COORDINATES:

IRRADIANCE > .81E-13 W/SQ CM
ECLIPTIC DECLINATION >29.30 DEGREES

DECL.	29.30	32.50	35.00	37.50	40.00	42.50
IRRAD.	4.30	2.90	2.05	2-11 1.47	1.10	.81

Figure 2-4.   100 Brightest Stars

The 15 degree requirement has been applied to all eight stars, keeping in mind that, on all but the weakest star, this requirement could be relaxed if it generated a problem.

A considerable number of star sets were evaluated during this investigation, utilizing as a principal tool a computer program (*VIS-1) which scans the entire celestial sphere and records the number of stars (of the eight selected stars) that meets the visibility criteria at every point checked. The output of this program is so formatted that it may be overlaid on a chart of the 100 brightest stars such as Figure 2-4, plotted on a rectangular right ascension - declination grid. Figure 2-5 is such a computer printout, using for the eight reference stars the set finally selected as the baseline set for the study, as given in Table 2-5. To improve legibility of the visibility chart, the computer was programmed to suppress the digit "3". As a result, it must be kept in mind that in all regions where the visibility chart is blank, three of the eight reference stars are visible above the minimum allowable elevation angle of 15 degrees. The 15 degree elevation contour for each of the eight stars has been drawn on the chart, so as to identify the particular stars visible at any selected position.

It will be noticed that over a very small portion of the celestial sphere, the visibility chart shows that only one of the eight selected stars is visible above 15 degrees elevation angle. To investigate this possible problem area, the computer was programmed to print out the star number, irradiance, and elevation angle of the four highest stars in those areas where only one star was located above 15 degrees. Table 2-6 shows both this printout and an assessment of star redundancy over the entire celestial sphere.

TABLE 2-5. BASELINE SET OF EIGHT SELECTED STARS

STAR NO.	STAR	IRRADIANCE 10^{-13} W/CM^2	EQUATORIAL COORDINATES		ECLIPTIC COORDINATES	
			RIGHT ASCENSION	DECLINATION	RIGHT ASCENSION	DECLINATION
4	RIGEL	9.00	78.25	- 8.24	76.36	-31.19
5	ACHERNAR	8.00	24.13	-57.40	344.72	-59.27
38	PEACOCK	2.00	305.78	-56.84	293.34	-36.14
41	DELTA VELA	1.80	130.96	-54.59	168.72	-67.10
10	ARCTURUS	5.30	213.55	19.35	203.70	30.76
13	ALTAIR	4.30	297.31	8.78	301.35	29.36
32	CIH	2.20	13.69	60.54	43.53	48.69
69	PHECDA	1.10	178.04	53.87	149.95	47.03
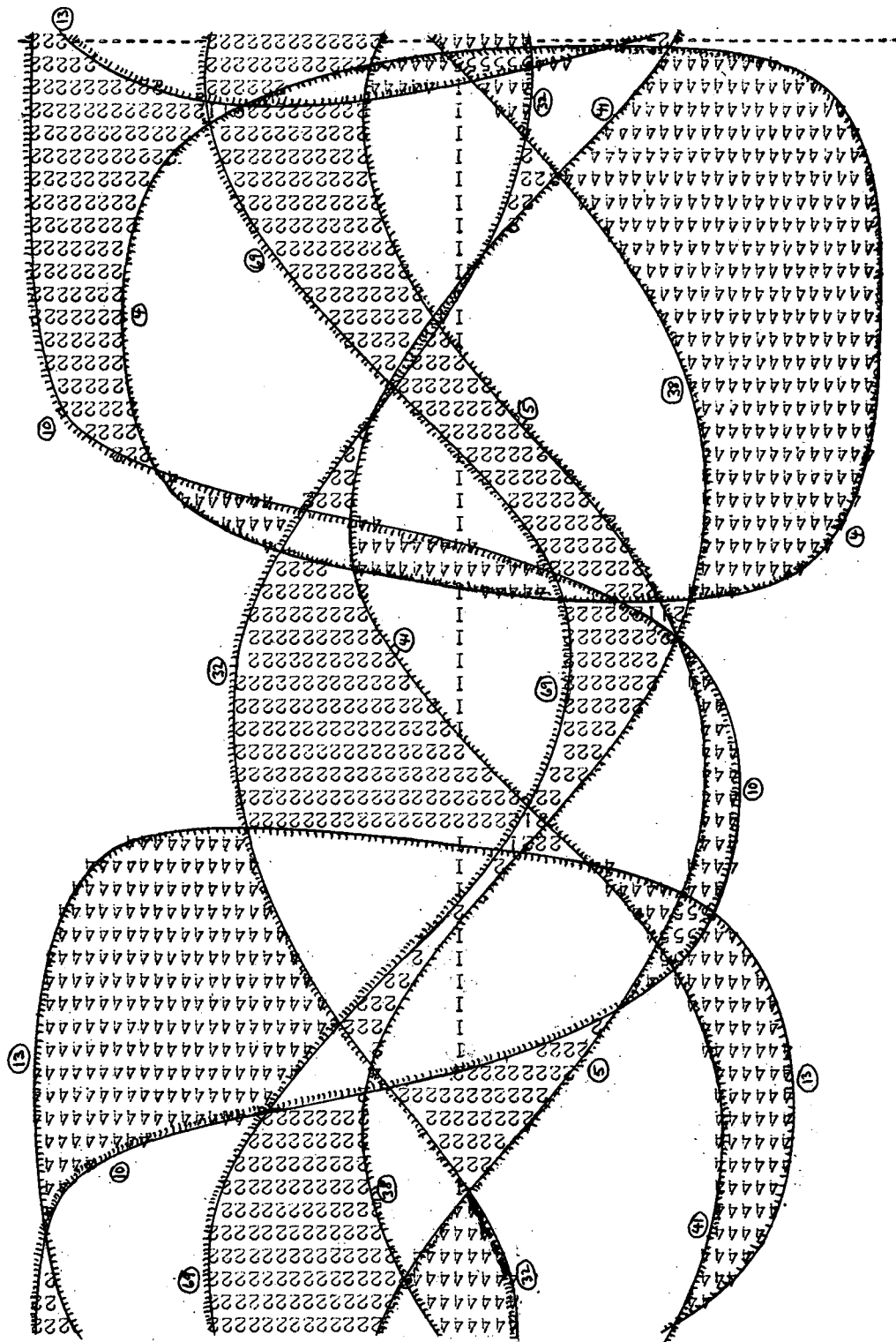
Figure 2-5. Star Visibility With Identifying Contours

10307-5(U)

TABLE 2-6.

THE NUMBER ØF TIMES EACH DIGIT APPEARS AND THE CØRRESPØNDING
PERCENT CØVERAGE ØF THE CELESTIAL SPHERE IS AS FØLLØWS:

DIGIT	FREQUENCY	PERCENT CØVERAGE
1	6	.20
2	753	24.45
3	2100	55.29
4	832	20.32
5	14	.49
6	0	.00
7	0	.00

AT THE LØCATIØNS WHERE ØNLY ØNE STAR IS VISIBLE ABØVE 15 DEGREES
THE FØUR HIGHEST STARS -'STAR NØ.(IRRAD.)ELEV.ANG.'- ARE AS FØLLØWS:

LØCATIØN [I-J]		1	2	3	4
35	-4	10[5.3]58.15	69[1.1]14.56	13[4.3]14.50	38[2.0]13.52
34	-5	10[5.3]56.92	69[1.1]14.69	41[1.8]12.91	38[2.0]12.26
25	-15	41[1.8]66.14	5[8.0]14.66	10[5.3]12.19	4[9.0]11.60
25	-14	41[1.8]64.14	10[5.3]13.88	5[8.0]12.17	4[9.0]11.55
3	17	32[2.2]75.01	4[9.0]14.56	13[4.3]11.91	69[1.1]11.38
3	18	32[2.2]77.66	69[1.1]14.01	4[9.0]13.25	13[4.3]11.92

As this table indicates, at the locations where only one star is visible above 15 degrees, the second star lies only slightly below 15 degrees. It is therefore apparent, particularly since the reflected light criterion depends strongly on the details of sunshade design and tends to be conservative, that this set of eight reference stars is entirely acceptable. Additional insurance exists in the fact that at the locations where the second reference star is lowest, a third and much brighter "backup" star is available at slightly lower elevation angle.

REDUNDANCY OF ATTITUDE REFERENCES

To evaluate the percent redundancy available from a given star set, considering the whole celestial sphere, the computer programs which generate the star visibility charts also keep track of the number of times each digit is printed and the declination at which it occurs. Thus data is then used to calculate the percentage coverage of the entire celestial sphere at each level of redundancy. Table 2-6 gives this information for the baseline star set. It can be seen that for more than 75 percent of the celestial sphere, complete attitude reference redundancy is available. Or, to say it another way, for any arbitrary, high inclination precessing orbit, three quarters of the time on the average more than two stars will be available for attitude reference purposes.

It is easily seen that the above described general redundancy values are strictly true only for a polar orbit since inclined, precessing orbits do not cover the entire celestial sphere. Thus, for any particular orbit the redundancy values should be evaluated separately. Such an evaluation was performed for the baseline star set for the specified 500 mile sun-synchronous orbit. Table 2-7 lists the average redundancy available in this orbit, in addition to specifying the redundancy at those times of the year when it is best and worst.

Clearly, since the inclination of this orbit is high the average redundancy is not markedly different from that of the entire celestial sphere. However, the two extremes do show a wide redundancy range.

TABLE 2-7.

PERCENT OF ORBIT OVER WHICH X STARS ARE VISIBLE

500 MILE SUN-SYNCHRONOUS ORBIT

No. of Stars X	Worst Case	Best Case	Average (1 Year)
1	0 percent	0 percent	0.2 percent
2	30.0	0.8	21.0
3	38.3	69.2	54.4
4	31.7	28.3	24.0
5	0	1.7	0.4
MORE THAN 2 STARS	70 percent	99.2 percent	78.8 percent

After the redundancy figures associated with the baseline star set were determined, two more stars were added to this set to cover those sections of the celestial sphere where the visibility chart showed poor or no redundancy. Redundancy for this augmented set of ten stars was then evaluated. The comparison between these two star sets, as shown in Table 2-8 indicates a significant increase in redundancy. Specifically, for the eight star (baseline) set, more than two stars are available over 75 percent of the time. When two more stars are added to this original set, the redundancy increases to over 91 percent.

TABLE 2-8.

PERCENT OF CELESTIAL SPHERE OVER WHICH X STARS ARE VISIBLE

No. of Stars X	8 Star Set	10 Star Set
1	0.2 percent	0 percent
2	24.1	8.5
3	55.1	33.0
4	20.1	38.5
5	0.5	19.6
6	0	0.4
MORE THAN 2 STARS	75.7 percent	91.5 percent

It was recognized at this point that still better overall redundancy might be obtainable for a set of ten stars if their selection were not based on the original set of eight. A completely new set of ten stars was then determined which improves the redundancy still more (to 95.5 percent). Thus it becomes clear that a set of ten stars, properly chosen, can provide almost complete redundancy over the entire celestial sphere.

2.3 Initial Acquisition

Approach

Initial acquisition of the stellar reference is a relatively straight-forward procedure, utilizing a conventional, passive, two-axis sun sensor mounted on the spacecraft with its sensitive axis preferably at right angles to the pitch axis. For a sun sensor, mounted to look along the spacecraft yaw axis, an illustrative acquisition or reacquisition sequence can be described as follows:

1) After orbit injection, the satellite is tracked for an appropriate period of time until ephemeris data are well established.

2) The on-board computer is directed to set the gimbal angles as determined from the ephemeris and local satellite time.

3) Sun acquisition is commanded by rotating the satellite successively about the roll and pitch axes until the sun sensor has acquired the sun in both axes.

4) The spacecraft is now rotated about the sun line as shown in Figure 2-6. Since the correct gimbal angles have been preset, star acquisition will occur automatically as the star trackers are rotated into the correct attitude.

The particular stars selected for acquisition purposes of course depend on spacecraft and earth occultation considerations at the time of acquisition. The whole acquisition procedure may be performed using ground commands or it may easily be automated.

False Acquisition

The details of the acquisition process and the possibility of false acquisition (acquisition of an incorrect star pair) were investigated in some detail. There are many star pairs that have the same included angle as any given pair of the eight reference stars, for a reasonable field of view for the STARS trackers. However, it is not immediately obvious whether a rotation about a sun line (any line lying in the ecliptic plane) could bring the corresponding pair of trackers into alignment with such an arbitrary but incorrect star pair. A digital computer program was written to investigate the possibility of such false acquisitions.

2-20

The question that had to be answered was: given a preselected pair
of reference stars (out of the set of eight), could the corresponding
star trackers accidentally see an incorrect pair of stars during the final
steps of the acquisition procedure?   The approach used to answer
this question was as follows:

1. Determine those star tracker pairs that could conceivably be
   used for acquisition.

2. Of all the stars (anywhere in the celestial sphere) that are
   bright enough to be detectable by a STARS star tracker, identify
   all those stars pairs whose included angle is essentially equal
   to that of any star tracker pair determined in 1. above.

3. For each star pair found in 2., determine whether a line exists
   in the ecliptic plane about which a rotation of the appropriate
   star trackers from the correct star pair could be performed
   to bring them into alignment with this alternate star pair.

4. Considering the field of view of the STARS trackers, could a
   false acquisition occur and if so, under what operational conditions.

Analysis

The initial step in evaluating the acquisition problem is step 1 above, i.e.,
the determination of those star tracker pairs that can be considered
eligible for use in the acquisition process. Table 2-9 is a list
of the included angles between all possible pairs of the eight baseline stars.
Now, since the 15 degree minimum elevation angle requirement specifies that
both stars of a pair be at least 15 degrees above the local horizontal
at the time of their use, the included angle for any usable pair must
be less than (180 - 2 x 15) = 150 degrees. This eliminates two out of the
28 possible star pairs listed.

Step 2 of the acquisition analysis is then to identify all the star
pairs (considering detectability by the STARS trackers) that have included
angles essentially equal of any of the 26 eligible values of Table 2-9.
Since the weakest of the eight stars used is No. 69 in our list of the 100
brightest stars (for an S-20 photocathode), the initial approach will be
to consider the first 99 brightest stars as candidates for possible false
acquisition.

2-21

TABLE 2-9.

STAR PAIR	INCL.ANGLE
4 - 5 :	64.3274
4 - 38 :	104.2308
4 - 41 :	62.3403
4 - 13 :	141.4102
4 - 10 :	135.3346
4 - 32 :	85.1662
4 - 69 :	102.4170
5 - 38 :	40.1304
5 - 41 :	53.4060
5 - 13 :	95.7012
5 - 10 :	141.3325
5 - 32 :	118.2249
5 - 69 :	164.9621
38 - 41 :	68.5031
38 - 13 :	65.9903
38 - 10 :	107.3073
38 - 32 :	128.8932
38 - 69 :	150.8771
41 - 13 :	132.9224
41 - 10 :	101.5117
41 - 32 :	147.1658
41 - 69 :	115.1912
13 - 10 :	81.2621
13 - 32 :	75.6944
13 - 69 :	99.3057
10 - 32 :	98.5225
10 - 69 :	43.9077
32 - 69 :	64.9237
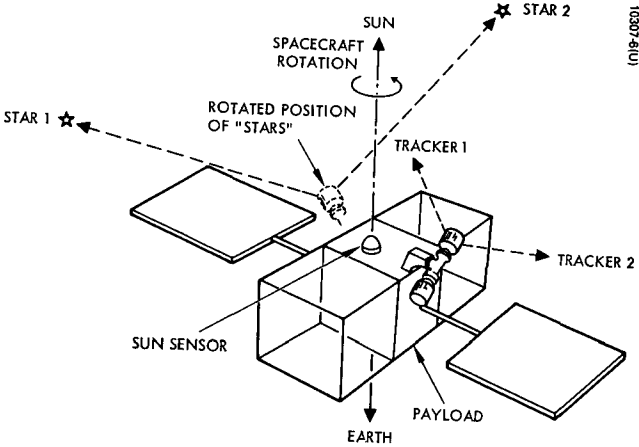
Figure 2-6. Star Acquisition by Rotation of Spacecraft About Sun Line

The approach taken is to examine all possible pairings of the 99 stars and compare the included angle of each pair with each of the 26 eligible tracker pair angles. If a match within two degrees is found, a record is made of the stars involved. A time-share computer program (ACQ-5*), developed to perform this search, takes each of the tracker pair angles of Table 2-9, and searches for corresponding matches among the 99 stars. The results are recorded, as shown in the appendix, and simultaneously written into computer files for later use by other programs. It will be noted that at this point, almost 3,500 possible star pairs have been found that must be considered as possible candidates for false acquisition.

The next step in the acquisition analysis is to determine for each star pair found above, if a line exists in the ecliptic plane (a sun line) about which a rotation of the appropriate star trackers from the correct star pair could be performed to bring them into alignment with this alternate pair. The initial step required is to locate the sun line which permits rotation of one star (No. 1) of the correct star pair (1, 3) into star 2 of the incorrect pair (2,4). This sun line lies at the intersection of the ecliptic plane and the plane which is the perpendicular bisector of the include angle between stars 1 and 2. Referring to Figure 2-7, the included angle between stars 1 and 2 is given by
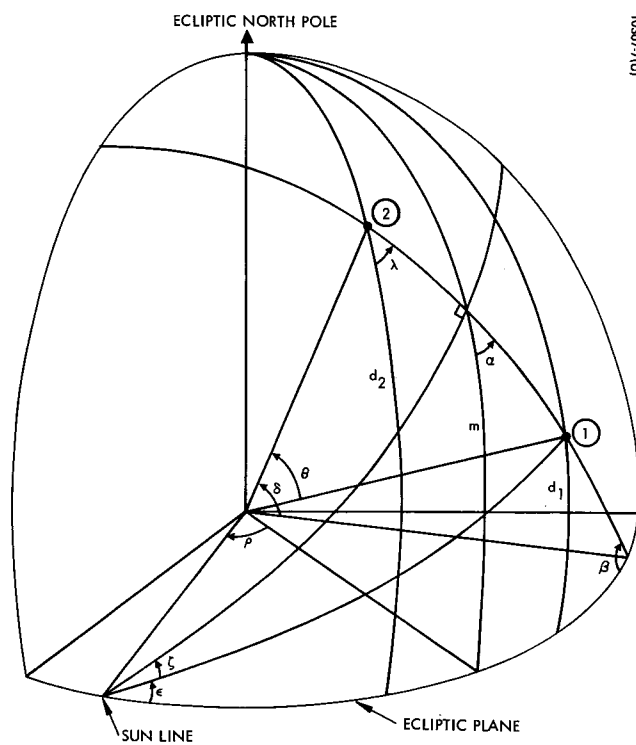
Figure 2-8. Rotation of Second Star About Sun Line
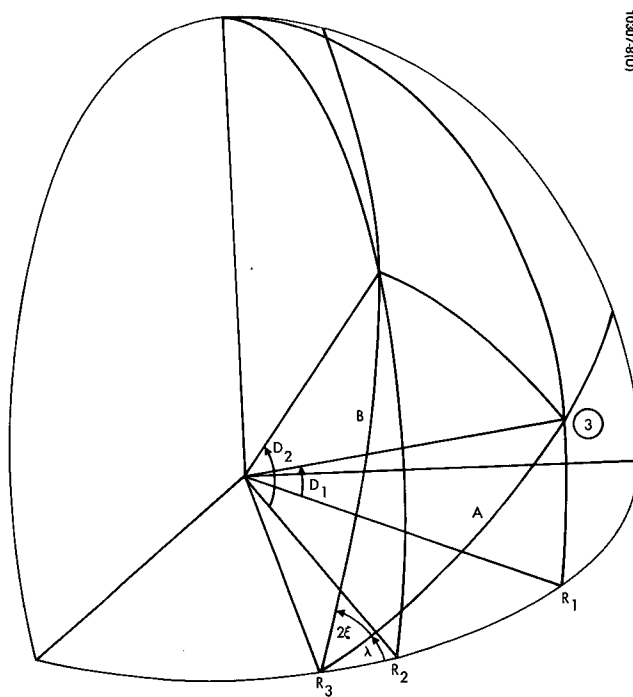
Figure 2-7. Determination Sun Line

1) $\quad \cos \theta = \sin d_1 \sin d_2 + \cos d_1 \cos d_2 \cos (r_2 - r_1)$

and the angles φ, β and δ are given by

2) $\quad \cos \varphi = \dfrac{\cos d_1 \cos (r_2 - r_1) \sin d_2 - \sin d_1 \cos d_2}{\sin \theta}$

3) $\quad \cos \beta = \sin \varphi \cos d_2$

4) $\quad \sin \delta = \dfrac{\sin d_2}{\sin \beta}$

The declination of the midpoint between stars 1 and 2 is then given by

5) $\quad \sin m = \sin \beta \sin (\delta - \theta/2)$

and the angle α is defined by

6) $\quad \sin \alpha = \dfrac{\cos \beta}{\cos m}$

The angle ρ which locates the required sun line is then found from

7) $\quad \tan \rho = \dfrac{\sin m}{\tan \alpha}$

The next quantity to be determined is the angle which defines the rotation of star 1 into star 2 about the sun line just determined. Referring again to Figure 2-7 angles ϵ and ζ are defined by

8) $\quad \cot \epsilon = \sin \left(\rho + \dfrac{r_2 - r_1}{2} \right) \cot d_1$

9) $\quad \cot (\epsilon + \zeta) = \sin \rho \cot m$

The angle to be rotated through is then 2ζ.

It is now necessary to rotate the second star (No. 3) of the correct pair through angle 2ζ. Referring to Figure 2-8, rotation occurs about the sun line at R_3. Now

10) $\quad \cos \lambda = \sin (R_3 - R_1) \cot D_1$

2-25

11) $\quad \sin A = \dfrac{\sin D_1}{\sin \lambda}$

and

12) $\quad \sin D_2 = \sin (\lambda + 2\zeta) \sin B.$

But, since the rotation occurs about OR_3,

13) $\quad B = A$

So that

14) $\quad \sin D_2 = \dfrac{\sin (\lambda + 2\zeta) \sin D_1}{\sin \lambda}$

and

15) $\quad \sin (R_3 - R_2) = \cot (\lambda + 2\zeta) \tan D_2$

Equations 14) and 15) give the location of the rotated star 3. It now remains to determine how close this rotated star is to the second star (No. 4) of the alternate set. This is easily done by using relation 1) to find the included angle between these two stars.
Clearly, if this included angle is within
the field of view of a star tracker, a false acquisition is possible.

Further thought will indicate that for each candidate star pair it is necessary to perform the above calculation four times since star 1 may be rotated into stars 2 or 4 and star 3 may be rotated into stars 2 or 4. Time share program ACQ-7* performs these calculations on all star pairs recorded previously as possible candidates for false acquisition and prints out details on those star pairs that come close to resulting in false acquisition. Table 2-10 shows a printout of this time share program using as a criterion the condition that only those cases will be recorded where the included angle between the stars to be matched is ten degrees or less. The number at the far left of each line printed indicates which of the four possible rotations has resulted in the particular line recorded.

2-26

TABLE 2-10.

ACQ-7*   15:39   MØN. 10/25/70

MISS(DEG)		TRACKER PAIR	OBSERVED PAIR	ECL-RA ØF SUN	APPRØX. DATE
2]	3.16	4- 5	1- 9	38.51	APRIL 29
1]	8.42	4- 5	9-27	38.51	APRIL 29
2]	9.12	4- 5	13-91	351.11	MARCH 12
3]	9.93	4- 5	17-49	5.23	MARCH 26
1]	9.21	4- 5	25-89	22.88	APRIL 13
3]	9.64	4- 5	38-75	283.90	JANUARY 3
4]	9.04	4- 5	44-95	21.93	APRIL 12
4]	8.70	4- 5	78-95	2.47	MARCH 23
2]	8.61	4-38	17-91	351.11	MARCH 12
4]	8.99	4-38	17-91	345.73	MARCH 7
3]	3.71	4-38	36-95	357.69	MARCH 19
1]	7.01	4-38	87-94	357.09	MARCH 18
2]	5.84	4-41	5-14	49.98	MAY 11
2]	2.32	4-41	5-97	52.31	MAY 13
4]	9.51	4-41	8-93	171.43	SEPTEMBER 11
2]	8.02	4-41	9-95	141.35	AUGUST 11
1]	5.30	4-41	11-56	86.53	JUNE 17
3]	5.73	4-41	11-56	82.76	JUNE 13
1]	8.60	4-41	22-51	79.90	JUNE 10
2]	6.23	4-41	25-66	156.02	AUGUST 26
3]	8.55	4-41	30-96	180.88	SEPTEMBER 20
2]	5.05	4-41	32-62	116.57	JULY 17
3]	6.95	4-41	34-54	136.34	AUGUST 6
3]	7.07	4-41	74-95	247.29	NØVEMBER 27
3]	6.89	4-13	19-45	169.02	SEPTEMBER 8
3]	4.57	4-13	43-54	311.51	JANUARY 31
4]	9.36	4-13	45-47	169.02	SEPTEMBER 8
4]	6.49	4-13	45-72	169.02	SEPTEMBER 8
4]	5.00	4-13	45-96	169.02	SEPTEMBER 8
1]	5.31	4-10	2-85	100.77	JULY 1
2]	.90	4-10	4-10	139.96	AUGUST 10
1]	.53	4-10	23-89	135.40	AUGUST 5
4]	8.93	4-10	85-91	224.56	NØVEMBER 4
2]	3.80	4-32	8-10	139.96	AUGUST 10
]	7.33	4-32	18-85	51.93	MAY 13
]	5.63	4-32	45-85	42.19	MAY 3
2]	2.01	4-32	55-56	120.26	JULY 21
4]	5.23	4-32	62-74	344.47	MARCH 5
2]	9.03	4-32	67-90	114.68	JULY 15
]	7.55	4-32	74-85	45.79	MAY 7
1]	8.79	4-32	84-95	21.75	APRIL 12
]	2.70	4-69	3-99	79.15	JUNE 9
]	9.33	4-69	4-52	23.50	APRIL 14
]	.56	4-69	12-66	156.02	AUGUST 26
]	8.88	4-69	16-69	121.78	JULY 22
]	6.23	4-69	22-75	80.71	JUNE 11
]	6.28	4-69	29-79	81.78	JUNE 12
]	9.03	4-69	48-64	119.39	JULY 20
]	4.14	4-69	48-69	121.78	JULY 22
]	8.63	4-69	61-69	121.78	JULY 22

TABLE 2-10. (Continued)

ACQ-7* CØNTINUED

MISS[DEG]		TRACKER PAIR	ØBSERVED PAIR	ECL-RA ØF SUN	APPRØX. DATE
2]	.94	5-38	5-38	345.35	MARCH 6
1]	1.67	5-38	8-91	288.05	JANUARY 7
2]	9.96	5-38	9-32	1.42	MARCH 22
1]	3.63	5-38	14-91	291.04	JANUARY 10
3]	1.93	5-38	17-32	352.49	MARCH 13
2]	6.97	5-38	18-77	10.62	APRIL 1
2]	8.98	5-38	18-78	2.47	MARCH 23
2]	1.32	5-38	20-82	5.60	MARCH 27
2]	5.62	5-38	24-77	10.62	APRIL 1
1]	3.53	5-38	25-34	9.19	MARCH 30
2]	7.62	5-38	33-82	5.60	MARCH 27
2]	8.82	5-38	45-78	2.47	MARCH 23
1]	4.95	5-38	49-84	5.23	MARCH 26
3]	5.94	5-38	54-93	267.46	DECEMBER 17
3]	6.03	5-38	67-93	267.46	DECEMBER 17
2]	.13	5-38	82-85	357.33	MARCH 18
4]	1.30	5-38	85-94	349.92	MARCH 11
4]	8.77	5-41	3-51	223.31	NØVEMBER 2
3]	1.30	5-41	10-64	146.49	AUGUST 17
3]	4.71	5-41	26-95	247.29	NØVEMBER 27
3]	1.40	5-41	51-95	247.29	NOVEMBER 27
2]	5.60	5-13	13-93	305.36	JANUARY 25
4]	8.21	5-13	17-40	359.85	MARCH 21
3]	4.92	5-13	40-48	18.84	APRIL 9
1]	8.28	5-13	43-88	312.62	FEBRUARY 1
1]	8.54	5-10	27-58	305.26	JANUARY 25
2]	5.31	5-10	57-70	272.67	DECEMBER 22
1]	.93	5-10	70-75	272.67	DECEMBER 22
3]	2.79	5-32	4-71	14.25	APRIL 4
3]	7.63	5-32	5-17	79.81	JUNE 10
3]	7.80	5-32	5-85	65.92	MAY 27
4]	7.33	5-32	26-31	70.53	JUNE 1
4]	7.61	5-32	46-89	40.90	MAY 1
4]	9.71	5-32	46-98	40.90	MAY 1
1]	7.64	5-32	55-79	48.82	MAY 9
2]	7.97	38-41	5-50	290.37	JANUARY 9
1]	9.69	38-41	26-94	340.43	MARCH 1
4]	7.03	38-13	3-35	13.51	APRIL 4
3]	3.03	38-13	58-96	250.15	NØVEMBER 30
2]	4.45	38-13	78-95	357.69	MARCH 19
2]	9.78	38-10	3-93	267.46	DECEMBER 17
2]	5.39	38-10	12-40	298.51	JANUARY 18
4]	4.73	38-10	12-40	291.46	JANUARY 11
2]	5.77	38-10	58-77	259.86	DECEMBER 9
4]	9.89	38-32	6-28	359.17	MARCH 20
2]	9.51	38-32	13-25	256.87	DECEMBER 6
2]	8.71	38-32	13-77	259.86	DECEMBER 9
3]	.41	38-32	16-80	31.60	APRIL 22
1]	9.87	38-32	22-74	210.73	ØCTØBER 21
3]	6.42	38-32	22-74	33.32	APRIL 24

TABLE 2-10. (Continued)

ACQ-7* CONTINUED

MISS[DEG]	TRACKER PAIR	OBSERVED PAIR	ECL-RA OF SUN	APPROX. DATE
3] 7.40	38-32	29-74	33.32	APRIL 24
3] 3.04	38-32	61-80	31.60	APRIL 22
1] 9.47	38-32	79-87	324.08	FEBRUARY 13
4] 7.77	41-13	29-65	329.36	FEBRUARY 18
2] 5.05	41-13	62-88	155.98	AUGUST 26
1] 5.94	41-10	3-68	223.31	NOVEMBER 2
2] 9.11	41-10	10-30	168.72	SEPTEMBER 8
2] 7.05	41-10	10-67	153.48	AUGUST 24
1] 2.62	41-10	12-66	131.41	AUGUST 1
1] 5.64	41-10	17-22	159.51	AUGUST 30
2] 9.00	41-10	23-52	165.35	SEPTEMBER 5
2] 3.14	41-10	23-75	147.63	AUGUST 18
3] 3.97	41-10	26-45	68.50	MAY 29
2] 7.34	41-10	51-93	161.89	SEPTEMBER 1
1] 1.31	41-10	53-69	165.27	SEPTEMBER 5
4] 9.03	41-10	59-66	140.08	AUGUST 10
2] 9.03	41-10	85-90	91.81	JUNE 22
1] 9.62	41-32	5-66	81.13	JUNE 11
2] 7.67	41-32	6-95	247.29	NOVEMBER 27
2] 9.88	41-32	52-95	247.29	NOVEMBER 27
4] 6.95	41-32	54-66	31.22	APRIL 22
2] 3.71	41-32	60-66	207.39	OCTOBER 17
4] 6.81	41-69	6-26	81.17	JUNE 11
4] 2.87	41-69	6-51	81.17	JUNE 11
4] 2.56	41-69	7-51	74.22	JUNE 4
1] 4.73	41-69	10-84	136.15	AUGUST 6
2] 3.28	41-69	11-76	161.89	SEPTEMBER 1
4] 4.42	41-69	23-39	181.47	SEPTEMBER 21
4] 9.37	41-69	23-48	181.47	SEPTEMBER 21
4] 7.80	41-69	26-39	200.24	OCTOBER 10
1] 6.99	41-69	31-64	164.33	SEPTEMBER 4
3] 3.60	41-69	31-64	168.03	SEPTEMBER 7
3] 8.57	41-69	37-93	21.57	APRIL 12
3] 4.03	41-69	39-51	195.03	OCTOBER 5
4] 4.51	41-69	46-66	43.02	MAY 4
4] 5.32	41-69	52-62	57.59	MAY 18
1] 4.57	41-69	54-62	136.34	AUGUST 6
1] 9.46	13-10	15-52	231.17	NOVEMBER 10
2] 3.23	13-10	15-53	183.23	SEPTEMBER 23
3] 7.49	13-10	27-99	102.46	JULY 3
2] 8.03	13-10	30-35	302.69	JANUARY 22
2] 7.03	13-10	93-98	307.78	JANUARY 27
] 3.18	13-32	1-57	264.11	DECEMBER 14
3] 7.99	13-32	2-84	21.75	APRIL 12
] 9.20	13-32	12-31	173.89	SEPTEMBER 13
2] 8.76	13-32	14-27	262.14	DECEMBER 12
2] 6.08	13-32	14-55	250.93	NOVEMBER 30
] 6.91	13-32	17-82	359.85	MARCH 21
] 6.87	13-32	27-60	262.14	DECEMBER 12
] 6.90	13-32	27-75	262.14	DECEMBER 12

TABLE 2-10.   (Continued)

ACQ-7* CONTINUED

MISS(DEG)	TRACKER PAIR	OBSERVED PAIR	ECL-RA OF SUN	APPROX. DATE
1) 9.41	13-32	27-97	262.14	DECEMBER 12
1) 3.16	13-32	28-39	176.10	SEPTEMBER 16
4) 9.86	13-32	40-59	278.86	DECEMBER 29
3) 8.85	13-69	2-46	43.02	MAY 4
4) 8.10	13-69	12-27	102.17	JULY 3
4) 3.50	13-69	14-18	102.55	JULY 3
4) 4.04	13-69	14-45	102.55	JULY 3
3) 6.75	13-69	22-79	137.67	AUGUST 8
2) 4.68	13-69	30-84	205.99	OCTOBER 16
3) 3.71	13-69	33-97	112.09	JULY 13
3) 7.63	13-69	45-60	99.32	JUNE 30
4) 5.23	10-32	10-32	82.14	JUNE 12
4) 5.01	10-32	10-85	82.14	JUNE 12
4) 9.43	10-32	16-21	10.97	APRIL 1
4) 9.54	10-32	18-21	10.07	MARCH 31
3) 1.64	10-32	21-24	4.60	MARCH 26
1) 9.19	10-32	25-54	123.57	JULY 24
3) 8.02	32-69	27-44	68.01	MAY 29
3) 5.85	32-69	58-66	203.39	OCTOBER 13
3) 2.48	32-69	61-77	78.57	JUNE 9

At this point, a realistic value must be selected for the acquisition field of view of the star trackers. Using two degrees as a typical value, the number of candiate cases for false acqusition is further reduced to the 17 listed in Table 2-11. Although this appears to be a relatively manageable number of possibilities, as far as operational limitations are concerned, a close look at the star visibility chart (Figure 2-5) applicable to this star set will show that the situation is really much better.

TABLE 2-11. CANDIDATE CASES FOR FALSE ACQUISITION

APPROX. DATE	TRACKER PAIR	OBSERVED PAIR	OFFSET (DEGREE)
January 7	5-38	8-91	1.67
March 6	5-38	38-5	0.94
March 11	5-38	85-94	1.30
March 13	5-38	17-32	1.93
March 18	5-38	82-85	0.13
March 26	10-32	21-24	1.64
March 27	5-38	20-82	1.32
April 22	38-32	16-80	0.41
May 13	4-41	5-97	2.32
July 21	4-32	55-56	2.01
August 5	4-10	23-89	0.53
August 10	4-10	10-4	0.90
August 17	5-41	10-64	1.30
August 26	4-69	12-66	0.56
September 5	41-10	53-69	1.31
November 27	5-41	51-95	1.40
December 22	5-10	70-75	0.93

It will now be noted that in all cases of Table 2-11 but one, the particular tracker pair listed need not be used for acquisition, since in those areas of the celestial sphere where the listed stars are both visible and needed for acquisition, at least one other star of our eight star set is also visible. Only the case of September 5 involves a star set (41-10) which must be used briefly during one orbit.

Further Studies

The initial acquisition study concerned itself with evaluation of false acquisition possibilities, considering the first 100 brightest stars, and based on the assumption that the STARS star trackers could be reliably thresholded so as not to detect signs weaker than No. 99. However, since No. 99 is only 0.75 as bright as No. 69, the weakest of our eight star set, the above assumption is not conservative. As a result, further acquisition studies were undertaken, this time considering the 200 brightest stars. This includes all stars whose irradiance is 0.4 times that of star No. 69 or brighter. Again, considering geometry only and a $\pm$ 1 degree acquisition field, the computer search identified 54 cases of possible false acquisition. However, as before, by choosing alternate stars for acquisition, 47 out of the 54 cases can be eliminated. Thus only seven cases remain at this point which could give rise to possible false acquisitions. These cases are listed in Table 2-12 where the numbers enclosed by parentheses represent (star No., irradiance), with irradiance in watts per cm^2 x 10^{13}. The particular matching of STARS trackers and observed stars as determined by the computer is indicated by the arrows.

It is possible, however to reduce this list of possible false acquisitions by taking advantage of the planned aperture reduction for the star trackers associated with the brighter stars. Specifically, it is assumed that the tracker associated with the brighter star (No. 69) does not see stars whose irradiance is less than 0.4 times that of star No. 69. Clearly, if the same criterion is applied to the brightest (No. 4) or any other of the eight stars, its tracker aperture can be reduced so that the tracker does not respond to stars weaker than 0.4 times the irradiance of No. 4.

TABLE 2-12. REMAINING CASES FOR FALSE ACQUISITION

DATE	TRACKER PAIR		OBSERVED PAIR
September 3	(41, 1.8)	→	(161, 0.53)
	(10, 5.3)	→	(10, 5.3)
September 5	(41, 1.8)	→	(54, 1.4)
	(10, 5.3)	→	(69, 1.1)
August 14	(4, 9.0)	→	(4, 9.0)
	(41, 1.8)	→	(179, 0.47)
August 1	(4, 9.0)	→	(111, 0.73)
	(41, 1.8)	→	(12, 5.0)
July 15	(4, 9.0)	→	(90, 0.92)
	(41, 1.8)	→	(144, 0.58)
August 17	(4, 9.0)	→	(115, 0.72)
	(41, 1.8)	→	(123, 0.68)
June 29	(4, 9.0)	→	(150, 0.56)
	(41, 1.8)	→	(125, 0.68)

Applying the above criterion to the first case listed in Table 2-12, the tracker assigned to star No. 41 (with irradiance of 1.8×10^{-13} w/cm^2) would not see stars weaker than 0.72×10^{-13} w/cm^2. Thus it could not see star No. 161 (whose irradiance is 0.53×10^{-13} w/cm^2) as indicated in the table. The aperture reduction scheme therefore could prevent a false acquisition in this case. It is seen that in every one of the other cases of Table 2-12, the appropriate aperture reduction will prevent any false acquisition since at least one star of each questionable pair is not observable by the associated tracker, with its aperture appropriately adjusted. As a result of these studies, it can therefore be stated unequivocally that false acquisition is not a problem for the STARS.
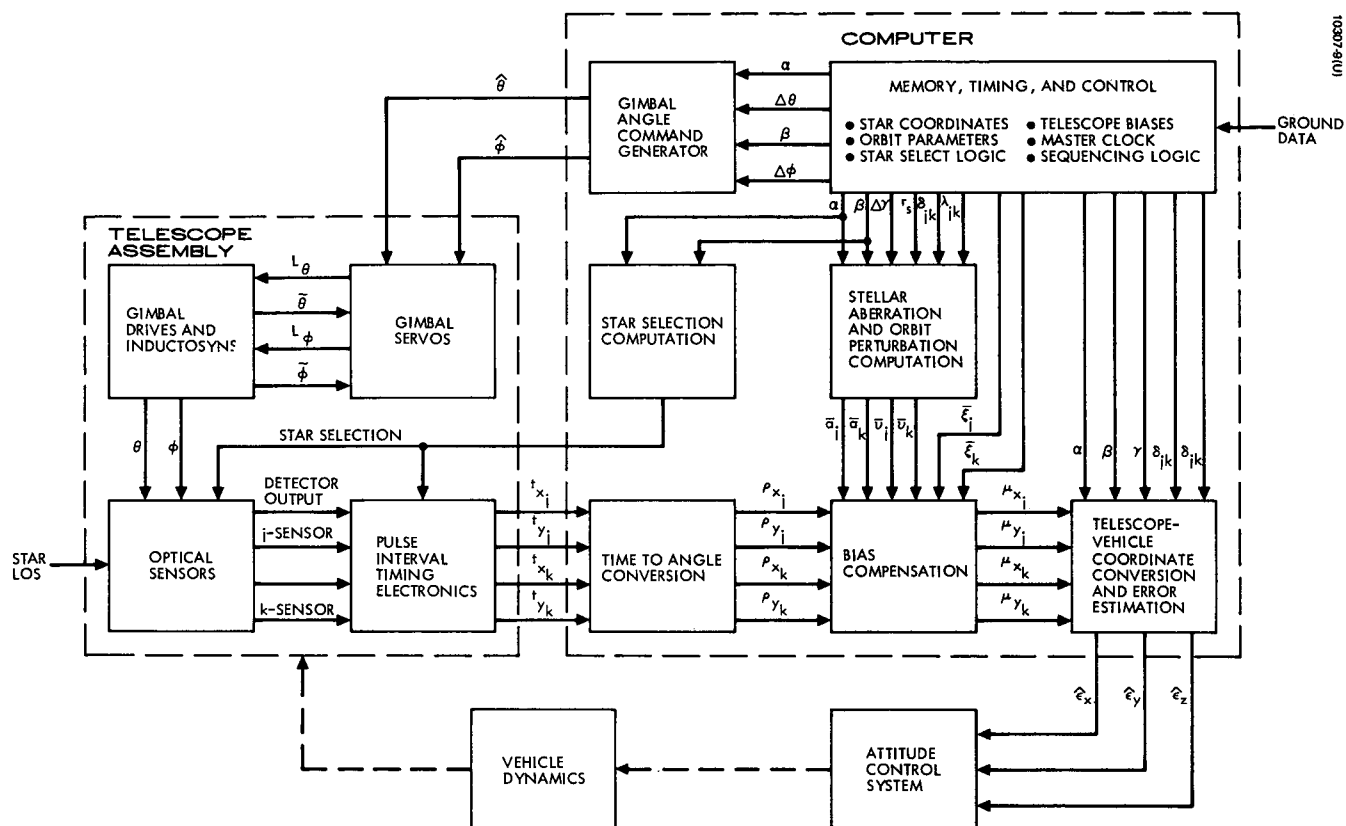
Figure 2-9. STARS Signal Flow Diagram

2.4 Computer Requirements

Introduction

A major component of the STARS as a complete system is the on-board electronics/computer unit which, although there are no feasibility questions associated with it, does require sufficient definition so that the entire system can be evaluated. To this end, the equations that are required to be evaluated by this on-board computer, have been developed. The basic functions of the computer are to:

1) Generate gimbal angle commands so that the telescope platform maintains the same orientation with respect to the vehicle axes that the celestial sphere has with the rotating local vertical reference frame.

2)   Convert pulse time interval measurements from the star sensor into signals proportional to the line of sight angular error components.

3) Compensate for known biases due to (a) stellar aberration, (b) orbit inclination error, and (c) telescope misalignments.

4) Transform the compensated error signals into vehicle coordinates and estimate the three vehicle attitude error components.

5) Provide master timing and control, including star selection based on star brightness and visibility constraints.

These operations and the functional interfaces between the computer, telescope assembly, and the vehicle attitude control system are depicted in Figure 2-9. A more detailed definition of the computer functions will be presented after first defining the appropriate coordinate frames and transformation matrices.
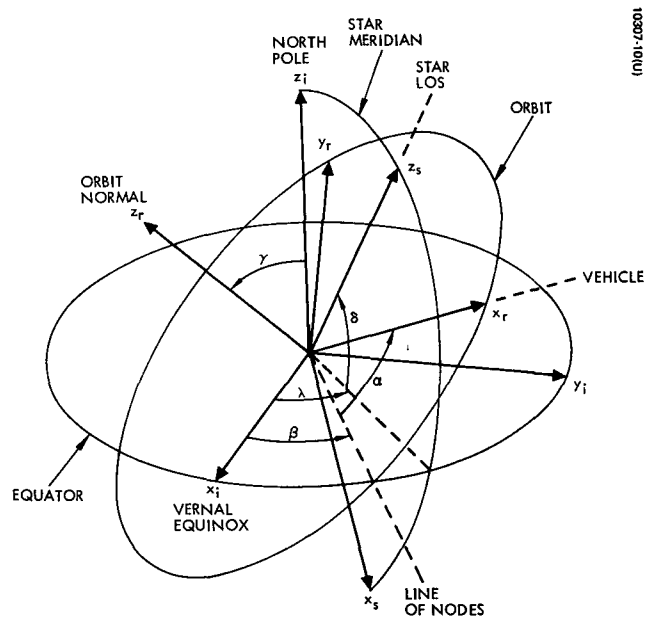
Figure 2-10. STARS Geometry

Coordinate Frames and Transformation Matrices

The simplicity of the STARS concept is based on the near coincidence of the gimbal and telescope axes with the corresponding orbit and star coordinate frames. Figure 2-10 defines the attitude reference and star coordinate frames with respect to the equatorial inertial frame. Except for certain small fixed and time varying biases, the angles and coordinate frames in the vehicle are identical to those shown in Figure 2-10.

The following coordinate frames will be used.

e-frame
Inertial frame with z_e along the ecliptic north pole and x_e along the vernal equinox.

i-frame
Inertial frame with z_i along the earth's north pole and x_i along the vernal equinox.

s-frame
Inertial frame with z_s along the star LOS and with $x_s z_s$ plane containing z_i.

r-frame
Attitude reference frame with z_r along the orbit normal and x_r along the local vertical.

b-frame
Frame fixed in the gimbal base and coinciding with the vehicle axes: x_b = yaw axis, y_b = roll axis, and z_b = pitch axis.

t-frame
Frame fixed in telescope platform (inner gimbal) with z_t along the boresight axis and the $x_t z_t$ plane containing z_a.

a-frame
Frame fixed in telescope platform with z_a along the gimbal polar axis and x_a coinciding with the "vernal equinox".

The two telescopes in use at any time are denoted by subscripts j and k, where it is understood j and k represent any of eight possible star/telescope.

Euler angles relating the various coordinate frames are as follows:

α = Orbit angle measured from ascending node (about $+ z_r$ axis)

β = Right ascension of line of nodes (about + z_i axis)

γ = Orbit inclination (about ascending line of nodes)

λ = Right ascension of star (about + z_i axis)

δ = Declination of star (about - y_s axis)

θ = Pitch gimbal angle (about "ascending line of nodes")

φ = Polar gimbal angle (about + z_a axis)

Ψ = Polar axis tilt (about "ascending line of nodes")

η = Right ascension of telescope boresight axis (about + z_a axis)

ζ = Declination of telescope boresight axis (about - y_t axis)

Transformation matrices relating the coordinate frames are as follows:

$$R^{se} = \begin{bmatrix} 1 & 0 & 0 \\ 0 & C\ 23.5^{o} & S\ 23.5^{o} \\ 0 & -S\ 23.5^{o} & C\ 23.5^{o} \end{bmatrix}$$

$$R^{si} = R_\delta\ R_\lambda = \begin{bmatrix} S\delta & 0 & -C\delta \\ 0 & 1 & 0 \\ C\delta & 0 & S\delta \end{bmatrix} \begin{bmatrix} C\lambda & S\lambda & 0 \\ -S\lambda & C\lambda & 0 \\ 0 & 0 & 1 \end{bmatrix}$$

$$R^{ri} = R_\alpha\ R_\gamma\ R_\beta = \begin{bmatrix} C\alpha & S\alpha & 0 \\ -S\alpha & C\alpha & 0 \\ 0 & 0 & 1 \end{bmatrix} \begin{bmatrix} 1 & 0 & 0 \\ 0 & C\gamma & S\gamma \\ 0 & -S\gamma & C\gamma \end{bmatrix} \begin{bmatrix} C\beta & S\beta & 0 \\ -S\beta & C\beta & 0 \\ 0 & 0 & 1 \end{bmatrix}$$

$$R^{ta} = R_\zeta\ R_\eta = \begin{bmatrix} S\zeta & 0 & -C\zeta \\ 0 & 1 & 0 \\ C\zeta & 0 & S\zeta \end{bmatrix} \begin{bmatrix} C\eta & S\eta & 0 \\ -S\eta & C\eta & 0 \\ 0 & 0 & 1 \end{bmatrix}$$

$$R^{ba} = R_\theta R_\psi R_\varphi = \begin{bmatrix} C\theta & S\theta & 0 \\ -S\theta & C\theta & 0 \\ 0 & 0 & 1 \end{bmatrix} \begin{bmatrix} 1 & 0 & 0 \\ 0 & C\Psi & S\Psi \\ 0 & -S\Psi & C\Psi \end{bmatrix} \begin{bmatrix} C\varphi & S\varphi & 0 \\ -S\varphi & C\varphi & 0 \\ 0 & 0 & 1 \end{bmatrix}$$

The symbol R^{nm} defines the transformation from the m-frame to the n-frame. Each of the above matrices is orthogonal and obeys the relation:

$$(R^{mn})^T = (R^{mn})^{-1} = R^{nm}$$

From these definitions, the following correspondences are seen to exist between the inertial set and vehicle set:

Inertial	Vehicle
i - frame	a - frame
s - frame	t - frame
r - frame	b - frame
α	θ
β	φ
γ	Ψ
δ	ζ
λ	η
R^{si}	R^{ta}
R^{ri}	R^{ba}

Gimbal Angle Commands

The STARS pitch axis and polar axis gimbals are nominally coincident with the orbit normal and earth's polar axis, respectively. The required gimbal motions, therefore, correspond to the orbital rate and nodal regression rate which are determined from ground track data.

y_t

y-SLIT   y-PIP

k

v

STAR IMAGE

ρ_y

x-PIP

-u

ρ_x

x_t

z_t

BORESIGHT
AXIS

x-SLIT
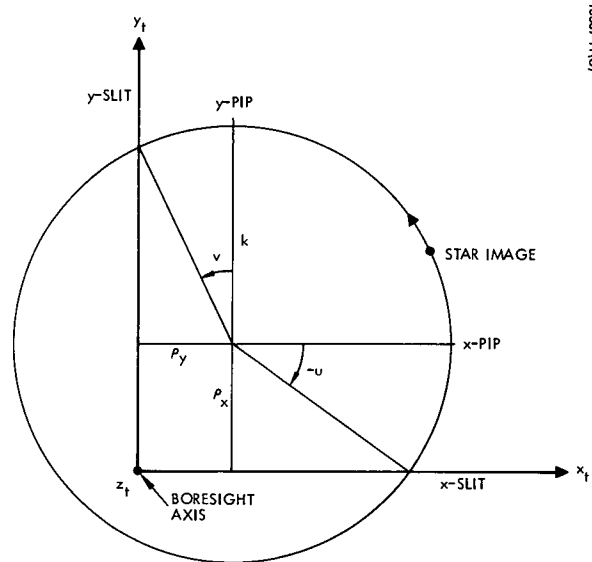
k = 0.7° $|\rho_x| < 0.5°$ $|\rho_y| < 0.5°$

$u = \sin^{-1} \rho_x / k$ $t_x = -\dfrac{T}{2\pi} u$

$v = \sin^{-1} \rho_y / k$ $t_y = \dfrac{T}{2\pi} v$

Figure 2-11. STARS Sensor Scan Geometry

Gimbal servo bias errors can be directly compensated in the commands. Thus

$$\theta(t) = \alpha(t) + \Delta\theta$$

$$\varphi(t) = \beta(t) + \Delta\varphi$$

where $\Delta\theta$ and $\Delta\varphi$ are the bias compensation terms. Normally only the fixed biases need to be compensated.

The signals to the gimbal servos are in the form of a pulse train where each pulse represents an increment of 1.8 arc seconds, corresponding to the resolution element of the incremental shaft encoders.

Sensor Error Conversion

A rotating prism in the telescope causes the star image to trace a circular path on the focal plane as shown in Figure 2-11. Two orthogonal slits in the focal plane gate the radiant energy into the photo detector. The reticle slits are aligned with the telescope reference axes x_t and y_t. Reference pulses are generated at 90 degree intervals in synchronism with the scan, and the error signals are produced by counting the time interval between the reference pulses and the respective star pulses. The sample period is 0.25 seconds, corresponding to the scan rate of 4 Hertz.

From the geometry it can be seen that the scan angle between reference pulse and star pulse varies as the inverse sine of the error angle. With a uniform scan rate the time intervals measured are:

$$t_x = -\frac{T}{2\pi} \sin^{-1} \rho_x/k$$

$$t_y = \frac{T}{2\pi} \sin^{-1} \rho_y/k$$

where T is the scan period, k is the scan circle radius, and ρ_x and ρ_y are the error angles.

The conversion from time interval to equivalent angular error therefore requires a sine function operation:

$$\rho_x = k \sin \frac{2\pi t_x}{T}$$

$$\rho_y = k \sin \frac{2\pi t_y}{T}$$

Since the computer will be equipped with a sine function, it is reasonable to include this operation in the computer instead of the sensor electronics.

Stellar Aberration

For arc second level accuracy, the effects of stellar aberration cannot be ignored. The component due to the earth's velocity about the sun can be as large as 20 arc seconds, and the component due to the spacecraft velocity about the earth can be as large as 5.0 arc seconds.

The aberration angle, $\underline{a}$, can be computed from the following expression:

$$\underline{a} = \frac{\underline{V} \times \underline{lc}}{c}$$

where $\underline{V}$ = total velocity of spacecraft

$\underline{lc}$ = unit vector along LOS.

c = speed of light

To determine the components of the aberration angle in the star coordinate frame, we must solve for the total velocity in the s-frame. We start by defining total velocity as:

$$\underline{V} = \underline{Vo} + \underline{v}$$

where $\underline{Vo}$ = velocity of earth about sun

$\underline{v}$ = velocity of vehicle about earth

In ecliptic coordinates (e-frame) this can be expressed as:

$$\overline{V}^{ev} = \overline{V}^{ei} + R^{ei} \, \overline{v}^{iv}$$

where
$$\overline{V}^{ei} = Vo \begin{bmatrix} C\Lambda t \\ S\Lambda t \\ 0 \end{bmatrix}$$

Vo = magnitude of $\underline{Vo}$

Λ = orbital rate of earth about sun.

and
$$\bar{v}^{iv} = r_o R_\beta^T R_\gamma^T \begin{bmatrix} -\dot{\alpha} \, S\alpha \\ \dot{\alpha} \, C\alpha \\ 0 \end{bmatrix}$$

r_o = distance from earth center to vehicle

Then applying the transformation $R^{se} = R^{si} R^{ie}$ we obtain

$$\bar{V}^{sv} = R^{se} \bar{V}^{ev} = R^{si} R^{ie} \bar{V}^{ei} + R^{si} \bar{v}^{iv}$$

Defining the components as

$$\bar{V}^{sv} = \begin{bmatrix} V_x \\ V_y \\ V_z \end{bmatrix}^{sv}$$

the components of $\bar{a}$ in star coordinates are given by:

$$\bar{a}^{s} = \frac{1}{c} \begin{bmatrix} 0 & -V_z & V_y \\ V_z & 0 & -V_x \\ -V_y & V_x & 0 \end{bmatrix}^{sv} \begin{bmatrix} 0 \\ 0 \\ 1 \end{bmatrix}^{s} = \frac{1}{c} \begin{bmatrix} V_y \\ -V_x \\ 0 \end{bmatrix}^{sv}$$

Note that there are three time varying terms: α, β, and Λt. The latter two vary slowly enough to permit ground computation and update of those terms. However, the terms in α would have to be evaluated on-board since they are of orbital period.

Orbit Inclination Error

Once the spacecraft has been injected into the desired circular orbit, its orbital characteristics will change due to the combined perturbative effect of aerodynamic, magnetic, and radiation pressure forces, the oblateness of the earth (zonal harmonics), ellipticity of the earth's equator (tesseral harmonics), and lunar-solar gravitational attraction. Since the STARS gimbal assembly has a fixed inclination angle, ψ, between the pitch and polar axes, the effect of launch dispersions and the above perturbations must be accounted for by the computer.

A study of inclination change can be carried out by numerically integrating the equations of motion, or the Lagrange planetary equation for inclination change over the desired mission lifetime. However, this approach becomes prohibitively expensive for preliminary design studies for mission lifetimes on the order of several years. A study has been performed at Hughes to determine the analytic character of these inclination perturbations. The resulting formulas for the inclination change due to lunar-solar effects when combined with the well-known results for asphericity perturbations greatly expedite the long-term prediction of inclination perturbations.

Lunar-Solar Perturbations

The combined effect of the sun and moon will result in a periodic variation as well as a secular change in the inclination of the reference orbit. In particular, it can be shown that the magnitude of the secular effects of the sun and moon can be approximated by

$$\Delta i_M = \frac{3\mu_M t}{r_M^3} \frac{\left| \sin \overline{i}_M \cos \overline{i}_M \right|}{4n} \quad \left.\begin{array}{c} \\ \\ \end{array}\right\} \text{ for polar or } \quad (1)$$

$$\Delta i_S = \frac{3\mu_S t}{r_S^3} \frac{\left| \sin \overline{i}_S \cos \overline{i}_S \right|}{4n} \quad \left.\begin{array}{c} \text{equatorial} \\ \text{orbits} \end{array}\right. \quad (2)$$

$$\Delta i_M = \frac{3\mu_M t}{4 n r_M^3} \left| \sin i \cos i \left(1 - \frac{3}{2} \sin^2 i_M \right) \right| \tag{3}$$

$$\Delta i_S = \frac{3\mu_S t}{4 n r_S^3} |\sin i| \left\{ \sin^2 2 (\Omega_o - U_{So}) + \frac{1}{4} \cos^2 i \left[1 - 3 \cos^2 i_S \right. \right.$$
$$\left. \left. + 2 \cos i_S \cos 2(\Omega_o - U_{So}) \right]^2 \right\}^{1/2} \tag{4}$$

for sun-synchronous orbits, In these expressions, Δi_M, Δi_S are respectively defined as the magnitudes of the inclination change due to the gravitational attraction of the moon and of the sun; μ_M, μ_S are respectively the gravitational constants associated with the moon and sun; r_M, r_S are respectively the geocentric radial distance to the moon and sun; $\bar{i}_M$, $\bar{i}_S$ are respectively the relative inclination of the moon's orbit or sun's orbit to the reference circular orbit plane; U_{So} is the argument of latitude of the sun's position vector at $t = 0^*$ (which corresponds to the epoch of insertion into the reference circular orbit); n is the mean motion of the reference circular orbit, $n = 2\pi/P$, P = period of orbit; Ω_o is the node of the reference orbit at $t = 0^*$; i is the inclination in the reference orbit*; i_M and i_S are respectively the inclination of the moon's and sun's orbit.*

For the special case of a twilight sun-synchronous orbit, the angle

$$\Omega_o - U_{So} = \frac{\pi}{2} \text{ or } \frac{3}{2} \pi,$$

i.e., the angle between the sun's position vector and the orbit plane of the reference orbit at $t = 0$; hence,

$$\Delta i_S = \frac{3\mu_S t}{8 n r_S^3} |\sin i \cos i| \left[1 - 3 \cos^2 i_S \pm 2 \cos i_S \right]^{1/2} \tag{5}$$

---

* These angles are measured in an equatorial vernal equinox coordinate system, i.e., $U_S o = 0$ when the sun crosses the equator at the ascending node.

TABLE 2-13. ORDER OF MAGNITUDE OF INCLINATION CHANGE
DUE TO PERTURBATIVE EFFECTS

Lunar - Solar Secular degrees	Lunar - Solar Periodic degrees	Earth Oblateness J_2, Periodic degrees	Earth Ellipticity J_{22}, Periodic, degrees
$0.13 \times 10^{-3} r^{3/2} t$	$7.0 \, r^{3/2} 10^{-3}$	$\dfrac{43.0 \times 10^{-3}}{r^2} \sin^2 i$	$\dfrac{0.15 \times 10^{-3}}{r^{7/2}} \sin i$

NOTE: r = earth radii,   t = days,   i = inclination of orbit

Similarly, for the baseline case of a noon-midnight orbit, the angle $\Omega_o - U_{So} = 0$ or π; hence,

$$\Delta i_S = \frac{3\mu_S t}{8nr_S^3} \left| \sin i \cos i \right| \left[1 - 3 \cos^2 i_S + 2 \cos i_S \right]^{1/2} \quad (6)$$

Asphericity Perturbations

The reference orbit will also be perturbed by the oblateness of the earth and by the ellipticity of the earth's equator. Neither of these effects will give rise to a secular growth in inclination. However, these effect will result in a periodic oscillation of inclination about its reference value.

The change in inclination due to oblateness (only J_2 has been considered) is given by

$$\Delta i = -\frac{3}{4} \frac{J_2}{r^2} \sin 2 i \sin^2 u \quad (\text{rad}) \quad (7)$$

where J_2 is the oblateness constant, r is the geocentric radius of the reference orbit (in earth radii), and u = nt. The node of the reference orbit will regress due to J_2 at a rate

$$\Delta \Omega = \frac{-1.5tn \; J_2 \cos i}{r^2} \quad (\text{rad}) \quad (8)$$

If $\Delta \Omega$ is set equal to the angular travel of the sun in its orbit, the resulting orbit will be sun-synchronous. Thus, the condition for a sun-synchronous orbit is simply

$$\cos i = -0.0995 \; r^{7/2} \quad (9)$$

The ellipticity of the earth's equator will only result in oscillations in inclination of amplitude on the order of $(3 \; J_{22} \sin i)/(2 \; r^{7/2})$, where J_{22} represents the first tesseral harmonic of the earth. The amplitude of this motion is considerably smaller than that associated with J_2. The relative magnitudes of the effects of asphericity and lunar and solar perturbations are given in Table 2-13.

2-47

Telescope Misalignments

In any practical system there will be misalignments due to fabrication and assembly tolerances. If these errors can be measured during final calibration, compensating biases can be applied on-board. Normally the telescope boresight errors are measured in platform coordinates (a-frame) and would require transformation (R^{ta}) to the respective telescope coordinates. However these transformations can be computed in advance and the results stored on-board so that no on-board computation is required for compensation.

Defining the boresight errors, as measured in a-frame coordinates, as b_x, b_y, b_z, the x and y components in the s-frame are obtained from the first two rows of:

$$\overline{\xi} = R^{ta} \begin{bmatrix} b_x \\ b_y \\ b_z \end{bmatrix}$$

The b_z error represents a rotational misalignment of the recticle slits relative to the x_t and y_t axes.

Compensation for Biases:

Based on the foregoing stored and computed bias errors, the sensor outputs ρ_x and ρ_y can be compensated to yield corrected error signals μ_x and μ_y by simple addition. For each sensor, the corrected error signals are:

$$\mu_x = \rho_x + a_x + \nu_x + \xi_x$$

$$\mu_y = \rho_y + a_y + \nu_y + \xi_y$$

Since the time varying components of the bias errors vary at a relatively low rate, it is not necessary to update those components at the same frequency as the sensor outputs, ρ_x and ρ_y, are generated. Typically, the aberration error and inclination error might be updated once every 100 seconds, whereas the sample period from the sensor is 0.25 seconds.

Star Sensor to Vehicle Attitude Error Transformation

The transformation relating the vehicle attitude error to the star sensor outputs can be derived from the following matrix equation:

$$R^{st} = R^{si} R^{ir} R^{rv} R^{va} R^{at}$$

We note first that R^{st} and R^{rv} are both nearly identities since the telescope fields of view limit operation to about $\pm$ 0.5 degree maximum error. These two matrices can therefore be represented by

$$R^{st} = I + \tilde{\rho}$$

$$R^{rv} = I + \tilde{\epsilon}$$

where I = identity matrix and $\tilde{\rho}$ and $\tilde{\epsilon}$ are skew-symmetric matrices whose components are the star sensor error angles and vehicle attitude error angles, respectively, i.e.,

$$\tilde{\rho} = \begin{bmatrix} 0 & -\rho_z & \rho_y \\ \rho_z & 0 & -\rho_x \\ -\rho_y & \rho_x & 0 \end{bmatrix} \qquad \tilde{\epsilon} = \begin{bmatrix} 0 & -\epsilon_z & \epsilon_y \\ \epsilon_z & 0 & -\epsilon_x \\ -\epsilon_y & \epsilon_x & 0 \end{bmatrix}$$

We also note that

$$R^{ir} R^{va} = I + \tilde{p}$$

which states that the two successive rotations indicated result in an identity except for small errors represented by the components of $\tilde{p}$. Similarly

$$R^{si} R^{at} = I + \tilde{q}$$

Substituting these relations into the original matrix equation and dropping terms involving products of small angles, there results:

$$\tilde{\rho} = R^{si} R^{ir} \tilde{\epsilon} R^{ri} R^{is} + R^{si} \tilde{p} R^{is} + \tilde{q}$$

This is equivalent to the following vector-matrix equation:

$$\bar{\rho} = R^{si} R^{ir} \bar{\epsilon} + R^{si} \bar{p} + \bar{q}$$

2-49

The components of $\bar{p}$ and $\bar{q}$ represent bias errors referred to the i-frame and s-frame, respectively. Defining

$$\bar{\mu} = \bar{p} - R^{si} \bar{p} - \bar{q}$$

we note that the two right hand terms correspond to the bias compensation discussed in the preceding sections. Assuming the compensation is exact we are left with the relation

$$\bar{\mu} = R^{si} R^{ir} \bar{\epsilon}$$

where
$$\bar{\mu} = \begin{bmatrix} \mu_x \\ \mu_y \\ \mu_z \end{bmatrix} \quad \text{and} \quad \bar{\epsilon} = \begin{bmatrix} \epsilon_x \\ \epsilon_y \\ \epsilon_z \end{bmatrix}$$

Each star sensor provides only two components of error, μ_x and μ_y. The component μ_z represents a rotation about the LOS and cannot be measured. Sufficient data is available to determine the three components of $\bar{\epsilon}$, however, by using the outputs of two sensors. We then have the relation:

$$\underset{4 \times 1}{\bar{\mu}^*} = \underset{4 \times 3}{A} \underset{3 \times 1}{\bar{\epsilon}}$$

where

$$\bar{\mu}^* = \begin{bmatrix} \mu_{x_j} \\ \mu_{y_j} \\ \mu_{x_k} \\ \mu_{y_k} \end{bmatrix} \qquad A = \begin{bmatrix} A_j \\ --- \\ A_k \end{bmatrix}$$

A_j = first two rows of $R_j^{si} R^{ir}$

A_k = first two rows of $R_k^{si} R^{ir}$

Attitude Error Estimate

Since $\bar{\mu}^*$ has four components and $\bar{\epsilon}$ has only three, there is obviously redundant information available. One method of dealing with this situation would be to select the three components of $\bar{\mu}^*$ which provide the greatest sensitivity in determing $\bar{\epsilon}$ and ignore the unused sensor component. This could be done by determining in advance and storing on-board the best three out of four sensor components for every possible pair of sensors.

A considerable improvement in accuracy could be gained, however, by using all four components of sensor error data and performing a least squares solution of the three attitude error components. This can be done in a straight-forward manner as follows:

Define the pseudo-inverse of A to be

$$A^* = (A^T A)^{-1} A^T$$

The least squares error estimate is then given by

$$\hat{\epsilon} = A^* \bar{\mu}^*$$

A further refinement in the estimation of the attitude error could be obtained using some form of recursive filter (e.g. Kalman filter). With an increase in the dimension of the state, the bias error could also be estimated. The computer load would of course increase. At the present time there does not appear to be a need for this refinement. However, this subject is worthy of further investigation, particularly if an accurate calibration of the bias errors should prove impractical.

Summary of Computer Equations

Gimbal Angle Commands

$$\hat{\theta} = \alpha + \Delta\theta$$

$$\hat{\varphi} = \beta + \Delta\varphi$$

Star LOS Error Angle for $j\underline{\text{th}}$ Sensor

$$\rho_{x_j} = k_i \; \sin \; \frac{2\pi \; t_{x_j}}{T}$$

$$\rho_{y_j} = k_i \; \sin \; \frac{2\pi \; t_{y_j}}{T}$$

Stellar Aberration Computation for $j\underline{\text{th}}$ Sensor

$$\bar{a}_j = \frac{1}{c} \; \bar{V}_j^{\,sv} \qquad (\text{only } a_{x_j} \text{ and } a_{y_j} \text{ required})$$

$$\bar{V}_j^{\,sv} = R_j^{se} \; \bar{V}^{\,ei} + R_j^{si} \; \bar{v}^{\,iv}$$

$$\bar{V}_j^{\,ei} = V_o \begin{bmatrix} C_{\Omega}t \\ S_{\Omega}t \\ 0 \end{bmatrix} \qquad \bar{v}^{\,iv} = r_o \; R_\beta^T \; R_\gamma^T \begin{bmatrix} -\dot{\alpha}S\alpha \\ \dot{\alpha}C\alpha \\ 0 \end{bmatrix}$$

Orbit Inclination Error Conversion for $j\underline{\text{th}}$ Sensor

$$\nu_{x_j} = \Delta\gamma \; S\delta_j C\lambda_j$$

$$\nu_{y_j} = -\Delta\gamma S\lambda_j$$

Telescope Misalignment

Calibration of boresight errors before launch.

Biases, ξ_x and ξ_y, for each telescope stored in memory.

Bias Compensation for $j\underline{\text{th}}$ Sensor

$$\mu_{x_j} = \rho_{x_j} + a_{x_j} + \nu_{x_j} + \xi_{x_j}$$

$$\mu_{y_j} = \rho_{y_j} + a_{y_j} + \nu_{y_j} + \xi_{y_j}$$

2-52

Star Sensor to Attitude Error Transformation

$$\bar{\mu}^{*} = A\,\bar{e}$$

$$\bar{\mu}^{*} = \begin{bmatrix} \mu_{x_j} \\ \mu_{y_j} \\ \mu_{x_k} \\ \mu_{y_k} \end{bmatrix} \qquad\qquad A = \begin{bmatrix} A_j \\ \overline{A_k} \end{bmatrix}$$

A_j = first two rows of $R_j^{si}\,R^{ir}$

A_k = first two rows of $R_k^{si}\,R^{ir}$

Attitude Error Estimate

$$\hat{e} = A^{*}\,\bar{\mu}^{*}$$

$$A^{*} = (A^{T}A)^{-1}\,A^{T}$$

$$\hat{e} = \begin{bmatrix} \hat{e}_x \\ \hat{e}_y \\ \hat{e}_z \end{bmatrix}$$

3. Gimbal System

3.1 Gimbal Requirements

The STARS gimbal is essentially a two-axis continuous rotation positioner as shown in Figure 3.1-1. Each sensor cluster is mounted to a single shaft whose center is the polar axis. The pitch axis is offset from an orthogonal condition by an amount equal to the inclination angle of the intended vehicle orbit so that the polar axis maintains a north pointing position.

The gimbal requirements shown in Table 3.1-1 include the sensor cluster characteristics, the gimbal performance specifications and the environmental conditions. The torque requirement for each axis is similar even though the inertia is different by a factor of 30 because friction of the bearings and electrical contact brushes determines the torque. A position transducer is necessary for position control as well as position information, but no specific rate transducer is required for the control of the gimbal. However, if rate information were required it would be derived from the position transducer since tachometers are not useful at these low speeds.

The need for a brake or clutch is considered unnecessary because the system is in operation full time. Motion of the gimbal during a non-operational period would in no way damage the gimbal elements or the structure since full rotation clearance is required for operation. An anti-rotation squib or solenoid lock could easily be added if full clearance is not available in the launch shroud. The gimbal is sized to contain itself during the launch environment without launch locks. A launch lock system is difficult to implement because it provides a redundant load path that must be less compliant than the ball bearings in order to be effective. This redundant load path could also cause binding and permanent distortions due to thermal effects of the launch phase. These problems only need to be solved in systems that have heavier suspended masses than the sensor clusters and thus need not be considered here.

The mild temperature environment during operation is a requirement to minimize the pointing errors resulting from structural distortions. The tight control of $80^{\circ}F$ to $100^{\circ}F$ is achieved through thermal insulation from the sun and surrounding structure as well as the use of electrical components with low heat dissipation. A wider temperature range for the non-operating condition may be imposed to allow conventional shipping, storage and launch without specialized thermal control. The $0^{\circ}F$ to $150^{\circ}F$ non-operating range is not a severe constraint on the design of the gimbal mechanism and components.

STAR CLUSTER

SHAFT ANGLE
TRANSDUCER (2)

OIL RESERVOIR (4)

PITCH AXIS

POLAR AXIS

DRIVE MOTOR (2)

116H BALL
BEARING (1)

SATELLITE
STRUCTURE

SLIP RINGS
(2 SETS)

112H BALL
BEARING (3)

BALL BEARING
SUSPENSION SPRING
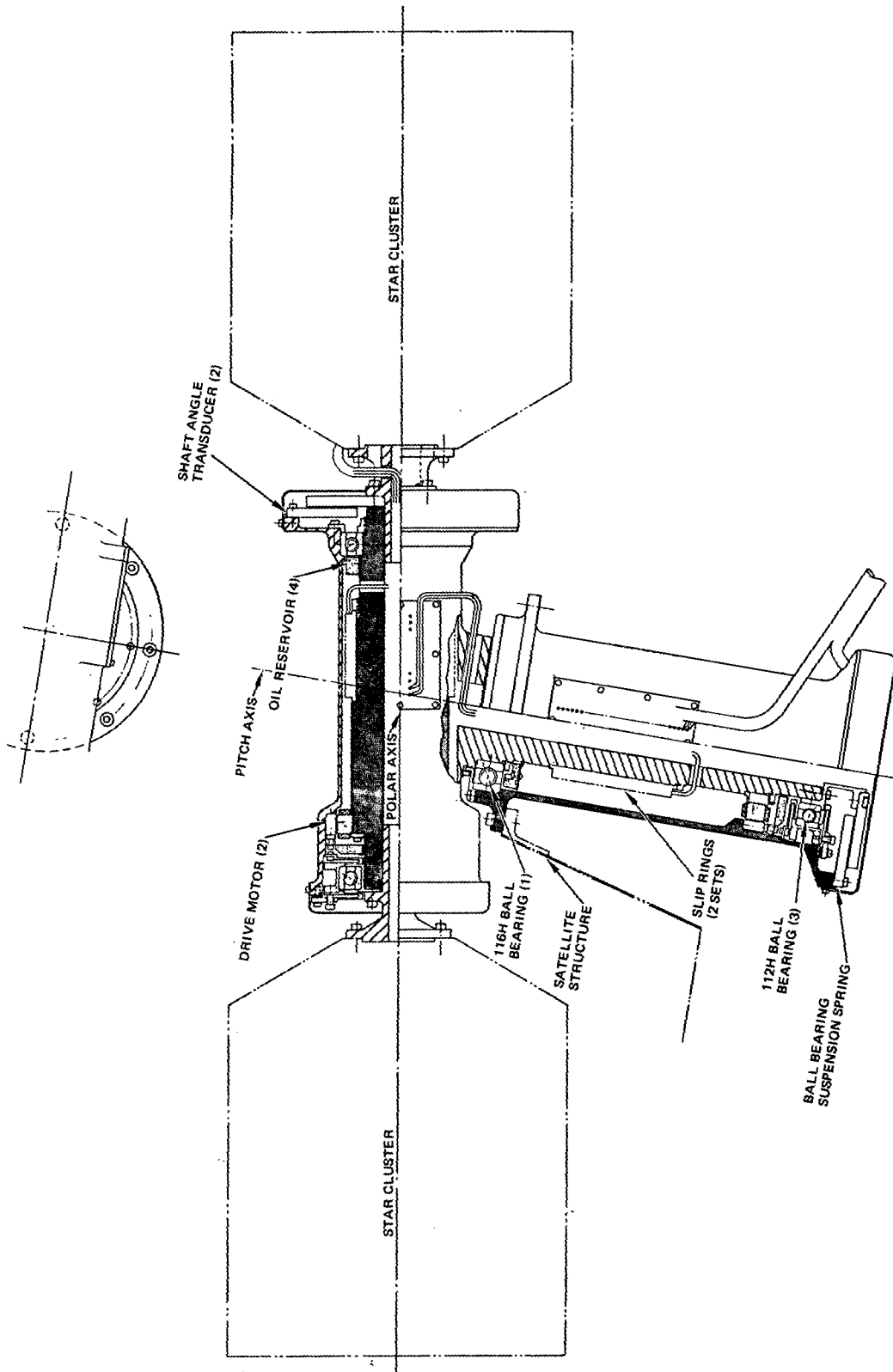
STAR CLUSTER

Figure 3.1-1. Gimbal Mechanism

TABLE 3.1-1. GIMBAL REQUIREMENTS

Star Cluster Description

Size, each cluster	13 inch diameter swept hemisphere
Weight, each cluster	15 pounds
Power dissipation	0.7 watts electronics
	4 watts wedge motor
	0.2 watts shutter motor
Electrical connections	44 slip ring channels (200 ma max.)
View angles gimbal	+15 degrees to zenith elevation
	0 to 360 degrees pitch
Inertia about rotation axis	1.5 slug-ft^2, pitch axis
	0.05 slug-ft^2, polar axis

Gimbal Performance

Axes		Two axis, continuous, unidirectional
Rates:	Slew or test	1 rev per 5 minutes both axes
	Track	1 rev per year, polar and 1 rev per 90 minutes, pitch axis
Gimbal accuracy per axis		1.8 arc seconds
Weight goal		35 pounds
Power		20 watts without thermal control
Incremental position		2^{19} resolution with ± 1.8 arcsec accuracy

Readout

Rate readout	none required
Brakes	none required
Life	3 years

Environment

Launch load	60 g, 3σ peak random vibration
temperature	80°F to 100°F, operating
	0°F to 150°F, non-operating
Pressure	vacuum of space
Temperature gradient	5.0°F ΔT across bearings
	5.0°F ΔT across gimbals
Ground test	must operate in 1-g field

The life requirement of 3 years was selected to cover all altitude missions. The low rates of the gimbal keep the revolutions of travel low compared to the wear life of gimbal components. The pitch axis travel amounts to only 17,500 revolutions in 3 years of orbit life, and only 3 revolutions in the polar axis. Since the wear life of ball bearings and electrical contact brushes have demonstrated vacuum life in millions of revolutions, there is therefore no wear-out problem.

3.2   Structural Description

The gimbal mechanism shown on Figure 3.1-1 results from a thorough
study of possible structural arrangements. The cantilever design of the
pitch axis is chosen over a yoke configuration because of the better control
of pointing with changes in thermal conditions. In a yoke configuration
the pointing accuracy is sensitive to dimensional changes in arm lengths
due to differential temperatures. While the cantilever design is subject
to the inaccuracy of a bow shape, the thermal control is easier with the
short thermal coupling paths of the cylindrical housing.

The reduced structural weight was another reason for the selection of the canti-
levered design. The structural support of the polar axis and payload under
launch loading is difficult with a yoke because of the long reach required for
sensor cluster clearance. The yoke weight alone is 30 pounds compared
to the 34.5 pounds now calculated for the total cantilevered two-axis
mechanism. Another disadvantage of the yoke is the high cost of the
beryllium material and extensive machining on a large block. The
cantilever design uses the structural advantage of a thin wall tube, and
shear loads are taken out close to the center of mass.

The general arrangement of the mechanism uses three major structural
elements: 1) the pitch housing mounted to the satellite structure, 2) the
pitch shaft and polar housing machined from one block   3) the ·single piece
polar shaft. The polar axis is designed to allow mounting the sensor clusters
after the total mechanism is fully assembled and functionally tested. The
single piece construction of the polar housing to the pitch shaft was necessary
to minimize the overhung moment on the pitch bearing and to avoid a separate flange
at the axes junction, which would be an alignment liability because of the high
launch forces. The block of beryllium required for the T-shaped part
is no larger than the blocks used in the Hughes beryllium despin assemblies
as described in Section 3.5.
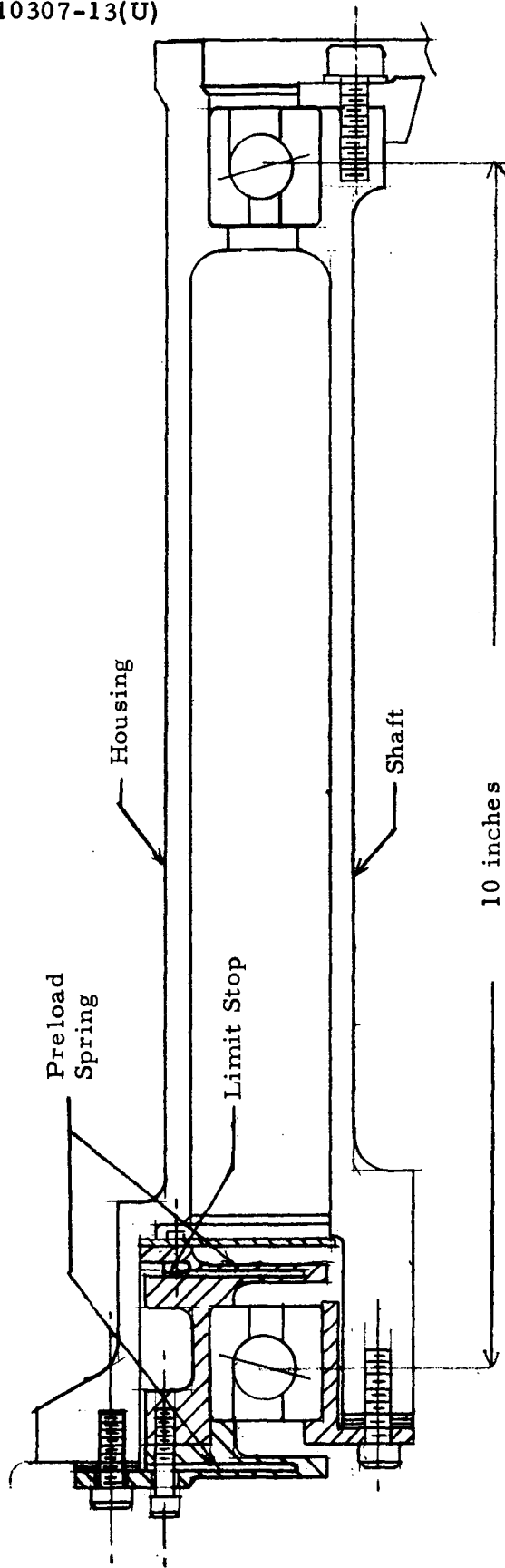
PRELOAD SPRING RATE   > 3500 POUNDS/INCH

NOMINAL PRELOAD   60 POUNDS - PITCH, 45 POUNDS - POLAR

BEARING HERTZIAN STRESS   60,000 PSI

Figure 3.2-1. Ball Bearing Suspension Schematic

Bearing Suspension

A single pair of angular contact ball bearings on each axis is used to stably support the sensor clusters. Duplex pairs were considered for higher radial load capacity, but a compliance analysis showed that very small radial temperature gradients caused unacceptable increases in friction. This sensitivity could be relieved by slip fits at the bearing ring interface but then equal radial load sharing would not be dependable. Single ball bearings with a larger one at the axes junction are a predictable and therefore more reliable suspension than duplex pairs.

A schematic of the bearing installation is shown on Figure 3.2-1. One bearing is installed with a light interference fit to both the shaft and the housing to prevent separation under all temperature conditions. Since the beryllium coefficient of expansion closely matches the 52100 bearing steel, a $\pm$ 10°F bulk change in temperature changes the diametral fit of the largest bearing by only 15 microinches. A radial temperature gradient has a large effect on the fit but would be less than a degree farenheit because of high conductance of the interference fit. The gradient from inner race to outer race could be about 5°F because of the lower thermal conductance across the balls. This change in diametral dimension is accommodated by a shift in the housing to shaft position and a slight increase or decrease in the preload spring force.

The preload spring contains four thin diaphragms machined from two pieces of steel. The diaphragms are designed to produce a low spring rate in the bearing thrust direction to insure a constant preload despite axial differential expansion of the shaft and housing. On the polar axis the 45 pounds preload requires 0.013 inches of initial spring deflection. A temperature difference across the shaft to housing of 5°F causes only a one pound change in preload compared to approximately 80 pounds that could occur in a system with all races fixed.

TABLE 3.2-1. BALL BEARING LOADS

	POLAR AXIS	PITCH AXIS
Ball Bearing Configuration	2-112H size	1-112 H size 1-116 H size
Thrust Capacity, Pounds	3500	3500[1]
Thrust Requirement at 60 "g", pounds	2300	3500
Hertzian Stress, psi	195,000	220,000
Radial Capacity, Pounds	2500	4500[2]
Radial Requirement at 60 "g", Pounds	900	4200
Hertzian Stress psi	210,000	230,000

NOTES: (1) 112H

(2) 116H

This system of axial compensation is very reliable compared to the conventional sliding race because its function does not depend on critical fits. A limit stop is provided to control motion during the launch and vibration loads. This suspension method has been qualified for high level vibration using 90 mm bore and 150 mm bore bearings for despin assemblies. Since the balls have less mass in the bearings for STARS, lower vibration unit loads should be expected from ball dynamics.

The suspension system has no radial free-play at the bearing interfaces. This aspect is basic to accurate pointing because a correction in pitch would have the uncertainty of the radial free play in the polar axis bearing. Also the natural frequency of the mode excited by a pitch correction is predictable because of the elimination of the polar bearing free-play. The diaphragms of the preload spring are inherently stiff in the radial direction but are the major contributor to the system compliance compared to the structure and ball bearings. The spring design is checked to insure that its compliance is compatible with bandpass frequency selected for the pitch servo.

Launch Loads

The launch loads and bearing capacities are shown on Table 3.2-1. The load requirements are based on the 60 "g" peak that could result from a 3 sigma point from the 20 "g" rms random vibration input. The sinusoidal accelerations are dependent upon analyses of an actual installation and have never been greater than the 60 "g" level on other Hughes satellites. The stress level shown is calculated from the ball bearing parameters of ball size, race curvature and the number of balls. The level of 285,000 psi has been considered acceptable for quiet running space applications. This stress could result in a brinell spot of 80 microinch depth. The highest stress listed on Table 3.2-1 is 230,000 psi which corresponds to a brinell depth of 38 microinches. Aside from being a small number, this is acceptable considering that: 1) it occurs in a radial direction so there is a a low probability that it occurs in the operational ball track, 2) the adjacent balls will have the major control on the raceway center at normal preloads. In the error budget of Section 3.4, three-fourths of the maximum dent size is used.

TABLE 3.2-2

STRUCTURAL MATERIALS TRADEOFF

FACTOR	BERYLLIUM	GRAPHITE-EPOXY	ALUMINUM	TITANIUM
Dimensional Stability	Acceptable - Used in Precision Gyros and Gimbals	Unknown because of lack of experience in the industry.	Acceptable - extensive experience	Acceptable - moderate experience
Thermal Conductivity BTU/hr$(ft^2)°F/ft$	104	10 to 17	109	4.2
Coefficient of Linear Expansion in/in/°F	6.4×10^{-6}	Adjustable by mix and lay	13×10^{-6}	5.3×10^{-6}
$\underline{Modulus\ of\ Elasticity}$ Density	6.3×10^8	3.2×10^8	$1.0 \times .0^8$	1.0×10^8
Density lbs/in^3	0.067	0.060	0.100	0.160
Ultimate Strength lbs/in^2	43,000	70,000 to 200,000	70,000	135,000
Cost	• High Material Cost • Must be Machined from a block	• Low material cost • High cost for first unit due to mold development	• Low material cost • Least machining cost - can be cast	• Medium material cost • Difficult machining.

Structural Materials

The STARS gimbal must be fabricated of a material that meets the following characteristics:

1) Dimensional Stability
2) High Thermal Conductivity
3) Coefficient of Linear Expansion close to 6.6 microinch/inch/°F
4) High Modulus of Elasticity to Density Ratio

The first two characteristics are required to maintain the pointing accuracy over extended periods of time in the presence of heat sources such as the motors and shaft angle transducers. The structure surrounding the ball bearings must have a matching coefficient of linear expansion or the fit could loosen and cause a pointing error. Should the fit tighten, the ball bearing friction characteristics could be adversely changed. The fourth characteristic is a combination of material properties that establishes the weight and inertia for a structure designed for stiffness. This characteristic is 10^8 inch for steel, aluminum, titanium and magnesium, so that other properties are the bases for selection amont these materials.

Beryllium has been selected as best suited to the requirements as shown on Table 3.2-2. Beryllium not only meets the requirements of stability, thermal conductivity and coefficient of linear expansion; it far exceeds the modulus of elasticity versus density ratio of conventional materials. The closest to this characteristic is that of graphite-epoxy laminates that are being used for satellite structural application. Although it might eventually become a serious contender, this material is not suitable at present for the following reasons:

1) Lack of history on stability
2) Inadequate information on coefficient of linear expansion parallel to the rotation axis (so that the error effect of the low thermal conductivity may be assessed).
3) Development costs of the molds for a demonstration unit are excessive.

3.3 Component Selection

Ball Bearings

The ball bearings size is selected based upon the bore required for the shaft and wire harness and the static load requirements for the launch environment. The detailed characteristics are listed in Table 3.3-1. At three points in the mechanism the 112H, extra-lightweight series, is used because it adequately meets the stated requirements. The ball bearing near the junction of the axes requires a higher radial load capacity, so the 116H is used. The 213H, lightweight series, would have sufficient radial capacity but the 116H, extra lightweight, selection is one-half pound lighter.

The contact angle of 25 degrees is selected over the more conventional 15 degrees because of the increased reliability in a bearing with more radial play. The 15-degree contact angle bearing has about 0.001 inch of diametral free play which allows insufficient margin over the collection of tolerances in the interference fits and the different thermal conditions. The 0.003 inch diametral play of the 25-degree bearing allows a factor of 3 margin.

The ball bearings should be manufactured to AFBMA ABEC-9 class and Grade 5 balls to optimize bearing fits and performance. The precision bearing of Class 9 will include a specification on change of radius per change in rotation of approximately 1.0 microinch per degree. Component tests must be conducted to fully evaluate this effect of raceway roundness.

The ball bearing material selected is 52100 steel because of its close match to the beryllium thermal coefficient of expansion. In gimbals with less critical fits, 440C stainless steel is used because of its improved corrosion resistance. The corrosion in the STARS bearings is considered less critical because the steps in cleanliness protection will also provide humidity protection. Other materials in use for ball bearings such as M50 steel were not selected because more history was available on 52100.

TABLE 3.3-1.   BALL BEARING CHARACTERISTICS

	112H	116H
Ball bearing size	112H	116H
Quantity required for STARS	3	1, pitch axis
Bore, inches	2.3622	3.1496
Outside diameter, inches	3.7402	4.9213
Balls, quantity/diameter	19-13/32	20-17/32
Contact angle, degrees	25 ±2	25 ±2
Weight per bearing	0.92	1.91
Ball retainer	Synthane Oaks Phenolic	
Material	52100 Steel, CEVM	
Radial capacity, pounds	2500	4500
Thrust	3500	6300

The ball bearing preload levels of 45 pounds and 60 pounds on the polar and pitch axes respectively are based upon concern for the 1-g environment. The 1-g loading could cause the preload to collapse if it is set too low. Preloads are low as 10 pounds would achieve intimate ball contact, but handling and calibration would be severely restricted. The preload selected with the proper mechanism orientation relative to gravity will allow ground testing without excessive friction.

The ball retainers must be specially manufactured from high porosity cotton phenolic laminate material to provide lubricant transfer to the balls. The retainers may be a one-piece design because the ball bearings are separable. A thorough design analysis of the ball retainer is necessary to insure adequate clearances, ball position control, low friction riding features and adequate lubricant capacity.

Lubrication

A wet lubrication system has been selected using a mixture of 95 percent Apiezon "C" low vapor pressure oil and 5 percent lead napthanate. The special additive material contains 31 percent lead which enhances the boundary lubrication characteristics. The Hughes designation is HMS 20-1727 which represents the material specification that controls the quality of the oil. The basic characteristics are listed in Table 3.3-2.

TABLE 3.3-2.   HMS 20-1727 OIL CHARACTERISTICS

Density	0.8715 gm/ml	
Vapor pressure	at 10°C	2×10^{-10} Torr
	at 20°C	7×10^{-9} Torr
	at 50°C	1.1×10^{-7} Torr
Molecular weight		574
Viscosity	at 20°C	1250 seconds

The selection of the wet lubrication system is based upon the concern for predictable and consistent friction characteristics because of the servo sensitivity. Dry lubrication is not ruled out because of travel distance even though the requirement for STARS is about three times further than demonstrated. One problem of the dry lubrication is the experimentally obse: deposition of the composite retainer material on the raceway. Should deposits occ in STARS, they could cause control problems at the low rotation rates expe-rienced, whereas the viscous torque of the wet system is very predictable over the life span and temperature range. A secondary concern against dry lubrication is the compatibility with the oil of the slip rings. The sections of the gimbal could be isolated, but the added complexity cannot be justified.

The wet lubricant storage and transfer must be designed from an overall system standpoint to ensure adequate bearing lubrication for the life of the spacecraft. All materials near the bearings must be screened for outgassing to prevent contamination of the lubricant.

Lubricant transfer migration across surfaces and by vapor transfer must be analyzed to assure proper quantity of lubricant on the bearings at all times. The conservatively designed lubricant storage system, consisting of oil impregnated Nylasint reservoirs close to the bearings and a thin oil coating on all internal shaft and housing surfaces around the bearings, will provide more than sufficient reserve lubricant application. This is shown schematically in Figure 3.3-1.

The effect on the optics of the small amount of lubricant lost through the labyrinth seal must be studied further. The labyrinth seals are not far from the view ports of the sensor cluster but are not in the line of sight. The effect of oil on visible light transmission is very small compared to IR but still requires laboratory tests to confirm acceptable limits of deposition.

Laboratory tests conducted on another program during the STARS study investigated the breakout friction required for various preloads. The test setup used two bearings of the 212 size and 15-degree contact angle. The balls were matched to five millionths of an inch and assembled using a conventional race riding retainer. The bearings were oiled with HMS 20-1727 to ensure the proper boundary lubrication and were run in at each preload setting. Figure 3.3-2 shows the test data and the extrapolations for the bearings selected for STARS.

Drive Motor

The drive motors selected for STARS are Inland brush DC motors as shown in Table 3.3-3 for both axes. The size was chosen to provide a 0.5 ft-lb stall torque at a low current to eliminate undesirable heating effects. The heating is undesirable because of distortion of the gimbal shafts and because of the limited current capacity of the slip rings. The motor selected draws only 0.32 ampere at stall and generally requires only 36 milliamps for tracking.

The motor fields are multipolar permanent assemblies with cartridge brush holders mounted on the edge. The armatures are wavewound so that it is not necessary to have as many brushes as poles. The motor is a 16-pole unit and has four brushes, two being redundant.

3-15
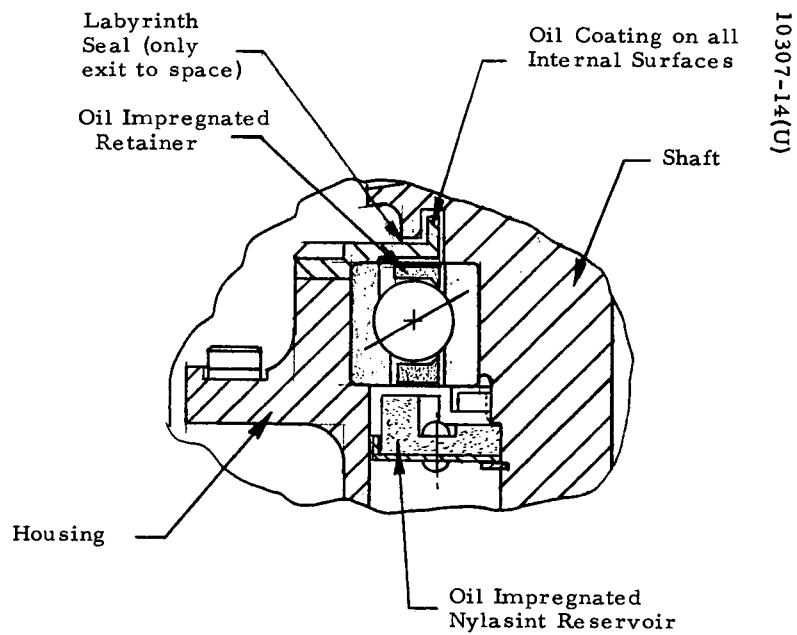
Figure 3.3-1. Schematic of Lubricant Storage and Transfer
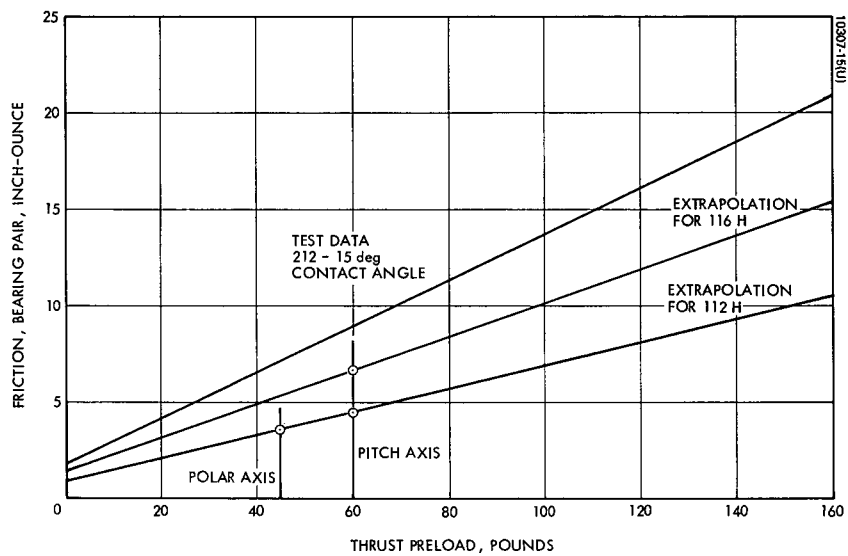
Figure 3.3-2. Ball Bearing Breakout Friction

TABLE 3.3-3. DC MOTOR CHARACTERISTICS

Motor designation	Inland T-3905
Stall torque	0.5 ft-lb
Motor size	
O. D.	4.44 inches
I. D.	2.93 inches
Length	0.875 inch
Weight	1.4 pounds
Torque constant	300 in-oz per ampere
Back EMF constant	0.94 volts/radian/second
Motor power, pitch axis	
Torque saturation	7.00 watts
Break-out friction	0.15 watts
Running friction	0.07 watts

The motors will have cartridge type brushes rather than the standard cantilever spring type so that the preload is carefully controlled and the brush length can be increased. The brush life is no problem based on a vacuum life test conducted on the TACSAT despin assembly. After six months the brush wear was negligible and the travel was 1,000 times farther than the STARS requirement. The brush material is 50/50 silver-graphite vacuum impregnated with the same lubricant used in the ball bearings.

A brushless dc motor is an alternate choice for the STARS gimbal drive. However, the increased cost and complexity of the motor drive electronics are the main reasons for not using the brushless design. The continuous rotation
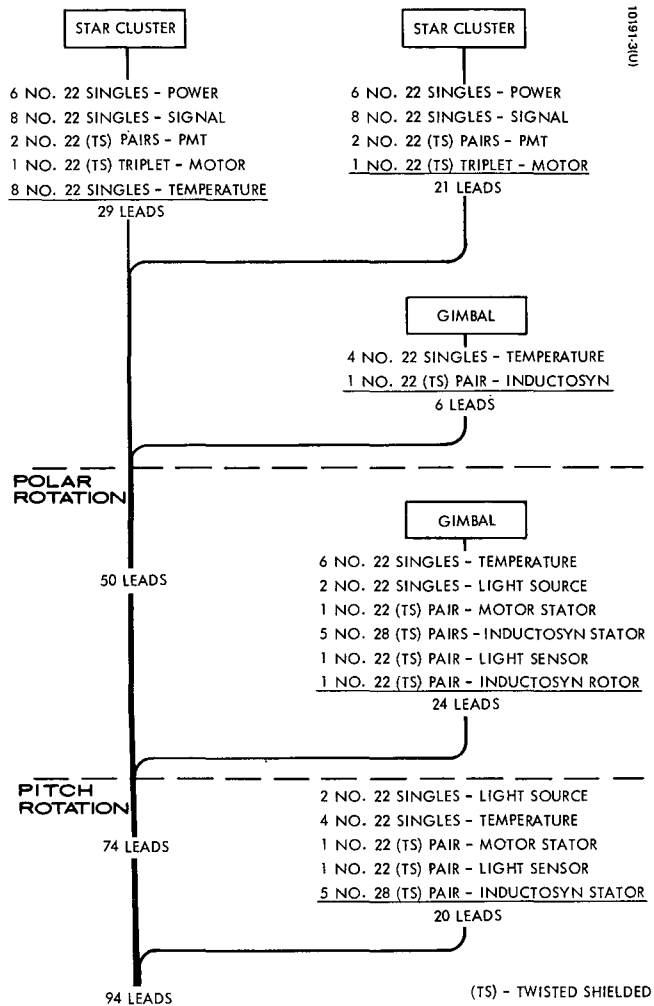
Figure 3.3-3. Harness Schematic

requirement eliminates the two-pole variety of brushless dc motors, and
the compliance of geared systems is unacceptable from the control standpoint.
The two advantages to the brushless dc motor would be the elimination of brushes
(wear, debris, friction) and the fact that the motor heating element is mounted
to the housing which is more easily cooled. However, since the travel is short,
the wear and debris are minimal, and debris shields can be placed between the
motor and the ball bearings. With the selected approach, the friction is low
but the charateristics of the friction must still be tested for affect on the
servo control concept. The heating aspects of the motor size selected are
insignificant.

Power and Signal Transfer

The electrical power and signal transfer across each axis requires slip
rings on both the polar and pitch axes. The sensor clusters have 44 wires
for the separate functions and power forms as listed in Figure 3.3-3.
When these requirements are added to the wiring for the gimbal, the pitch
axis requires 74 slip rings. A number of considerations were given to
methods of reducing the quantity of slip rings. The six low voltage power
leads could be reduced to two by placing an electrical conversion circuitry
on the gimbal. The wedge motor drivers could also be placed on the gimbal
to reduce the wire count. These options were not recommended because
of   increased weight causes growth in all structural elements of the
gimbal and the increased power causes additional thermal dissipation problems.
The photomultiplier high voltage power supply is placed on the gimbal because
of the difficulty of transferring high voltage in conventional slip rings.
Signal multiplexing was considered, but since 14 of the 24 signals are
timing pulses the additional complexity of the clock and sample circuitry
are not worth the wire count reduction. Further definition on the signals
and multiplexing methods may make it worthwhile to reevaluate this option.

The slip ring design selected is a hard gold-plated finish with wire
brushes of Ney-Oro-G gold alloy. Figure 3.3-4 shows the basic arrangement
of a 75 slip ring design. Poly-Scientific was consulted on the spacing and
size required for the STARS pitch axis. The slip ring assembly is molded
in the form of a hollow cylinder with the leads exiting the edges as
shown in Figure 3.3-4. The cylinder is slipped on the shaft and secured with
a nut. The brush blocks are separately mounted to the housing and aligned
to the slip ring after the gimbal is assembled. Brush pressure can be tested
by inserting a hook through access ports on the brush block. The brush block
contains redundant brushes on each ring.

4.375 DIA OUTSIDE HOUSING

3.937 DIA INSIDE HOUSING

2.700 DIA SLIP RING I.D.

3.437 DIA SLIP RING O.D.

HOUSING.

2.68

SOLDER TERMINALS

GOLD WIRE BRUSHES

ELECTRODEPOSITED GOLD

NEY-ORO G

.0085

.0055

3.80

.050

NUT
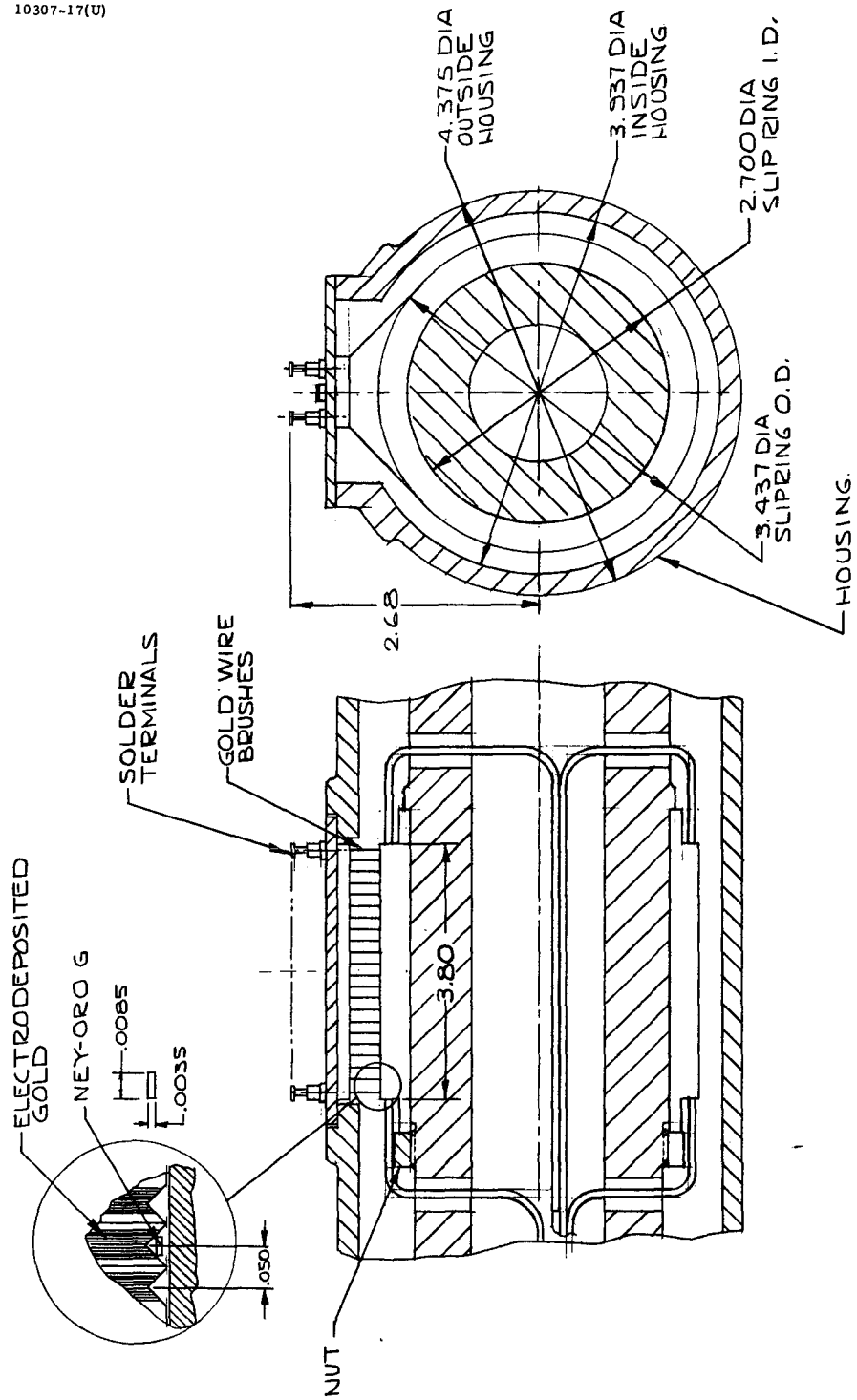
Figure 3.3-4. Slip Ring Assembly

The slip rings are lubricated with HMS 20-1727, the same oil as used in the ball bearings. Hughes has conducted vacuum testing on two small diameter versions of the design proposed. The test articles had 17 slip rings of 1/8 inch diameter, one article lubricated with HMS 20-1727 and the other lubricated with F-50 oil. The slip rings were turned at 60 rpm and carried a total of 1.5 ampere continuously. The signals circuits operated with noise of less than 1 millivolt for 9000 hours using either lubricant. The power circuits operated better with HMS 20-1727 oil but power circuit noise started to increase after 2600 hours. After power interruption at 5400 hours and a few days of idle time, the power circuits operated satisfactorily for another 3600 hours. The reason for the noise on the power circuits is most likely due to local oil depletion due to the high speed and high continuous current.

The STARS slip ring assembly contains a larger mass of ring material and is coupled to the large gimbal shaft so that temperature is well controlled. The STARS rotation rate is so low that mechanical heating is not a significant factor on oil depletion. These items combined with careful current derating will allow the oil lubricated slip ring to meet the noise and life requirements for STARS. Should any other experience indicate a further oil depletion problem, the addition of an oil wick that contacts the slip ring would solve the problem.

Alternate slip rings designs using silver - MoS_2 brushes with silver slip rings were considered for STARS. These designs are well developed for the Hughes despin assemblies on the communication satellites for long life at 60 rpm. The main disadvantage of the dry composite brush design is the increased volume. The slip ring assembly would have to be twice as long as for the gold wire assembly and have a larger cutout on the housing for brush access. Another disadvantage is the high friction torque of the dry brush because the preload is at five times higher for equivalent noise performance. The resulting 4 in-oz increase in torque is quite significant considering the total budget of 14 in-oz.

TABLE 3.3-4. INDUCTOSYN CHARACTERISTICS

Manufacturer	Farrand Controls, Inc.
Rotor (input)	5.75 inch OD, 2.00 inch ID, .312 inch thick
Stator (output)	7.00 inch OD, 2.67 inch ID, .312 inch thick
Base material	Beryllium
Weight	2.3 pounds
Configuration	512 poles, binary coded
Electronic quantization	2^{19}, 2.47 arc-seconds
Excitation frequency	2 kHz
Electrical dissipation	1 watt
Accuracy:	
1/revolution	0.68 arcseconds
512/revolution	1.32 arcseconds
Repeatability	0.20 arcseconds
Decentering error per .001 inch	0.40 arsecond
Air gap	0.005 to 0.010 inches

Shaft Angle Transducer

The system error budget sets a resolution requirement for the gimbal shaft angle transducer of 2^{19} bits (2.47 arcseconds). However, an absolute angle measurement is not necessary because a register with a once-per-revolution reset can maintain the total angular position. The disadvantage of the absolute transducer is the complexity of the device compared to digital registers. However, there is a minor operational disadvantage to the incremental system because initialization is necessary after power interruption.

The Farrand Inductosyn as described in Table 3.3-4 was chosen as suitable for STARS. The Inductosyn transducer is an inductive device that functions as a multispeed resolver. The rotor and stator windings are flat metallic deposits bonded to flat annular rings. These devices have been used for precision machine tools, air bearing tables and for space. The Inductosyn is the only device that is completely developed and meets the gimbal requirements of signal accuracy with 2^{19} bit resolution, long life with no apparent wear-out modes, and configuration compatible with the gimbal.

The Inductosyn also has the following desirable features for the STARS gimbal application:

1)   Low error sensitivity to misalignment and runout. This feature will allow installation at the gimbal assembly without separate bearings.

2)   Analog output allows finer resolution if required for servo control or for position readout.

3)   Disc substrate may be metallic for enhanced structural capability for launch survival as compared to translucent materials used in optical encoders.

The less desirable aspect of the Inductosyn is the electronics required for the accurate sine and cosine input signal generation. The input sine and cosine also requires amplitude determination and conversion to digital data to be compatible with commanded inputs and telemetry. The CVN pulse converter electronics has been developed by Farrand for the Inductosyn. The CVN system consists of an analog amplifier, digital logic, clock and counter circuits. The Inductosyn produces a position error signal which closes the loop of an electronic servo based upon the excitation signal. Digital output signals are supplied to count up, count down and for no motion. The

TABLE 3.3-5. SHAFT ANGLE TRANSDUCER

COMPANY	DYNAMICS RESEARCH	BALDWIN ELECTRONICS	FARRAND CONTROLS
NAME	THEODOSYN	SOLID STATE MICRO-ENCODER	INDUCTOSYN
RESOLUTION	2^{20} ABSOLUTE	2^{19} ABSOLUTE	$> 2^{19}$
RELIABILITY	o OPTICAL USING LAMPS o REQUIRES SEPARATE BALL BEARINGS FROM GIMBAL	o OPTICAL USING GaAs SOURCES o REQUIRES SEPARATE BALL BEARINGS FROM GIMBAL	o INDUCTIVE COUPLING HAS HIGH RELIABILITY o CAN BE MOUNTED TO GIMBAL BALL BEARINGS
CONFIGURATION	SOLID CYLINDER 4.5 INCH DIAMETER BY 2.5 INCHES HIGH (1 INCH DIAMETER HOLE COULD BE PROVIDED)	SOLID CYLINDER 3.9 INCH DIAMETER BY 2.5 INCHES HIGH	2-5/16 INCH DISCS 7 INCH MAXIMUM DIAMETER 1.732 THROUGH HOLE
WEIGHT ON GIMBAL	NOT AVAILABLE	NOT AVAILABLE	~ 2.3 POUNDS
POWER ON GIMBAL	1.5 WATTS	NOT AVAILABLE	1 WATT
ELECTRONIC COMPLEXITY/	INPUT IS SIMPLE POWER TO SOURCES OUTPUT DIGITAL TO 2^{15} -- ANALOG FOR HIGHER BITS	INPUT IS SIMPLE POWER TO SOURCES OUTPUT DIGITAL TO 2^{14} -- ANALOG FOR HIGHER BITS	INPUT IS ACCURATE SIN WAVEFORM OUTPUT IS ANALOG SIN/COS

pulse rate can be as high as 500,000 per second (STARS only requires 600 per second).

Other shaft angle transducer concepts were considered for STARS including optical types, variable reluctance, variable capacitance, magnetic core, variable inductance and contact brush types. The requirement for 2^{19} resolution eliminates all of these devices except the optical and the variable inductance types. The other concepts involve mechanical tolerances that are beyond state-of-the-art control considering the fine resolution required.

Several companies in the transducer business produce 19-bit optical encoders with a configuration compatible with the STARS gimbal concepts. Many of these designs are qualified to military specifications but all require some modifications for the vacuum environment. The basic incompatibility with the STARS requirement is the incandescent lamp life. The MTBF for the lamps is at best 20,000 hours which is unacceptable for even a one-year mission. The reliability for two lamps in standby redundancy for one year is 0.87 without consideration for launch degradation. This low reliability forces the consideration of devices not using incandescent lamps.

Table 3.3-5 lists three different encoders that were designed for space application. The Theodosyn utilizes incandescent lamps, so that it is not a serious candidate. This device is shown however because it has been qualified for very severe environments for NASA, Air Force and Navy programs. The concept of using a V-scan pattern up to a 2^{14} type resolution and then processing the analog output to higher resolution was used in the Theodosyn and the Baldwin encoders listed in Table 3.3-5. Baldwin extended the life by using gallium arsenide emitters to eliminate the wear-out mode. The STARS gimbal configuration requires a through hole in the shaft angle transducer to pass the structural mounting for the star sensors and wires to the star sensors. The Baldwin miniature is a compact device without a through hole, so it will not fit as presently configured.

It must be recognized that even if an incremental optical encoder using gallium arsenide sources were developed, the highest 3 or 4 bits would be achieved by amplitude interpolation of the output. Since the position is interpolated by amplitude, the accuracy is dependent on gain stability over the orbit life. To avoid interpolation, a direct readout grid yielding 2^{19} incremental output would have to be about 60 inches in diameter because of refraction problems. Even at the grid spacing for 2^{15} bits the gallium aresenide sources must be run at high power levels for useable signals and therefore, the reliability is not much greater

than lamps. The Inductosyn is therefore the logical choice for the STARS application since the stability of the resistance windings is hardly questionable.

Since the Inductosyn with the DVN converter is an incremental system, a reset signal is required once per revolution. The accuracy of the signal is less critical than the Inductosyn output because it just has to repeat within the same 2.47 arc-second interval to reset the register. The index pulse may be generated by a light sensor when a mask opening allows view of a light source. Gallium arsenide sources are readily available in a dual form for redundancy and an optical index is more suitable than a magnetic device because of the requirement for a sharp crossover at very low rates. Life is no problem because of redundancy, and this device is only turned on if a reset is required. Hughes has qualified a dual LED for use on the Multispectral Scanner System for ERTS that could be used for STARS.

3.4 Gimbal Characteristics

The baseline gimbal configuration is designed to optimize the weight, power and volume while meeting the functional requirements of STARS. The component selection of Section 3.3 and the structural description of Section 3.2 outline the basis for the weight list shown in Table 3.4-1. The total weight of the mechanism is 34.5 pounds with over half of the weight in the installed components. This comparison is an indication that the choice of a design without launch locks is appropriate. Any structural weight saving by the addition of launch locks would be very small since.

1. The accuracy requirements impose 10 inch spacing on the ball bearings.

2. The high bandpass gimbal servo requires a stiff structure about the rotation axes.

3. The bearing weights cannot be significantly reduced because of the bore requirements.

In addition, the structural weight savings of a launch locked system are offset by the weight of the locks, the lock supports and the squib driver system. However, since the bearings selected are an efficient size for the calculated loads, increases in the payload weight or launch loads could force reexamination of this design approach because larger bearings are less efficient.

Torque Budget

The gimbal torque budget is listed in Table 3.4-2. The torque requirement for the pitch axis is higher than that of the polar axis because the preload on the bearings is different and one bearing is larger. However, the requirements are so close that the same motor is used on each axis. The torque listed is the breakout friction based on the measurements described in Section 3.3; the running torque is expected to be about two-thirds of the breakout level for the ball bearings. The breakout characteristics require further definition for the ball bearings as well as the slip ring and motor brushes. The torque margin is more than adequate so the addition of dither of 24 inch-ounces could be accommodated for test purposes. If dither were incorporated in a flight design, the motors would be wound with less resistance to provide as least 4 times torque margin at 22 volts. The power budget associated with this gimbal drive design is listed in Table 3.4-3.

TABLE 3.4-1. STARS WEIGHT LIST

Major Components

Motors (2)	2.8 pounds
Inductosyn (2)	3.2
Ball bearings (4)	4.7
Preload springs (2)	4.0
Slip rings and brush block (2)	1.6
Oil reservoirs	.2
Wire harness and connectors	1.0
Thermal wrap	0.3
	17.8 pounds

Structure - Beryllium

Pitch housing	3.4
Pitch shaft/polar housing	6.9
Polar shaft	3.8
Fittings and covers	1.8
Bolts and fasteners	0.8
	16.7
Total Gimbal Weight	34.5 pounds

TABLE 3.4-2.   TORQUE BUDGET
(Inch-Ounces)

	Polar Axis	Pitch Axis
Ball bearings breakout	7.4	11.2
Slip rings	1.3	1.0
Motor brushes	1.8	1.8
	10.5	14.0
Torque saturation	96	96
Torque margin	9.1	6.8

TABLE 3.4-3.   POWER BUDGET

	Peak	Running
Motors	14.00	0.30
Inductosyn	2.00	2.00
Position Reference	.06	0
	16.06	2.30

Error Analysis

The ball bearing error analysis based upon the 10-inch spacing is listed in Table 3.4-4. The total error of 1.15 arc-second results from detailed considerations of tolerances and some uncertainties such as particle size of contamination and residual brinell spots due to launch loads. Early in the study a spacing of 15 inches was considered, but this was reduced to 10 inches in view of the weight saving and of the small impact on errors.

A breakdown of the errors of the Inductosyn including the CVN converter electronics is shown in Table 3.4-5. The Inductosyn is calibrated against a master unit at Farrand, Inc. where the least error centering position is marked on the stator. The errors shown in Item A and B-1 are the best fit for a disc pair. The rotor is aligned to the bearing center of rotation of the shaft using a dial gage mounted to the housing. This procedure requires the ball bearings and preload system to be intact prior to installation of the Inductosyn. The runout of the rotor can be as great as 0.0003 inches to be within the error budget. The stator is then installed with a runout of the magnitude and direction as marked by Farrand, Inc. The tolerance of matching the required installation is the same as the rotor installation requirement 0.0003 TIR. The discs may be out of plane (wobble) by as much as one arc minute with only a 0.2 arc second effect on the accuracy. There are also separate budgets to allow for the random shift of the bearings due to ball effects and a bias shift of the bearing centers after launch such as asymmetrical thermal effects and brinell marks.

After the installation, a polygon can be used to verify the accuracy within the resolution of the register. The discs can then be drilled and pinned into the final position. The pinning method is the most reliable method of minimizing shifts of the bolted surfaces under thermal and load cycles. Since the beryllium is difficult to work with at this stage of assembly, steel inserts are required in both parts of each junction. A number of plugs are necessary as an allowance for disassembly.

Life Comparison

Many of the elements of the gimbal have basic wear-out modes which still allow large safety margins over the life requirements of the STARS gimbal. The experience developed at Hughes on each of the wear items is listed in Table 3.4-6. The applicable in-orbit data are based on TACSAT performance. The other data were developed in vacuum chambers at Hughes.

Item	Error Class*	Error Quantity	Definition	Assigned Value Maximum, microinches	Angular** Contribution in Assembly, microradians	Remarks
1	E	L (IRB-IRG)e	Eccentricity. Inner race groove to inner race bore (TIR)	60	Not applicable	Each inner race marked with high spot. High spots of bearing pair aligned, thus causing residual error due to a) magnitude difference between race eccentricities and b) deviation in true high spot location and alignment.
2	RE	L (IRB-IRG)e	Residual error of 1	15	$\frac{15}{10} = 1.5$	
3	U	L (IRB-IRG)e	Uncertainty of 1	15	$\frac{15}{10} = 1.5$	Uncertainty in (E) L (IRB-IRG)e measurement.
4	U	L (IRRF-IRG)AW	Orthogonal component (radial direction). Axial wobble of inner race groove to inner race reference face	7.5	$\frac{15}{10} = 1.5$	Axial wobble high spot rarely coincides with eccentricity high spot so that correction cannot be made simultaneously for wobble. Assumed worst case for opposite bearing pairs diametrically opposed; however, mean was assumed within each bearing pair.
5	U	L (B-B)V	Variance. Ball-to-ball diameters (for bearing ball complement)	5	$\frac{10}{10} = 1.00$	Assuming: larger balls (1/2 of the complement) diametrically oppose smaller balls. Worst possible case — both bearing pairs.
6	U	L PC	Size of particulate contamination	45	$\frac{45}{10} = 4.5$	Assuming: some particles at times enter ball to race contact and not necessarily simultaneously in both bearings and pairs in diametrically opposed locations.
7	E	L (SH-IR)f	Fit between inner race bore and shaft	Interference	0 ⎫	Interference to exist over entire operational thermal range.
8	E	L (H-OR)f	Fit between outer race and housing	Interference	0 ⎭	
9	E	$L(B_1-B_2)e, SH$	Shaft eccentricity between bearing locations 1 and 2 (TIR)	60	Not applicable	Combined with item 1, races are angularly positioned to minimize effective total eccentricity; i.e., shaft rotational axis defined by race grooves.
10	RE	L [(#1-#9)] e, SH	Residual error of shaft axis definition (1 and 9 combination)	30	$\frac{30}{10} = 3$	
11	U	L [(#1-#9)] e, SH	Uncertainty of shaft axis definition (1 and 9 combination)	15	$\frac{15}{10} = 1.5$	
12	U	L [(#1-#9)] e, SH, TH	Uncertainty in 1 and 9 combination due to nonhomogeneous response to thermal changes***	2.5	$\frac{5}{10} = 0.50$	Thermal differential expansion induced change in initial interference fits may not take place equally everywhere due to nonhomogeneity of structures and materials.
13	U	L_{BC}[IR-OR] e, TH	Ball contact position change due to outer race to inner race thermal condition change	2.5	$\frac{5}{10} = 0.50$	Even if both inner and outer races experience identical change in temperature (no gradient) and if both bearings experienced identical change, larger outer race will change at a higher rate than inner race. Contact angle shifts. Assume: bearing pair (1) experiences thermal shift larger or smaller than that experienced by bearing pair (2) this causes angle uncertainty (13) due to difference in race curvatures and ball sizes between bearing pairs (1) and (2).
14	U	L (OR-HSG)e, TH	Housing to outer race induced eccentricity change due to nonhomogeneous interference fit change due to thermal variations	2.5	$\frac{5}{10} = 0.50$	Original outer race and housing errors (as assembled) are lumped in an offset angle error — a constant. However, if changes occur, the offset angle changes in an unpredictable manner.
15	U	I_{DS}(LE)	Uncertainty due to launch environment caused Brinell spots	30	$\frac{30}{10} = 3.0$	75% Brinell spot depth of indentation in one bearing, taking total load in radial direction, (60 g peak acting for > 1 second).

*E: error, RE: residual error, and U: uncertainty.
**1 microradian = 0.206 arcsec.
***Bulk temperature variation limited to ±10°F; radial gradient limited to 5°F maximum.

TABLE 3.4-4. (continued)

Item	Error Quantity, microradians	Quantity Squared, microradians	Extension
		SUMMARY	
2	1.5	1.5	$\Sigma = 5$ (errors)
10	3.0	9.0	Rss = 3.24 microradians
			~ 0.7 arcsec
3	1.5	2.25	$\Sigma = 37.8$ (uncertainties)
4	1.5	2.25	
5	1.00	1.00	Rms = $\sqrt{\dfrac{37.8}{Q-1}}$
6	4.5	20.3	$\Sigma = 2.17$ microradians
11	1.5	2.25	~ 0.45 arcsec
12	0.50	0.25	
13	0.50	0.25	
14	0.50	0.25	
15	3.0	9.00	

Therefore: Total error and uncertainty contributions (maximum) =

0.70 + 0.45 = 1.15 arcsec

TABLE 3.4-5.   INDUCTOSYN ACCURACY

A.	Errors systematic with poles (512 per revolution)		0.45 arcseconds
B.	Errors systems per revolution		
	1.	Centering indication on Inductosyn discs	0.68
	2.	Effect of bearing bias	0.50
	3.	Rotor to housing alignment	1.00
	4.	Stator to shaft alignment	1.00
	5.	Wobble	0.20
	6.	Bearing random effect	0.10
RSS TOTAL			1.72 arcseconds

TABLE 3.4-6.   LIFE COMPARISONS

	Hughes Experience (Revolutions)	Goal (Rev. - 3 years)
Motor brushes		
TACSAT	$\sim 67 \times 10^6$	1.8×10^4
Laboratory test (vacuum)	21×10^6	
Ball bearings		
TACSAT	$\sim 67 \times 10^6$	1.8×10^4
Slip rings		
Laboratory test (vacuum)	$> 32 \times 10^6$	1.8×10^4
Lubrication supply		
TACSAT (2-1/3 years at 55 rpm)	$\sim 67 \times 10^6$	3 years at 16 rev/day

The laboratory data is actually more suitable for engineering evaluation because the articles can be examined for failure modes after the test period. The laboratory test on the TACSAT despin motor for instance showed less than 0.005 inch of wear on the brushes after 21×10^6 revolutions. The wear life of all elements is also dependent on the lubrication supply for the duration of the mission. TACSAT has already verified 2-1/2 years and current despin assemblies have a design life far in excess of 10 years for the oil supply. The STARS lubrication system also has the advantage that all elements use the same oil lubricant so there is no requirement for special sealing between elements. However, extra care on the labyrinth seal design will be required on STARS due to the proximity of optical elements to rotary interfaces.

3.5   Servo Analysis and Simulation

Introduction

To establish a baseline design capable of meeting the high
accuracy requirements (1.8 arc sec, rms, per axis) of the STARS and to
investigate the effects of friction and other non-linearities on performance,
a preliminary design study of a direct drive servo suitable for the STARS
gimbal drives was undertaken.

The performance requirements and design constraints for the STARS gimbal
servos are listed in Table 3.5-1. The required positioning accuracy
(8.72 μ rad, rms) is that allocated to servo, exclusive of errors in
the gimbal angle sensor itself. The principal sources of error that have
been considered include the effects of friction and stiction, and error
signal quantization. Of prime importance is the stiction characteristic.
The baseline servo design is predicated on an elastic stiction model
which presents a much more difficult constraint than that of the classical
stiction model.

There are many candidate approaches which could be considered in the
servo design. Since feasibility was the principal question to be answered,
however, attention was concentrated on the most promising mechanization.
The servo employs a direct drive torque motor, an Inductosyn operated
as an incremental shaft encoder, digital error signal processing, and analog
shaping. The problem of initial angle acqusition was also studied, and the
requirements for such acqusition have been established.

TABLE 3.5-1

SERVO LOOP REQUIREMENTS AND CONTRAINTS

	PITCH AXIS	POLAR AXIS
Load Inertia, Slug-ft^2	1.5	.05
Friction Torque, ft-lb	.05	.05
Stiction Torque, ft-lb	.1	.1
*Stiction Break Away Angle, μ rad	200	200
Nominal Rate, μ rad/sec	1000	.02
**Position Error, μ rad RMS	< 8.72	< 8.72

* Applicable only to elastic stiction model. See discussion in section on Friction Model.

** Applies to total random error, excluding error in gimbal angle sensor. See discussion in Error Summary.
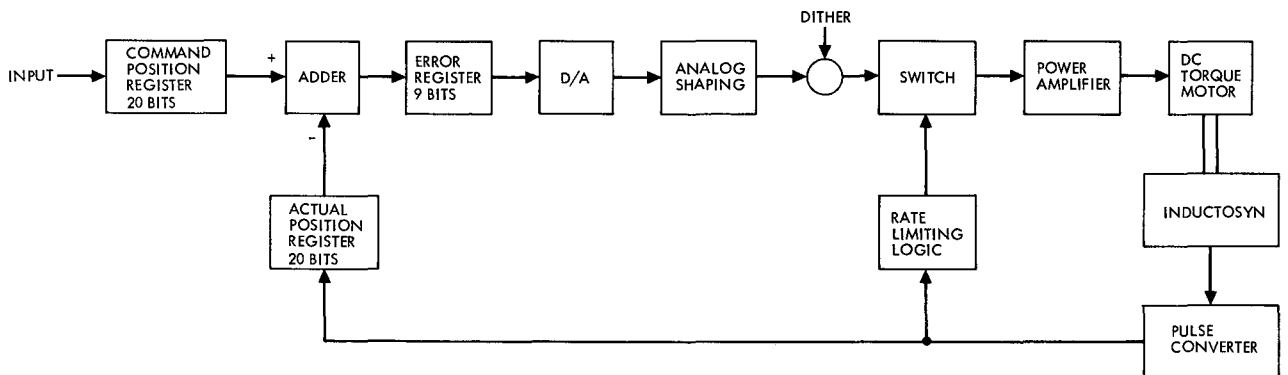

Figure 3.5-1. Gimbal Servo Functional Block Diagram

FUNCTIONAL DESCRIPTION

A block diagram of the servo under consideration is shown in Figure 3.5-1
The operation is as follows:

The commanded position is contained in a 20-bit register (CPR) which is
incremented at the required gimbal angular rate. The actual position is con-
tained in a second 20-bit register (APR) which is updated by signals from a
pulse converter and Inductosyn. The pulse converter generates a pulse and
direction sense signal for each .0005 deg (8.75 μ rad) change in the shaft
position. Provision is also included for an initialization pulse at a cali-
brated shaft position. The Inductosyn and pulse converter together operate as
an incremental shaft encoder.

The position error, represented by the difference between the CPR and APR
data, is sampled at a high rate ($\geq$ 2000 per second). Only the 8 least significant
bits and the sign bit are stored, providing a linear range of $\pm$ 0.128 degrees for
the error signal. Appropriate logic is employed to saturate the error register
for larger error angles.

After conversion to analog form in a 9-bit D/A, the error signal is operated
on by a lag-lead, lead-lag shaping network, using an operational amplifier and
R-C elements. The amplifier output is limited to the desired saturation torque
capability. This prevents excessive capacitor charge for large errors which
could prove troublesome for initial acquisition.

Torque dither is employed in the polar axis servo (inner gimbal) only for
the inelastic stiction model. Dither is ineffective and therefore not used in the
elastic stiction model (baseline). It is not required in the pitch axis servo
since the gimbal rate and inertia are high enough to preclude stick-slip operation.
The torque generated by the brush-type d-c motor is controlled by a power amplifier
using armature current feedback.

To enable acquisition when large initial servo errors exist, the gimbal rate
is limited to a relatively low value. This is done by using the pulse rate from
the pulse converter as a measure of the angular rate, and applying a decelerating
torque whenever the reference rate is exceeded. This results in a bang-bang rate
control loop which is operative only at the high rates encountered during initial
acquisition.

FRICTION MODEL

The dynamics of the servo for very small motions is quite dependent on the friction-stiction characteristics. The classical model (referred to here as the inelastic model) assumes that whenever the bearing is "stuck", no motion will occur until the applied torque exceeds the stiction torque. Once in motion, a constant friction torque opposes the motion. Any change in the direction of the motion will result in a "stuck" bearing unless or until the applied torque exceeds the stiction torque.

Recent tests on a representative bearing have provided a rather different picture of the stiction characteristic. The tests appear to indicate that there is an elastic region about the stuck position. A restoring torque approximately proportional to the deflection angle acts on the shaft. Break away occurs only after the deflection exceeds some angle which appears to be large compared to the allocated error of 8.7 μ rad.

This has a significant effect on the dynamical behavior at small error angles. It also places some important constraints on the servo parameters and on the mode of operation. In particular, the polar axis servo must be powered continuously rather than intermittently as would be possible if stiction were of the inelastic type. Dither is of little value in minimizing the errors due to elastic stiction, and therefore the torque gain must be higher than would otherwise be necessary. As noted earlier, the stick-slip mode can be avoided in the pitch axis servo during steady state operation because of the higher angular rate and load inerta.

Because of its more serious impact on servo design and performance, the elastic stiction model has been assumed in the baseline design. However until more definitive tests of the bearing stiction can be performed, the appropriate stiction model must be considered in doubt. Therefore both models have been investigated in the simulation study.

SIMULATION MODEL

A block diagram of the servo loop used in the simulation is shown in Figure 3.5-2. Besides the linear model of load dynamics shown, two friction-stiction models are provided as shown in Figures 3.5-3 and 3.5-4. A complete listing of the program is attached. Definitions of the principal parameters are contained in the listing and correspond to those used in Figure 3.5-2.

In evaluating the servo performance, the true error signal is used. This is obtained by taking the difference between the inputs to the two quantizers.

Limiters have been included on the quantized error signal and the shaping network output to represent the effects of such limit levels in an actual mechanization. These limit levels are reached only during the initial acquisition transient, however.

The shaping network, though programmed in a cascade configuration, would actually be implemented with a single-stage operational amplifier. Because of the large differences in inertias between pitch axis and polar axis gimbals, different shaping network parameters are required. However the transfer functions are of the same form in both cases.

Table 3.5-2 lists the baseline parameters for each servo. Assuming the elastic stiction model, the d-c torque gain, K, for the polar axis servo must be greater than $L_2/Q = 11400$ ft-lb to insure that a one-step error will produce break away torque. A lower gain may be used in the case of inelastic stiction, if the amplitude of the dither exceeds L_2.

Using a value of K = 15000 ft-lb/rad, and the specified inertia of .05 ft-lb-sec^2, it is seen that the undamped natural frequency of the polar axis servo loop is $\omega_N = \sqrt{K/J} = 547$ rad/sec = 87 cps. With the shaping parameters selected, the damped natural frequency is about 55 cps. At such high frequencies, the effect of elastic structural modes on stability must be carefully considered. This has not been done in the present study because the necessary modal data is not available. However it represents an important additional constraint which must be accounted for in a detailed design.

Figure 3.5-2.   Servo Loop Simulation Model

Figure 3.5-3.   Elastic Stiction Model

Figure 3.5-4.   Inelastic Stiction Model

TABLE 3.5-2

SERVO LOOP PARAMETERS

	PITCH AXIS	POLAR AXIS
Error-To-Torque Gain, ft-lb/rad	10,000	15,000
Lead Time Constants, sec. $\{T_1$	0.1	0.02
$\{T_3$	0.075	0.015
Lag Time Constants, sec. $\{T_o$	0.5	0.25
$\{T_2$	0.01	0.0015
$\{T_4$	0.0025	0.001
Error Sampling Period, sec.	<.0005	<.0005
Damped Natural Frequency, Hertz	~ 14	~ 55
Shaft Angle Data Quantization, μ rad	8.8	8.8
Error Saturation, μ rad	2253	2253
Rate Limit for Acquisition, μ rad/sec	35000	50000
Torque Saturation, ft-lb	0.5	0.5
*Dither Torque Amplitude, ft-lb	0.125	0.125
*Dither Frequency, Hertz	170	650
Motor Constant, ft-lb/$\sqrt{\text{watt}}$ (Based on Inland Motor T3905)	0.189	0.189
Motor Power, watts		
At Torque Saturation	7.0	7.0
At Stiction Torque	0.28	0.28
At Friction Torque	.07	.07

*Applicable only to inelastic stiction model. Dither not used in elastic stiction model.

For the pitch axis, the d-c torque gain need only be high enough to avoid excessive droop error due to running friction since the stick condition does not occur in the steady state. Thus $K \geq L_1/E_{ss}$, where E_{ss} is the allowable steady state droop error. The value of $K = 10000$ ft-lb/rad chosen for the pitch servo implies a nominal droop of 5 μ rad.

TABLE 3.5-3

ERROR SUMMARY

PITCH AXIS	
Systematic Bias	5 μ rad Mean Droop
Random Bias	100 μ rad per ft-lb Uncertainty in Friction Torque
Short Period Variations	± 0.2 μ rad Due to Quantization at Frequencies above 5 cps.
Long Period	Diurnal Temperature Effects (Same Error Coefficient as Random Bias)
POLAR AXIS	
Systematic Bias	5 μ rad Mean Droop
Random Bias	∼ 27 μ rad per ft-lb Uncertainty in Stiction Torque
Short Period Variations	± 2 μ rad Due to Quantization at Frequencies Above 5 cps. ∼ 30 to 35 μ rad Peak Error Lasting ∼ 0.1 sec, every ∼ 1000 sec.
Long Period Variations	± 4.4 μ rad Cyclic Error with 44 sec Period ± 2.7 μ rad Cyclic Error at Stick-Slip Period (∼ 1000 sec) Diurnal Temperature Effects (Same Error Coefficient as Random Bias)

ERROR SUMMARY

In considering the various types of servo positioning errors, it is important to distinguish between those which have an effect on the accuracy of the spacecraft attitude control system and those which do not. The servo errors may be grouped into bias errors and time varying errors. Bias errors may further be categorized as systematic (those which can be compensated) and random (those which cannot). Time varying errors may be categorized as short period and long period. Short period errors are of concern primarily as noise sources which must be adequately filtered to avoid problems due to saturation in the attitude control loops. Long period errors in general cannot be compensated and may be considered essentially equivalent to random bias. In the present study, time varying errors whose frequency components are above 1 Hertz are treated as short period errors.

The principal source of systematic bias error is that caused by friction and finite d-c torque gain, sometimes referred to as servo droop error. In the pitch axis the droop error is proportional to the nominal friction torque. In the polar axis, the droop error is proportional to the nominal stiction torque, being the mean of the cyclic error in the stick-slip mode. By definition, the nominal friction and stiction torque levels are known and thus can be compensated.

Random bias errors are due principally to deviations from the nominal friction and stiction levels caused by off-nominal temperatures and/or wear-in effects. The uncertainty in these levels is, by definition, uncompensatable and must therefore be treated as a random effect.

The principal sources of time-varying error in the polar axis are due to error signal quantization and to stick-slip effects. They have both short term and long term components. Additional sources affecting both pitch and polar axis servos include a short period limit cycle due to error signal quantization, and long period errors due to diurnal temperature changes. A more detailed discussion and evaluation of the polar axis servo errors is contained in the section on Simulation Results.

Table 3.5-3 presents a summary of the error sources and magnitudes obtained from the results of computer simulations. In computing the total RMS error for each servo, only the random biases and long period time varying errors have been included. Based on an assumed $\pm$ 50% (1σ) bias uncertainty and diurnal variation in the friction and stiction torque levels, the total RMS error in the pitch axis servo is 3.5 μ rad, and in the polar axis servo is 7.7 μ rad.
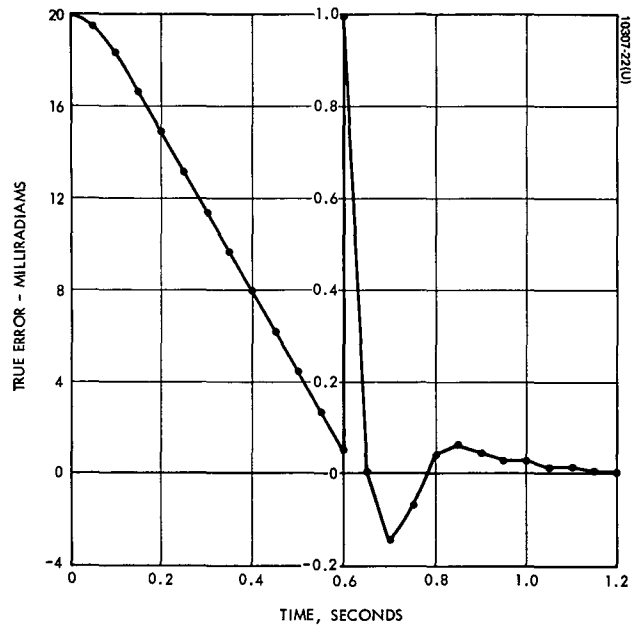
Figure 3.5-5.   Plot of Pitch Axis Initial Acquisition
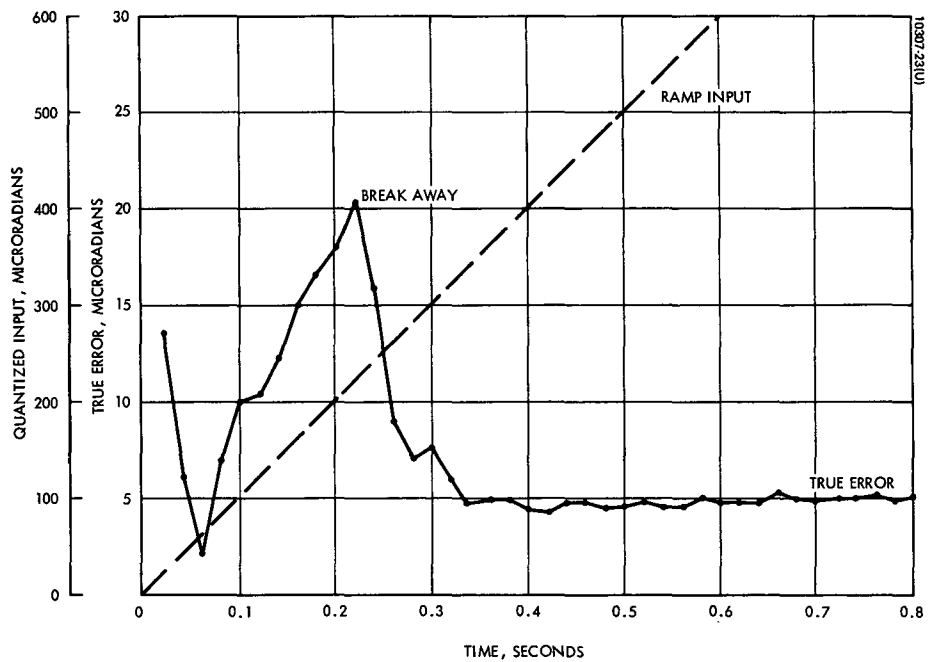
Figure 3.5-6.   Plot of Pitch Axis Ramp Response

SIMULATION RESULTS

The output of the PDDSS* simulation program provides a sampled-data tabulation of the following variables:

Q-INPUT	Quantized Input (μ rad)
Q-ERROR	Quantized Error (μ rad)
T-ERROR	True Error (μ rad)
RATE	Angular Rate (μ rad/sec)
TORQUE	Motor Torque (ft-lb)

The values of 20 parameters are identified in the heading and may be varied as desired. The definitions of these parameters are contained in the program listing. Note that angles and angular rates in the printout are in units of μ rad/sec.

Six computer runs are presented to show the characteristic ramp and step input responses. To avoid excessively long computer printouts, the sample period has been made longer in some cases than would be desirable for showing all of the detail. A discussion of each computer run follows:

Figure 3.5-5 shows the pitch axis acquisition with an initial error of .02 radians. This is a large enough error to saturate the servo amplifier input for about 0.6 sec, and is therefore representative of the acquisition behavior for arbitrarily large initial errors. The rate limiter prevents the average rate from exceeding .035 rad/sec. during saturation. Without this limiter the rate could become too large for successful acquisition. The computer run was terminated somewhat before steady-state conditions were achieved.

Figure 3.5-6 shows the pitch axis behavior while following a ramp input of 1000 μ rad/sec, starting with zero rate initial condition. The stiction break away angle was set at 200 μ rad. Break away occurred at 0.22 sec, after which the rate remained positive and the error settled down to the nominal droop error of 5 μ rad. The error jitter of about $\pm$ 0.2 μ rad in the steady-state is due to the effect of error signal quantization. Note that the quantized error limit cycles between 0 and 8.8 μ rad to maintain an average motor torque equal to the friction torque.

Figure 3.5-7. Plot of Polar Axis Initial Acquisition

Figure 3.5-7 shows the polar axis acquisition with an initial error of .02 rad. As in the case of the pitch acquisition example, this is large enough error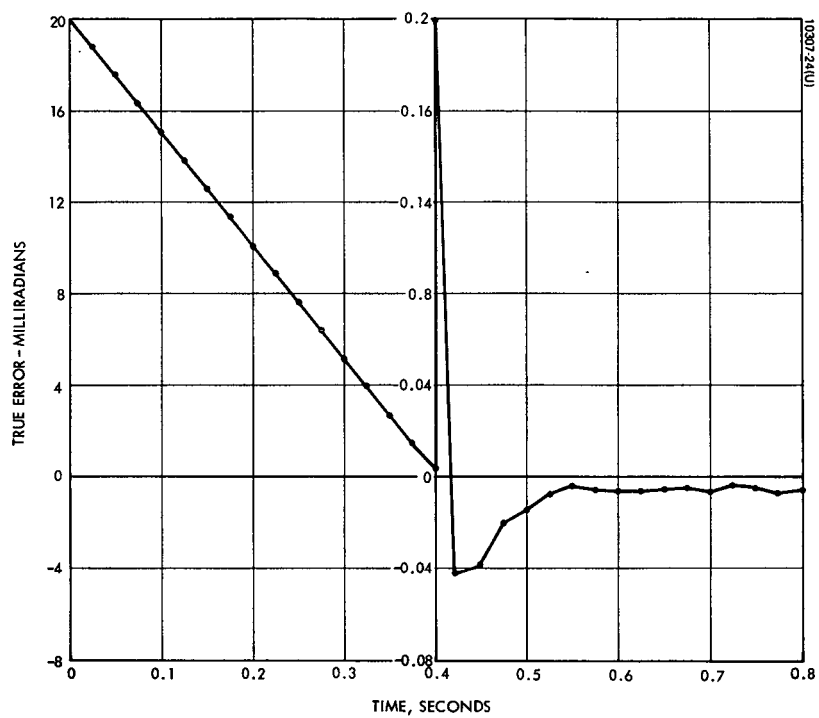 to be representative of arbitrarily large initial conditions. Stiction break away occurred at .0066 sec and the bearing restuck at .4236 sec when the rate changed polarity. Since the error never exceeded the break away angle of 200 μ rad thereafter, the bearing remained stuck and all subsequent motion was due to the elasticity. In the latter end of the run, the beginning of a limit cycle between 0 and -8.8 μ rad (quantized error) is apparent. This is due to the residual stiction torque. Note that the range of jitter in the true error is considerably less than 8.8 μ rad.

The nominal polar axis rate is 0.2 μ rad/sec. For a quantization of 8.8 μ rad/sec per step, the period between steps will be 44 seconds. Since the transient settling time is only a fraction of a second, the principal polar axis motion is characterized by a staircase waveform. Thus the long period error waveform is a saw-tooth with an amplitude of $\pm$ 4.4 μ rad and a period of 44 seconds.

The effect of elastic stiction is to add an additional cyclic error whose period depends on the stiction break away angle. The steady-state droop error builds up with each step, due to the elastic stiction torque, until the break away angle is reached, whereupon the cycle starts over. A larger than normal transient occurs on the break away step because of the large change in stiction torque after break away.

Assuming a stiction break away angle of 200 μ rad, there will be about 23 steps per stick-slip cycle with an overall period of about 1000 seconds. It is impractical to simulate the servo response over such a long period. However it is possible to simulate the response to any single step by establishing the appropriate initial conditions. If we examine the response for the break away step and for the step immediately preceding, we can infer what the short and long period errors will be over the entire stick-slip cycle. These are presented in Figures 3.5-8 and 3.5-9, respectively.

The initial conditions in Figure 3.5-8 were set as follows: $X_3 = X_4 = X_5 = 0.1$ ft-lb, and $C_0 = -195$ μ rad. Break away occurred at .0064 sec. after the input step of
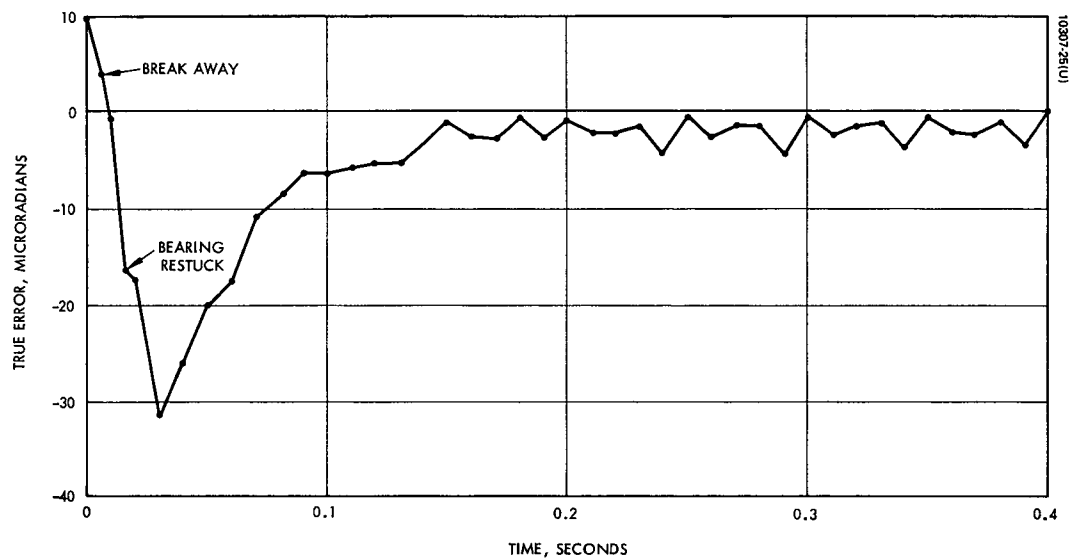
Figure 3.5-8. Plot of Polar Axis - Single Step Response
Elastic Stiction Breakaway Transient
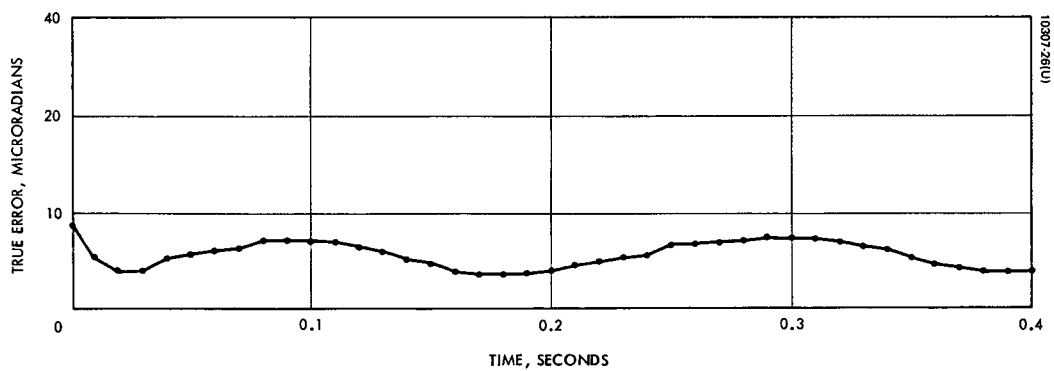
Figure 3.5-9. Plot of Polar Axis - Single Step Response
Elastic Stiction Model Last Step Stiction Breakaway

8.8 μ rad, and the bearing restuck at .0178 sec. an overshoot of about 32 μ rad occurred during the transient with the principal part of the transient lasting about 0.1 sec. The droop error after the transient will depend somewhat on the servo parameters but will generally be less than 1.0 μ rad. In Figure 3.5-8 steady-state conditions have not quite been reached in the 0.4 sec. period shown.

The initial conditions in Figure 3.5-9 were set as follows: $X_3 = X_4 = X_5 = .095$ ft-lb, and $C_o = -190$ μ rad. Although the input step size was 8.8 μ rad, the resulting output step was only about 3.4 μ rad. This difference of about 5.4 μ rad is the droop error caused by the elastic stiction torque, modified by an effect due to the limit cycle resulting from error quantization. If there were no quantization, the droop error could be computed directly from $E = \dfrac{L_2 (C - C_o)}{K C_2}$ and would be 6.7 μ rad just before break away for the assumed parameters.

In summary, the polar axis response involves two long period cyclic errors plus a sizable short period transient. One of the long period errors is due to error signal quantization ($\pm$ 4.4 μ rad amplitude, 44 sec. period), and the other is due to elastic stiction ($\pm$ 2.7 μ rad amplitude, $\sim$ 1000 sec period). At times during each stick-slip cycle these errors will add. A short period transient error of about 32 μ rad, lasting about 0.1 sec, occurs at stiction break away. There is also a short period jitter of about $\pm$ 2 μ rad amplitude due to the limit cycle effect.

By way of comparison the single step response of the polar axis, using the inelastic (classical) stiction model is shown in Figure 3.5-10. A dither torque of 0.125 ft-lb amplitude at a frequency of 650 Hertz has been added. When the dither amplitude exceeds the stiction torque level, the shaft will oscillate continuously through a small angle. This virtually eliminates the effect of stiction on the servo response. After the step-induced transient subsides the servo error goes to zero, except for the small residual effect of dither. The only attitude control system error resulting is the $\pm$ 4.4 μ rad amplitude saw-tooth referred to earlier.
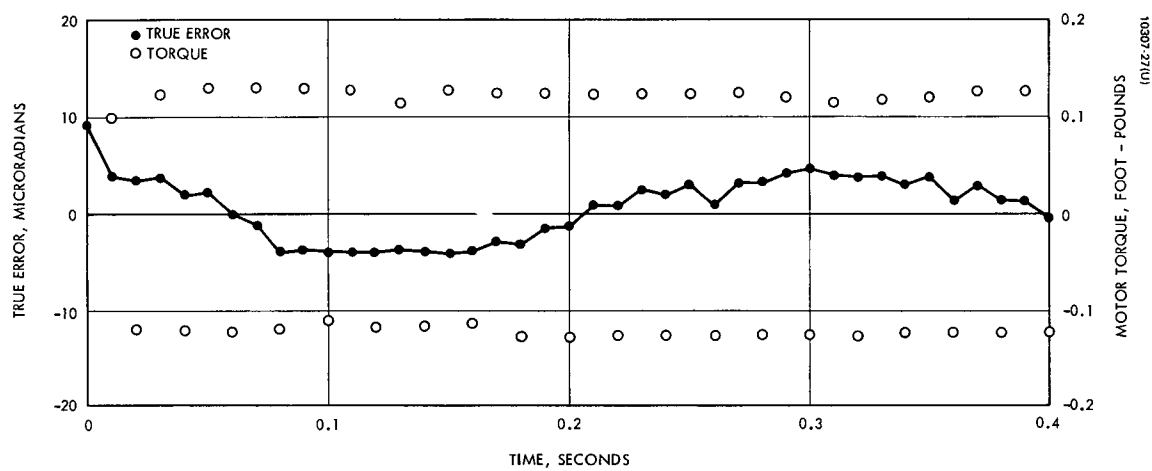
Figure 3.5-10. Plot of Polar Axis Single Step Response
Stiction With Torque Dither, Classical Stiction Model

PITCH AXIS INITIAL ACQUISITION

T0 = .5	T1 = .1	T2 = .01	T3 = .075	T4 = .0025
R = 20000	R1 = 0	E0 = 2253	X0 = 35000	Q = 8.8
L0 = .5	L1 = .05	L2 = .1	L5 = .0	F5 = 0
K = 10000	J = 1.5	D = .0005	B = 0	C2 = 1000.

TIME	Q-INPUT	Q-ERROR	T-ERROR	RATE	TORQUE
.0	20000.0	2253.0	20000.0	.0	.0
.05	20002.4	2253.0	19593.1	16054.5	.5
.079	20002.4	2253.0	18989.3	24544.9	.5
.1	20002.4	2253.0	18421.5	30694.9	.5
.15	20002.4	2253.0	16701.9	35028.3	.5
.2	20002.4	2253.0	14952.5	35028.3	.5
.25	20002.4	2253.0	13203.2	35028.3	.5
.3	20002.4	2253.0	11453.9	35028.3	.5
.35	20002.4	2253.0	9704.5	35028.3	.5
.4	20002.4	2253.0	7955.2	35028.3	.5
.45	20002.4	2253.0	6205.9	35028.3	.5
.5	20002.4	2253.0	4456.5	35028.3	.5
.55	20002.4	2253.0	2707.2	35028.3	.5
.6	20002.4	1012.0	1006.4	29150.5	-.5
.65	20002.4	17.6	11.8	10817.1	-.5
.6795	20002.4	-140.8	-145.1	-182.9	-.5
.7	20002.4	-70.4	-74.1	-6355.3	-.2428
.75	20002.4	44.0	42.9	898.8	-.1339
.8	20002.4	61.6	57.3	16.9	.0843
.85	20002.4	44.0	42.4	24.7	-.0079
.9	20002.4	26.4	27.8	354.4	-.0381
.95	20002.4	26.4	23.4	372.2	.0168
1.	20002.4	17.6	11.9	-233.1	.0383
1.05	20002.4	8.8	10.1	-85.8	-.0103
1.1	20002.4	8.8	5.3	332.3	.0021
1.15	20002.4	8.8	2.6	263.1	.0415
1.2	20002.4	.0	.6	298.8	-.0471
1.25	20002.4	.0	1.4	-99.4	-.015
1.3	20002.4	.0	-1.9	41.0	-.0139
1.35	20002.4	.0	-5.3	105.0	-.0114
1.4	20002.4	.0	-4.1	42.4	-.0075
1.45	20002.4	.0	-4.3	-82.3	.0085
1.5	20002.4	.0	-6.3	-267.8	-.0459
1.55	20002.4	-8.8	-6.9	149.6	-.0094
1.6	20002.4	.0	-6.5	141.3	-.0087
1.65	20002.4	.0	-5.6	128.3	-.0082
1.7	20002.4	.0	-5.3	114.0	-.007
1.75	20002.4	.0	-5.1	104.1	-.0062
1.8	20002.4	.0	-4.9	95.5	-.0054
1.85	20002.4	.0	-4.9	88.1	-.0047
1.9	20002.4	.0	-4.8	82.3	-.0041
1.95	20002.4	.0	-4.2	63.5	-.003
2.	20002.4	.0	-4.1	25.0	.0013

RAN   47 SEC.

STOP.

3

PITCH AXIS RAMP RESPONSE

PDDSS*   8:51   THURS. 05/13/71

TO = .5	TI = .1	T2 = .01	T3 = .075	T4 = .0025
R = 0	RI = 1000.	EO = 2253	XO = 35000	Q = 8.8
LO = .5	LI = .05	L2 = .1	L5 = .0	F5 = 0
K = 10000	J = 1.5	D = .0005	B = 0	C2 = 200

TIME	Q-INPUT	Q-ERROR	T-ERROR	RATE	TORQUE
.0	.0	.0	.0	.0	.0
.02	17.6	8.8	13.3	985.3	.0775
.04	44.0	8.8	6.4	1485.8	-.0324
.06	61.6	.0	2.1	924.3	.0379
.08	79.2	8.8	7.0	723.8	.0745
.1	96.8	8.8	10.0	960.8	.0441
.12	123.2	17.6	10.3	930.4	.057
.14	140.8	8.8	12.4	871.5	.1145
.16	158.4	17.6	15.1	900.2	.1096
.18	176.0	8.8	16.7	954.9	.0934
.2	202.4	17.6	18.0	898.8	.084
.22	220.0	17.6	20.4	929.5	.1206
.22	220.0	17.6	19.9	932.2	.1079
.24	237.6	17.6	15.9	1463.1	.07
.26	264.0	8.8	8.5	1227.9	.0187
.28	281.6	8.8	7.1	950.1	.0418
.3	299.2	8.8	7.6	1036.2	.0728
.32	316.8	.0	6.0	1130.1	.0518
.34	343.2	8.8	4.8	968.2	.0187
.36	360.8	8.8	5.0	971.8	.0843
.38	378.4	.8	5.0	1047.3	.0952
.4	396.0	.0	4.4	1022.5	.0076
.42	422.4	8.8	4.3	947.6	.0453
.44	440.0	8.8	4.9	975.9	.0924
.46	457.6	.0	4.9	1057.3	.0499
.48	484.0	8.8	4.6	1004.9	.0029
.5	501.6	8.8	4.6	958.2	.0703
.52	519.2	.0	4.9	1016.6	.0955
.54	536.8	.0	4.6	1055.2	.0205
.56	563.2	8.8	4.6	948.1	.0256
.58	580.8	8.8	5.0	991.2	.0836
.6	598.4	.0	4.8	1036.5	.0673
.62	616.0	.0	4.8	1016.0	.0127
.64	642.4	8.8	4.8	934.1	.0419
.66	660.0	8.8	5.3	981.1	.0878
.68	677.6	.0	5.0	1066.3	.0452
.7	704.0	8.8	4.9	979.8	.0016
.72	721.6	8.8	5.0	969.4	.0666
.74	739.2	.0	5.1	1009.7	.093
.76	756.8	.0	5.1	1054.7	.0309
.78	783.2	8.8	4.9	950.6	.0227
.8	800.8	8.8	5.1	992.5	.0816
.82					

RAN   29 SEC.

STOP.

3-52

PDDSS*   8:31   THURS. 05/13/71

TO = .25	T1 = .02	T2 = .0015	T3 = .015	T4 = .001
R = 20000	R1 = 0	E0 = 2253	X0 = 50000	Q = 8.8
L0 = .5	L1 = .05	L2 = .1	L3 = .0	F3 = 0
K = 15000	J = .05	D = .0002	B = 0	C2 = 200

TIME	Q-INPUT	Q-ERROR	T-ERROR	RATE	TORQUE
.0	20000.0	2253.0	20000.0	.0	.0
.0066	20002.4	2253.0	19793.4	49350.8	.5
.025	20002.4	2253.0	18885.9	49150.8	-.5
.05	20002.4	2253.0	17639.7	50150.8	.5
.075	20002.4	2253.0	16393.4	51150.8	.5
.1	20002.4	2253.0	15147.6	48150.8	-.5
.125	20002.4	2253.0	13900.8	49150.8	-.5
.15	20002.4	2253.0	12654.6	50150.8	.5
.175	20002.4	2253.0	11408.3	51150.8	.5
.2	20002.4	2253.0	10162.5	48150.8	-.5
.225	20002.4	2253.0	8915.7	49150.8	-.5
.25	20002.4	2253.0	7669.6	50150.7	.5
.275	20002.4	2253.0	6423.2	51150.7	.5
.3	20002.4	2253.0	5177.4	48150.7	-.5
.325	20002.4	2253.0	3930.7	49150.7	-.5
.35	20002.4	2253.0	2684.5	50150.7	.5
.375	20002.4	1443.2	1438.1	51150.7	.5
.4	20002.4	211.2	204.8	43995.2	-.0856
.4236	20002.4	-44.0	-43.7	-194.1	.0007
.425	20002.4	-44.0	-43.5	8.4	.0137
.45	20002.4	-35.2	-39.6	85.6	-.009
.475	20002.4	-17.6	-20.2	-412.2	-.0071
.5	20002.4	-17.6	-15.7	244.6	-.0392
.525	20002.4	-8.8	-7.7	1370.0	-.0347
.55	20002.4	.0	-4.4	10.7	.0093
.575	20002.4	.0	-6.3	847.4	-.0142
.6	-20002.4	-8.8	-6.9	761.7	-.0157
.625	20002.4	-8.8	-7.1	595.6	-.0374
.65	20002.4	.0	-6.3	624.7	-.0162
.675	20002.4	.0	-5.3	531.7	-.0162
.7	20002.4	.0	-4.3	375.0	-.0152
.725	20002.4	.0	-3.9	77.0	-.01
.75	20002.4	.0	-4.4	-694.6	.0044
.775	20002.4	-8.8	-7.0	-778.3	-.0713
.8	20002.4	.0	-6.5	637.6	-.0164
.825	20002.4	.0	-5.1	511.8	-.0162
.85	20002.4	.0	-4.1	309.8	-.0146
.875	20002.4	.0	-3.8	-112.4	-.006
.9	20002.4	.0	-5.0	-1087.1	.0027
.925	20002.4	-8.8	-7.3	72.0	-.0681
.95	20002.4	.0	-5.9	593.5	-.0164

RAN   48 SEC.

STOP.

PDDSS*　　8:07　　THURS. 05/13/71

TO = .25	TI = .02	T2 = .0015	T3 = .015	T4 = .001
R = 8.8	R1 = 0	EO = 2253	XO = 50000	Q = 8.8
LO = .5	L1 = .05	L2 = .1	L5 = .0	F5 = 0
K = 15000	J = .05	D = .0002	B = 0	C2 = 200

TIME	Q-INPUT	Q-ERROR	T-ERROR	RATE	TORQUE
.0	8.8	8.8	8.8	.0	.0
.0064	8.8	.0	3.7	1122.6	.0694
.01	8.8	.0	-.8	1739.9	.0731
.0178	8.8	-17.6	-16.4	-13.3	.0169
.02	8.8	-17.6	-17.5	1110.2	.0347
.03	8.8	-35.2	-31.7	-1453.5	-.019
.04	8.8	-26.4	-26.2	-546.2	-.0062
.05	8.8	-17.6	-20.2	473.8	.0014
.06	8.8	-17.6	-17.5	-1363.8	-.0126
.07	8.8	-8.8	-10.9	616.4	-.001
.08	8.8	-8.8	-8.6	-665.4	-.0021
.09	8.8	-8.8	-6.4	647.2	-.0399
.1	8.8	-8.8	-6.4	257.4	-.0457
.11	8.8	-8.8	-5.8	-233.0	-.049
.12	8.8	-8.8	-5.4	-355.9	-.0539
.13	8.8	-8.8	-5.4	204.7	-.0573
.14	8.8	.0	-3.3	700.1	-.0033
.15	8.8	.0	-1.1	272.8	-.0017
.16	8.8	.0	-2.5	-1152.8	.0143
.17	8.8	.0	-2.8	427.9	-.0052
.18	8.8	.0	-.7	-154.8	.0006
.19	8.8	.0	-2.7	385.9	-.0057
.2	8.8	.0	-1.0	-245.1	.0015
.21	8.8	.0	-2.2	289.1	-.0059
.22	8.8	.0	-2.4	-818.5	.0102
.23	8.8	.0	-1.6	176.3	-.0061
.24	8.8	.0	-4.4	340.8	-.0059
.25	8.8	.0	-.7	30.7	-.0058
.26	8.8	.0	-2.6	317.5	-.006
.27	8.8	.0	-1.5	-425.6	.0044
.28	8.8	.0	-1.5	194.5	-.0061
.29	8.8	-8.8	-4.5	343.7	-.0059
.3	8.8	.0	-.7	29.2	-.0059
.31	8.8	.0	-2.5	308.9	-.0061
.32	8.8	.0	-1.6	-535.4	.0065
.33	8.8	.0	-1.3	173.8	-.0062
.34	8.8	.0	-4.1	342.9	-.006
.35	8.8	.0	-.7	-15.9	-.0056
.36	8.8	.0	-2.2	284.3	-.0061
.37	8.8	.0	-2.4	-919.7	.0097
.38	8.8	.0	-1.1	136.9	-.0062
.39	8.8	.0	-3.6	337.1	-.006
.4	8.8	.0	-.7	-91.8	-.0044

P4Q

RAN　　27 SEC.

STOP.　　　　　　　　　　3-54

POLAR AXIS - SINGLE STEP RESPONSE
ELEASTIC STICTION MODEL SHOWING LAST STEP
BEFORE STICTION BREAK AWAY

PDDSS*   8:14   THURS. 05/13/71

TO = .25	T1 = .02	T2 = .0015	T3 = .015	T4 = .001
R = 8.8	R1 = 0	E0 = 2253	X0 = 50000	Q = 8.8
L0 = .5	L1 = .05	L2 = .1	L5 = .0	F5 = 0
K = 15000	J = .05	D = .0002	B = 0	C2 = 200

TIME	Q-INPUT	Q-ERROR	T-ERROR	RATE	TORQUE
.0	8.8	8.8	8.5	.0	.0
.01	8.8	8.8	5.1	-1573.8	.0869
.02	8.8	.0	3.9	-677.4	.0476
.03	8.8	.0	3.9	693.5	.0651
.04	8.8	8.8	5.1	834.0	.1017
.05	8.8	8.8	5.7	735.3	.1031
.06	8.8	8.8	6.1	651.6	.1046
.07	8.8	8.8	6.3	571.5	.1064
.08	8.8	8.8	7.0	408.9	.109
.09	8.8	8.8	7.2	138.1	.1152
.1	8.8	8.8	7.1	-194.7	.1221
.11	8.8	8.8	6.9	-534.6	.1271
.12	8.8	8.8	6.5	-919.8	.1289
.13	8.8	8.8	5.9	-1285.9	.1281
.14	8.8	8.8	5.0	-1452.6	.0839
.15	8.8	8.8	4.6	-1264.7	.058
.16	8.8	.0	3.9	-743.5	.0508
.17	8.8	.0	3.6	-367.6	.047
.18	8.8	.0	3.6	39.4	.0459
.19	8.8	.0	3.6	657.7	.0565
.2	8.8	.0	3.8	783.0	.0664
.21	8.8	.0	4.4	981.9	.1025
.22	8.8	8.8	4.7	930.0	.103
.23	8.8	8.8	5.1	875.1	.1034
.24	8.8	8.8	5.5	817.7	.1039
.25	8.8	8.8	6.6	657.4	.1056
.26	8.8	8.8	6.5	498.4	.1092
.27	8.8	8.8	6.8	416.1	.1102
.28	8.8	8.8	6.9	239.4	.1139
.29	8.8	8.8	7.1	79.9	.1169
.3	8.8	8.8	7.0	-183.3	.1221
.31	8.8	8.8	7.0	-409.8	.1256
.32	8.8	8.8	6.6	-771.0	.1291
.33	8.8	8.8	6.3	-1044.5	.1278
.34	8.8	8.8	6.0	-1284.8	.1201
.35	8.8	8.8	5.0	-1434.5	.0839
.36	8.8	8.8	4.4	-1246.7	.058
.37	8.8	.0	4.0	-934.0	.0532
.38	8.8	.0	3.5	-360.4	.047
.39	8.8	.0	3.8	837.8	.0661
.4	8.8	.0	3.9	924.3	.0813
.41	8.8	.0	4.4	966.8	.1027

\T

RAN   27 SEC.

STOP.

PDDSS*   8:23   THURS. 05/13/71

TO = .25	T1 = .02	T2 = .0015	T3 = .015	T4 = .001
R = 8.8	R1 = 0	EO = 2253	XO = 50000	Q = 8.8
LO = .5	L1 = .05	L2 = .1	L5 = .125	F5 = 650
K = 15000	J = .05	D = .0002	B = 0	C2 = 0

TIME	Q-INPUT	Q-ERROR	T-ERROR	RATE	TORQUE
.0	8.8	8.8	8.8	.0	.0
.01	8.8	.0	3.8	.0	.0972
.02	8.8	.0	3.4	-692.2	-.1225
.03	8.8	.0	3.6	820.1	.1227
.04	8.8	.0	1.7	-643.9	-.1214
.05	8.8	.0	2.0	868.8	.1285
.06	8.8	.0	-.1	-446.2	-.1216
.07	8.8	.0	-1.4	1011.9	.1282
.08	8.8	.0	-4.1	-355.8	-.1219
.09	8.8	.0	-3.8	651.6	.128
.1	8.8	.0	-4.0	-624.8	-.1139
.11	8.8	.0	-4.0	651.9	.1289
.12	8.8	.0	-4.1	-589.3	-.118
.13	8.8	.0	-3.9	333.1	.1128
.14	8.8	.0	-4.0	-564.8	-.1183
.15	8.8	.0	-4.2	670.0	.1262
.16	8.8	.0	-4.1	-485.1	-.114
.17	8.8	.0	-3.0	499.8	.1234
.18	8.8	.0	-3.4	-730.9	-.1272
.19	8.8	.0	-1.6	437.8	.1229
.2	8.8	.0	-1.5	-776.6	-.127
.21	8.8	.0	.6	425.3	.123
.22	8.8	.0	.7	-757.2	-.1269
.23	8.8	.0	2.4	475.4	.1232
.24	8.8	.0	1.8	-677.7	-.1267
.25	8.8	.0	2.6	583.1	.1233
.26	8.8	.0	.8	-542.9	-.1266
.27	8.8	.0	3.2	744.0	.1235
.28	8.8	.0	3.3	-756.8	-.1265
.29	8.8	.0	4.1	430.9	.1199
.3	8.8	8.8	4.5	-757.0	-.1285
.31	8.8	.0	4.0	519.3	.114
.32	8.8	.0	3.7	-779.0	-.1252
.33	8.8	.0	3.8	676.8	.1174
.34	8.8	.0	2.9	-657.1	-.1242
.35	8.8	.0	3.7	720.2	.12
.36	8.8	.0	1.4	-487.1	-.124
.37	8.8	.0	2.9	503.6	.1259
.38	8.8	.0	1.1	-513.0	-.1241
.39	8.8	.0	1.1	863.3	.1259
.4	8.8	.0	-.6	-567.4	-.1242
.41	8.8	.0	.1	795.2	.1258
.42	8.8	.0	-.9	-648.5	-.1242
.43	8.8	.0	.6	701.7	.1257
.44	8.8	.0	-.0	-754.0	-.1243

RAN   40 SEC.

STOP.   3-56

Servo Electronics

To obtain a preliminary estimate of electronic complexity and possible mechanization problems, a more detailed block diagram of the gimbal servo electronics was developed (see Figure 3.5-11). Due to the uncertainties associated at this stage with the input and output interfaces, power conditioning, and redundancy considerations, this block diagram must be considered relatively flexible. However, the values shown in Table 3.5-4 may be considered representative of the STARS servo electronics design parameters at this stage.

TABLE 3.5-4. GIMBAL SERVO ELECTRONICS PRELIMINARY DESIGN PARAMETERS

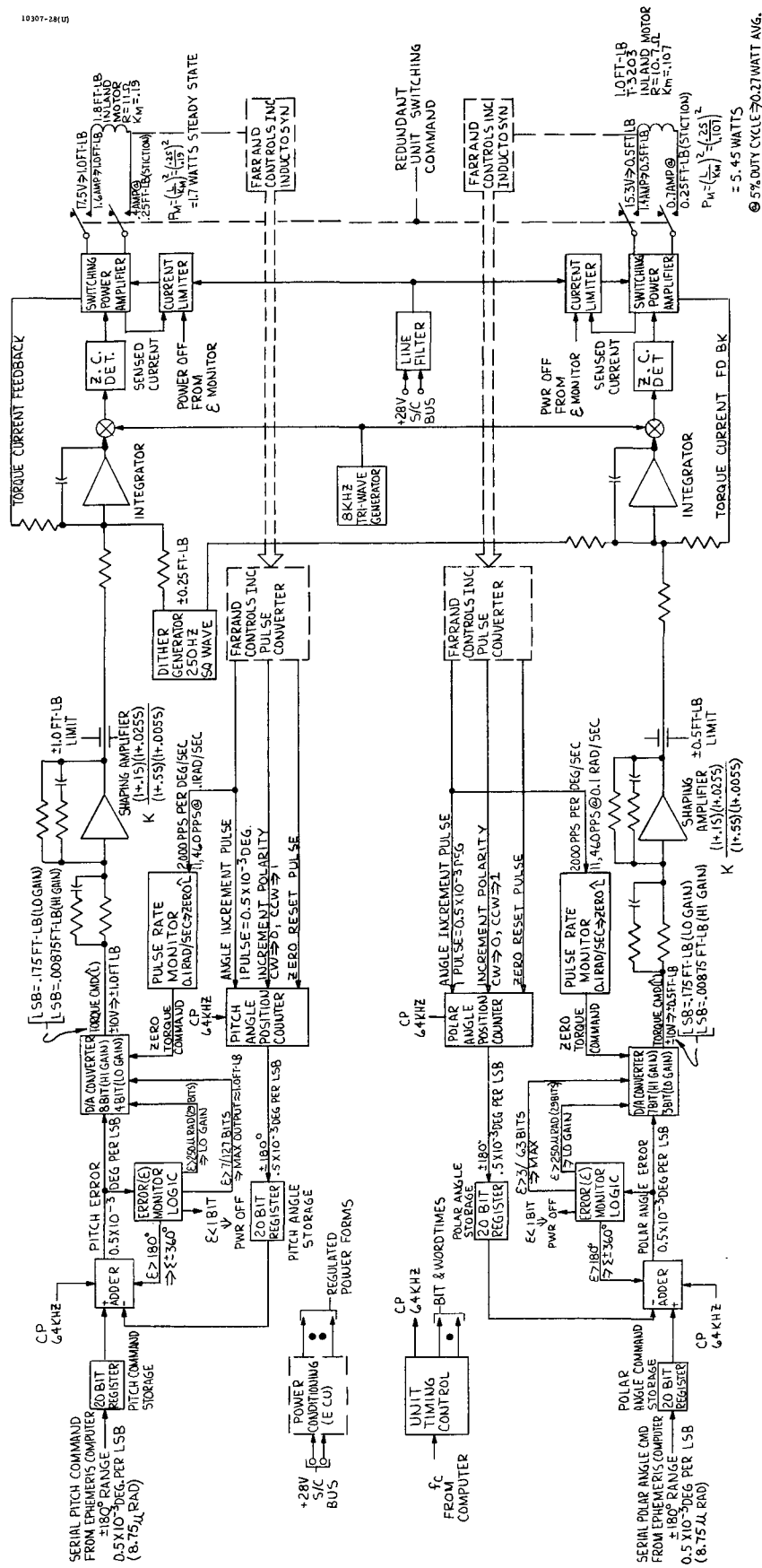| Design Parameter	CONFIGURATION		
	No Pwr. Condit. No Redundancy	Pwr. Condit. No Redundancy	2 Redundant Units Pwr. Condit.

Parts Count
  IC
  Discrete
	144
	609
		149
		784
			304
			1794

Weight (lbs)	3.9	5.7	12.8
Volume (cu. in)	146	198	480
Preferred Dimensions (inches)	9 x 6 x 2.7	12.2 x 6 x 2.7	2(10 x 6 x 4)
Power Dissipation (Watts)	7.6	10.1	10.6

Figure 3.5-11. Preliminary Block Diagram of STARS
Gimbal Servoelectronics

3.6 Assembly and Test Methods

The design, development and manufacture of the STARS gimbal requires detailed planning at each stage of buildup for component procurement through subsystem testing. Figure 3.6-1 displays the flow of hardware, division of work in-house and subcontracted, and typical tests conducted at each stage. The complex beryllium machined parts are subcontracted to a precision manufacturer experienced with this material. Even though the ball bearings are procured as components and lubricated at Hughes. The flow is planned to screen deficiencies at each stage to minimize the faults and trobleshooting at assembly testing.

The STARS components and assembly are very similar to the Hughes Gyrostat despin mechansims, but the despin control is quite different since STARS does not rotate continuously at 50-80 RPM. Typical flight despin assemblies are shown in Figures 3.6-2, 3.6-3 and 3.6-4. Two of these incorporate beryllium shaft and housing materials, and the third uses titanium. All units are space-qualified, and flight systems have been delivered. The TACSAT assembly shown in Figure 3.6-2 has operated successfully in orbit since February 1969. This system uses a brush type DC motor and slip rings for power and signal transfer. The other two assemblies use brushless dc motors. One unit for Intelsat IV (Figure 3.6-4) was launched in January 1971.

Since the STARS precision requirements are much greater than the capabilities of existing systems much more detailed investigations of manufacturing and assembly procedures are required. At the piece part level a study on stabilizing techniques is required for the beryllium parts. On most beryllium systems thermal shock processes have been substituted with a chemical etch of the finished machined parts. At the assembly level studies are required to plan the facilities, tooling and instruments necessary to maintain and check the precision during the assembly operations. For instance, the Inductosyn installation requires definition of the reference surfaces, of the instrument that will be used to set the runout, and of the tooling required to hold the instrument. The detailed definition of these techniques should be established to insure that the proper reference surfaces are built into the gimbal hardware.
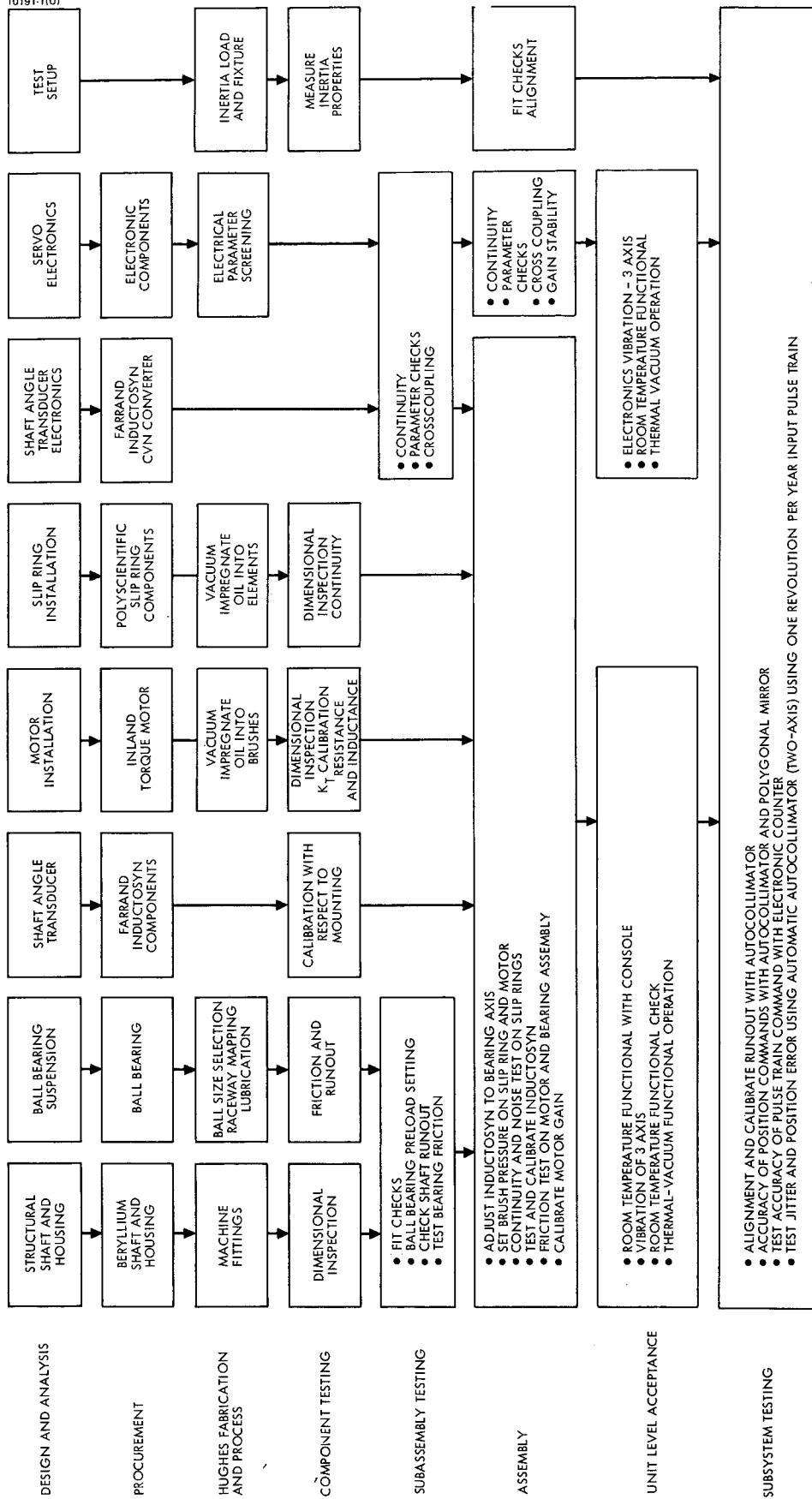
Row labels (left side):

DESIGN AND ANALYSIS

PROCUREMENT

HUGHES FABRICATION AND PROCESS

COMPONENT TESTING

SUBASSEMBLY TESTING

ASSEMBLY

UNIT LEVEL ACCEPTANCE

SUBSYSTEM TESTING

Flow chart boxes:

STRUCTURAL SHAFT AND HOUSING → BERYLLIUM SHAFT AND HOUSING → MACHINE FITTINGS → DIMENSIONAL INSPECTION

BALL BEARING SUSPENSION → BALL BEARING → BALL SIZE SELECTION RACEWAY MAPPING LUBRICATION → FRICTION AND RUNOUT

SHAFT ANGLE TRANSDUCER → FARRAND INDUCTOSYN COMPONENTS → CALIBRATION WITH RESPECT TO MOUNTING

MOTOR INSTALLATION → INLAND TORQUE MOTOR → VACUUM IMPREGNATE OIL INTO BRUSHES → DIMENSIONAL INSPECTION K_T CALIBRATION RESISTANCE AND INDUCTANCE

SLIP RING INSTALLATION → POLYSCIENTIFIC SLIP RING COMPONENTS → VACUUM IMPREGNATE OIL INTO ELEMENTS → DIMENSIONAL INSPECTION CONTINUITY

SHAFT ANGLE TRANSDUCER ELECTRONICS → FARRAND INDUCTOSYN CVN CONVERTER

SERVO ELECTRONICS → ELECTRONIC COMPONENTS → ELECTRICAL PARAMETER SCREENING

TEST SETUP → INERTIA LOAD AND FIXTURE → MEASURE INERTIA PROPERTIES → FIT CHECKS ALIGNMENT

Subassembly box:
- FIT CHECKS
- BALL BEARING PRELOAD SETTING
- CHECK SHAFT RUNOUT
- TEST BEARING FRICTION

Assembly box:
- ADJUST INDUCTOSYN TO BEARING AXIS
- SET BRUSH PRESSURE ON SLIP RING AND MOTOR
- CONTINUITY AND NOISE TEST ON SLIP RINGS
- TEST AND CALIBRATE INDUCTOSYN
- FRICTION TEST ON MOTOR AND BEARING ASSEMBLY
- CALIBRATE MOTOR GAIN

- CONTINUITY
- PARAMETER CHECKS
- CROSSCOUPLING

- CONTINUITY
- PARAMETER CHECKS
- CROSS COUPLING
- GAIN STABILITY

Unit level acceptance box:
- ROOM TEMPERATURE FUNCTIONAL WITH CONSOLE
- VIBRATION OF 3 AXIS
- ROOM TEMPERATURE FUNCTIONAL CHECK
- THERMAL-VACUUM FUNCTIONAL OPERATION

- ELECTRONICS VIBRATION - 3 AXIS
- ROOM TEMPERATURE FUNCTIONAL
- THERMAL VACUUM OPERATION

Subsystem testing box:
- ALIGNMENT AND CALIBRATE RUNOUT WITH AUTOCOLLIMATOR
- ACCURACY OF POSITION COMMANDS WITH AUTOCOLLIMATOR AND POLYGONAL MIRROR
- TEST ACCURACY OF PULSE TRAIN COMMAND WITH ELECTRONIC COUNTER
- TEST JITTER AND POSITION ERROR USING AUTOMATIC AUTOCOLLIMATOR (TWO-AXIS) USING ONE REVOLUTION PER YEAR INPUT PULSE TRAIN

Figure 3.6-1. STARS Assembly and Test Flow Chart

Figure 3.6-2. TACSAT Beryllium
Despin Bearing Assembly

Figure 3.6-3. Advanced Satellite
Beryllium Despin Bearing Assembly

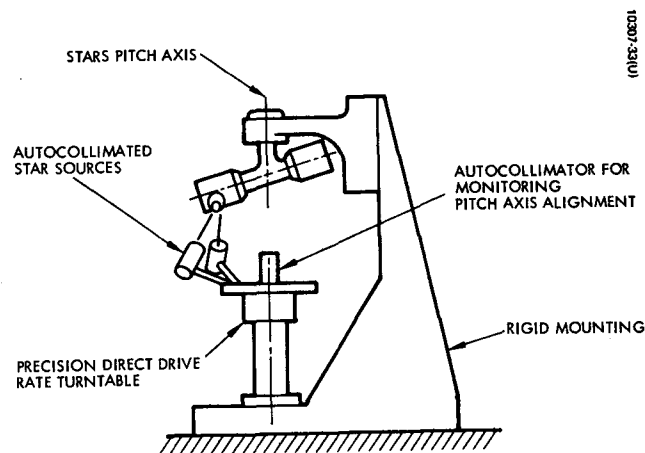Figure 3.6-4. Intelsat IV Despin Bearing Assembly

3-61

Figure 3.6-5. Tracking Test Stand for STARS

At completion of the STARS gimbal assembly a number of measurements should be made to provide data to aid in troubleshooting any subsystem test problems. Examples of these measurements are: 1) ball bearing breakout friction versus displacement, 2) gimbal run-out, 3) slip ring and motor brush friction levels and characteristics, 4) Inductosyn error, 5) Inductosyn noise sensitivity, and 6) Inductosyn sensitivity due to gimbal compliance.

System testing of the completed STARS may be accomplished using an arrangement as shown in Figure 3.6-5. The pitch axis of the STARS is made parallel to the axis of a high accurate rate table which supports two collimated star sources. The rate table is rotated at the appropriate orbital pitch rate, such as one rotation in 96 minutes (corresponding to a 300 mile orbit). The STARS control system rotates the pitch axis at an (ideally) matching rate, commanded by the STARS electronics uni The outputs of the star trackers on the STARS then represent the error signals that would be available to position a spacecraft. These error signals are then also available for the system error analysis.

4.   Star Trackers

4.1   Tracker Design Analysis

Introduction

       As described in section 2.1, the STARS concept utilizes eight star
trackers, fixed with respect to each other, to provide an inertial reference.
Each tracker is pointed to a preselected star chosen in such a manner that
at least two stars are always available for tracking independent of orbit
and spacecraft geometry.

       The eight trackers are divided into two four-telescope clusters
with one cluster observing the northern celestial hemisphere and the other,
the southern celestial hemisphere.

       Figure 4-1 is a layout showing one of the baseline sensor clusters.
Each tracker is required to accurately determine the location of the star
in its field of view and provide the data to the on board computer for
attitude control. In the baseline sensor cluster the stellar energy from
two telescopes is relayed to one photomultiplier tube. Signal separation
is accomplished utilizing an L-shaped reticle in each telescope with the
two L's reversed with respect to each other (superimposing the L's would
result in a cross). Since the nutation wedge for all telescopes in a
cluster is common, the nutating stellar images are synchronous and signals
from the two telescopes are separated in time (See Figure 4-2).

       The primary purpose of each star tracker is to convert an irradiance
from a star into a number which accurately defines the location of the
star in the tracker field of view. In addition, because of noise in the
system, a finite probability exists that a false data point may occur or
a real star pulse may be missed. Thus, a secondary requirement for the star
tracker is that missed pulses and false alarms be held to acceptable numbers.

       The interrelationships of the basic parameters and their effects on
star tracker performance are herein discussed and fundamental system para-
meters such as aperture and slit width are defined. The characteristics
of the stars and noise sources of interest will first be described, the
equations associated with them will then be developed and finally the
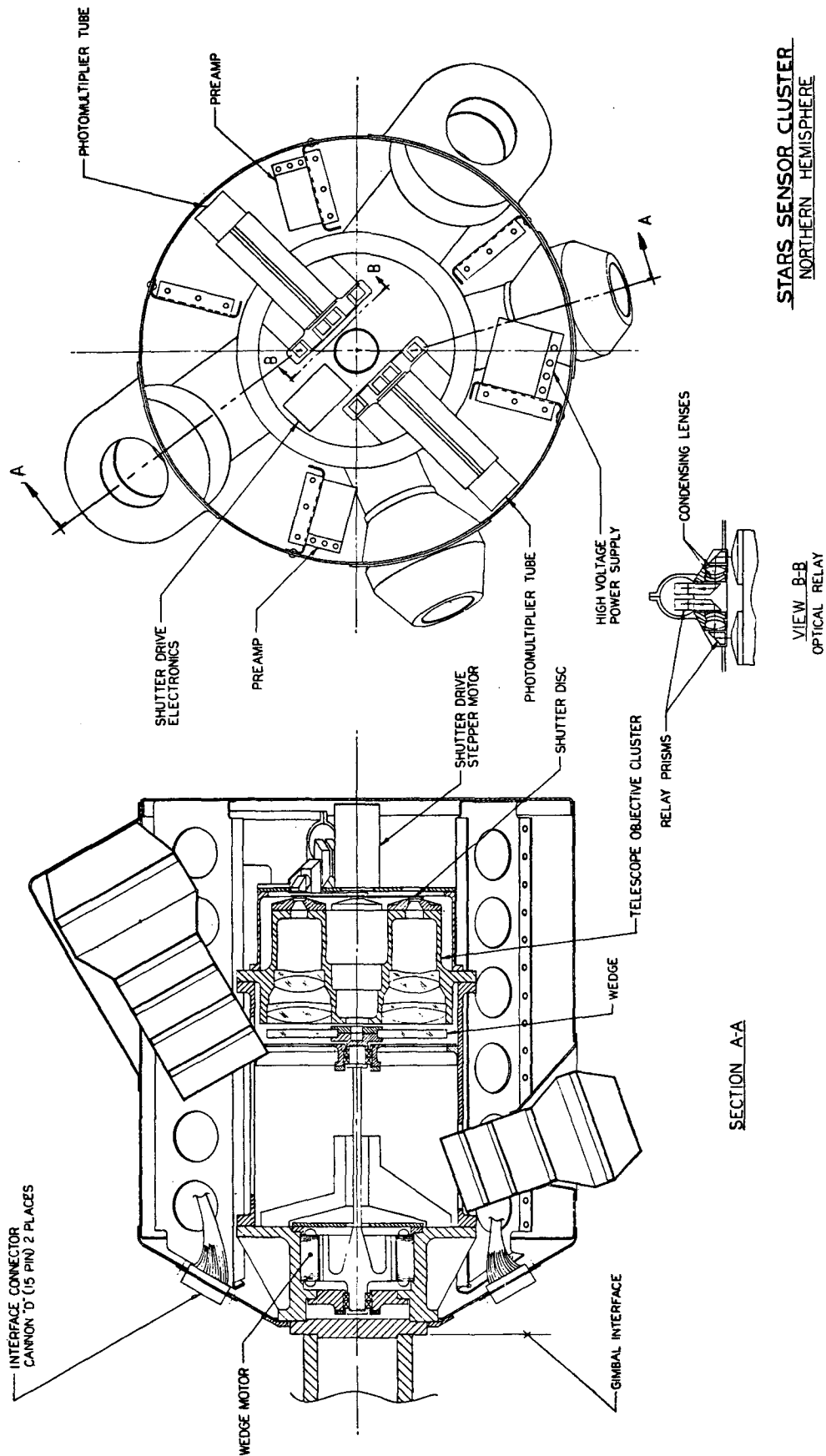values of system parameters will be selected.

Figure 4-1. STARS Sensor Cluster – Northern Hemisphere

Qualitative Summary

Figure 4-3 illustrates the relationships of the basic parameters of the star tracker. Every star produces a characteristic amount of spectal radiant energy h (λ) as measured near the earth outside of the atmosphere.

Incident photons from a preselected star are collected at the star tracker aperture and this stellar energy is nutated by a rotating wedge in front of the first lens element. The nutated image crosses slits on the reticle pattern on the focal plane of the telescope. A photomultiplier tube (PMT) detects the energy passing through a slit and the time of slit crossing is used to determine star position in the tracker field of view.

Since the spectral characteristics of every star are constant and the quantum efficiency of the photodetector is relatively invariant, the size of the aperture and of the reticle pattern can be selected on a knowledgeable basis.

However, the detection of stars is hampered by the statistical fluctuation in photon noise present in all radiant energy. The sources of radiant energy that contribute photon noise are stars in the background, stray light within the sensor coming from the sun, earth, or spacecraft, and the fluctuations in photon noise in the signal itself. All of this noise in addition to the dark current noise of the PMT limits the sensitivity of the tracker.

Star Characteristics

The surface temperatures of the stars of interest range from approximately $30,000^{\circ}K$ to $2,000^{\circ}K$. The spectral distribution at each of these temperatures is different.

The brightness of a star is termed its stellar magnitude. Stellar magnitude is most often measured in terms of photographic, bolometric, or visual magnitude.
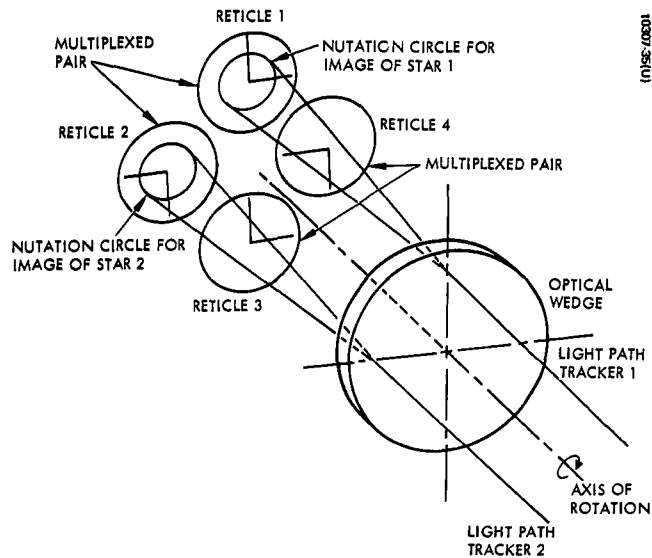
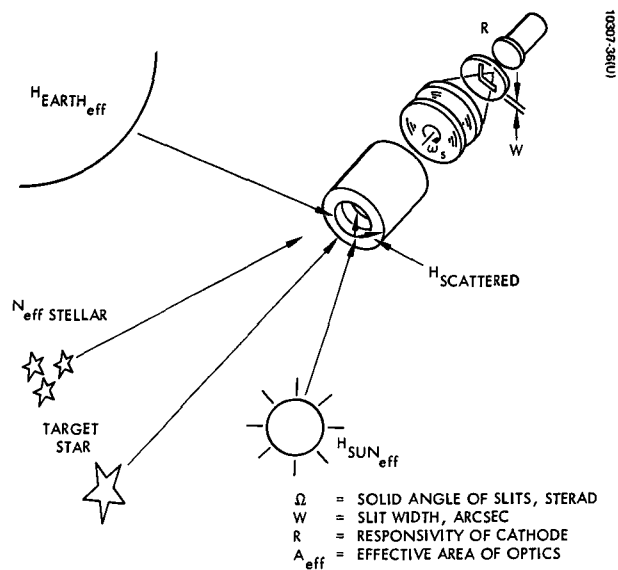Figure 4-2. Scanning of Multiple Reticles by Single Wedge

Ω = SOLID ANGLE OF SLITS, STERAD
W = SLIT WIDTH, ARCSEC
R = RESPONSIVITY OF CATHODE
A_{eff} = EFFECTIVE AREA OF OPTICS

Figure 4-3. Basic Parametric Relationships

4-4

In equating these different measures of magnitude, the magnitude scales
are generally adjusted to yield a magnitude equivalent to that of an
A_o star, i.e., one having an equivalent surface temperature of $11,000^oK$.
The magnitude of the radiation is

$$m = 2.5 \log_{10} \frac{H_o}{H} \text{ ,}$$

where

   H = irradiance, w/cm^2

   H_o = irradiance of zero-magnitude star

The visible irradiance of a star of zero magnitude is defined as equal to
2.1×10^{-10} lumen/cm^2 or 3.1×10^{-13} w/cm^2 at the peak sensitivity of the
human eye $(5500\overset{o}{A})$.

Each star is assigned a visual magnitude and a spectral class(on the
basis of its temperature). This defines the curve $h\ (\lambda)$, where $h\ (\lambda)$ is the
absolute spectral irradiance (w/cm^2 micron) at the sensor aperture. This
energy passes through the optical system which has a relative spectral
transmittance defined by $t(\lambda)$ and is detected by a S-20 photocathode
having an absolute spectral responsivity $r(\lambda)$. In order to compare stars,
we define an effective irradiance as

$$H_{eff} = \frac{1}{R} \int_{3,000\overset{o}{A}}^{8,000\overset{o}{A}} r(\lambda)\ h(\lambda)\ t(\lambda)\ d(\lambda)$$

By using available star catalogues and performing the integration,
a listing of stars (in descending order of brightness) was prepared
(Table 2-2) which shows which stars will be best detected by the star sensor.
From this listing as described in Section 2.2, a set of eight stars was
selected on the basis of brightness and location in the celestial sphere.
These stars are repeated in Table 4-1. The dimmest of the selected stars
(Phecda) has an effective irradiance (H_{eff}) of 1.1×10^{-13} watts/cm^2, and
this value is used as the worst case irradiance for the tracker design.

TABLE 4-1. BASELINE STAR SET

STAR	Visual Magnitude	Irradiance $w/cm^2 \times 10^{-13}$	Right Ascension (Degrees)	Declination (Degrees)
1. Cih	2.13	2.2	13.69	60.54
2. Phecda	2.44	1.1	178.04	53.87
3. Arcturus	-0.06	5.3	213.55	19.35
4. Altair	0.77	4.3	297.31	8.78
5. Achernar	0.51	8.0	24.13	-57.40
6. Rigel	0.14	9.0	78.25	-8.24
7. Delta Vela	1.95	1.8	130.96	-54.59
8. Peacock	1.95	2.0	305.78	-56.84

Background Noise Sources

Following is a brief summary of the background noise sources which limit system performance

o **Average Celestial Background:** The average luminous flux (over the entire sky) is 2.2×10^{-12} lumen/cm^2 deg^2 or 7.8×10^{-11} w/cm^2 sterad. The irradiance at the entrance aperture of the sensor is

$$H_{stellar} = N_{T_{stellar}} \Omega,$$

where Ω = solid field of view of sensor, sterad.

o **Stray Light Scattering:** Light from bright sources such as the sun or the earth if allowed to enter the optics is a significant noise contributor. The amount of light scattered is a function of sunshade design and angle between the bright source, and the tracker optical axis.

o **Radiation in the Van Allen Belts:** Particle radiation can interact directly with the Photomultiplier Tube (PMT) and cause an output. The noise is a function of the PMT, the type of radiation (electronics or protons), energy level and amount of incident flux. In addition, secondary gamma radiation caused by stopping or slowing electrons in a shield can also introduce noise in the tube.

4-7

Sensitivity

The sensitivity of any sensor system is limited either by the noise outside of it or by the noise within it. A properly designed system using a Photomultiplier Tube is background noise limited, which means that the amount of internally generated noise does not significantly impair system performance.

Noise is created by the statistical variations in the d-c current from the photocathode of the PMT. The four sources of noise are the

- o Photocathode dark current
- o Current due to the background photon flux
- o Fluctuations in current due to the signal energy
- o Particle radiation

The steady state current I_{ss} due to input irradiance is

$$I_{ss} = H_{eff} A_{eff} R ,$$

where

H_{eff} = effective irradiance, w/cm^2

A_{eff} = effective area of entrance aperture, cm^2 (this includes the transmission effects of the optics, i.e., $A_{eff} = A_{actual} \times T_o$, where T_o = transmission).

R = responsivity of photocathode, amperes/watt.

The complete description of the d-c current in the PMT includes the irradiance from the background H_B, the irradiance from the star H_{eff}, and the dark current of the tube caused by thermionic emission of the photocathode, i.e.,

$$I_{avg} = I_{dark} + A_{eff} R (H_B + H_{eff}).$$

The rms current i_n, which is caused by the statistical fluctuations of the d-c current is

$$i_n = \sqrt{2e I_{avg} \Delta f (\frac{G}{G-1})}$$

where

G = gain of first dynode stage

Δf = pre-detection bandwidth

e = 1.602×10^{-19} coulomb

The complete expression becomes

$$i_n = \sqrt{2e \left(\frac{G}{G-1}\right) \left[I_{dark} + A_{eff} R (H_{eff} + H_B) \right] \Delta f.}$$

A basic measurement of system sensitivity is the signal-to-noise ratio (SNR) which is defined as the ratio of the peak signal to rms noise.

If pre-detection bandwidth is narrowed to reduce noise, the peak pulse height becomes smaller

$$i_{peak} = \left(\frac{i_p}{i_{ss}}\right) H_{eff} A_{eff} R$$

where

i_p = peak filtered pulse amplitude

i_{ss} = steady state value of input

The signal-to-noise ratio is therefore

$$SNR = \frac{i_p}{i_n} = \frac{\left(\dfrac{i_p}{i_{ss}}\right) H_{eff} A_{eff} R}{\sqrt{2e \dfrac{G}{G-1} \left[I_{dark} + A_{eff} R (H_{eff} + H_B) \right] \Delta f}}$$

Dark current for the PMT is typically less than 10^{-10} amps at a tube gain of 10^6. Typical tube current caused by minimum stars of interest at the same gain will be 10^{-7} amps, thus

$$I_{dark} \ll A_{eff} R H_{eff}$$

This can be verified by substituting actual system parameters in the above expression. Hence, the system is not dark current noise limited.

$$SNR = \frac{\left(\dfrac{i_p}{i_{ss}}\right) H_{eff} \, A_{eff} \, R}{\sqrt{2e \left(\dfrac{G}{G-1}\right) A_{eff} \, R \, (H_{eff} + H_B) \, \Delta f}}$$

$$H_B = \underbrace{H_{RAD}}_{\substack{\text{Radiation} \\ \text{Induced}}} + \underbrace{H_{stellar}}_{\substack{\text{Stellar} \\ \text{Background} \\ \text{Induced}}} + \underbrace{H_S}_{\substack{\text{Scattered from} \\ \text{Bright Sources}}}$$

In the 500 mile altitude, high noon, sun synchronous baseline orbit, there is essentially no radiation and the radiation induced term can be dropped. It is worth noting that orbits which pass into the Van Allen Belts would require PMT shielding to limit this noise source to acceptable values.

Using the expression $H_{stellar} = N_T \, \Omega$, the stellar background at the aperture can be determined. Ω is the solid field of view of the sensor in steradians which is determined by the reticle pattern. As will be shown later, typical reticle slit widths in the direction of star image travel will be about 90 arcseconds. The length of one side of the L-shaped reticle is 1.2°.

Therefore

$$\Omega = WL$$

where

W = slit width

L = total length of all slits in radians

For

W = 90 arcsec = 4.37×10^{-4} radians,

$\Omega = (2) \left(\dfrac{1.2}{57.3}\right) (4.37 \times 10^{-4}) = 1.83 \times 10^{-5}$ steradian

$H_{stellar} = (7.8 \times 10^{-11}) (1.83 \times 10^{-5}) = 1.43 \times 10^{-15}$ watts/cm^2

Of the total stellar irradiance at the aperture, only that which is within the sensor spectral band (determined by the optical transmission and S-20 photocathode) is effective. The spectral efficiency is taken to be 0.4.

Therefore

$$H_{eff_{stellar}} = (0.4)(1.43 \times 10^{-15}) = 5.6 \times 10^{-16} \text{ w/cm}^2$$

It should be noted that the celestial sphere as viewed from near earth is very non-uniform and the above calculation provides only an average value which will vary with the star tracker look angle. However, this average is over two orders of magnitude less than the 1.1×10^{-13} w/cm^2 design requirement for the maximum amount of scattered light from bright sources (15° from earth or spacecraft, 30° from the sun).

The limiting system noise for the STARS star tracker is thus caused by scattered light from bright sources. The magnitude of this noise source is a function of sun shade design and angle and intensity of the source. A considerable amount of design and test experience has been accumulated at Hughes Aircraft Company on at least two other star sensors as well as on numerous electro-optical sensors operating throughout the IR spectrum. Appendix 6.3 provides a summary of some of the sunshade design and test efforts done by Hughes Aircraft Company.

With this background, a detailed sunshade design for the STARS star tracker was performed and is described in Section 4.3. The sunshade is required to yield an effective irradiance at the aperture of less than 1.1×10^{-13} w/cm^2 for sun angles greater than 30° and earth or spacecraft angles greater than 15°. As shown in section 4.3, the baseline sunshade meets the requirements with two orders of magnitude margin. Based on Hughes' experience, which has shown significant differences between measured and predicted performance, two orders of magnitude is not an excessive over-design but is considered a comfortable margin. With this reasoning, the scattered noise source will be taken to be the sunshade design requirement (a conservative approach) and for a scattered light limited system the SNR relationship becomes

$$SNR = \frac{\left(\dfrac{i_p}{i_{ss}}\right) H_{eff} \, A_{eff} \, R}{\sqrt{2e \left(\dfrac{G}{G-1}\right) A_{eff} \, R(H_{eff} + H_s) \, \Delta F}}$$

The fixed parameters in the expression are:

$$e = 1.6 \times 10^{-19} \text{ coulombs}$$
$$G = 3$$
$$R = 0.075 \text{ amp/watt}$$

thus

$$\text{SNR} = \frac{3.8 \times 10^8 \; H_{eff} \; A_{eff} \left(\dfrac{i_p}{i_{ss}}\right)}{\sqrt{A_{eff} \, (H_{eff} + H_S) \, \Delta f}} \qquad (1)$$

The pre-detection bandwidth Δf and correspondingly $\left(i_p/i_{ss}\right)$ are a function of pulse width and shape. The pulse width is a function of slit width and nutation rate. In addition, as a star angle varies and the reticle crossing angle changes, the effective slit width increases with a corresponding pulse width increase. Thus,

$$t_p = \frac{W}{\omega_s \, R \, \sin \Theta}$$

where
ω_s = nutation scan frequency (radian/sec)

R = nutation circle radius (arcsec)

Θ = angle between the nutation center and a perpendicular to the reticle slit

In the baseline system R is 0.7° and Θ varies between plus and minus 45°. These values result from the requirement for ± 0.5° off-axis tracking and a maximum allowed pulse shift in time (required for pulse/train separation) of ± 45° of nutation rotation. Since Θ is limited to ± 45°, the pulse width increases at most by the $\sqrt{2}$ from the zero track angle case. Although the optimum filter bandwidth is a function of pulse width, measured performance on a similar system shows that performance degradation is negligible for bandwidth variations of ± 20% from nominal. The filter bandwidth is therefore chosen as a compromise between the maximum and minimum pulse widths and sin Θ is taken to be 0.83.

Substituting these values

$$t_p = \frac{W}{\omega_s (0.7)(3600)(0.83)} = 4.78 \times 10^{-4} \frac{W}{\omega_s} \qquad (2)$$

for W in arcseconds

ω_s in radians/sec

For any pulse shape, there is an optimum relationship between Δf and t_p which can be expressed as

$$t_p \, \Delta f \;=\; K$$

where

$\quad t_p \quad = \quad$ signal pulse duration

$\quad \Delta f \quad = \quad$ pre-detection bandwidth

$\quad K \quad = \quad$ constant

For this system, the pulse is assumed to have an approximate gaussian shape and K is taken to be 0.4.

Therefore

$$\Delta f \;=\; \frac{K}{t_p} \;=\; \frac{0.4 \, \omega_s}{4.78 \times 10^{-4} \, W} \;=\; 8.4 \times 10^2 \, \frac{\omega_s}{W} \qquad (3)$$

Choosing a filter to optimize for a particular pulse shape and width determines the peak filtered output pulse. Because of pulse width variation the system is not always optimum and at the worst case (the narrower pulse case), (i_p/i_{ss}) is taken to be 0.73.

$$\left(i_p / i_{ss} \right) \;\approx\; 0.73$$

Substituting in equation (1) and rearranging terms,

$$\text{SNR} \;=\; \frac{(9.66 \times 10^6) \, H_{eff} \, \sqrt{A_{eff} \, W}}{\sqrt{(H_{eff} + H_S) \, \omega_s}} \qquad (4)$$

This expression provides a means for convenient parameter trade-off for SNR in terms of effective aperture, slit width and nutation frequency.

The H_{eff} from the dimmest of the selected stars is taken to be 1.1×10^{-13} watts/cm^2 and the sunshade is required to yield a worst case $H_S = 1.1 \times 10^{-13}$ watts/cm^2. In the baseline design, one photomultiplier tube services two telescopes and if these two telescopes happen to be observing the two selected stars, the scattered noise energy (H_S) from each telescope will be summed in one photomultiplier tube. An extremely pessimistic case would be to assume $H_S = 2.2 \times 10^{-13}$ watts/cm^2 for SNR determination.
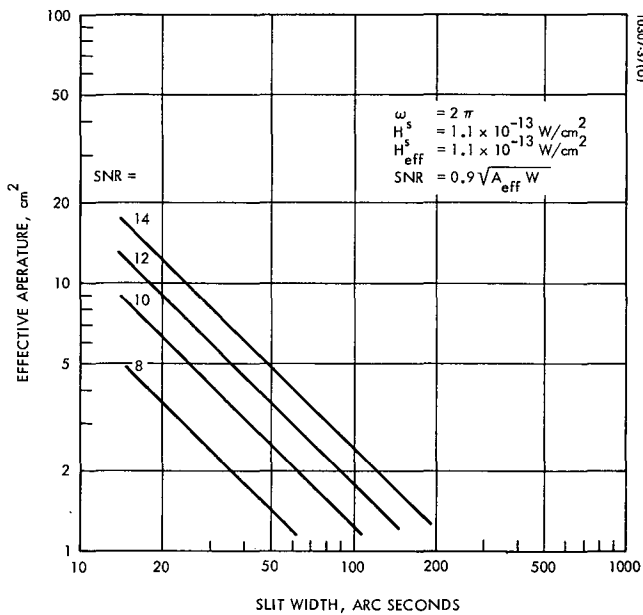
Figure 4-4. SNR as Function of Effective Aperture and Slit Width ($\omega_s = 2\pi$)
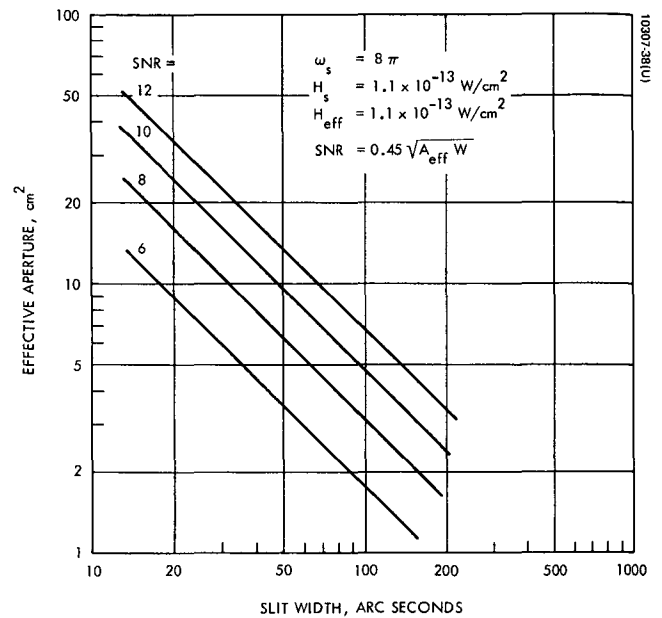

Figure 4-5. SNR as Function of Effective Aperture and Slit Width ($\omega_s = 8\pi$)
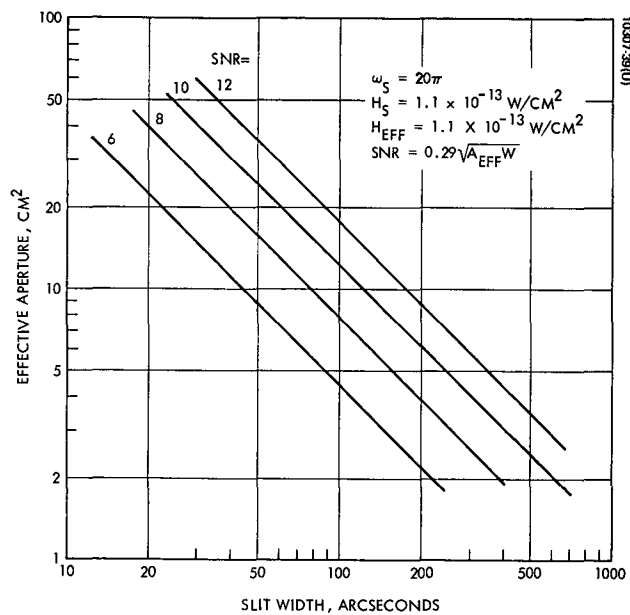

Figure 4-6. SNR as Function of Effective Aperture and Slith Width ($\omega_s = 20\pi$)

4-14

The percentage of time which two telescopes, pointing at widely varying angles, can be expected to be both in use and seeing the worst case scattered noise is expected to be trivial. In addition, analysis of the baseline shade indicates its performance far exceeds the design requirement of less than 1.1×10^{-13} watt/cm^2. For parametric trade-offs, the worst case H_S has therefore been chosen to be $H_S = 1.1 \times 10^{-13}$ watts/cm^2.

Using $H_{eff} = 1.1 \times 10^{-13}$ watts/cm^2, $H_S = 1.1 \times 10^{-13}$ watts/cm^2 and equation (4). Figures 4-4, 4-5, and 4-6 have been constructed to provide SNR as a function of A_{eff} and W for nutation scan rates of 1, 4, and 10 hz.

Accuracy

Resolution of a pulse in time and hence the angular error associated with detection of the signal depends directly on pulse (or slit) width and inversely on signal-to-noise ratio. For a filter matched to a gaussian pulse the standard deviation (1 sigma) in time is given by

$$1\sigma_{sec} = 0.7 \frac{t_p}{SNR}$$

Correspondingly, since the pulse width in time scales to the slit width in arc seconds, the standard deviation (1σ) in arcseconds can be written as

$$1\sigma_{arcseconds} = \frac{0.7W}{SNR} \quad \text{(Theoretical)}$$

It should be realized that W is the nominal slit width and the effective slit width will vary $\pm$ 20% as a function of star angular location. This will result in some filter mismatch; also, the optical imagery varies somewhat with field angle and the resulting output pulse will not actually be gaussian in shape. To account for these practical considerations, the standard deviation in arcseconds is assumed degraded by 10% and taken to be

$$1\sigma_{arcseconds} = \frac{0.77W}{SNR} \quad \text{(Achievable)}$$

Using the expression for SNR given in equation (4)

$$1\sigma_{arcseconds} = \frac{7.9 \times 10^{-8} \sqrt{W (H_{eff} + H_S) \omega_s}}{H_{eff} \sqrt{A_{eff}}}$$

The above expression gives the angle noise at the star tracker output. When applied to the track loop, track angle noise is a function of track loop bandwidth. The track loop angle noise (Ψ) can be shown to be

$$\Psi_{arcseconds} = 1\sigma_{tracker} \left(\frac{2f_t}{f_s}\right)^{\frac{1}{2}} = \left(\frac{4\pi f_t}{\omega_s}\right)^{\frac{1}{2}}$$

where

f_t = track loop bandwidth

f_s = scan frequency = $\dfrac{\omega_s}{2\pi}$

Thus

$$\Psi = 7.9 \times 10^{-8} \frac{\sqrt{W(H_{eff} + H_S) \omega_s}}{H_{eff} \sqrt{A_{eff}}} \frac{\sqrt{4\pi f_t}}{\sqrt{\omega_s}}$$

$$= 7.9 \times 10^{-8} \frac{\sqrt{W(H_{eff} + H_S) 4\pi f_t}}{H_{eff} \sqrt{A_{eff}}}$$

For this study, the track loop bandwidth is taken to be 0.1 hz.

$$\Psi_{arcseconds} = \frac{8.85 \times 10^{-8} \sqrt{W(H_{eff} + H_S)}}{H_{eff} \sqrt{A_{eff}}} \qquad (5)$$

With this expression, the effect of variation of slit width and effective aperture on one sigma pulse jitter can be determined. It is interesting to note that with the assumptions and expressions used, track loop angle noise is not a function of nutation rate. The change in SNR as a function of ω_s is balanced by the change in track loop filtering of star tracker angle noise.

Using $H_{eff} = 1.1 \times 10^{-13}$ w/cm^2, $H_S = 1.1 \times 10^{-13}$ w/cm^2 and equation (5) Figure 4-7 has been constructed to provide Ψ (track loop angle noise) as a function of A_{eff} and W.

Missed Pulse and False Alarm Rate

Detection statistics, that is, missed pulse probability and probability of detecting a false pulse, are a function of SNR. All discussions and derivations thus far have assumed gaussian statistics as appropriate where large numbers are concerned. In this region, the relationship between signal, noise and the probabilities of detection are given in Figure 4-8 If the signal (number of signal events) is small in comparison with the noise, the SNR is very nearly equal to the sum of standard deviations of noise and signal-plus-noise required from the threshold for a particular set of missed pulse and false alarm numbers.

The star angle computation technique is such that a missed pulse or a false alarm perturbate the track loop in essentially the same fashion. An incorrect number will be sampled in a register and inject a step error into the track loop. Pending a more detailed study of requirements, it is assumed that missed pulse and false alarm rates of from 1 to 100 per day per tracker will include the range of interest.
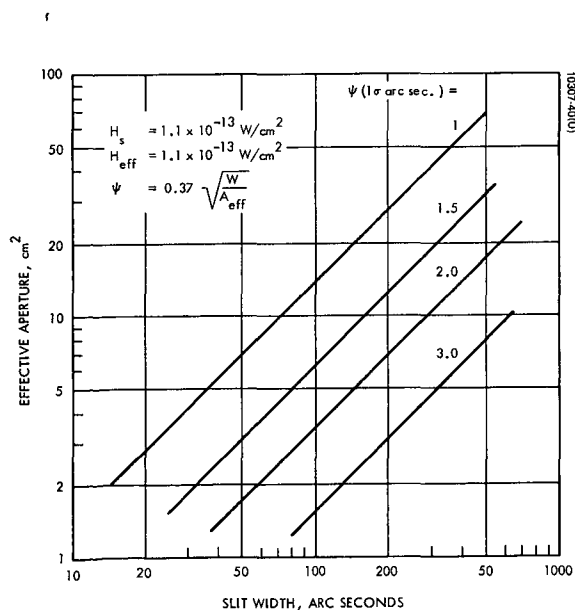
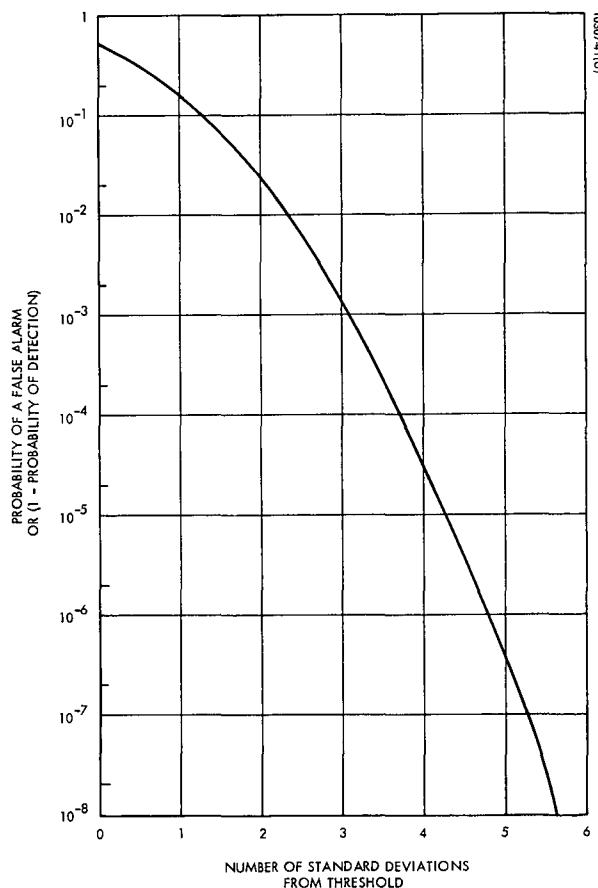Figure 4-7. Track Angle Noise as Function of Effective Aperture and Slit Width

Figure 4-8. Probability of Detection as Function of Standard Deviations From Threshold

4-17

Table 4-2 provides a tabulation of the signal-to-noise ratio (SNR) required
for various missed pulse and false alarm rates in this range. The procedure
used to generate the Table follows:

● False Alarm Probability

The false alarm rate at the detection point is related
to the probability of a false alarm (P_{FA}) and the system pre-
detection bandwidth by the expression

$$P_{FA} = \frac{\text{false alarm rate}}{\Delta f} \quad (\text{number/sec})$$

P_{FA} is the probability that the noise level h_s (t) alone exceeds the threshold
(H_t) for detection in an interval of time equal to the reciprical of
Δf, i.e., a time equal to the impulse response of the filter. On any
tracker, a false alarm will only be observed during two 90° windows
(sample intervals). Thus the false alarm rate at the detection point
can be twice the acceptable tracker false alarm rate. For any tracker false
alarm rate (FAR) the acceptable probability of a false alarm at the
detection point is therefore

$$P_{FA} = \frac{2 \text{ FAR}}{\Delta f} \quad (6)$$

As discussed earlier, the pre-detection filter is a function of nutation
rate, slit width and star location in the field of view. Repeating equation (3)
which assumes the nominal slit width to be .83W

$$\Delta f = 8.4 \times 10^2 \left(\frac{\omega_s}{W} \right) \quad (3)$$

The width of the slit (W) will typically approach the same size as the optical blur which is approximately 90 arcsec (Ref. Section 4.4). For a nominal spin rate of 8π radians/sec,

$$\Delta f = (8.4 \times 10^2) \ \frac{8\pi}{90} = 235 \ hz$$

It should be noted that for any given SNR Equation (4), assuming all other parameters constant, the ω_s/W ratio remains constant; thus, an increase in nutation rate would require an increase in slit width and Δf (+ 100% - 50%) will only cause negligible ($< \pm$ 3%) changes in SNR requirement.

Using Δf = 235 hz

$$P_{FA} = \frac{(2) \ (FAR)}{235}$$

o Missed Pulse Probability (P_{MP})

For any missed pulse rate, the probability of a missed pulse is the number of missed pulses allowed over an interval divided by the number of true pulses expected in that interval. The baseline tracker data rate is four per second per channel, therefore, the total samples per day is (2) (4) (60) (60) (24) = 3.46×10^5 pulses/day and

$$P_{MP} = \frac{\text{Missed Pulse Rate} \ (^{pulses}/day)}{3.46 \times 10^5 \ pulses/day}$$

o SNR Required to Meet False Alarm and Missed Pulse Probabilities

Using the above equations to determine the P_{FA} and P_{MP} for various False Alarm and Missed Pulse rates, and referring to Figure 4-8 for the number of standard deviations from threshold required to meet these probabilities, Table 4-2 was generated to indicate SNR requirements. As stated earlier, the required SNR is approximately equal to the sum of standard deviations of noise and signal-plus-noise required from the threshold for a particular set of missed pulse numbers and false alarm numbers.
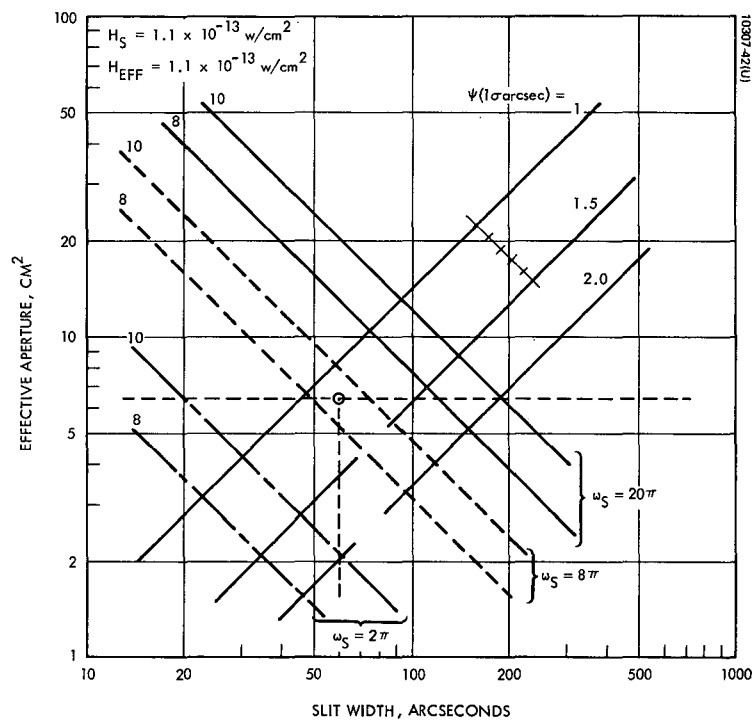
Figure 4-9. SNR and Track Angle Noise as Function of
Effective Aperture and Slit Width

TABLE 4-2. SNR REQUIREMENTS FOR

VARIOUS MISSED PULSE AND FALSE ALARM RATES

MISSED PULSE RATE	FALSE ALARM RATE	≈ SNR REQUIRED
1/day	1/day	9.9
10/day	10/day	8.8
100/day	100/day	7.7

Conclusions and Baseline Tracker Parameters

For a given target nutation rate, the signal energy is directly proportional to the slit width (instantaneous field of view) and the effective collecting aperture of the star tracker. At the same time, the limiting noise, whether it results from the signal statistics or from background, will increase as the square root of the slit width or effective aperture. Thus, the SNR is proportional to the square root of the slit width and effective aperture (see Equation 4).

On the other hand, for a given nutation rate, resolution of the pulse in time and hence the angular error associated with the detection of the signal depends directly on the slit width and inversely on SNR. Where other parameters remain fixed, the angular error will increase in proportion to the square root of the slit width (See Equation 5).

The SNR is inversely proportional to the nutation rate, however, because of track loop filtering, the track angle noise is independent of nutation rate. (The star sensor output angle noise is directly proportional to the square root of the scan rate.)

From missed pulse and false alarm considerations, it is required to have SNR's in the 8 to 10 region. For pointing accuracy, it is necessary to hold track loop angle noise to the 1 to 1.3 arcsec (1σ) regime. Figure 4-9 is obtained by superimposing previously generated curves for SNR and Y on one plot and provides a very convenient means for parametric trade-offs.

The most desirable system from a weight (and cost) point of view, is one that has the smallest aperture but meets performance requirements. Nutation rate is influenced by track loop bandwidth (sample rate requirements). It is desirable from SNR considerations to have a slow nutation rate but the rate

must be reasonably high with respect to track loop bandwidth (for an assumed bandwidth of 0.1 hz a scan rate less than 1 hz is considered marginal). From a mechanization point of view, as discussed in section 4.5, the higher the scan rate, the more practical scan motor design and electronic drive implementation becomes. There are practical limitations on reticle slit width; for optimum determination of pulse position in time, it is necessary that the slit width and image blur at the focal plane be approximately equal. The exact optimum width is dependent upon signal intensity distribution on the image plane. In the baseline design, 90% of the energy lies in a blur < 90 arcseconds in diameter across the full field.

From these considerations and referring to Figure 4-8 the baseline design has been chosen to have the parameters listed in Table 4-3.

TABLE 4-3. STARS BASELINE TRACKER PARAMETERS

Effective Aperture	(A_{eff})	6.4 cm^2
Slit Width	(W)	60 arc seconds
Scan Rate	(ω_s)	8π radians/sec
Signal-to-Noise Ratio (minimum target)	(SNR)	9
Track Loop Angle Noise	(Ψ)	1.15 arcsec (1σ)

Baseline Improvement and Study Areas

Although the baseline star tracker appears capable of satisfying performance requirements, a number of possible improvement areas have become evident as well as potential problem areas.

The quality of the imagery on the focal plane is considered to be the highest risk area in the baseline design. Recognizing this, a short study was undertaken as to the feasibility of improving imagery (Ref. last part of section 4.4). This study indicated that by the addition of one additional lens element (5 versus 4) the imagery could be improved by over a factor of two (from 90 arcseconds to 40 arcseconds) with only a moderate increase in telescope length of 0.7 inches.

The desirability of incorporating this modification deserves serious consideration.

The stellar energy from two telescopes is routed to a single PMT via a relatively complex optical relay which uniformly spreads the energy across the tube faceplate. It is believed that this design can be simplified significantly by relaxing the relay uniformity requirements.

Along these same lines, a trade-off which merits serious consideration is using a PMT for each telescope. Although this would increase the total tube quantity from four to eight for two sensor clusters, significant advantages accrue. Performance under PMT Failure is obviously enhanced and the complex optical relay is no longer required. Since signal separation comes naturally, the L reticle can be replaced with a cross and data rate is doubled. Electronic selection of telescopes can be incorporated and the use of a mechanical shutter is no longer necessary (although protection of the PMT's from bright sources may still be desirable).

In the realm of additional intricate studies, much work is required in the thermal area if a development program is undertaken. A key question is the effect of sunshade heating when the bright sun is illuminating interior portions of the shade. A second question is the effect of bright sources in the field of view of the unused telescopes both from a temperature/ accuracy viewpoint as well as possible damage to the PMT.

Finally, very important to the STARS concept, are the techniques which will be used for alignment, calibration, and evaluation of the star trackers. Much effort is required to establish techniques for aligning the telescopes to attain the required image quality and verifying off-axis tracking accuracy. Some preliminary conceptual ideas in this areas are discussed in section 5.5.

4.2 Sensor Cluster Mechanical Design

Configuration Trade-Offs

The original concept for the sensor clusters called for four independent and identical telescopes mounted radially in a hemisphereical dome. Each telescope would have its own sunshade, wedge, wedge motor, and objective. The images from the four telescopes would be relayed via fiber optics bundles to a single Photomultiplier Tube (PMT) at the center of the hemisphere. Although this initial concept appeared to be the obvious configuration, a number of drawbacks were discovered as the design progressed. A discussion of these drawbacks and the steps leading to the final baseline design follow:

After a preliminary optical design of the telescope objective and sunshade had been completed, a rough mechanical layout and weight estimate indicated that each cluster would require a swept volume for about a 19" diameter hemisphere and would weight approximately 20 pounds. Attempts to reduce the size and weight within the constraints of the original configuration and the required optical geometry proved to be hopeless.

An investigation of available fiber optics materials indicated that there were no commonly used materials that would transmit adequately over the entire spectral range $(0.3\mu$ to $0.8\mu)$. Because of this, and because it appeared desirable to add a 2nd PMT in each cluster for both redundancy and ease of signal separation, the use of fiber optics for the optical relay did not seem to be a practical design. Other techniques using mirrors and/or relay prisms could work, but because of the variety of angles between the various telescopes and the PMT's it would be necessary to design a unique relay assembly for each of the eight telescopes which would result in an awkward and expensive design.

At any given time, only two of the eight telescopes are in use. A shutter or shutters must be used to completely block any energy which enters an unused telescope from reaching the PMT. Again, because of the variety of telescope angles and the desirability of more than one PMT, each telescope was required to have its own shutter.

Perhaps the most serious drawback to this initial concept was the problem of signal identification and separation in the signal processor. Unless a separate detector is used for each telescope, some technique for separating multiple signals from a single detector is required. Each technique considered required that the individual wedges be driven with some fixed and predetermined phase angle with respect to a reference and each other. Various schemes of electrically and mechanically coupling the wedge drives were investigated, but none of them provided the required wedge rotational accuracy needed to meet the tracking accuracy requirements.

A configuration which appeared to eliminate most of these problems involved the concept of "aperture sharing". Instead of four telescopes per cluster, one larger telescope would be used. A set of four mirrors would be used to direct the energy from each of the stars through a common wedge into different portions of the entrance aperture of this single telescope. This approach reduced the weight and volume requirements and, due to the single wedge, eliminated the wedge synchronization problem. In addition, unfortunately, it tended to complicate the task of signal separation since now the four stars in each cluster utilize a common reticle. One approach at separating signals involved doubling the field of view of this single telescope and having a quadrantized reticle, one quadrant being for each star. In addition to involving a relatively difficult alignment task, since the four channels must be independently aligned, a considerable amount of internal baffling would be required to prevent cross-talk between channels with this configuration. What finally evolved, therefore, was an approach which reverted to four independent telescopes, but symmetrically configured such that the advantages of the single telescope are retained.

BASELINE DESIGN

Figure 4-1 represents the baseline configuration of the "Sensor Cluster" for the case of the northern hemisphere. It has been verified that the southern hemisphere cluster is essentially the same except for the angles of the pointing mirrors and the sunshades. The eight reference stars for this design are as given in Table 4-1.

The optical system is described in detail in Section 4.4. Each telescope objective consists basically of two cemented doublets with an entrance aperture diameter of 1.25 inches and focal length of 2.50 inches.

The primary structure consists of a beryllium baseplate, which bolts directly to the gimbal shaft with an adapter plate, and a beryllium cylinder which supports the telescope assembly. The pointing mirrors are polished as facets on a solid block of beryllium. This mirror cluster is mounted directly on the baseplate and through a long shaft drives a single wedge directly in front of the telescope assembly. The PMT's, relay optics, and shutter assembly are mounted to a housing which attaches to the telescope assembly mounting flange.

The sunshades, high voltage power supply, and two preamps are supported by an outer structure which attaches to the primary structure at the gimbal mounting interface. Not shown in the layout is a blanket of superinsulation which covers the entire exterior of this outer structure.

Energy from a star which enters a sunshade is reflected by a facet on the mirror cluster into its telescope. The image of this star is nutated by the optical wedge across reticle slits at the focal plane of the telescope. The energy passing through the reticle is relayed to a PMT by folding prisms and distributed on the PMT faceplate in a 0.25 inch diameter blur by two condensing lenses. One PMT is used for two telescopes and signal separation is accomplished by using "L" shaped reticle slits in the two telescopes and rotating them so that their pulse trains are 180° out of phase. This technique provides inherent synchronization created by the use of a single wedge.

Figure 4-10 is a preliminary configuration of the reticle pattern for the baseline design. The critical requirement for the reticle is to minimize variations in slit width which would produce centroid shifts in the output pulses. The tolerance selected ($\pm$ 0.000012 inches) for line straightness and irregularities is the maximum tolerable consistent with over-all accuracy requirements. The reticle requirements were reviewed with two possible vendors and both considered the requirements achievable.

The critical items from the standpoint of alignment stability are the mirror cluster and the telescope assembly (the machined housing containing the four telescope objectives). The relationship between these items and the gimbal interface completely determines the boresight stability of the cluster. The angle between the wedge and the telescope optical axis is not critical since the deviation produced by the wedge is dependent only the angle between the wedge faces. The function of the relay prisms and condensing lenses is only to transfer the energy which passes through the reticle slit to the PMT and therefore has no effect upon alignment accuracy. The alignment of the sunshades is important only from the standpoint of sun rejection and preventing vignetting of the optical system.

MATERIALS

The material selected for the primary structure supporting the mirror cluster and telescope assembly is beryllium for two primary reasons - 1) dimensional stability with respect to time and temperature and 2) high thermal conductivity. Dimensional stability of a material is primarily a function of the degree to which internal stresses can be relieved. Beryllium, because of the sintering process by which it is formed, is inherently a very homogeneous material. Its dimensional stability is therefore superior to most metals even after rather servere temperature cycling.

Any telescope or telescope assembly, regardless of how stable the material from which it is made, will not maintain a precise boresight alignment if temperature gradients exist within the structure. In the case of this design, a temperature differential of 1°F from one side of the beryllium cylinder to the other will produce a boresight shift of approximately 2 arcseconds. The high thermal conductivity of beryllium tends to minimize temperature differentials and this resultant distortion.
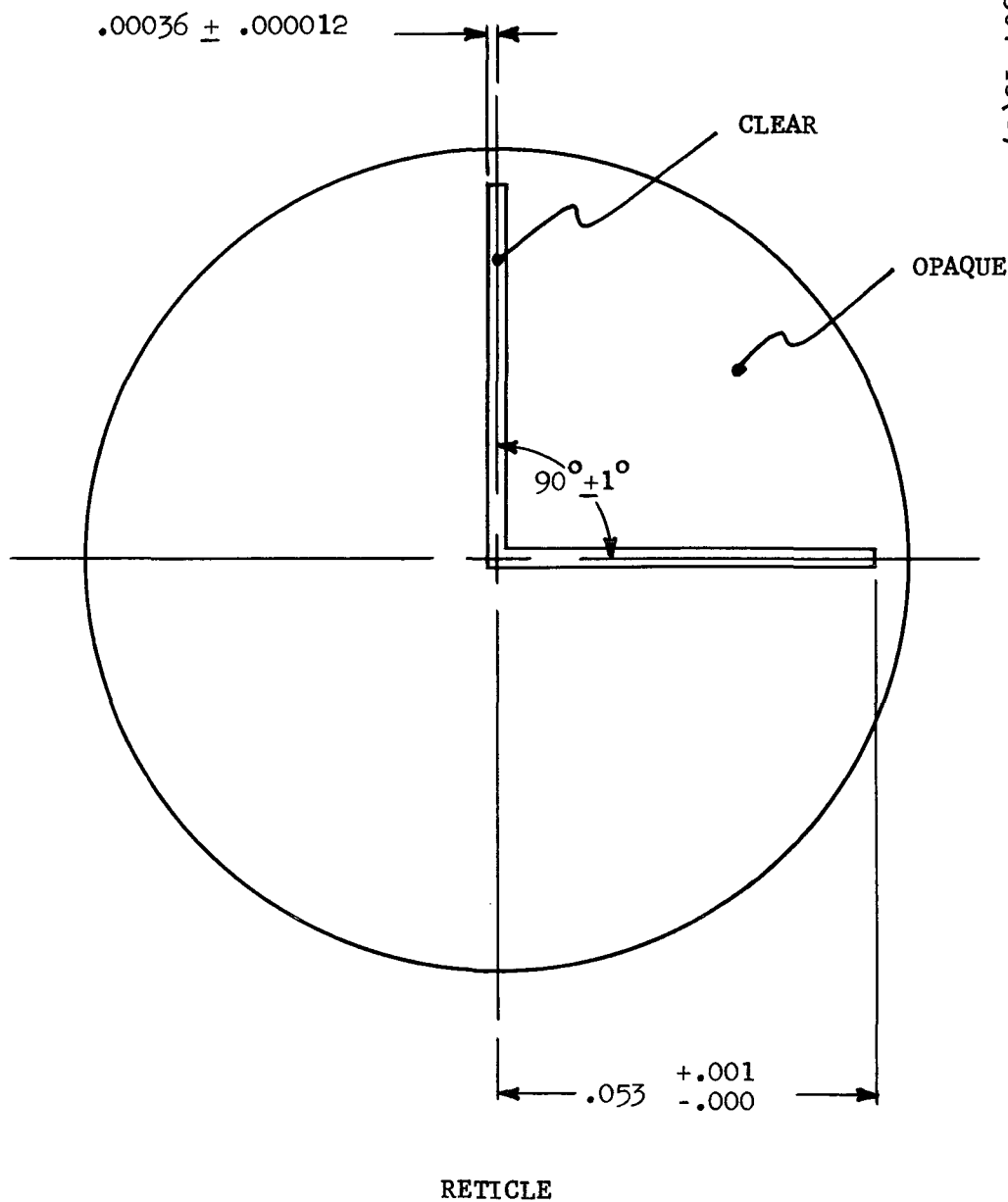
.00036 ± .000012

CLEAR

OPAQUE

90°±1°

.053 +.001 −.000

RETICLE

Figure 4-10. Baseline Reticle Configuration (Not to Scale)

THERMAL CONSIDERATIONS

As mentioned above, temperature gradients within a precision optical assembly can create intolerable distortions. In addition to the employment of material with high thermal conductivities, gradients can be minimized by having a symmetrical structure and eliminating unsymmetrical heat loads. The wedge motor produces approximately 90% of the overall heat load in a cluster. For this reason it was located at the base of the structure where its heat can be dissipated readily with minimal effect on the critical elements of the system. The exterior of the outer structure is covered with a blanket of super-insulation to protect it from the unsymmetrical heat load of solar radiation. Any heating in the outer structure, along with the heat load produced by the electronics, is dissipated by conduction at the base of the primary structure and is not coupled into the telescope assembly.

The most severe source of unsymmetrical heating will result from solar illumination on the interior of the sunshades. A preliminary thermal analysis has indicated that in the worst case sunshade temperatures in the order of 250°F may be attained. Reradiation from the sunshade to the primary structure and telescope would result in intolerable temperature gradients. Although not shown in the baseline design, it appears that an intermediate thermal shield between the outer structure and the beryllium inner structure will be required. This intermediate radiation shield would control this reradiation and would conduct and distribute this heat load in a more symmetrical fashion into the base of the primary structure.

SHUTTER ASSEMBLY

The shutter consists of a coded disc which is rotated behind the four reticles. The holes in the disc are arranged such that none, any one, or any two telescopes can be selected. The disc is driven by a stepper motor/gearhead with a potentiometer for position readout.

WEDGE MOTOR

The requirements for the wedge motor are that it must rotate the wedge at 4 revolutions per second and the short term (within one revolution) speed variation must be negligible with respect to system tracking requirements. Studies show that a specially designed hysteresis synchronous multiple-pole motor will satisfy motor requirements, and this is the baseline choice. Another possible selection would be an induction motor which, although subject to long term speed variation, has better short term speed stability since it

does not tend to "hunt" like a synchronous motor. The disadvantage of an induction motor lies in more complex electronics to slave the signal processor and the motor frequency.

The bearings for the wedge drive assembly have been tentatively selected as duplexed pairs of MPB #3 TAR 8-12 with a dry film lubricant. The dry film lubricant is very desirable from the standpoint of minimizing outgassing around an optical system and is acceptable because of the light bearing loads and low speed operation.

Sunshade Design

Of the 8 selected stars, they can be generally classified with respect to Sensor Cluster geometry as either high stars or low stars as a function of their angle of declination. Since there are not stars of interest between 20° and 50° declination, all stars below 20° are defined as "low" and all stars above 50° are "high".

Referring to Figure 4-1, it can be observed that the diameter of the Sensor Cluster is determined by the length of the sunshade for the low stars, if all sunshades are made equal in size. Sunshade length is a direct function of aperture diameter, and originally all were made equal, based on the dimmest star. However, the dimmest of the low stars (Altair) is approximately 4 times brighter than the absolute dimmest star (Phecda). This allows a reduction in aperture diameter and sunshade length of up to one-half for all low stars, thereby producing a significant reduction in cluster diameter.

The critical aspects of manufacturing sunshades are producing knife edges on the baffles and producing highly absorbing diffuse surface finishes. A considerable effort has been expended on previous programs in developing the techniques and processes for achieving both of these features. Key to both is the type of surface finish used to produce the low reflectance. There are a number of black paints which are acceptable optically, but paint has two primary disadvantages. First it tends to build up on knife edges and degrade their sharpness, and secondly it tends to flake off during launch vibration and produce particle contamination. This contamination must

be avoided since sun-illuminated particles in the FOV of a star sensor appear very much like a star. A special process was developed for a very similar application in which 1% diffuse reflection was obtained by a combination of chemical etch and black anodizing. In the

0.3 to 0.8 micron region it was found to be optically superior to any other finish studied. Since it is basically an anodize, it is also a "clean" and relatively durable surface.

Mass Properties

The total weight of one Sensor Cluster is estimated at approximately 14.8 pounds. A breakdown of this estimate is given in Table 4-4. The mass moment of inertia of one Sensor Cluster about the inner gimbal axis was estimated at 0.025 slug-ft^2.

TABLE 4-4.

STARS SENSOR CLUSTER WEIGHT SUMMARY

A.	TELESCOPE ASSEMBLY			<u>10.71</u>
	1. Beryllium Baseplate		0.85	
	2. Beryllium Cylinder		1.07	
	3. Telescope Housing (Al)		2.15	
	4. Reticle Assemblies		.08	
	5. Optics		.67	
	a. Objectives	0.45		
	b. Wedge	0.22		
	6. Beryllium Mirror Cluster		0.85	
	7. Motor		1.08	
	a. Stator	0.83		
	b. Rotor	0.25		
	8. Bearings, Retainers, Supports		0.35	
	9. PMT/Shutter Support Housing		0.10	
	10. PMT/Relay Assembly		2.26	
	a. PMT's (2)	1.76		
	b. Brkts (2)	0.40		
	c. Misc	0.10		
	11. Shutter Assembly		0.25	
	12. Misc Hardware, etc		1.00	
B.	OUTER STRUCTURE			<u>4.08</u>
	1. Main Structure		1.48	
	2. Sunshades		0.60	
	3. Electronics		1.00	
	4. Super Insulation		0.50	
	5. Misc Hardware, etc		0.50	
	Total (One Hemisphere)			<u>14.79 #</u>

4.3   Sunshade Design

Introduction

Each STARS individual star tracker is required to track its selected star when the sun is $\geq 30^{\circ}$ from the optical axis and when the spacecraft or earth is $\geq 15^{\circ}$ from the optical axis. To accomplish this, a baffled sunshade is required in front of the telescope to shade the optics and thereby limit the amount of light from the sun, earth or spacecraft which can enter the optical system and reach the detector. The baffling must attenuate the energy from the bright off-axis source to values which are tolerable relative to the energy from the star of interest. The dimmest star of the selected set is a 2.3 visual magnitude star whose irradiance in the spectral passband of interest is almost 12 orders of magnitude less than the sun, so that this is approximately the order of magnitude attenuation required of the sunshade.

A perfect sensor sunshade is of course an infinite baffle. With such an infinite baffle the only sources of off-axis energy that can enter the telescope aperture results from scattering from the edge of the baffle aperture and diffraction off the baffle aperture. The remainder of the energy that enters the baffle aperture is allowed to proceed uninterrupted. This of course, is not practical for real systems, so that a sunshade normally consists of an aperture and a baffling system designed to best simulate a perfect absorber. The baffle surfaces have a low reflectivity finish, either diffuse or specular, or a combination of the two, and off-axis light is attenuated to acceptable values by forcing it to go through multiple reflections before it can enter the telescope.
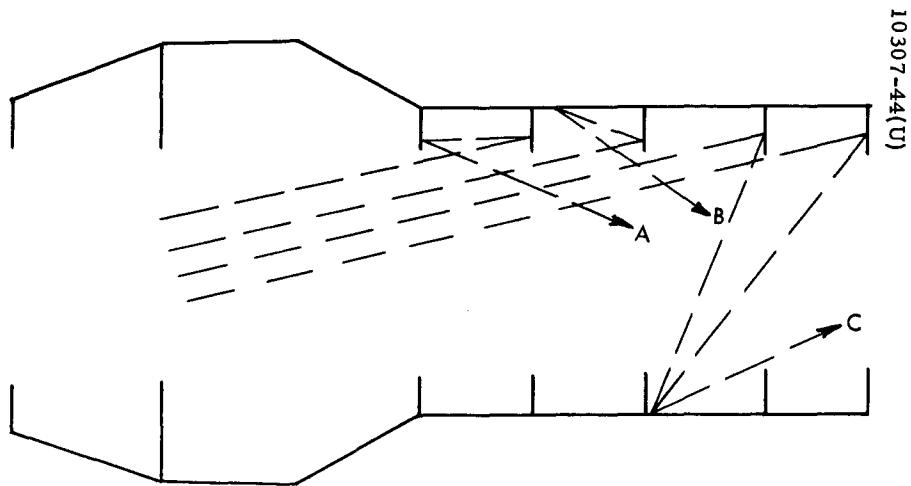
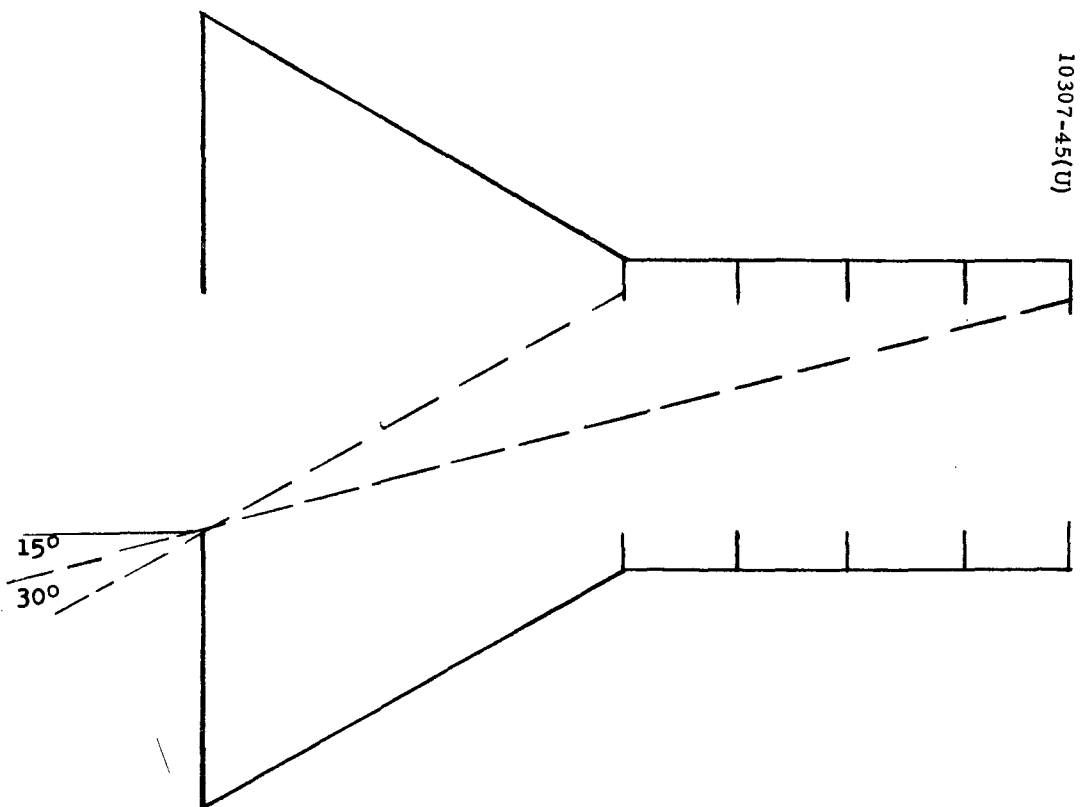Figure 4-11. Paths by Which Light Can Scatter From Sunshade

Figure 4-12. Candidate Sun/Earth Sunshade for STARS Using Cone-shaped Entrance

Referring to Figure 4-1, energy from a star of interest passes through the sunshade, is folded by a mirror, nutated by a rotating wedge in front of the telescope, and finally reaches a reticle at the focal plane of the optical system. The shade is designed to shadow the folding mirror from direct radiation from the off-axis bright sources.

With any practical sensor shade, energy can enter the optical system and reach the detector via a multitude of paths. Both diffraction from edges and scattering from the baffles provide the mechanism by which unwanted energy reaches the detector. As will be shown later, the amount of energy reaching the detector through diffraction is not significant; the dominant mechanism is scattering of the sunshade surfaces and optical elements.

Sunshade Configuration

Two sunshades, shown in Figures 4-11 and 4-12, received detailed analysis for the STARS application. The length and entrance diameter of both shades are chosen such that all rays within the optical field of view enter the optics unobscured and rays $\geq 15^{o}$ off axis cannot strike the first optical element a folding mirror. The interior of the shade at the narrower portion of the sunshade is lined with baffles arranged so that no light can enter the optical system without undergoing at least two diffuse reflections for a source greater than 15° from the optical axis. Both sunshades are designed with an increased diameter for rays entering at angles greater than 30° thereby providing a greater baffle volume for sun energy rejection (the sun is always greater than 30° from any optical axis). The shape of the front portion of both sunshades is designed such that any energy must also go through at laast two diffuse reflections before it can enter the optical system. All baffles are always out of the field of view of the optical system and the baffle edges must be manufactured as sharp as possible to reduce the light directly reflected from them into the optical system. All baffle surfaces (and all non-optical surfaces) are diffuse, low-reflecting surfaces.

Scattered Light Analysis

The criterion used to evaluate baffling effectivenss is in terms of the equivalent irradiance due to each unwanted light source. Equivalent irradiance is defined to be the irradiance at the optics entrance aperture which results in the same output from the detector as would result from a star with the same effective irradiance. For the STARS tracker, the sunshade must limit the equivalent irradiance to values less than 1.1×10^{-13} watts/cm^2.

Energy reaches the detector by first scattering off the sunshade surfaces and then exiting the rear of the sunshade. Since all portions of the sunshade are out of the field of view of the optical system, only energy which is scattered off the portions of the folding mirror, wedge, or telescope elements can reach the reticle. Finally, only energy which impinges on the clear portions of the reticle can reach the detector.

In calculating the radiant intensity reflected from the shade there are three different paths, of two reflections each, to be considered. These are illustrated in Figure 4-11. They are A) from the sun illuminated baffle to the adjacent baffle, B) from the sun illuminated baffle to the adjacent wall of the sunshade, and C) from a number of sun illuminated baffles to the wall on the opposite side of the sunshade.

Consider scattering along paths A & B. The power falling on the illuminated surface if $H_o A_i \cos \theta_s$, where H_o is the incident irradiance within the spectral band. This is multiplied by ρ/π to get the reflected radial intensity moved to the surface, where ρ is the reflectivity of the surface. The solid angle subtended by an infinitely long strip at a point on an adjacent strip was used to approximate the solid angle subtended by the wall or baffle adjacent to the sun illuminated baffle. This modified solid angle, which contains a factor to account for the cosine falloff, was calculated to be approximately equal to $(\pi \omega_2 \cos \theta_{i2} \cos \theta_{ri}) / 2 d_{12}$. This approximation is valid for curved baffles if they are reasonably close together, and the radii of curvature are not too small.

The subscripts 1 and 2 refer to the first and second reflecting surfaces in the sunshade. Therefore, ω_2 is the illuminated width of the second baffle, $\theta_i 2$ is the angle of incidence on the second baffle, θ_{r1} is the angle of reflection from the first baffle to the second baffle, and d_{12} indicates the distance between the first and second reflecting surfaces of the sunshade.

The reflected radiant intensity normal to the second surface is obtained by multipling the power on the surface by ρ/π. The resultant expression for radiant intensity normal to the second surface for the ith baffle after normalization to the incidence irradiance

$$\frac{J_i}{H_o} = \left(\frac{\cos \theta_{s\rho}{}^2}{2 \pi} \right) \left(\frac{A_i \omega_2 \cos \theta_{ri} \cos \theta_{i2}}{\varphi_{12}} \right)$$

where ρ_s is the source angle, and A_i is the illuminated baffle area normal to the optical axis and projected onto the entrance aperture of the sunshade.

Consider scattering along path C. The same procedure is followed as in paths A and B, where $H_o A_j \cos \theta_s$ is the incident power on the illuminated surface facing baffle j, and $(\rho \cos \theta_{rl})/\pi$ is the factor which gives the radiant intensity reflected from the surface.

The solid angle subtended by the second surface at the ith baffle across the sunshade was approximated by $\pi r_2 \omega_2 \cos \theta_{12}/d_{12}^2$, where r_2 is the radius of the sunshade. The reflected radiant intensity normal to the second surface is the solid angle times the projected illuminated area times ρ/π. The resultant expression for irradiant intensity normal to the second surface at the ith baffle is

$$\frac{J_i}{H_o} = \sum_{j=1}^{N} \left[\left(\frac{\cos \theta_s}{\pi} \right) \left(\frac{\rho^2}{d_{12}^2} \right) \left(A_j \; r_2 \; \omega_2 \; \cos \theta_{rl} \; \cos \theta_{12} \; f_{12'} \right) \right]$$

where N is the number of baffles in the sunshade and f_{12} is the extended fraction of the second surface illuminated by radiation reflected from the first surface.

The edges of the baffles also scatter energy into the optics. Assume the baffle edges are diffuse reflecting surfaces, whose cross section is circular. The radiant intensity reflected from a cylindrical edge of length l and radius r is given by $\quad \dfrac{J_i}{H_o} = \dfrac{\rho \ell r}{2\pi} \left[\sin (\theta_s + \theta_r) - (\theta_s + \theta_r) \cos(\theta_s - \theta_r) \right]$
where ρ_r is the angle the reflected rays make with the optical axis. It is determined by the location of the surface which is being illuminated by the radiation from the baffle edges.

The undesired radiation exits from the sunshade and illuminates the folding mirror and the wedge in front of the telescope (other surfaces such as the interior of the telescope are negligible contributors). All optical surfaces have imperfections, such as scratches, pits and digs, and bubbles in refractive elements, as well as dust which is on the surface. These imperfections act as diffuse scatterers of any radiation which falls upon them. Light scattered from them can go directly to the detector.
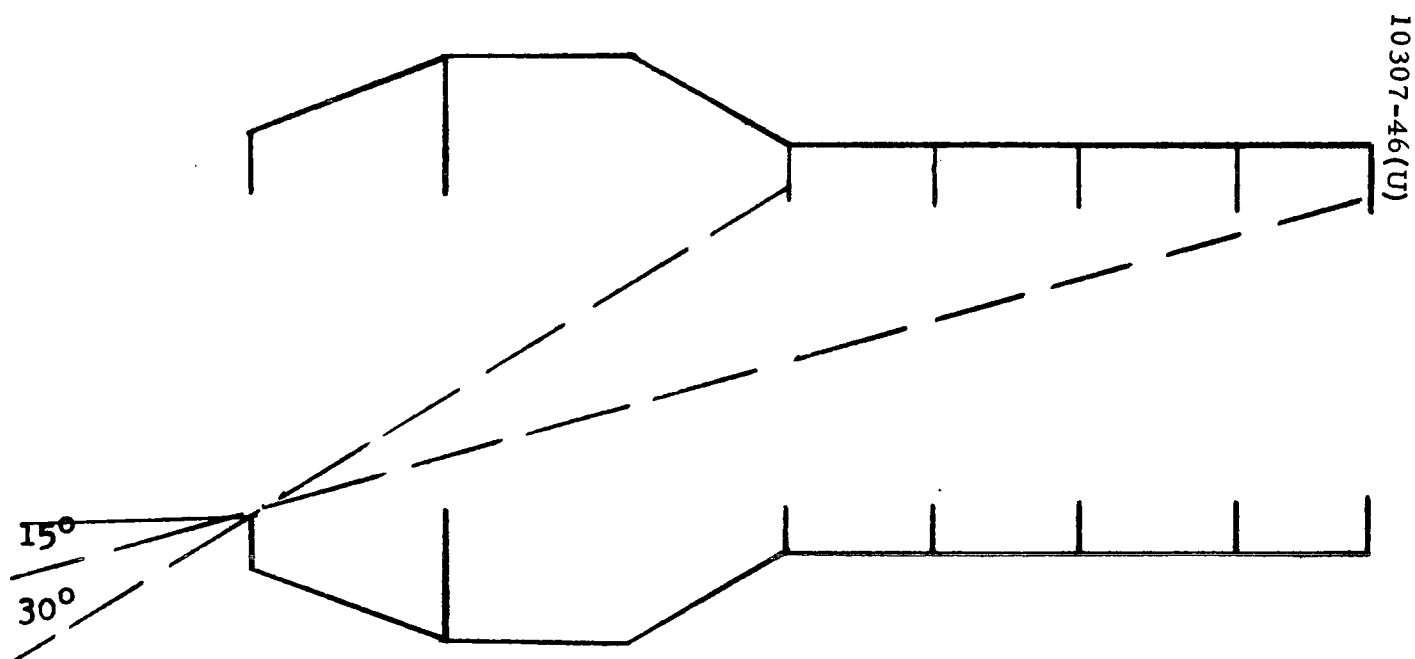
15°

30°

Figure 4-13. Baseline Sun/Earth Sunshade for STARS
Using "Smoke Stack" Shape

It is assumed that the amount of light that is scattered is proportional to the areas of these imperfections. The ratio of the scattering area to the area of the optical surface is a function of the optical surface specifications, and of the dust content of the air in which the telescope was assembled. It was assumed that the folding mirror was a super polished mirror, the optical surfaces conform to 60-40 specs, the amount of dust on each surface was equal to that in one cubic foot of air from a class 100,000 clean room, and the total amount of light intercepted by surface defects and dust was forward scattered with a Lambertian distribution.

Scattering Analysis

The two sunshades which were evaluated are shown in Figures 4-12 and 4-13. It was believed that the "cone-shaped" sunshade would be the most effective, however, the "smoke-stack" sunshade is a better configuration from the point of overall sensor cluster geometry. The calculations were made using the already discussed approach with the help of a computer to speed up the rather tedious calculation process. Both sunshades were evaluated for two cases. 1) The sun 30° from the optical axis and 2) the sun illuminated spacecraft 15° or more from the optical axis.

The assumptions as to parameter values used with calculations are as follows:

1) The baffle surfaces and sunshade walls are assumed to have a diffuse reflectance of 4% and scatter energy in a Lambertian manner. (This corresponds to measured performance from sunshades manufactured on previous programs).

2) The amount of energy scattered off the baffle edge is proportional to the radius of the "knife-edge". From measured samples (using photographic techniques) 0.002 inch radius is taken to be a practical value.

3) The clear reticle aperture is taken to be 1.2×10^{-5} radians^2.

4) The sun is assumed to be a point source having an irradiance in the spectral passband of 5×10^7 w/μm^2 (0.325μm to 0.800μ).

5) The sun illuminated spacecraft is assumed to be a diffuse reflector with 80% reflectivity. The total irradiance of the spacecraft was determined by integrating the irradiance form 15° off axis to 89° off-axis (at 90°, no light can enter the shade.)

This analysis was performed with the help of a FORTRAN computer program which evaluates an integral of any function over an extended source (see Figure 4-14). The integral to be evaluated is

$$2 \int_{\theta_1}^{\theta_2} \int_{0}^{\beta} F(\theta) \sin \theta \; d\varphi \; d\theta \text{ where } \beta = \cos^{-1} \left(\frac{\sin \theta_h - \cos \theta \sin E}{\sin \theta \cos E} \right)$$

θ_h = angle between local horizontal and extended source,

E = angle between local horizontal and optical axis,

θ_1 and θ_2 = angle from optical axis to integration limits, and

F (θ) is the value of any function of θ at a particular θ.

The spacecraft was assumed to reflect 80% of the energy falling on it from the sun. The irradiance due to point sources 15°, 20°, 30°, 45°, 60°, 75° and 85° off axis was calculated and the integration was performed over the curve of the irradiances of these point sources. The result is the irradiance of the spacecraft from 15 degrees off axis to 89° off axis.
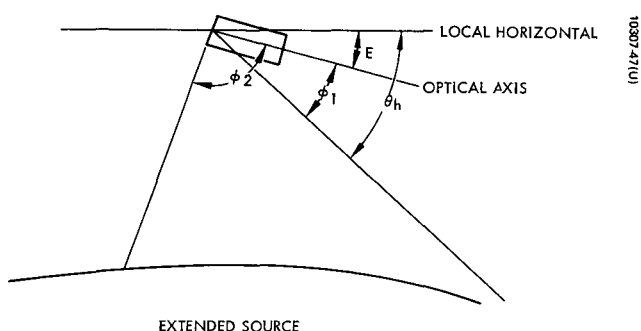

Figure 4-14. Geometry for Integration Over Extended Source

Diffracted Energy from Bright Off-Axis Sources

It is possible for energy to reach the detector through the mechanism of diffraction. A simplified (but worst case) calculation has been made to determine whether this source of energy can be a significant contributor.

Diffracted energy can reach the detector via two paths. Referring to a simplified sketch of the STARS telescope/shade, Figure 4-15, energy can diffract off the baffle edges and then rediffract off the entrance aperture and reach the detector. It is also possible for energy to diffract off the baffle edges and then scatter off of the optical elements and reach the detector via this path. No energy can reach the detector without undergoing at least two diffractions or a diffraction-scattering since the baffles are designed to always be out of the optical field of view and diffracted energy appears to emanate from the diffracting edge. It is noteworthy that during the diffraction analysis it was observed that the swept field of view (from the nutating wedge) comes quite close to including some of the baffles. This cannot be allowed to occur since energy reaching the detector from diffraction (and for that matter, scattering) will increase orders of magnitude if baffle edges enter the field of view. To guard against this occurence, it is recommended that the clear field of view for the shade be increased slightly by increasing its length and baffle edge diameters.

As the worst case, the energy resulting via diffraction for the sun 15° from the optical axis has been considered. This case is obviously worse than the 30° sun requirement but was chosen to encompass the 15° extended source (earth or spacecraft) requirement. Calculation for an extended source is tedious and time-consuming, however, analysis of similar systems indicate that the sun 15° off-axis would be a worse condition.

Diffraction - Diffraction

The calculation of the amount of energy that enters the field stop by diffraction is not a trivial task. This determination has been simplified by recognizing that the formulas for diffraction from a straight edge are adequate and that the diffracted energy can be considered as emanating from a point at the intersection of baffle edges and the plane formed by the bright source (sun) and the optical axis.
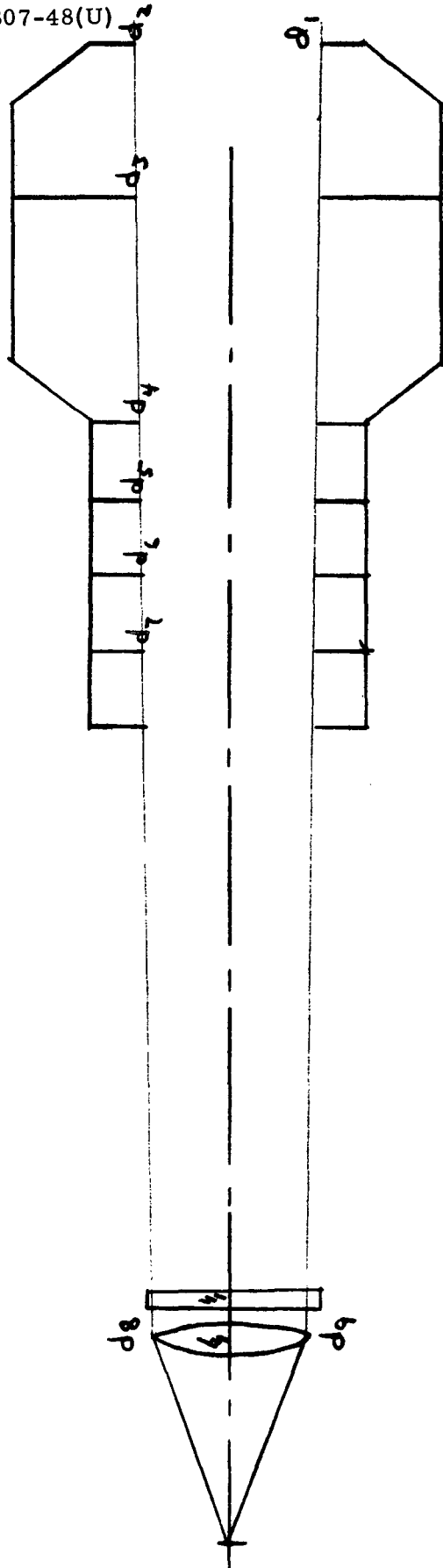
Figure 4-15. Equivalent Telescope for Diffraction Analysis

By this technique, a estimate of the diffracted energy is made through successive application of the straight edge diffraction formula which is given by:

$$\frac{H_2}{H_1} = \frac{\lambda\, s}{4\, \pi^2\, x^2}$$

where

H_2 = diffracted irradiance

H_1 = incident irradiance

λ = wavelength = 0.5×10^{-4} cm (0.2×10^{-4} in.)

x = perpendicular distance into the shadow where H_2 is measured

s = distance from diffracting edge where H_2 is measured

Figure 4-15 is a sketch of the cross section through the optic axis of an equivalent STARS telescope in the plane of the sun and optical axis. The diffracting edges of interest are labeled d_1 through d_9 for the geometry given in the sketch. To reach the field stop, the energy must rediffract at the aperture stop edges labeled d_8 and d_9. The energy at a point on the reticle is thus determined by calculating the irradiance from the first diffraction which reaches the second diffracting edge by the straight edge formula and then reapplying the formula to determine the energy at a point on the reticle. The optical transmission of ≈ 0.8 should be applied to the second diffraction. An estimate of the total energy at a point on the reticle is then the sum of all the path energies. The energy at the center of the reticle for a number of paths is tabulated below where the effective incident irradiance from the sun is taken to be 0.32 watts/in^2 (0.05 watt/in^2).

PATH	H (AT RETICLE CENTER)
d_{18}	0.63×10^{-11} watt/in^2
d_{19}	2.8×10^{-11}
d_{28}	1.5×10^{-11}
d_{29}	1.11×10^{-12}
d_{78}	1.5×10^{-11}
d_{79}	1.0×10^{-13}

It is evident that paths d_{18}, d_{19}, and d_{28} are the major contributors and the total energy at the reticle center is estimated to be $\approx 1.2 \times 10^{-10}$ watt/in^2.

An estimate of the energy passing through the reticle is necessarily difficult because of the complexity of the reticle pattern and the lack of symmetry about the optical axis of the diffraction pattern. The reticle diameter is quite small and from the calculations, it appears that the diffracted energy will vary at most plus and minus a factor of four across the reticle and the summation of the various paths will tend to average. The baseline reticle slit in an L-shape with each leg 1.2° long and 60 arc-seconds wide. This is equivalent to $\left[(2)(0.053)(0.00072) = 7.6 \times 10^{-5} \text{in}^2\right]$ and assuming the irradiance across the reticle constant.

P through reticle = $(7.6 \times 10^{-5})(1.2 \times 10^{-10}) = 9.1 \times 10^{-15}$ watts. The equivalent irradiance at the aperture due to diffraction-diffraction is therefore,

$$H_{eq} \text{ (15° sun)} = \frac{P}{A_{eff}} = \frac{9.1 \times 10^{-15}}{6.4} = 1.4 \times 10^{-15} \text{ watt/cm}^2$$

This value is well below that which can be tolerated (1.1×10^{-13} watt/cm^2) and is about the same order of magnitude as the scattering prediction for the sun 30° off the optical axis. Although the calculation just performed appears excessively simplified, the approximations and assumptions are quite sound. Two similar systems have received comparable analysis and in both cases the analysis indicated diffraction to be negligible. Both systems were subsequently tested and the results correlated.

Diffraction-Scattering

Another path by which energy can reach the field stop is through scattering off the folding mirror or telescope elements after diffraction from the baffle edges. An estimate of this unwanted energy contribution is made by first using the straight edge diffraction formula to calculate the diffracted irradiance at a potential scattering surface and then calculating equivalent irradiance at the aperture due to the scattering.

All the scattering surfaces are assumed to forward scatter with a Lambertian distribution and having a diffuse reflectance of 5×10^{-4}. Using these assumptions, the equivalent irradiance due to diffraction-scattering off the folding mirror and the first lens of the telescope were estimated to be

$$H_{eq} \, (\text{ sun at } 15^{\circ}) = 5.3 \times 10^{-16} \text{ watt/cm}^2 \text{ (Folding Mirror)}$$

$$H_{eq} \, (\text{ sun at } 15^{\circ}) = 3.4 \times 10^{-16} \text{ watt/cm}^2 \text{ (First Lens)}$$

This source of energy is significantly less than the other calculated noise contributors and almost three orders of magnitude less than the maximum acceptable level.

TABLE 4-5. CALCULATED EQUIVALENT IRRADIANCE AT STARS SUNSHADE

Configuration	Equivalent Irradiance due to the sun at 30° off axis	Equivalent Irradiance due to the spacecraft 15° or more off axis
"Cone-Shaped"	3.5×10^{-15} watts/cm^2	2.0×10^{-15} watts/cm^2
"Smoke Stack" Shaped	4.0×10^{-15} watts/cm^2	1.8×10^{-15} watts/cm^2

The results of the above analyses are summarized in Table 4-5. It can be seen that both configurations are well below the maximum acceptable level $(1.1 \times 10^{-13} \text{ w/cm}^2)$. It should be kept in mind that these numbers are based on many approximations and assumptions, and it is estimated that an order of magnitude error could exist. If one assumes that the actual performance will be a factor of ten worse than predicted, the equivalent irradiance is on the order of 10^{-14} watts/cm^2 which still provides comfortable margin.
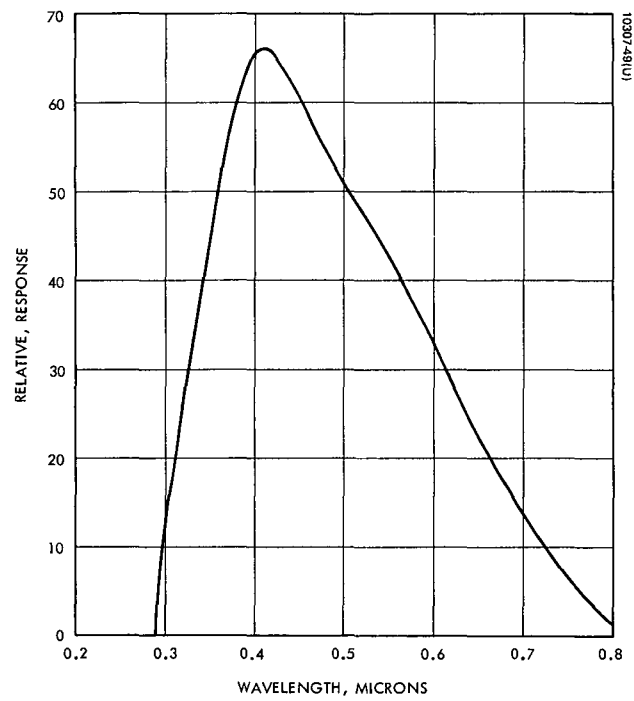
Figure 4-16. Spectral Response of S-20 Photo Surface

4.4 Optical System

Introduction

The STARS tracker requires the use of eight essentially identical sensors, each tracking a certain star in the celestial sphere from an orbiting spacecraft. To keep the size and weight of the STARS mechanism within reasonable limits, a length restriction of 2.65 inches was placed on the optical design for the front vertex to reticle distance; a focal length of 2.5 inches was considered reasonable for this length restriction. For sensitivity requirements, an entrance aperture diameter of 1.25 inches was required, making the speed of each lens f/2.0. A circular field of view of $\pm 1^{\circ}$ was felt to be adequate. The spectral region of 0.3 to 0.8 microns was determined by the response of the S-20 photo surface of the photomultiplier tube (PMT). As described in the previous sections, tracking is accomplished by using a nutating wedge in front of the objective lens to circularly scan the star image over the reticle pattern. A condensing lens images the entrance aperture onto the PMT. In order to star track successfully, the objective lens is required to have an image blur size less than 0.5 mrad.

Optical Materials

Perhaps the most demanding requirement on the optical design is its ability to transmit energy in the near ultraviolet down to 0.3 microns wavelength. Figure 4-16 is a sensitivity profile of the S-20 photo surface of the PMT; this response limits the wavelength region at either end of the extended visual spectrum. The difficulty lies in finding suitable optical materials that transmit over this region, especially in the near ultraviolet.
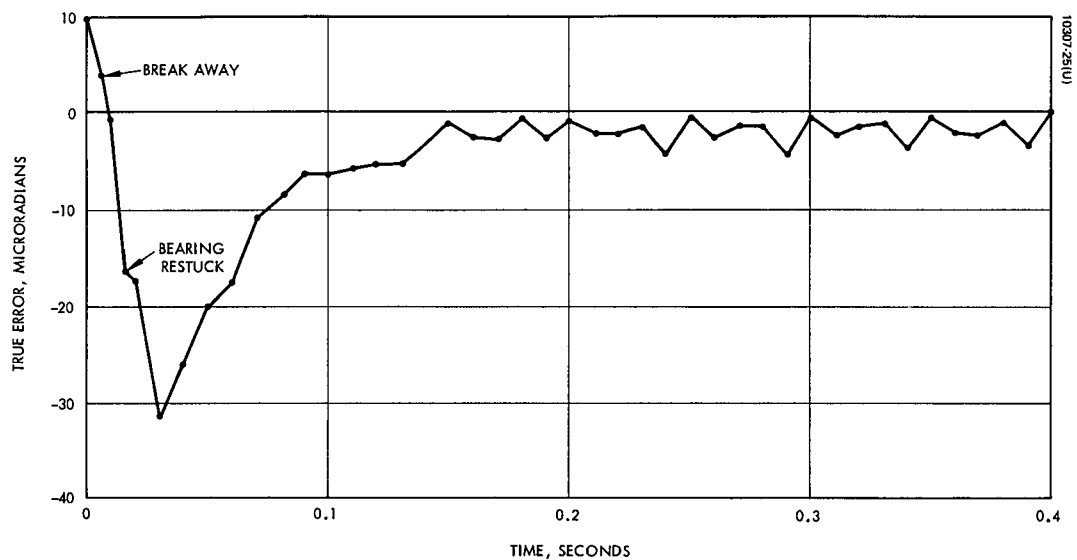
Figure 3.5-8. Plot of Polar Axis - Single Step Response
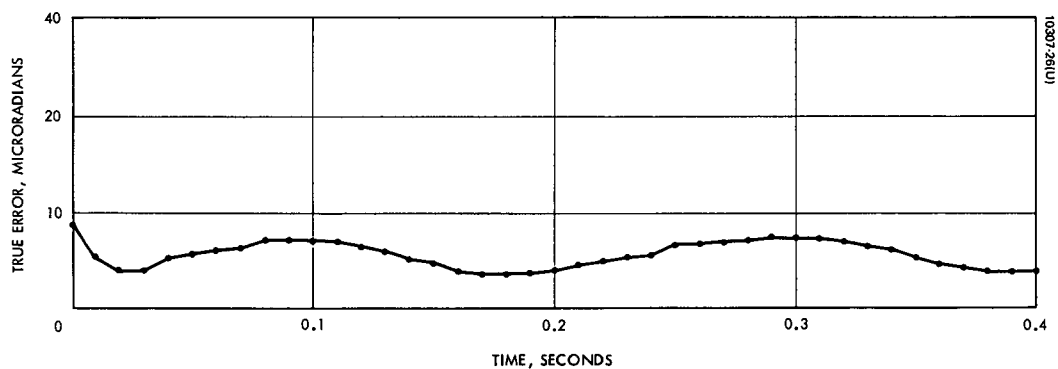Elastic Stiction Breakaway Transient

Figure 3.5-9. Plot of Polar Axis - Single Step Response
Elastic Stiction Model Last Step Before Stiction Breakaway

Most optical glasses transmit well from 0.4 to 2.0 microns, but very few transmit well at 0.35 microns or transmit at all near 0.30 microns. Furthermore, the handful of optical glasses that do transmit at 0.3 microns all have very similar optical properties (refractive index and dispersion). Since chromatic aberration will be a severe optical design problem, a material with optical properties differing sufficiently from those of standard optical glasses must be used to obtain control over chromatic aberration.

Numerous crystalline materials transmit very well into the near ultraviolet (some even transmitting below 0.2 microns); unfortunately, most of these have undesirable optical properties, such as water absorption and birefringence, that make them unsuitable for use in the STARS program. Three materials have been found with acceptable optical properties: calcium fluoride, sapphire, and fused quartz. Sapphire and fused quartz have optical properties somewhat similar to the ultraviolet-transmitting optical glasses so that there would be no significant benefit gained in aberration control due to using these materials in place of a standard optical glass. Calcium fluoride (CaF_2), however, does have a refractive index slightly lower than the transmitting optical glasses and, more importantly, has significantly less dispersion than do these glasses. CaF_2 was therefore chosen to be used as the "crown" for positive elements in the optical design. The standard ultraviolet-transmitting optical glass with properties differing most from CaF_2 is Schott K10; this material, normally used as a "crown" in optical design, will be used as the "flint" elements in this optical design.

The condenser portion of the STARS sensors requires the use of a reticle substrate and right angle prisms. Since the dispersion properties of these plane-parallel elements are not as critical as those of spherical-surfaced lens elements, the more common material, fused quartz, will be used in place of CaF_2, K10 not being considered due to transmittance requirements. Refractive index data for General Electric type 151 (GE 151) fused quartz has been used for the prisms and reticle substrate; since the refractive index of various types of fused quartz differs only slightly from manufacturer to manufacturer, the use of another type of fused quartz having special properties can be accommodated with only minor, if any, change in the optical design. Figure 4-17 depicts the ultraviolet internal transmittance (that is, neglecting surface reflection) of CaF_2, GE 151, and K10, the three materials used in the optical design calculations.
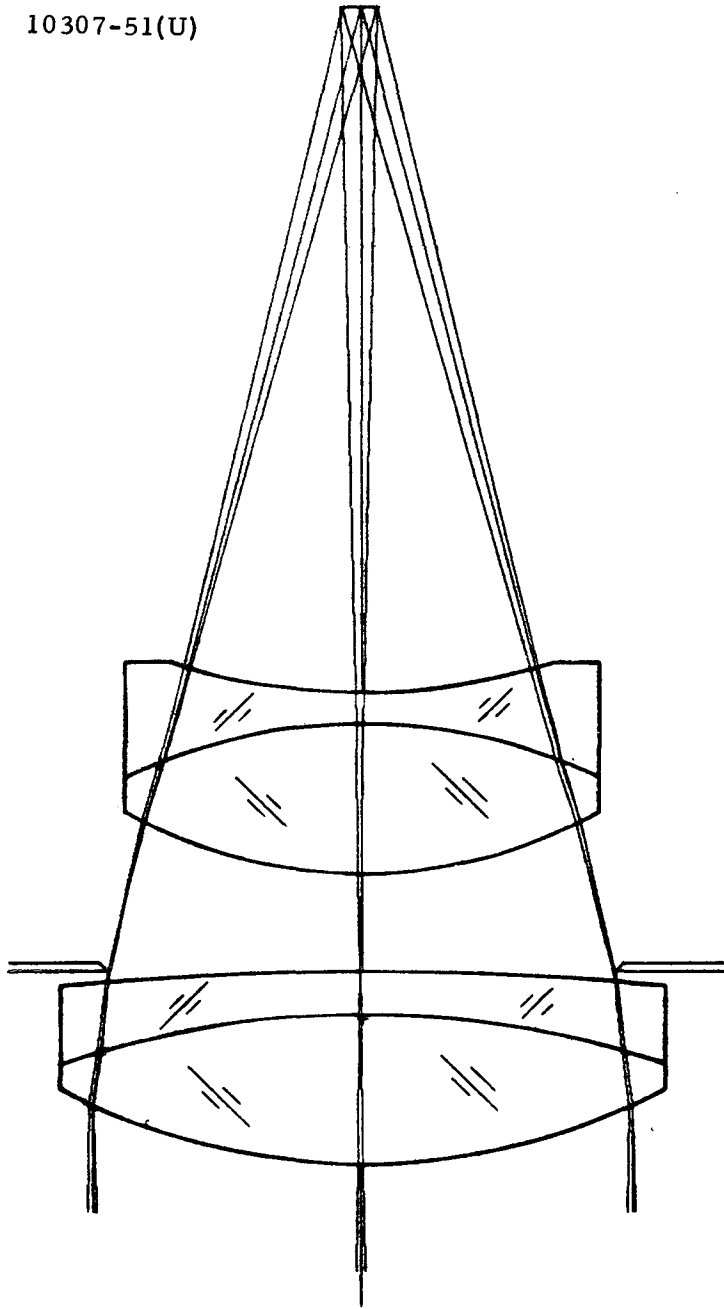
10307-51(U)

Figure 4-18. Optical Schematic of Objective Lens

Optical Design of the Objective Lens

Due to the fact that CaF_2 is more sensitive to vibration and thermal shock than optical glass, it was decided to have cemented surfaces between CaF_2 and K10 elements to minimize the possibility of damage to the CaF_2 elements. Under this restraint, a design concept of two cemented doublets, separated by an airspace, was adopted; as mentioned previously, CaF_2 would be the positive "crown" elements and K10 the negative "flint" elements. Due to the small field of view, the position of the aperture stop was not critical; it was placed between the two doublets.

During the optical design stage, the major difficulty lay in controlling spherical aberration while maintaining small chromatic aberration. Due to the small field of view, off-axis aberrations such as coma, astigmatism, and field curvature were easily controlled and presented no problem. The final design resulted after a careful balance of chromatic and spherical aberration; thus the image quality is limited by sphero-chromatism (as is to be expected in a small field-of-view, high f/number lens covering the extended visual spectrum). Figure 4-18 is an optical schematic of the objective lens; nearly all of the optical power of the lens lies in the first doublet, the second doublet having very little optical power, its function being primarily aberration control. Table 4-6 lists optical parameters pertinent to this design.

Figure 4-19 is a plot of knife edge scans of the on-axis and full field images formed by the objective lens. A knife edge scan can be interpreted as the increasing percent energy covered up by a knife edge as it is passed over the image of a point source. An expanding slit function shows percent energy uncovered by an infinitely long slit as a function of slit width, the slit always being centered on the image; this is analogous to the more-familiar radial energy distribution plot. Figure 4-20 shows the expanding slit functions; from this figure it can be seen that the slit width containing 90% of the transmitted energy is 0.44 mrad on-axis and for full field is 0.46 mrad in the sagittal plane and 0.57 mrad in the tangential plane. These data do not include the effects of diffraction; however at 0.55 microns wavelength (the center of the 0.3 - 0.8 micron band), the diameter of the Airy disc is only 0.042 mrad. Thus the effects of aberrations are about an order of magnitude greater than diffraction effects and, for the purpose of evaluating image quality, diffraction may be ignored.
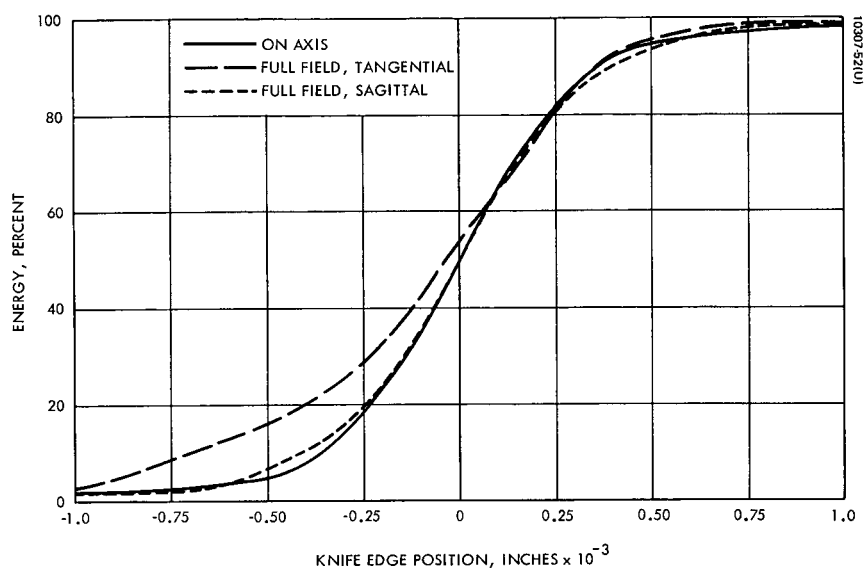
Figure 4-19. Knife Edge Scan Traces (Geometrical Aberrations Only)
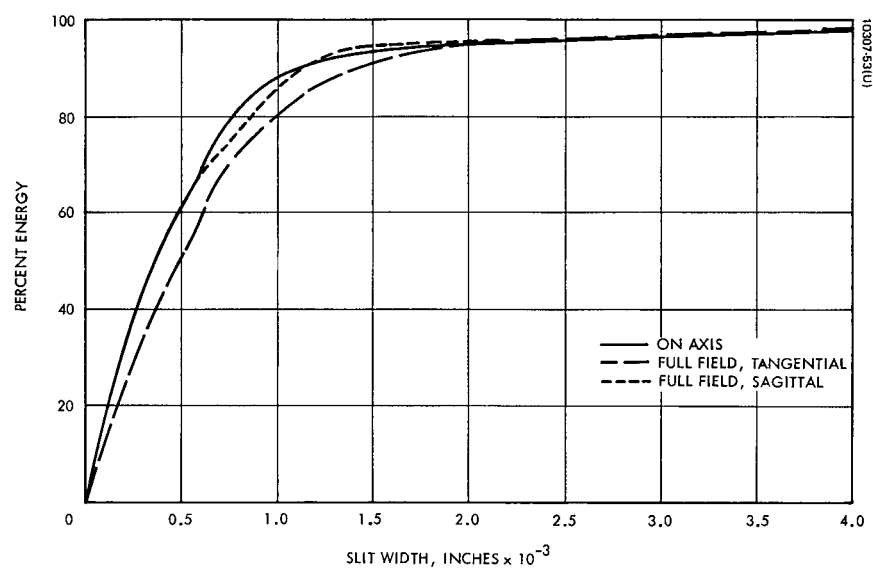
Figure 4-20. Expanding Slit Functions (Geometrical Aberrations Only)

TABLE 4-6. OPTICAL PARAMETERS OF OBJECTIVE LENS

Parameter	Value
Design Configuration	Two cemented CaF_2 - KlO doublets separated by an airspace
Effective focal length	2.50 inches
Entrance aperture diameter	1.25 inches
f/number	2.0
Field of view	± 1.0°
Overall length	2.70 inches
Spectral region	0.3 - 0.8 microns (See Figure 4-16)
Transmittance	(See Figure 4-21)
Airy disc diameter	0.042 mrad at 0.55 μ wavelength
Slit width containing 90% of transmitted energy (geometrical aberrations only)	0.44 mrad on-axis 0.46 mrad full field sagittal plane 0.57 mrad full field tangential plane

Figure 4-21. Transmittance of STARS Sensor

Figure 4-22. Optical Schematic of STARS Sensor

Transmittance data for the objective lens have been calculated assuming that no anti-reflection coatings will be used on the lens elements. Due to the low refractive indices of the materials used, 1.44 for CaF_2 and 1.51 for K10, no effective single-layer anti-reflection coating exists that may be used.
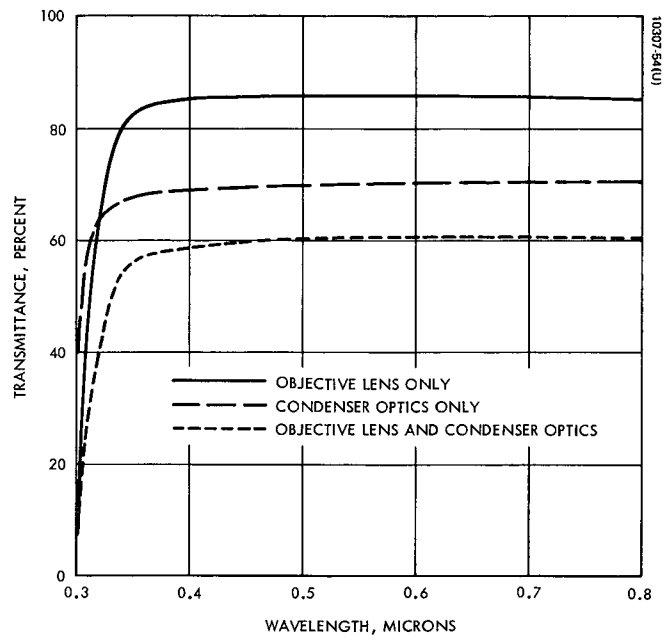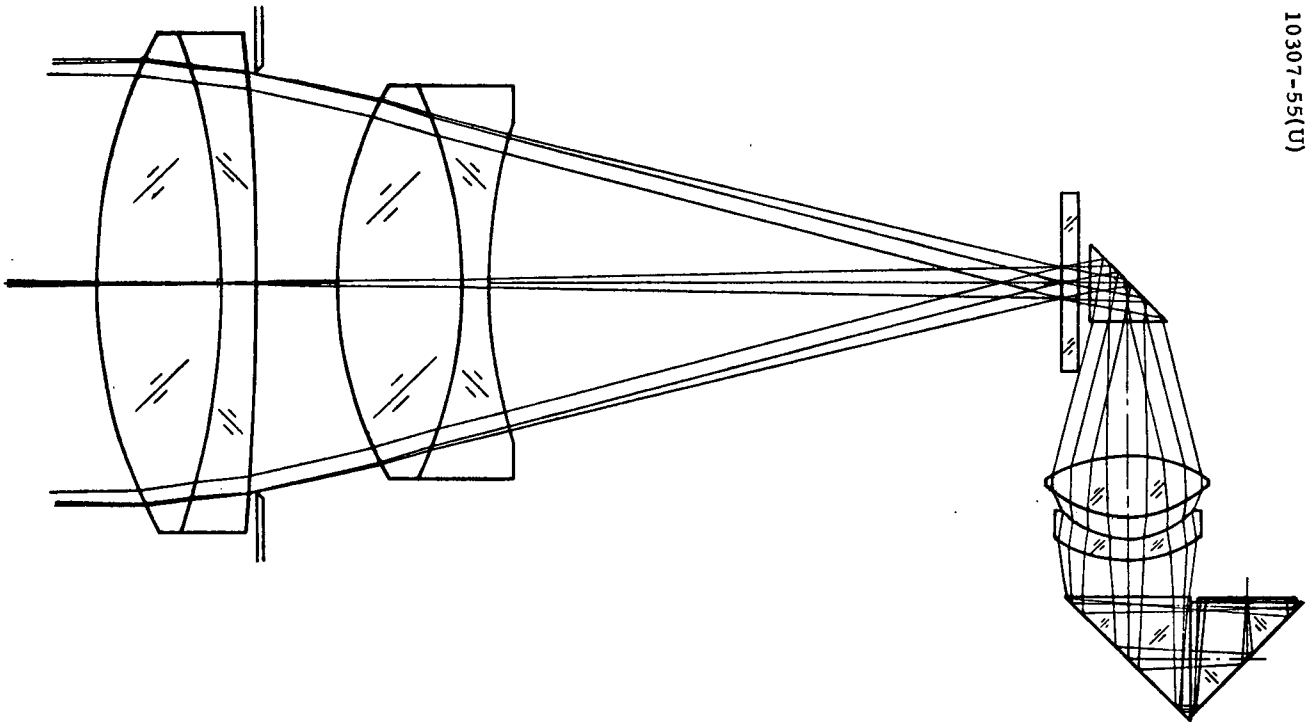
Multi-layer coatings have not been investigated; it was felt that such coatings on a low-index substrate covering the extended visual spectrum would be very expensive if obtainable at all. However, also due to the low refractive index, the Fresnel surface reflection losses are small: 3.3% per surface for CaF_2, 4.4% per surface for K10, and 0.1% at a CaF_2 - K10 interface. By combining the Fresnel reflection losses with material absorption losses (presented for ultraviolet wavelengths in Figure 4.16), uncoated lens transmittance data may be obtained as a function of wavelength; this data is shown in Figure 4-21.

Optical Design of the Condenser System

Energy transmitted through the reticle located at the image plane of the objective lens must be transferred to the PMT surface; this is the task of the condenser optics. The condenser optics consists of an air-spaced CaF_2 K10 doublet and three GE 151 fused quartz right angle prisms; together they image the exit pupil of the objective lens onto the PMT. Due to optical design difficulty, the CaF_2 - K10 doublet could not have a common cemented interface. GE 151 was used for the prisms as it has as high an ultraviolet transmittance as CaF_2 without the associated environmental problems, refractive index and dispersion not being overly significant parameters for the prisms.

The condenser optics must form a 0.28-inch diameter spot of reasonably uniform intensity on the PMT surface from all fields of view. The major concern is to have no "hot spots" over the field of view falling on the PMT as this could adversely affect the PMT output when the system was tracking a star at the "hot spot" object position. The major problem during the optical design stage was the proper positioning of the condenser lens in the beam among the three prisms in order to obtain the correct longitudinal and angular magnifications required to image the exit pupil of the objective lens onto the PMT surface with uniform illumination. Figure 4-22 is an optical schematic showing the condenser optics as well as the objective lens. In this preliminary design, the positive condenser element vignettes very slightly the extreme field of view; this vignetting (4% of the energy) eliminates possible total internal reflection at the rear surface of the positive condenser element.
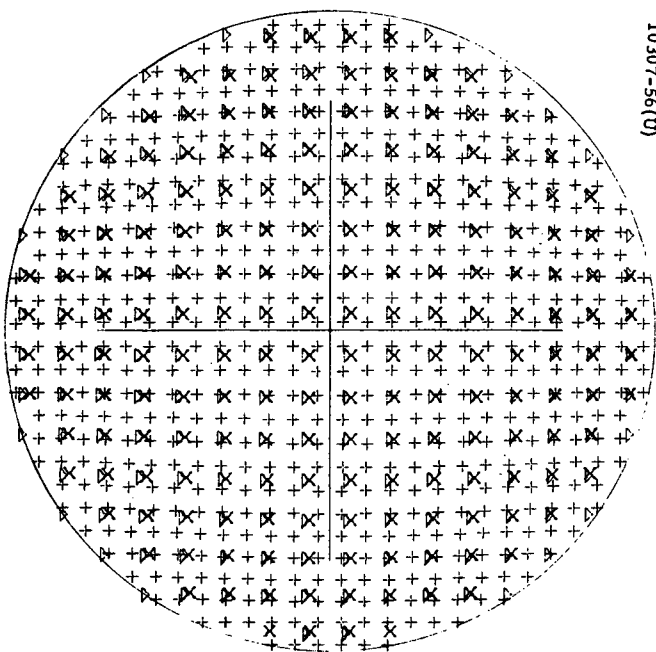
a) From On-Axis Object
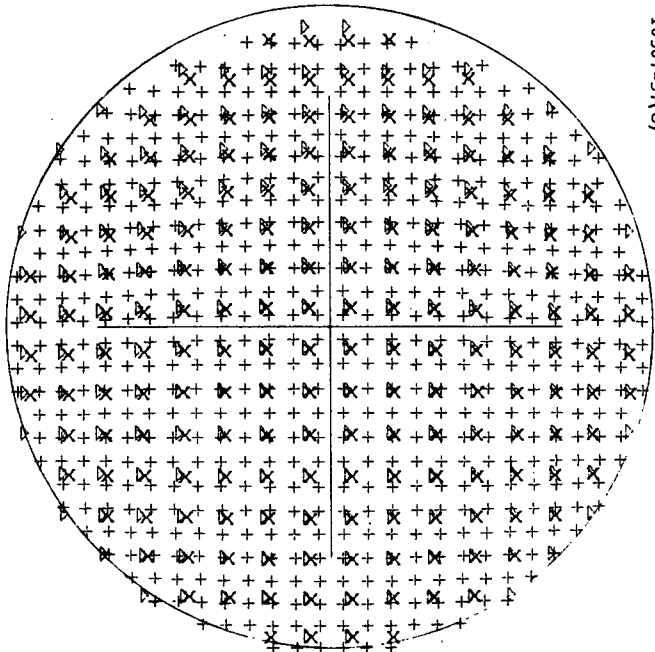
b) From 0.7 degree Off-Axis Object
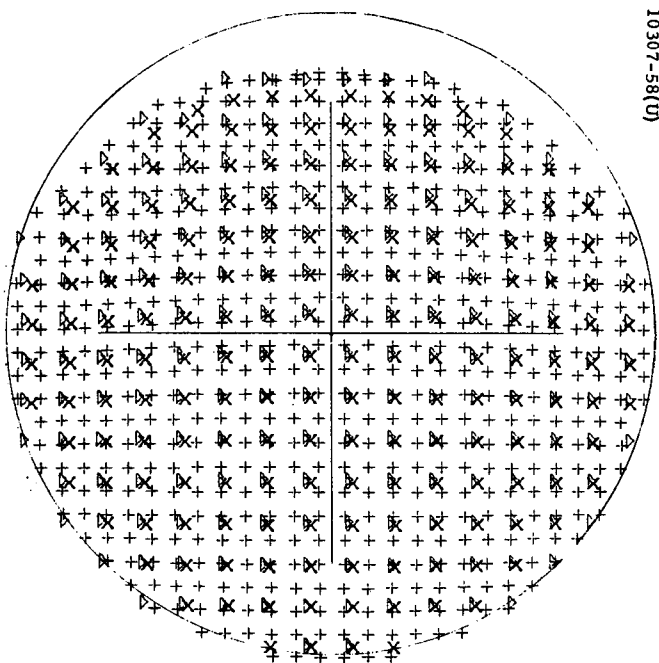
c) From 1.0 degree Off-Axis Object

Figure 4-23. PMT Illumination

Figures 4-23a, b, and c are spot diagrams of the beam striking the PMT surface from axial, 0.7° field of view, and full field object points, respectively. The crosses represent 4861Å light, the "X's" 3341Å light, and the triangles 7065Å light; the large circle shows the outline of the 0.28-inch diameter circle that should be evenly illuminated on the PMT surface. Each figure is centered at the center of this 0.28-inch circle so the three figures may be directly superimposed to give a composite view of the PMT illumination from three field points. It can be seen that the illumination on the PMT will be very uniform from all field points except for the slight vignetting effects visible at the top of the illuminated circle for the full field case.

Transmittance data for the condenser optics have been calculated in a manner analogous to that of the objective lens assuming no anti-reflection coatings. Figure 4-21 shows transmittance vs. wavelength for the condenser optics as well as for the entire sensor. Table 4-7 lists optical parameters pertinent to the condenser optics.

Additional Considerations

The star tracking system depends on locating the center of the star image as it is scanned over the reticle pattern by the nutation wedge. Any asymmetry in the star image will give rise to inaccuracies in the tracking system. The reticle pattern will be positioned so that the star image will always be scanned across a reticle slit in the sagittal plane of the image. For a centered optical system, the sagittal plane of an image always exhibits symmetry even in the presence of aberrations. However, manufacturing tolerances can give rise to an asymmetric image in the sagittal plane. Very tight manufacturing tolerances can be assigned to the lens radii, thicknesses, and glass quality to minimize these effects. However, the optical alignment of the elements must be very precise to insure no errors arise due to tilting or decentering of optical elements. Naturally, the smaller the theoretical image blur is, the easier it will be to detect errors due to alignment problems. It is therefore desirable to have a smaller theoretical blur size than the 0.45 mrad exhibited by the current design. It is felt that no significant improvement in image quality can be made using the current two-doublet design concept. However, use of additional optical elements, such as making each doublet a triplet, or splitting the CaF_2 - K10 bond, should result in a smaller image blur size.

TABLE 4-7. OPTICAL PARAMETERS OF CONDENSER OPTICS

Parameter	Value
Design Configuration	Air-space achromatic CaF_2 - KlO doublet with associated GE 151 quartz prisms
Overall length	1.75 inches
Magnification of entrance pupil	0.324
Numerical aperture	0.075
Spectral region	0.3 - 0.8 microns (See Figure 4-16)
Transmittance	(See Figure 4-21)
Uniformity of illumination	(See Figures 4-23a,b,c)

To explore this possibility a feasibility study, described in a later sub-section (see "Further Studies") was undertaken, exploring the possibility of achieving 0.1 mrad blur width.

The condenser optics currently consists primarily of an achromatic doublet. Achromatization of the spot size on the PMT, however, may not be necessary. A condenser system should therefore be designed using two GE 151 fused quartz lenses. This will eliminate any environmental problems associated with the CaF_2 element as well as greatly increase the transmittance below 0.35 microns of the condenser optics since the K10 element in the current design begins to absorb energy at this point (see Figures 4-16 and 4-20). A trade-off between image quality on the PMT surface and cost and environmental problems will determine which approach should be used for the final condenser optics.

The transmittance data presented in Figure 4-20 were calculated assuming uncoated optics. An investigation into the availability, cost and efficiency of antireflection coatings should be carried out. The decision as to the type of coatings, if any, to be used should be made as a result of a trade-off between cost and increase in transmittance.

CaF_2 is not the best optical material to use from a physical properties standpoint. It is, for example, susceptible to damage from thermal shock as well as having poor working properties in the optical shop. It is definitely felt, however, that CaF_2 must be used in the objective lens in order to obtain control over chromatic aberration. The concept of cementing the CaF_2 elements to the K10 elements arose primarily due to a desire to strengthen the CaF_2 element to protect it from vibrational shock. The coefficient of expansion of CaF_2 is significantly different from K10 (much more so than in a more-conventional "crown-flint" cemented doublet using standard optical glasses) so that a problem may arise due to variations in temperature. Although the operating environment will be thermally controlled to about $\pm 5°F$, it is definitely possible that the ambient temperature during, say, storage and transportation could range from $30°$ to $100°F$. This could pose a problem at the cemented CaF_2 - K10 inter-faces, causing the bond to break, or in a more severe case, cause the CaF_2 elements to shatter due to stresses built up in them arising from differences in thermal expansion of the two cemented materials. It is felt, however, that if temperature changes are gradual, no damage will occur to either the bond or

the CaF_2 elements. Thermal shock, however, could damage the bond and/or the CaF_2 element. An investigation should be undertaken to determine the thermal properties of the CaF_2 - K10 cemented doublets. It may turn out that it will not be possible to cement these two materials together. It is thus clear that the concept of using CaF_2 - K10 cemented optics should be heavily investigated in the future not only from thermal and vibrational considerations but also from an image quality standpoint.

Further Studies

A feasibility study was conducted in order to see how the telescope design could be changed in order to reach a goal of 0.1 mrad blur width while keeping the same focal length, f-number and spectral region as the baseline STARS optical design. The overall length of the system was to remain unchanged, but this was not possible as the distance between the lenses plays a significant role in correcting the aberrations of the system. However, the overall length of the system was kept under control as much as possible during the correction of the aberrations.

Performance vs Number of Elements

The performance (blur size) of the baseline design is limited by chromatic aberrations. The two achromatic cemented doublets of the original design have a blur width of approximately 0.45 mrad both on axis and at full field.

The first attempt to minimize the blur size was to uncement the two doublets and use the curvatures as additional degrees of freedom. This did not reduce the blur size much below that of the baseline design.

In order to reduce the sphero-chromatism significantly, an apochromatic cemented triplet was designed to replace the front doublet. An apochromatic lens is one which is designed to correct the axial chromatic aberration for three wavelengths. Again, as in the case of the doublets, the available materials suitable for color correction are very limited. GE 151 was chosen as the best suitable material to make up the third element of the triplet. The blur width containing 85% of the transmitted energy is approximately 0.25 mrad both on axis and at full field.

The next step in trying to reduce the blur width was to use two apochromatic cemented triplets. The extra element does little to improve the performance of the lens, and the resulting blur width is still approximately 0.25 mrad.

In all of the above mentioned cases, the performance of the lens is limited by both spherical aberration and chromatic aberration. Since it is extremely difficult to color correct an optical system over the extended visible spectrum (0.3 μm to 0.8 μm), spherical aberration correction had to be reduced in order to improve color correction.

In order to reduce the blur size, the surface closest to the aperture stop of the triplet-doublet combination could be made aspheric. It is therefore recommended that this design be investigated in future studies.

Since only a first level investigation was undertaken, no design was optimized to its fullest capability. It would therefore not be unreasonable to expect that the blur widths could probably be reduced to 0.2 mrad in the final design which, although still a factor of two over the desired goal of 0.1 mrad, is a considerable step in the right direction.
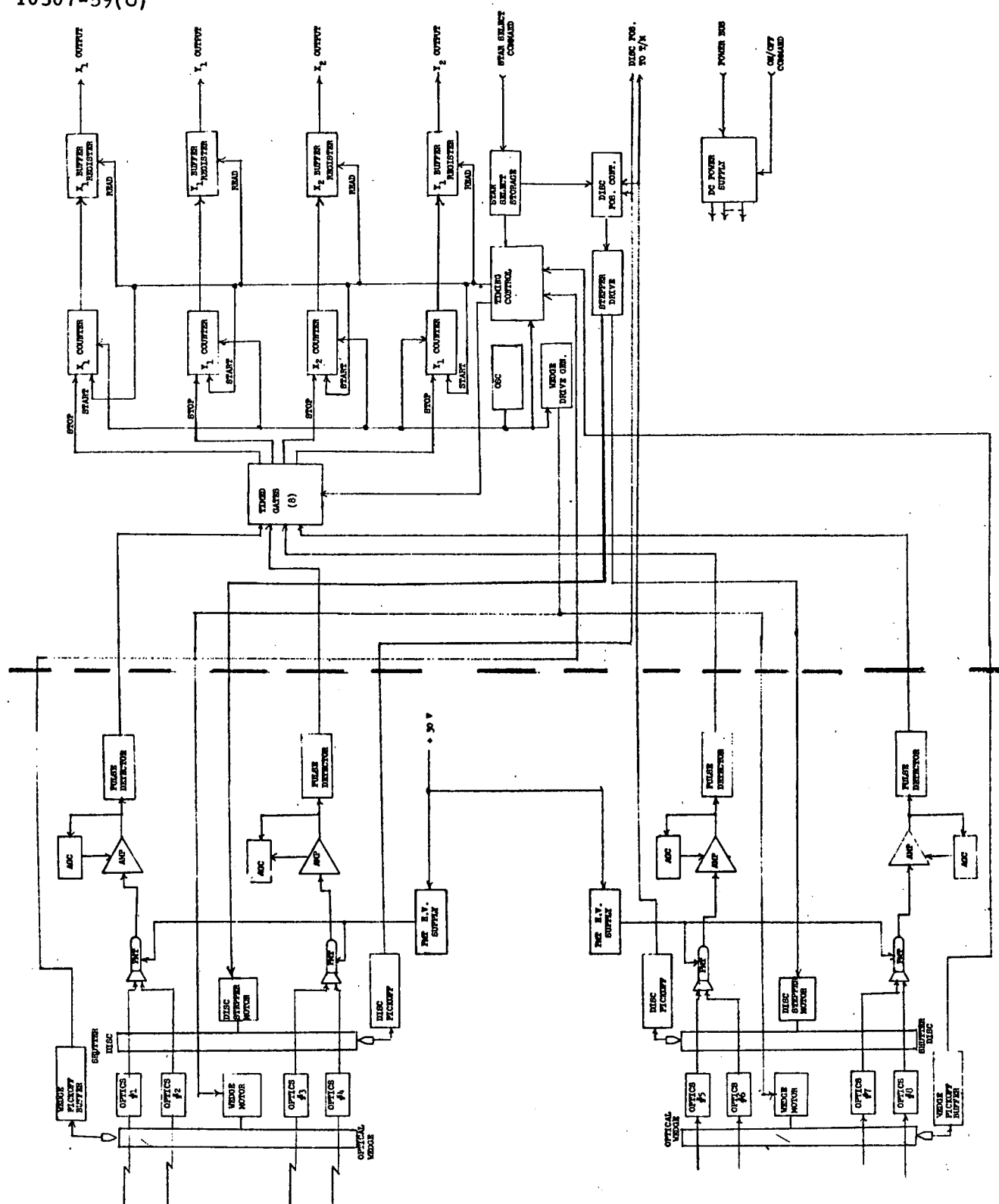
Figure 4-24. STARS Signal Processor and Electronics Block Diagram

4.5 Signal Processing

Introduction

The function of the STARS signal processor is to determine to the required accuracy the angular position of any two selected stars from the eight reference stars used. In the baseline design, each telescope has an "L" shaped reticle at its focal plane and utilizes a rotating optical wedge to nutate the star image across the reticle slit. A star image crossing a slit generates a pulse which is sensed by a detector (a photomultiplier tube). The timing of the pulse is dependent upon the angular position of the star in the telescope field-of-view.

The signal processing consists of measuring the period between a position reference pulse from a pick-off on the optical wedge and the time the image crosses the slit. This time period will be stored in an output register to make it available to the STARS tracker servo, while the next position measurement is being made. Four measurements per second are made, so an output register is updated every 250 milliseconds. A block diagram of the baseline processor design is shown in Figure 4-24, and the baseline design parameters are shown in Table 4-8. Table 4-9 summarizes the various error sources in signal processing along with an estimate of their magnitude.

TABLE 4-8. STARS SIGNAL PROCESSING PARAMETERS

Total number of stars	8
Number of stars used at any one time	2
Off axis tracking range	0.5°
Sampling rate	4/second
Output precision	13 Bit (1 Bit = 0.45 second)
Power Requirements	
On-Gimbal	10 Watts
Off-Gimbal	39 Watts

TABLE 4-9. STARS SIGNAL PROCESSING ERROR SOURCES

SOURCE	ESTIMATED RMS ERROR IN ARC SEC
Wedge Position	0.5
Wedge Position Pick-off	0.5
Processing Electronics	
Filter Delay Variation	1.0
Quantization Error	.14 to .10
Threshold Accuracy	0.1
Detection and Logic Delay	Negligible
Image Asymmetry	1.0

SIGNAL PROCESSING BASELINE DESIGN

The baseline STARS design utilizes an "L" shaped reticle at the focal plane of each of the eight telescopes. The corner of the "L" is located at the center of the field of view. The image is nutated by a rotating optical wedge in front of the telescope objective. For a star whose position is on the center line of the telescope, the center of the nutation circle will be at the intersection point of the two segments of the reticle. The phasing of the reticle crossing with respect to the wedge position will change as the position of the star changes with respect to the telescope pointing direction. This change will be measured to provide the X and Y angular information. Figure 4-25 shows the reticle pattern with the nutated image path and indicates the pulse phasing for a typical offset angle.

Each star produces two pulses per revolution of the nutation circle. With the geometry of the reticle as shown, and by limiting off axis pointing requirements to 0.5° both these pulses are confined within one-half of the nutation circle. The outputs of two telescopes can thus be combined into one photomultiplier tube (PMT) without ambiguity by having two "L"'s rotated 180° with respect to each other.

The output pulses from each PMT are processed in a pulse position detector. The output of the detectors is routed to the proper position counter by the timed gates and used as the stop pulse for the appropriate position counter. Four optical wedge position pulses are generated by the nutation wedge pick off coils and available as the start pulses for the position counters.

Each position counter counts the same basic clock that is divided down to generate the wedge motor drive signal. This clock has a frequency of 131,072 Hz. Since each counter has a capability of 13 bits (8192) its output will go from zero to full scale in one fourth a revolution of the wedge motor. After the count is completed it is shifted into the output storage register and available for use by the position servo.
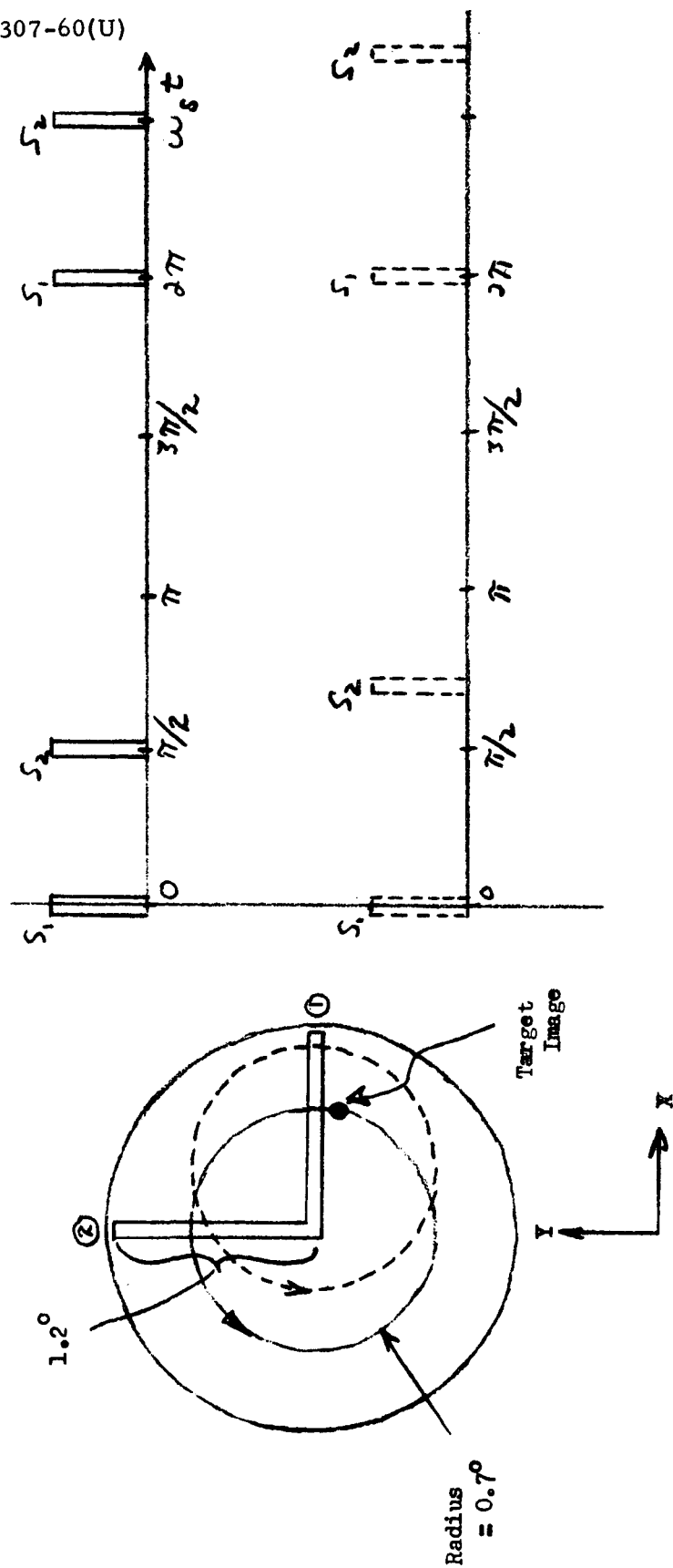
Figure 4-25. STARS Reticle Pattern and Modulation Technique

Star selection is accomplished by utilizing a rotating shutter in each of the four-sensor clusters. The shutter consists of a coded disc driven by a stepper motor with a position pick off and is used to select none, one, or any two telescopes in a cluster. The shutter performs two additional functions in that it keeps system noise down by blocking stray light from unused telescopes and protects the photomultiplier tubes from excessive current in the event that bright (sun, earth, spacecraft) sources scatter light into the telescope.

The output of the photomultiplier tube (PMT) is amplified in an automatic gain control (AGC) amplifier that keeps the peak amplitude of the signal at a constant value. In the case where both stars of interest happen to be routed to the same PMT, the AGC circuit sets the gain based on the amplitude of the pulse from the brighter of the two stars. The dynamic range of the electronics will be sufficient to enable it to detect the dimmer star within the required accuracy. The pairing of stars proposed has a maximum ratio of 5:1 in brightness between any two stars using the same PMT which will be well within the dynamic range of a system of the type proposed. The ratio will be further reduced since the baseline design reduces the effective entrance aperture for brighter stars.

The baseline design proposes to use a pulse time detector that consists of:

1. A filter that is as closely matched to the expected shape of the PMT output pulse as is practical.

2. A pulse detector that determines the presence or absence of the pulse using a fixed threshold level that is set to provide the desired ratio of false alarms and missed pulses.

3. A centroid detector that detects the center of the pulse by differentiating the output of the matched filter and detecting the zero crossing.

4. Logic that requires outputs from 2 & 3 above to produce an output.
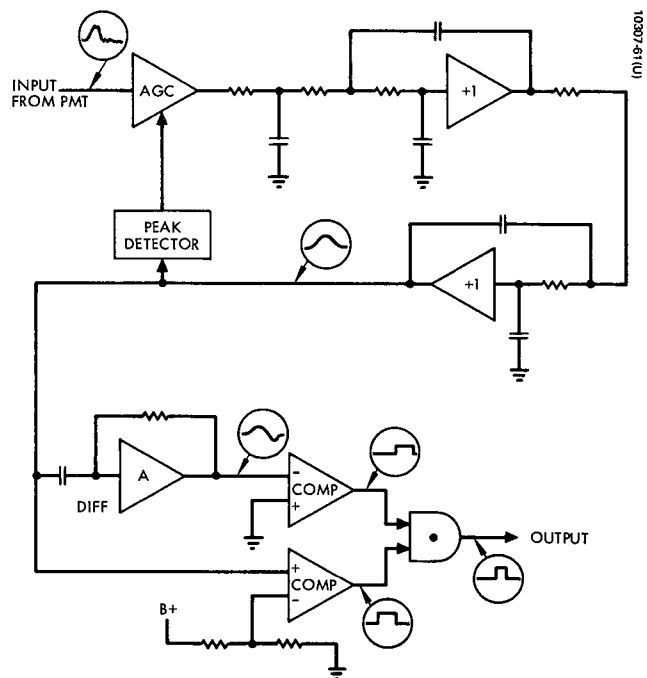
Figure 4-26. Baseline Detector Block Diagram

This detection which is shown in Figure 4-26 has been used successfully on previous programs and is not difficult to implement. Previous analysis as well as measured system performance has shown that its operation is close to optimum.

The output of the detector is a pulse that is delayed some fixed amount from the time the star image crosses the center of the reticle slit. By counting between the pulse generated by the pick-off on the nutation wedge and the detector output pulse a digital output is generated which relates to star angular position. Since the oscillator that generates the count is also divided down to generate the drive to the nutation wedge motor oscillator, frequency errors are eliminated.

The output is proportional to the sine of the nutation angle which introduces a known non-linearity. This produces an increase in sensitivity of about 40% at the edge of the field of view compared to that at the center, since the nutation angle is limited to $\pm 45^{\circ}$ to keep pulses from various telescopes separated.

Wedge Motor Drive

A critical element from the point of accuracy is the precision with which the nutation wedge can be driven. Critical to this are the motor characteristics and the motor drive electronics. The baseline design utilizes a hysteresis synchronous motor and requires a two-phase motor drive.

The wedge motor drive can be generated from a countdown from the digital clock. The stability and accuracy required to maintain the required angular position accuracy of the nutation wedge (0.018 degree) for a six pole motor are:

Phase error $\leq 0.33^{\circ}$

Relative Amplitude Variation ≤ 1.0 %

Waveforms of this accuracy can be generated by filtering a precision square wave, but at these low frequencies (12 Hz for a six-pole motor) passive filter mechanization becomes a problem.

The most efficient method (from a power consumption standpoint) is to use a passive LC filter whose output directly drives the wedge motor. A driver of this type can be highly efficient, the limit set only by the extent of the space and weight available. Because of the very low frequency, stable inductors and capacitors tend to become large.

Filtering at a high impedance level and using the filter output to operate a low-output impedance driver makes the filtering problem easier, at the expense of efficiency. This also allows the use of an active filter eliminating the need for inductors.

Most of the variation in phase will be due to unequal time delay between the sine and cosine filters as square waves can be generated with very high precision. Component accuracies and stabilities of better than 1% are needed to realize these requirements. This is not unreasonable and offers a potential practical solution.

An alternative to generating the sine and cosine drive waves by filtering square waves is to synthesize the sine and cosine functions by summing a series of rectangular waves (Walsh functions) to produce an acceptable drive function. A detailed discussion of this technique is provided in Section 4.6.3. This method is very attractive in that no phase-delay problems related to component stability are present. Digital circuits needed to generate the function to be summed are small and inexpensive, which increases the desirability of this approach.

A generator of this type would consist of digital microcircuits, and a summing operational amplifier and driver. Amplitude variations would tend to be the same for both sine and cosine drives as the electronics temperatures and supply voltages would be the same. Phase variations would be almost non-existent as the digital circuits would be many times more precise (time-wise) than needed.

The sine wave, whether generated by filtering a square wave or summing Walsh functions, can drive a Class "B" driver, which means that theoretical

efficiencies approaching 50% can be obtained. Assuming a practical efficiency of 35% to 40% is realizable, the drivers may have to dissipate up to eight watts per motor. Since these drivers are off gimbal the heat load from the drivers is not as serious as it would be if they were required to be on the gimbaled portion of the structure.

While careful design will be required, no fundamental problem exists in generating sine-cosine functions to drive the wedge motors.

Wedge Pick Off

Since any error in the wedge pick-off time is directly translated into an error in the system, extreme care must be used in its design. It is necessary to detect the wedge position directly because of the unknown phase error between the motor drive and the shaft. This is because the torque output depends on the phase angle and the torque required depends on the bearing friction. Since friction is difficult to control and can vary over life, it is necessary to detect the wedge position directly. A maximum of 0.5 arc sec (1 σ) has been assigned for the wedge pickoff error. The detector therefore must detect the position of the edge of the wedge to 5×10^{-4} inches, if a 4" diameter wedge is used.

The exact method of accomplishing this has not been chosen, but two approaches suggest themselves.

1. A high-quality magnetic tape head and a magnetic strip around the edge of the wedge.

2. An optical pick off.

A number of factors must be investigated, such as long-term stability, reliability, power consumption and weight, before a choice of pick off can be made.

It appears that it is quite feasible to obtain the accuracy required to keep the error below 0.5 arc sec within the existing state of the art.

Power Consumption

The on-gimbal power consumption is estimated at 10 watts, 5 watts per hemisphere. The breakdown is as follows:

Motor	4 Watts
High Voltage Supply	0.25 Watts
Electronics	0.75 Watts
	5.00 Watts

Since the motor requires 80% of the power, any reduction in motor drive will result in considerable power saving.

The off-gimbal estimate is as follows:

Motor Drives (8 Watts each)	16 Watts
Processing Electronics	5 Watts
	21 Watts
Power Converter Output:	31 Watts (includes on-gimbal)
Power Converter Input (63% eff.)	49 Watts
Power Dissipated in Converter	18 Watts
Power Dissipated in Off-Gimbal Elect.	39 Watts

Of the total 49 watts required for the system, 38 are required because of the wedge motor and drive requirements. Any reduction in the motor-power requirements will scale this downward on a one-to-one basis. The numbers used here are "conservative" and some improvement may be possible in an actual design.

SIGNAL-PROCESSOR ERRORS

The Signal-Processor Errors are considered for the purposes of this discussion to be those errors introduced by the processor due to imperfect mechanization. Fundamental sources of error, such as photon noise, were considered in the tracker systems analysis and that analysis will not be repeated here. It should be stated that the electronics after the PMT does not introduce any significant random noise into the signal.

The signal processing will introduce errors due to imperfections in mechanization. Some of the errors are caused by:

o   non-uniform wedge speed

o   wedge position pick-off jitter

o   optical imperfections

o   time delay variations in the processing filter

o   threshold variation

o   logic and detection delays

o   quantization error of the digitizing process

Wedge Speed

Errors introduced by variation in wedge speed can be analyzed from a position vs time standpoint.

Assuming:

o $\pm 0.5°$ off-axis tracking range

o $\pm 45°$ on nutation circle for $\pm 0.5°$ off axis

o   A sinusoidal speed variation

Based on the above assumptions which correspond to the baseline design, the angular position of the wedge must be within $\pm 0.018°$ of its ideal position at all times to keep the RMS error, due to the wedge speed variations under 0.5 arc sec of arc.

An analysis of the wedge motor (see Section 4.6.1) indicates that this is feasible, provided certain requirements are met in the motor-drive waveforms. Assuming a 6-pole two-phase motor for the baseline design, these turn out to be:

1. Phase differences of ≤ 0.33 degree

2. Current amplitude drives balanced to $\leq 1\%$ between phases.

The effect of the drive imperfections decreases as the square of the number of poles, so if an increase in the number of poles is feasible, then drive restrictions can be relaxed or the error reduced. The number of poles used is limited by practical considerations such as fabrication problems, tolerances, etc., and is not a theoretical limit. A preliminary analysis has been made by a designer experienced in design of special-purpose motors and the estimate is that within the size available, 8 poles is the practical limit (see Section 4.6.1) without increasing the diameter. Generation of the proper waveforms does not appear to be a serious problem, so an increase in the number of motor poles will be required only if an unforeseen problem develops.

Pulse Shape

A star image on the focal plane has a finite blur size which in the baseline design is less than or equal to 0.45 millirad. The reticle slit width is also approximately 0.45 millirad. Therefore, with a nutation radius of 0.7° and a wedge frequency of 4 RPS, the nominal pulse is approximately gaussian in shape with a width of 1.4 millisec. As a star angle varies and the reticle crossing angle changes, the effective slit width increases with a corresponding pulse width increase. The effective slit width will increase by a factor of sec θ where θ is the angle between the nutation center and a perpendicular to the reticle slit, a maximum of 45° in the baseline design. The maximum pulse width is thus 1.9 millisec.

The optimum filter processing bandwidth is a function of pulse width as well as pulse shape, however, measured performance on similar systems shows that performance degradation is minimal for bandwidth variation of up to $\pm$ 20% from nominal. The filter bandwidth will be chosen to be a compromise between the maximum and minimum pulse width.

Fron an error point of view, the more significant consideration is related to the pulse symmetry as star angles vary and the center of the nutation circle moves about on the focal plane. If perfect radial symmetry is assumed in the optics and the center of the nutation circle and the reticle exactly coincides with the (known) optical axis, no error is generated by optical aberrations. Any telescope design theoretically meets the axial symmetry requirements, however, imperfections in manufacture cause the image of a point source to be non-symmetrical, producing an output pulse that lacks symmetry about its centroid. If we were to use a true centroid detector the error produced would be equal to the difference between the center of the pulse for an ideal system and the centroid of the actual pulse.

To assess the effect of sagittal asymmetry change on system accuracy, an analysis was made to determine the error as a function of asymmetry under certain assumptions. A perfectly symmetrical pulse, $f(t)$, was postulated plus a small impulse $K \delta (t - T_\delta)$ located at some arbitrary time T_δ. The output of the processor, $e_o(t)$ is therefore

$$e_o(t) = \int_{-\infty}^{+\infty} F(\tau) \, h(t - \tau) \, d\tau$$

where $e_o(t)$ = output of filter

$F(\tau)$ = $f(\tau) + K \delta (\tau - T_\delta)$

$h(t)$ = impulse response of filter

The filter is followed by a detector that detects when the derivative of the filter output pulse is zero.

Section 4.6.2 provides the solution of the above expression for Δt where Δt is the variation in output time from the symmetrical case as a function of the assumed non-symmetry.

$$\Delta t = \frac{Kh'(T_D + T_\delta)}{\int_\infty^\infty F(\tau) h''(T_D + \tau) d\tau}$$

where

K = Impulse Amplitude

T_D = Detector output time for $K = 0$

Δ_t = Variation in output time from T_D for $K \neq 0$

T_δ = Time of occurrence of impulse

$h'(t) = \frac{d}{dt}[h(t)]$

this reduces to

$$\Delta t = \frac{\left(\begin{array}{l}\text{derivative of output at the time of detection due to} \\ \text{an impulse at time } T_\delta\end{array}\right)}{\left(\text{slope of derivative of the output at zero}\right)}$$

Reflected to the input and assuming a Gaussian filter impulse response with pulse width σ

$$\Delta t = \frac{K T_\delta \exp\left(\frac{-(T_D - T_\delta)^2}{2\sigma^2}\right)}{\text{second derivative of output at } T_D}$$

This can be interpreted to mean that the error will be proportional to the first moment change due to the asymmetry weighed by the impulse response of the filter since we use a Gaussian approximation in our baseline design. Actual estimation of this error source has been simplified by realizing that the error is bounded by the change in the centroid of the pulse, a worst case. Thus the manufacturing tolerance and alignment of the optical system will be specified to keep the centroid

of the blur within the allocated error estimate.

Quantization Errors

Star angular position is determined by measuring the time from wedge position reference pulses to pulses generated by star image crossings across appropriate slits. By referring to Figure 4-24, it can be seen that if the star angle, for example, varies ±0.5° in the x direction, the star slit (2) crossing will vary ±45° of a wedge revolution. The mechanization uses a counter starting at -45° with countdown to zero at 0° and then count up to +45° with the count terminated by the slit crossing pulse.

The pointing angle is given by

$$\theta_x = 0.707 \sin (wt - \pi/4) \text{ degree}$$

where

θ_x = point angle in the x-direction

w = 8π $^{rad}/sec$ wedge rate

Because of the sine relationship, a single count value varies as a function of pointing angle. Taking the derivation of θ_x,

$$\frac{d\theta_x}{dt} = 0.707 \, w \cos (wt - \frac{\pi}{4})$$

for $w = 0, \pi/2$

$$(\theta_x = 0.5°, + 0.5°)$$

$$\frac{d\theta_x}{dt} = 0.707 \, w \cos - \frac{\pi}{4}$$

$$= 0.707 \, w \cos + \frac{\pi}{4} = 0.5w$$

for $w_t = \pi/4$

$(\theta_x = 0)$ $\dfrac{d\theta_x}{dt} = 0.707w$

From this, it can be seen that a count at zero off axis angle corresponds to a larger angle ($\sqrt{2}$ larger) than a count at

the edge of the Field of view.

If a 13-bit counter is used, 8192 counts represent $\pi/2$ radian and each count represents $\dfrac{\pi/2}{8192}$ or 1.92×10^{-4} rad. of nutation circle rotation. At the center of the field of view one count corresponds to $(1.92 \times 10^{-4})\, 0.707$

$= 1.36 \times 10^{-4}$ degree (≈ 0.5 arc sec.) pointing angle. The peak error is 1/2

count and the RMS is $\dfrac{1}{\sqrt{3}}$ of the peak. Therefore, the quantization error at

the center of the field of view is $(0.5 \text{ arc sec}) \left(\tfrac{1}{2}\right) \left(\dfrac{1}{\sqrt{3}}\right) = 0.14$ sec (RMS).

At the edge of the field of view the sensitivity is 0.707 times

what it is at the center so the RMS quantization error varies between 0.14 arc

sec. and 0.10 arc sec.

Detector Delay

The baseline design calls for the output pulse from the PMT to be filtered

by a matched filter and the filtered output is peak detected. The filter

introduces a delay between the center of the PMT pulse and the peak detection

of the filter output of approximately one pulse width. An error is introduced

if a variation in the delay of the filter occurs due to filter characteristic sh

The output of the PMT is the convolution of the optical blur and the slit.

The optical blur in the sagittal plane is 0.45 milliradian and the slit

subtends 0.43 milliradians. This yields a pulse with the half-power points

representing about 0.45 $\sqrt{2}$ or about 0.63 mrad.

For an approximate determination of the required component stabilities,

assume that an active RC filter is used. If all time constants in a filter

of this type are multiplied by a constant, the filter response is changed by the same constant. Therefore, the stability of this filter can be examined by examining the stability of the individual RC time constants.

If $R' = R + \Delta R$

$C' = C + \Delta C$

$R'C' = RC + R \Delta C + C \Delta R + \Delta R \Delta C.$

If $\Delta R \ll R$, $\Delta C \ll C$

$$\frac{R'C'}{RC} = 1 + \frac{\Delta C}{C} + \frac{\Delta R}{R}$$

Where ΔR and ΔC are the variations in R & C respectively due to temperature or time.

If a 4 pole filter is used and if the R's and C's are not identical so the variations can be considered independent.

$$\frac{\Delta T_D}{T_D} = \left(\sum_{n=1}^{4} \left(\frac{\Delta C_n}{C_n} \right)^2 + \left(\frac{\Delta R_n}{R_n} \right)^2 \right)^{\frac{1}{2}}$$

where T_D = filter time delay.

If the error due to the source is to be limited to 1 sec (4.85×10^{-6} radians)

$$\frac{4.85 \times 10^{-6}}{.63 \times 10^{-3}} = 7.7 \times 10^{-3} \leq \left(\sum_{n=1}^{4} \left(\frac{\Delta C_n}{C_n} \right) + \left(\frac{\Delta R_n}{R_n} \right)^2 \right)^{\frac{1}{2}}$$

This allows a component value shift of $\pm 0.27\%$ for each component if all components change the same amount and the value changes are completely random in nature.

If, on the other hand, all capacitors change together and all resistors change together, the shift allowed per component is now $\pm$ 0.14%.

Considering the relatively limited temperature range during operation these stabilities are not unreasonable for precision components. Using 100 PPM/C$^{\circ}$ capacitors and 50 PPM/C$^{\circ}$ resistors this stability can be maintained over $\pm$ 10° C. These are quite reasonable temperature stability requirements.

Change in component value due to aging effects must also be held to within these tolerance limits since absolute accuracy is required over life. This may be a source of more difficulty than temperature variation.

Filter delay variation is considered to be the dominant error contribution in the detection process. Other potential error sources such as threshold variation or non-linearities can be held considerably below the error contributed by filter delay variation.

4.6   Supporting Analysis

4.6.1   STARS Wedge Motor Considerations

The STARS wedge motor rotates at 4 rev/sec and as presently configured, the inertia of the moving group is 0.45 lb-in^2 of which 80% is in the glass wedge. (See Table 4-10)

TABLE 4-10.   INERTIA OF STARS MOVING GROUP

Source	Moment of Inertia (lb-in^2)
Optical Wedge	0.37
Hub	0.0094
Shaft	0.00013
Motor	0.075
TOTAL	0.45453

Torque Perturbation due to Stator and Rotor Out-of-Round

To produce a torque perturbation mechanically, both rotor and stator must be out-of-round (not eccentric; eccentricity in any combination between stator, rotor and shaft produces much less torque perturbation than out-of-roundness).

The perturbation would be roughly sinusoidal at 2 cycles per revolution. At first and third quarter points, the rotor would be ahead of position by some angle, $\Delta\Theta$, and at second and fourth quarters it would lag by the same angle. Thus, in 90°, the position would change 2 $\Delta\Theta$ in a time interval of 1/16 sec. Assuming for the sake of simplicity, a constant acceleration over the interval

$$2 \Delta\Theta = \frac{\alpha t^2}{2} \quad \text{or} \quad \alpha = \frac{4\Delta\Theta}{t^2}$$

It is required that $\Delta\Theta \leq 0.018"$ or 10^{-4} πrad

then

4-81

$$\alpha = \frac{(4)(10^{-4})\pi}{(1/16)^2} = 0.1024 \ \pi^{rad}/sec^2$$

$$Torque = \alpha J = \frac{(0.1024\pi)(0.45)}{(32.2)(12)} = 3.74 \times 10^{-4} \ in\text{-}lb.$$

This is the largest permissible peak-to-center value of torque perturbation at twice per revolution with the given inertia.

From this point on, only a hysteresis-synchronous motor will be considered. PM "stepper" motors do not start reliably without complex commutation; DC and induction motors have speed control and slot-lock problems.

The general equation for torque is given by

$$T = 14.12 \times 10^{-8} \ (NI)^2 \ \frac{dP}{d\Theta}$$

where

NI = Ampere turn

P = Permeance

Θ = Angle between rotor and stator from reference

To determine the maximum $dP/d\Theta$ and thereby the maximum torque perturbation for stator and rotor out-of-round, the following quick calculation was made using simplifying assumptions:

Assume a stator and rotor out-of-round which is eliptical as shown in the Figure 4-27 (out of proportion) where

G is the gap

A is the nominal Rotor Radius

B is the nominal Stator Radius
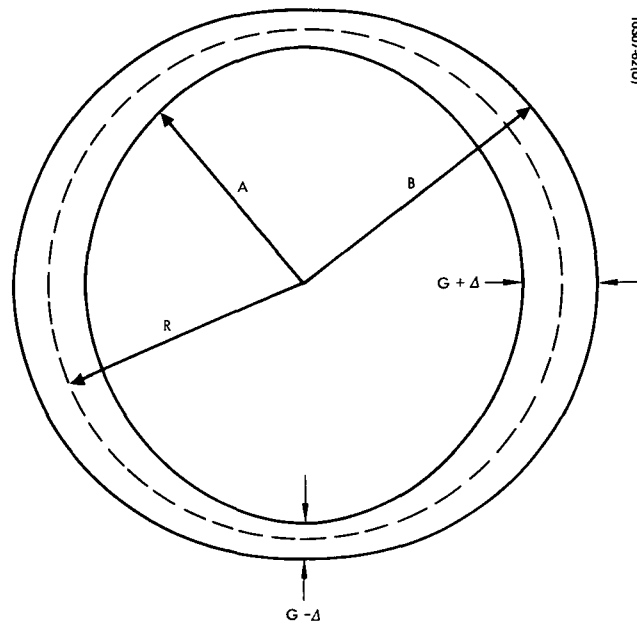
Figure 4-27. Stator/Rotor Ellipticity

The pitch radius of the gap (R) is

$$R = \frac{A+B}{2} \; .$$

the average gap (G) is

$$G = B\text{-}A \; .$$

If the out-of-round varies sinusoidally in the position shown, the gap varies according to the relationship

$$G(\theta) = G + \Delta \cos 2\, \phi \quad \text{where}$$

ϕ is defined as an angle on the stator from reference. The permeance, in (in^2/in) is given by

$$P = RL \int_0^{2\pi} \frac{d\phi}{G + \Delta \cos 2\phi}$$

where L is the axial length.

Integrating,

$$P_o = \frac{2\pi \; RL}{\sqrt{G^2 - \Delta^2}} \; .$$

The permeance with the rotor swung $90°$ from the position in Figure 4-27

is

$$P_{90°} = \frac{2\pi \; RL}{G} \; .$$

The change in permeance over $90°$ is therefore

$$\Delta P = \frac{2\pi RL}{\sqrt{G^2 - \Delta^2}} - \frac{2\pi \; RL}{G} \; .$$

In practice $G \gg \Delta$ and the numerator of the first term can be rewritten to give

$$\Delta P \approx \frac{2\pi \; RL}{G(1 - \frac{1}{2} \frac{\Delta^2}{G^2})} - \frac{2\pi \; RL}{G}$$

$$\Delta P \approx \frac{\pi RL \frac{\Delta^2}{G^2}}{G(1 - \frac{1}{2} \frac{\Delta^2}{G^2})} \approx \frac{\pi \; RL \; \Delta^2}{G^3}$$

This change in permeance occurs over $90°$ or $\pi/2$ radians

$$\frac{\Delta P}{\Delta \Theta} = \frac{2RL \; \Delta^2}{G^3}$$

Using this expression and the general equation for torque, a tabulation of motor parameters can be formulated to indicate performance for some realizable motors. Assume the following:

6-pole synchronous hysteresis motor.

Drive frequency equal to 12 hz.

Rotor material is "Simonds 81" cobalt steel drawn to 700° F after quenching.

Drive at 250 ampere/inch. At this drive, the flux density is 68 kiloline/in^2 and the energy is 0.27 joules/in^3-cycle.

Ring volume is 0.30 in^3 for all four designs; this produces a maximum useful torque of 0.34 in-lb. and a flux per pole of 8.7 kilolines.

The stator and rotor are both assumed to be 0.001" out of round.

TABLE 4-11.   ALTERNATE MOTOR CHARACTERISTICS

Characteristic	Motor			
	A	B	C	D
① Gap radius	0.75	1.5	1.5	1.5
② Axial length	1.00	0.500	1.000	1.000
③ Ring thickness	0.064	0.064	0.032	0.032
④. Radial gap	0.010	0.010	0.010	0.020
⑤ Gap-flux density kiloline/in^2	11.1	11.1	5.55	5.55
⑥ Ampere-turns to gap	34.7	34.7	17.3	34.7
⑦. $dP/d\theta$ for .001" out of round	0.1875	0.1875	0.3750	0.0469
⑧ $(\text{Ampturns})^2 \times \dfrac{dP}{d\theta}$	226	226	113	56.5
⑨. $14.12 \times 10^{-8} \times ⑧ = $ Torque Ripple	3.19×10^{-5}	3.19×10^{-5}	1.6×10^{-5}	0.8×10^{-5}
⑩ Ampere turns to ring	98	196	196	196
⑪. Total ampere turns per pole	133	231	213	231
⑫ Ampturns per inch circumference	169	147	136	147

From Table 4-11, it can be seen that for quite reasonable motor designs, Line ⑨ torque ripple, is less than the maximum limit by at least a factor of ten.

Torque perturbations from improper drive phasing

A hysteresis motor looks like a spring-mass system in rotating coordinates. The spring constant is approximately such that the motor puts out maximum torque when the rotor lags the rotating field by $20°$ electrical (=$6.67°$ mechanical for a 6-pole motor).

For the designs postulated, max torque = 0.34 in-lb., "spring constant" = 2.92 in-lb./radian. Natural resonant frequency against 0.45 lb-in^2 of inertia = 8 Hz.

If, in a 2-phase motor, one phase leads the other by some angle β, then twice per cycle of drive the rotor will be pushed forward, and twice per cycle i will be deaccelerated. This amounts to an AC torque component at 24 Hz for a 6-pole motor with a peak-to-center amplitude of $\frac{1}{2}$ x 2.92 or

Torque = 1.46 β sin wt

where w = 151 ^{rad}/sec (24 Hz)

$$\text{Acceleration} = \frac{\text{Torque}}{\text{Inertia}} = \frac{(32.2)(12)1.46\beta}{0.45} \text{ sin wt}$$

$$= 1250\beta \text{ sin wt}$$

Position is the double integral of the acceleration

$$\text{Position} = \iint 1250 \text{ sin wt} = \frac{1250\beta}{w^2} \text{ sin wt}$$

$$= -0.055\beta \text{ sin wt}$$

For the position error to never exceed 0.018°, β must never exceed $\frac{.018}{.055} \approx 0.33^{\circ}$.

This is a tight spec, but could be eased if necessary by lowering the "spring constant" (at the price of maximum torque) increasing the motor inertia, or having more poles on the motor and thus, increasing the drive frequency. The baseline design does not have room for more than 8 poles. However, if necessary the diameter could be increased. Twelve poles instead of six would ease the phasing requirements by a factor of four.

Torque perturbations from unequal amplitude of phases

If one phase has greater amplitude than the other by a factor $K > 1$, there will be two sorts of torque perturbation. First, twice per cycle the "spring constant" mentioned earlier will be increased by approximately K^2. The rotor would then see an AC component, at 24 Hz, of magnitude $\frac{1}{2}(K^2 - 1) \times$ (Average Load torque). If the load could be zero (reasonably good bearings) the phase angle of lag of the rotor is zero, and this perturbation becomes zero also.

The second perturbation is considered to be the more critical. At the quarter points of a drive cycle, the resultant field vector should be at $+45^{\circ}$ to the axes, whereas it actually makes an angle Arctan K. The angular error is Arctan $\frac{K-1}{K+1}$.

Since this occurs at twice drive frequency, it may be treated in the same manner as a phasing error

Thus,

$$\text{Arctan } \frac{K-1}{K+1} \leq 0.33^\circ$$

$$\frac{K-1}{K+1} \leq .00576$$

$$K-1 \leq .00576 \quad K+ \quad .00576$$

$$.99424K \leq 1.00576$$

$$K \leq 1.0115$$

The relative amplitudes of the 2 phases must therefore be within 1%. This requirement could also be loosened using the same methods that applied to phase angle error.

Wedge Motor Options

It is also possible to consider use of a sub-synchronous or "gear-tooth" motor (for example, the "slo-syn" manufactured by Superior Electric). This motor has 50 teeth on the rotor, hence, makes 1 revolution for 50 cycles of drive. It has 2 phases, and is available with 4 half-phases, that is, bifilar windings. As built by Superior Electric, it is not space-qualified, but Hughes Aircraft Company has rebuilt and rewound such motors using space-qualified materials throughout, and full engineering details are available.

The calculations for out-of-round apply to this type of motor without change. Since this motor would be driven at 200 Hz instead of 24, allowable phase shifts and amplitude variations would be greater by the factor $(\frac{200}{24})^2$ or 69.

This type of motor, torquing against a locked shaft, produces a sinusoidal torque with a DC average of zero. In order to start, it must bring the load to full speed within the time of one cycle. This means that for any one drive frequency and voltage, there exists a maximum value of inertia that the motor can start at all. What value this is could be readily determined by experiment.

Assumed Impulse Perturbating the Nominal Symmetrical Filter Input.

The output of the signal processor $e_o(t)$ is

$$e_o(t) = \int_{-\infty}^{\infty} f(\tau)\, h\,(t-\tau)\, d\tau$$

where

$f(t)$ is the filter input

$h(t)$ is the impulse response of the filter

Differentiating,

$$\frac{de_o}{dt} = \int_{-\infty}^{\infty} f(\tau)\, \frac{d}{dt} \left[h(t-\tau) \right]\, d\tau$$

If both the input function, $f(t)$ and the impulse response of the filter are assumed symmetrical

$$h(t) = h(-t) \qquad h'(t) = -h'\,(-t)$$

$$f(t) = f(-t)$$

Define T_D to be the time when $\dfrac{de_o}{dt} = 0$

then $\displaystyle\int_{-\infty}^{\infty} f(\tau) \frac{d}{dt} \left\lfloor h(T_D - \tau) \right\rfloor d\tau = 0$

Now, if the symmetrical $f(t)$ is perturbed by a Dirac delta function

$K \delta (t - T_\delta)$

So: $f(t) = F(t) + K \delta (T_\delta - t)$

where $F(t) = F(-t)$

$\dfrac{de_0}{dt} \displaystyle\int_{-\infty}^{\infty} \left\lfloor F(\tau) + K \delta (\tau - T) \right\rfloor \; h'(T_0 + \Delta t + \tau) = 0$

where Δt = change in detection time due to K

$\displaystyle\int_{-\infty}^{\infty} F(\tau) h' (T_D + \Delta t + \tau) \, d\tau + Kh' (T_D + T_\delta + \Delta t) = 0$

if $\Delta t \ll T_D$

$h' (T_0 + \tau + \Delta t) = h'(T_D + \tau) + \Delta t h''(T_D + \tau) + \ldots$

$\displaystyle\int_{-\infty}^{\infty} F(\tau) h' (T_D + \tau) d\tau + \Delta t \int_{-\infty}^{\infty} F(\tau) h''(T_D + \tau) \, d\tau$

$\qquad + Kh'(T_D + T_\delta) = 0$

since $F(t)$ is an even function

and $h'(T_D + \tau)$ is an odd function

$\displaystyle\int_{-\infty}^{\infty} F(\tau) h'(T_D + \tau) \, d\tau = 0$

and $\quad \Delta t = \dfrac{Kh'(T_D + T_\delta)}{\displaystyle\int_{-\infty}^{\infty} F(\tau) h''(T_D + \tau) d\tau}$

4.6.3 _____ Generation of Sine and Cosine Waves by Summing ___

Rectangular Waves. ___

It is necessary to generate sine and cosine waves with a very precisely

controlled phase relationship. One method of accomplishing this is to sum

a series of rectangular waves generated by logic circuits where timing is

provided by a precision clock.

A set of complete orthogonal rectangular function exists called Walsh

functions.[1] Any well-behaved function can be generated to any desired

degree of accuracy by summing the appropriate Walsh functions just as it

can by summing sines and cosines. Figure 4-28 shows a sine wave which is the

sum of eight Walsh functions, and Figure 4-29 shows the eight functions used and

their relative values to form the sine wave. The approximation can be made

better and better as more functions are used.

The advantage, as far as STARS is concerned, is that relative phase can

be controlled to a very high degree of accuracy and amplitude ratios will

tend to remain constant as both sine and cosine drives will be identical

circuits driven from the same power supply. The primary uncontrolled source

of amplitude variation will be the weighting and feedback resistors in the

summing amplifier, which can be made very stable.

This approach offers a practical method of generating precision, low-

frequency sine waves without requiring large stable reactive elements.

---

[1] HARMUTH, H.F., "Applications of Walsh Functions in Communications",
IEEE Spectrum, Vol. 6, No. 11, Nov. '69.
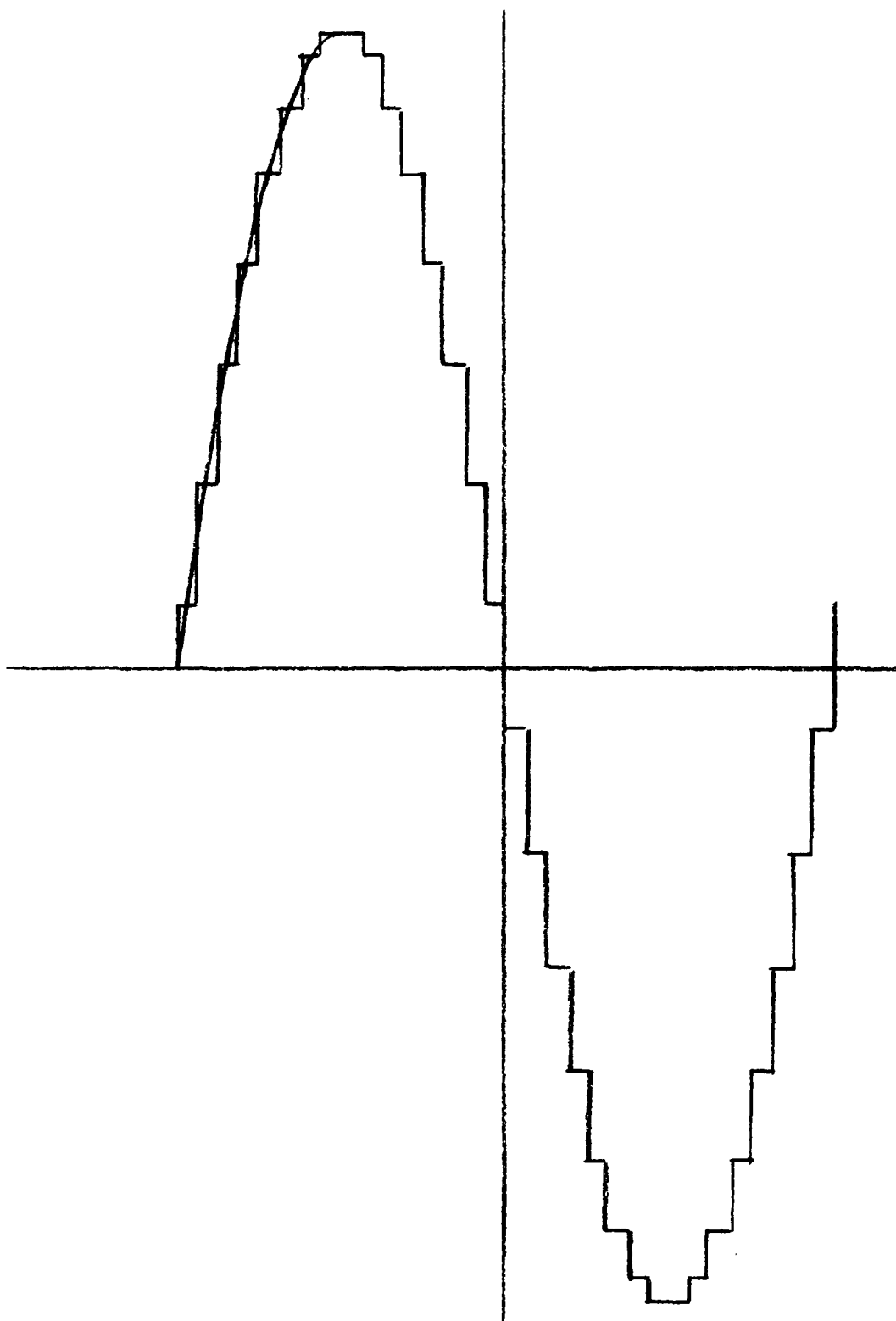
Figure 4-28. Sine Wave Approximation From Eight Walsh Functions

1.00

0.41

0.08

0.20

0.02

0.04

0.10

0.01

10307-64(U)
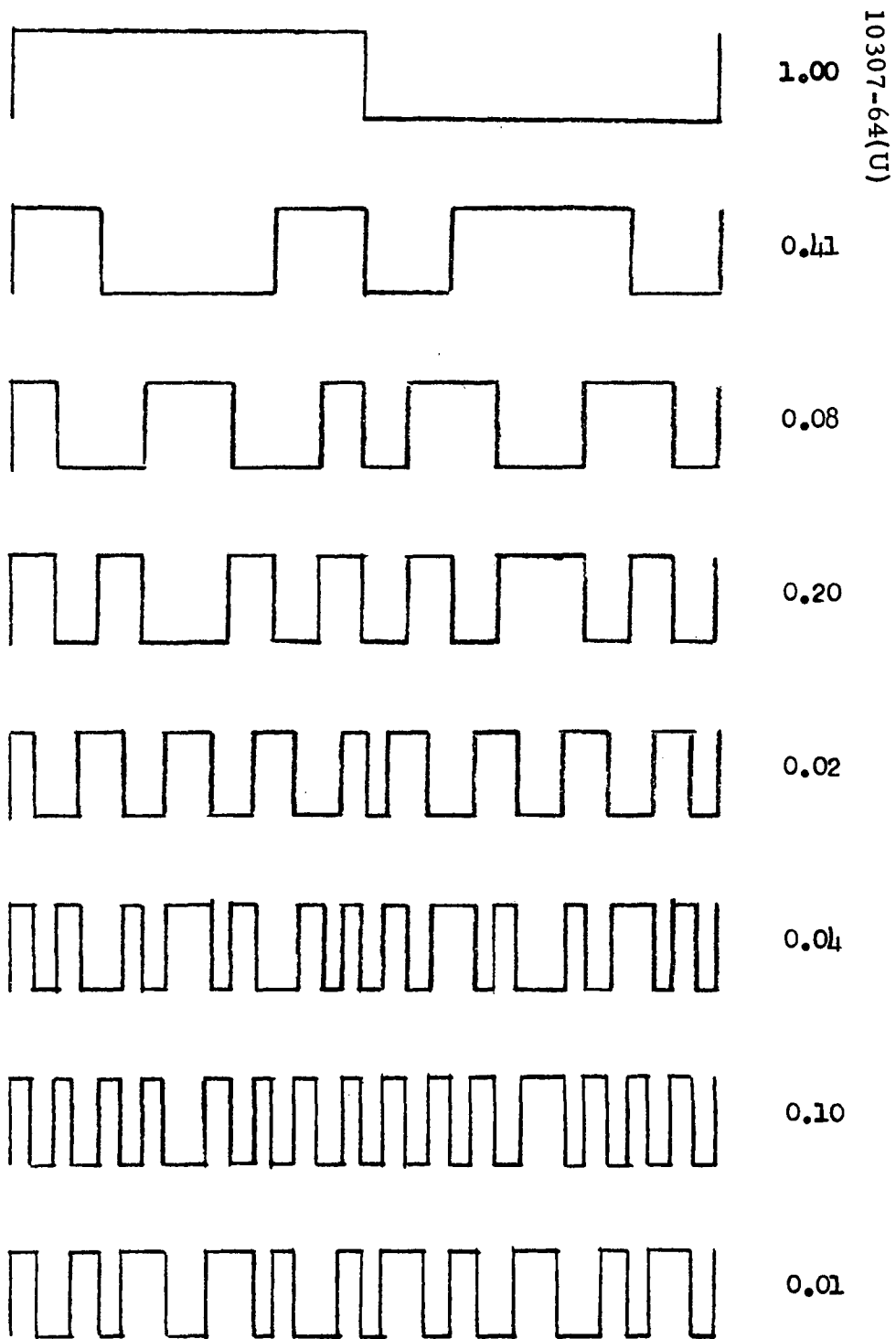
Figure 4-29. Walsh Functions Used to Generate Sine Wave

5. ERROR ANALYSIS

5.1 Summary

5.1.1 Objectives

The objectives of this task were to provide the basic framework for an error analysis, determine reasonable baseline values for the primary sources of error, calculate probable pointing errors for orbital operation and to study laboratory and in-orbit calibration techniques.

5.1.2 Methods

The error model chosen was to sum the errors from individual sources on each of six coordinate sets in the STARS system and transform them to vehicle roll, pitch and yaw axes. This was done independently for each of the four subsystems which comprise STARS: star sensors, gimbals, gimbal angle encoders and the STARS control system. Three classifications of error were used:

1. Bias. Systematic errors considered to be largely compensatable.

2. Thermal Distortion. Systematic errors due to temperature gradients caused by solar radiation.

3. Random. Non-systematic errors or uncertainties considered to be uncompensatable.

A check list of possible error sources was distributed to team members along with a preliminary error allocation of 8.72 microradians one-sigma to each of the four subsystems for a total root-sum-squared error of 17.45 microradians (0.001 degree) about the roll axis and about the pitch axis. The determinations of the actual errors were done by the design specialists for each subsystem and are described in the previous sections. The method of compilation of these errors and the results obtained are described in this section.

The influences of many input parameters were considered including:

- Offset tracking due to orbital inclination error.

- Signal-to-noise characteristics of the star trackers when tracking specific stars.

- Specific stars in use at a given point in orbit including right ascension and declination.

- Gimbal angles for given points in orbit.

- Solar radiation and eclipses.

- Acceleration errors during laboratory testing.

Errors were calculated at 45° increments about high noon orbits at the vernal equinox, summer solstice and November 6. These orbits cover a large portion of the sky so that the selection of STARS in use is complete and the range of sun angles is large.

The errors presented are one-sigma and include all significant sources of error so far identified within the STARS system. Errors which are not included are errors in spacecraft attitude control, errors in star ephemeris data and errors in spacecraft ephemeris data. Proposed tolerances for critical components were often used in the error analysis. Tolerances were considered to be two-sigma because the difficulty of meeting the tolerances and the likelyhood of special adjustments and selection of components would not result in standard distributions.

Bias and random errors were normally summed by the method of root-sum-squares which implies that the polarities of the errors being summed are independent. The predicted thermal distortion errors have known polarities so they are summed algebraically.

5.1.3   Results

The one-sigma errors for the STARS system in high-noon sun-synchronous orbit at three different times of year are listed in Tables 5.1-1, 5.1-2, and 5.1-3. The error is less than 0.001 degree about each axis at each of the 24 orbital conditions for which error was calculated except for the pitch axis at 315° at the vernal equinox. The root-mean-squared error for all axes and all orbits considered is less than 0.001 degree. The feasibility of developing a STARS system with typical errors less than 0.001 degree is thus demonstrated.

Each of the errors at a specific angle is the average of the errors resulting from the use of the two stars listed. This is a conservative approach. The bias and random contributions to errors are of approximately equal magnitude. This suggests that extensive calibration, such as might be accomplished in orbit using a method outlined in the calibration subsection, might further improve the accuracy potential of the STARS.

Thermal distortion due to sun load on the structure was not a major error contributor. Careful thermal insulation and thick sections in the beryllium structure limited error from this source to a maximum of 2.34 microradians. The major individual sources of error were in the star tracker signal processing and the dimensional stability of the gimbal structure. Peak instantaneous errors of up to 35 microradians in the polar axis servo due to stick-slip were disregarded because they would be filtered by the spacecraft inertia and attitude control system.

It is suggested that studies of microinch dimensional stability of beryllium structures similar to those proposed for STARS be added to the projected studies of the star sensors and the polar axis servo. A great deal of experimental effort has been devoted to beryllium and a literature search may locate pertinent data.

TABLE 5.1-1. STARS ERRORS AT VERNAL EQUINOX

PHI Orbiting Central Angle Degrees	Stars in Use (Star Number)		Errors in Microradians About		
	Brightest	Next Brightest	Roll	Pitch	Yaw
45	Arcturus 10	Cih 32	12.22	15.33	13.79
90 Sunrise	Cih 32	Phecda 69	13.41	16.76	13.78
135	Altair 13	Cih 32	14.93	16.37	11.72
180	Achernar 5	Altair 13	14.20	13.73	14.32
225	Achernar 5	Altair 13	13.74	12.85	14.78
270 Sunset	Achernar 5	Peacock 38	13.08	16.71	13.47
315	Arcturus 10	Peacock 38	13.59	18.06	12.30
360	Arcturus 10	Delta Vela 41	15.24	16.59	11.11
RMS for Orbit		Microradians	13.83	15.88	13.21
		Seconds of Arc	2.85	3.27	2.72
		Degrees X 1000	.79	.91	.76

TABLE 5.1-2. STARS ERRORS AT SUMMER SOLSTICE

PHI Orbiting Central Angle Degrees	Stars in Use (Star Number)		Errors in Microradians About		
	Brightest	Next Brightest	Roll	Pitch	Yaw
45	Arcturus 10	Altair 13	15.33	12.79	13.77
90 Sunrise	Arcturus 10	Cih 32	14.87	14.03	15.34
135	Rigel 4	Cih 32	15.42	16.86	13.33
180	Rigel 4	Achernar 5	15.14	17.10	11.39
225	Rigel 4	Achernar 5	13.05	15.37	13.76
270 Sunset	Achernar 5	Peacock 38	14.18	14.83	14.84
315	Achernar 5	Altair 13	14.52	16.34	12.95
360	Arcturus 10	Altair 13	16.40	13.55	12.66
RMS for Orbit		Microradians	14.89	15.23	13.55
		Seconds of Arc	3.07	3.14	2.79
		Degrees X 1000	.85	.87	.78

TABLE 5.1-3. STARS ERRORS ON NOVEMBER 6

PHI Orbiting Central Angle Degrees	Stars in Use (Star Number)		Errors in Microradians About		
	Brightest	Next Brightest	Roll	Pitch	Yaw
45	Rigel 4	Cih 32	15.10	12.51	14.84
90 Sunrise	Arcturus 10	Altair 13	12.65	15.40	15.56
135	Arcturus 10	Altair 13	13.55	16.68	14.61
180	Arcturus 10	Phecda 69	15.19	15.10	14.98
225	Arcturus 10	Peacock 38	14.96	14.11	13.91
270 Sunset	Rigel 4	Achernar 5	11.89	14.96	16.12
315	Rigel 4	Achernar 5	15.41	15.67	12.77
360	Rigel 4	Achernar 5	16.11	14.78	11.88
RMS for Orbit	Microradians		14.42	14.95	14.40
	Seconds of Arc		2.97	3.08	2.97
	Degrees X 1000		.83	.86	.82

5.2 Error Model and Definitions

5.2.1 Error Model Equations

Errors originating in the STARS subsystems are the only errors considered in this error analysis. The four major subsystems considered are:

STARS Subsystem	Symbols for Errors About:		
	Roll Axis	Pitch Axis	Yaw Axis
Star Sensor Cluster Assemblies	ERS	EPS	EYS
STARS Gimbals	ERG	EPG	EYG
Gimbal Angle Encoders	ERE	EPE	EYE
STARS Control System	ERC	EPC	EYC

If the actual errors from each source were known, such as by measurement, they would be summed algebraically. The errors to be used are estimates of one-sigma deviations and are considered independent of each other with respect to polarity, thus they will be root-sum-squared.

$$ER = (ERS^2 + ERG^2 + ERE^2 + ERC^2)^{1/2}$$

$$EP = (EPS^2 + EPG^2 + EPE^2 + EPC^2)^{1/2}$$

$$EY = (EYS^2 + EYG^2 + EYE^2 + EYC^2)^{1/2}$$

One exception to this practice is the thermal distortion errors. As estimated, these errors have a known polarity and are therefore kept separate and are added algebraically.

The basic form used for the compilation of errors from each subsystem is

	Type of Error
$E(a,b) = E(a,b)B$	Bias (mean error)
$+ E(a,b)R$	Radiation Sensitive (thermal distortion)
$+ E(a,b)U$	Uncertainty (non-systematic on random)

Where (a,b) identifies the axis and subsystem respectively.

Bias errors are systematic errors which could be compensated if sufficient computer capability could be provided. The thermal radiation sensitive errors are also systematic and can be compensated if suitable measurements can be provided. The uncertainty errors are not reasonably correlated with known input variables except in stochastic terms and are thus not compensatable.

Each of the above listed types of error include sensitivities to system inputs such as gimbal angles, offset tracking angles, sun angle, temperature, time and, during testing: the direction of gravity, atmospheric pressure, and the optical effects of the ambient atmosphere.

Errors which are oscillatory and have short periods (e.g.,1 second) are herein considered non-systematic. Errors due to quantization are also considered to be non-systematic. The RMS values of non-systematic errors are used in the compilations except where they can be shown to have lower effective values (e.g., smoothing due to high moments of inertia of spacecraft).

The three types of errors are assumed to be independent and are root-sum-squared.

5.2.2   Definitions

The following definitions are used in the error analysis. Many commonly understood terms are not herein defined. The astronomical definitions found in Appendix 2 of Reference 1 have generally been used. Other terms are defined later in the text as appropriate.

Actual Pointing: The attitude of the spacecraft axes at a given point in time, geographical location and altitude of the spacecraft.

Perfect Pointing: The error-free attitude of the spacecraft axes which corresponds to the given point in time, geographical location and altitude of the spacecraft.

Error in Pointing = Actual pointing - perfect pointing (or actual = perfect + error). This definition establishes the polarity of an error.

Spacecraft Axes: The roll, pitch and yaw axes defined by the mounting base of the STARS.

Gimbal Axes: The directions of the inner and outer gimbal axes of the STARS which minimize the squares of the errors in the respective instantaneous axes of rotation.

Right Ascension: The angle measured eastward along the celestial equator from the vernal equinox to the great circle passing through the celestial poles and a body (sun, star, spacecraft, etc.).

Declination: The angular distance north or south of the celestial equator to a body, measured along the great circle passing through the celestial poles and the body. Positive is north, negative is south.

Celestial Sphere: The apparent sphere of the sky; a sphere of large radius centered on the observer.

Celestial Equator: The circle of intersection of the celestial sphere with the plane of the earth's equator.

Celestial Poles: Intersections of the earth's polar (rotational) axis with the celestial sphere.

Vernal Equinox: The point on the celestial sphere where the sun crosses the celestial equator passing from south to north.

Mean Sun: An imaginary sun that moves eastward with uniform angular velocity along the celestial equator, completing one circuit of the sky with respect to the vernal equinox in the same time as the true sun.

Ecliptic: The apparent annual path of the sun on the celestial sphere.

Right-Hand Rule: If the thumb of the right hand represents the positive direction of an axis or vector, then the natural curl of the fingers represents the direction of positive angular rate or displacement about the axis or vector. In a right-handed coordinate set of three axes, positive rotation per the right-hand rule about the first named axis produces displacement from the second named axis to the third named axis through the shortest arc. Example: orthogonal coordinate set with axes X, Y, Z. Rotation about X of a line in the Y, Z plane from Y to Z is +90 degrees or -270 degrees. A right-handed screw driven in the direction of X carries Y into Z.

Orthogonal: Mutually perpendicular.

Precession: The motion of the angular momentum vector of a rotating body in response to a disturbing torque. The angular momentum vector rotates in a direction so as to become parallel with the disturbing torque vector, per the expression $T = \omega \times H$ where T is the torque vector, ω is the precession vector, H is the angular momentum vector and X indicates a vector cross product.

TABLE 5.2-1. STAR TRACKER DESIGNATIONS

Tracker No.	Star Name	Irrad.*	Star No.	Right Ascension **	Declination **
1	CIH	2.2	32	13.69	60.54
2	PHECDA	1.1	69	178.04	53.87
3	ARCTURUS	5.3	10	213.55	19.35
4	ALTAIR	4.3	13	297.31	8.78
5	ACHERNAR	8.0	5	24.13	-57.40
6	RIGEL	9.0	4	78.25	- 8.24
7	DELTA VELA	1.8	41	130.96	-54.59
8	PEACOCK	2.0	38	305.78	-56.84

* 10^{-13} w/cm^2

** degrees in equatorial coordinates

Average or Mean:
$$\overline{X} \equiv \sum_{n=1}^{N} X_n/N$$

Root-Sum-Squared (RSS):
$$X\ RSS \equiv \left[\sum_{n=1}^{N} (X_n)^2 \right]^{1/2}$$

Root-Mean-Squared (RMS):
$$X\ RMS \equiv \left[\sum_{n=1}^{N} (X_n)^2/N \right]^{1/2}$$

Standard Deviation or One Sigma:

$$X\ SIG \equiv \left[\sum_{n=1}^{N} (X - \overline{X})^2/(N - 1) \right]^{1/2}$$

Systematic Error: An error or a part of an error that occurs as a reasonably definable function of an input variable such that the knowledge of the input variable permits calculation of the expected error magnitude and direction. The systematic part of an error can be compensated so as to reduce its effect to zero.

Non-Systematic Error: An error or part of an error that is not reasonably correlated with the known input variables except in stochastic terms. Non-systematic error is also referred to as random error and uncertainty.

Residual Error: The error remaining after compensation for a systematic error. If the compensation is perfect the residual error is non-systematic.

Star Tracker: One of the eight telescopes in the two star sensor clusters, including the data processing for that tracker which is done on-gimbal. A star tracker provides outputs which "track" (indicate the position of the line of sight of) its assigned star (see Table 5.2-1) within the field of view.

Offset Tracking Angle: The angle between a star tracker optical axis and the line of sight to the star. The offset tracking angle is measured about two axes: angle DD, a difference in declination; and angle DA, measured in a plane perpendicular to the plane of DD and through the star line of sight.

5.2.3 Symbols

Axes

E	the vernal equinox (the direction of the sun from the earth at the vernal equinox)
N	the spin axis of the earth, positive is towards the North Pole and the star Polaris
IA	inner gimbal axis, STARS, nominally parallel to the polar axis N and in the opposite direction from N
OA	outer gimbal axis, STARS, nominally parallel to the pitch axis PA and in the direction of PA
RA	roll axis, spacecraft, roll to the right is positive
PA	pitch axis, spacecraft, pitch up is positive
YA	yaw axis, spacecraft, yaw right is positive
X4	an axis through the spacecraft in the plane of the spacecraft orbit, perpendicular to the perfect vertical axis Z4, and in the direction of the spacecraft motion (coordinate set 4)
Y4	an axis through the spacecraft, perpendicular to axis X4, perpendicular to axis Z4, and forming a right-hand set with axes X4 and Z4 (coordinate set 4)
Z4	an axis through the spacecraft which defines the "perfect" vertical and points away from the earth (coordinate set 4)
X(d) Y(d) Z(d)	orthogonal right-hand coordinate sets or frames of reference used in the error analysis. X4, Y4, and Z4 are an example. See subsection "Coordinates".

Angles

Actual	Perfect	Error	
I	IO	EI	angular displacement of the inner gimbal (with sensor clusters) with respect to the outer gimbal
$\emptyset$	$\emptyset$0	E$\emptyset$	angular displacement of the outer gimbal with respect to the base
A(e)	A(e)0	EA(e)	right ascension of a star tracker pointing axis with respect to the inner gimbal
D(e)	D(e)0	ED(e)	declination of a star tracker pointing axis with respect to the inner gimbal
DA(e)	DA(e)0	EDA(e)	Offset tracking angle between a star tracker optical axis and the line of sight to the star, measured perpendicular to declination.
DD(e)	DD(e)0	EDD(e)	Offset tracking angle in declination from a star tracker optical axis to the line of sight to the star.
CLN	CLN0	ECLN	inclination of the spacecraft orbit to the equatorial plane
R	R0	ER	spacecraft roll with respect to orbiting coordinates X4, Y4, Z4
P	P0	EP	spacecraft pitch with respect to orbiting coordinates X4, Y4, Z4
Y	Y0	EY	spacecraft yaw with respect to orbiting coordinates X4, Y4, Z4
LAT			latitude of the spacecraft
LON			longitude of the spacecraft
OBL			obliquity of the earth's orbit with respect to the ecliptic plane
PHI			orbiting central angle between the spacecraft and the ascending node

Angles

<u>Actual</u>   <u>Perfect</u>   <u>Error</u>

                              E(a)   error in angle (a) or about axis (a)

                              E(a,b)   error in angle (a) or about axis (a)
                                        originating in subsystem (b)

                              E(a,b,c) error in angle (a) or about axis (a)
                                        originating in subsystem (b) and of
                                        error type (c)

Subscripts

(a) R, P, Y, X(d), Y(d), Z(d), I, ϕ, A(e), D(e)   see "Axes" and "Angles"

(b) <u>Subscript</u>   <u>Subsystem</u>

        T   <u>T</u>otal for STARS System
        C   STARS <u>c</u>ontrol
        E   gimbal angle <u>e</u>ncoders
        G   <u>g</u>imbals and base
        S   <u>s</u>tar trackers

(c) <u>Subscript</u>   <u>Type of Error</u>

        B   <u>b</u>ias (mean error)
        R   thermal-<u>r</u>adiation-sensitive
        U   non-systematic (random, <u>u</u>ncertain)

(d) <u>Subscript</u>   <u>Coordinate Set</u>

        0   sun centered
        1   earth-moon barycenter
        2   earth-centered
        3   precessing frame
        4   spacecraft "perfect" frame
        5   spacecraft axes (STARS base)
        6   outer gimbal
        7   outer gimbal (inclined)
        8   inner gimbal
        9   star tracker

5

(e) Subscript   Description

    1 thru 8   star tracker numbers, see Table 5.2-1.

Angular Rates

    ω_c spacecraft in orbit, d PHI/dt

    ω_e earth's rate of rotation about its poles

    ω_M Moon's rate of rotation about the earth

    ω_p Precession rate of the spacecraft orbit

    ω_y Earth's rate of rotation about the sun

Angular Units

    deg, ^{o} degrees

    rad   radians

    μ rad   microradians

    arc sec, "   arc seconds

Temperature   T(g) where subscript (g) is a point at which
the temperature is being considered. See
"Thermal Distortion".

5.2.4   Coordinates

5.2.4.1 Orbital Coordinates

The feasibility of the STARS concept is to be determined in a con-
figuration suited to sun-synchronous orbits. High noon and twilight orbits as
shown in Figure 5.2-1 are the most likely applications. The obliquity of
the earth's axis is denoted as OBL and the inclination of the satellite orbit
is denoted as CLN. For the present study we are considering the high noon
orbits a and c. Orbit a moves north in the sun while orbit c moves south in
the sun. The error analysis uses orbit c wherein the sun shines on the front
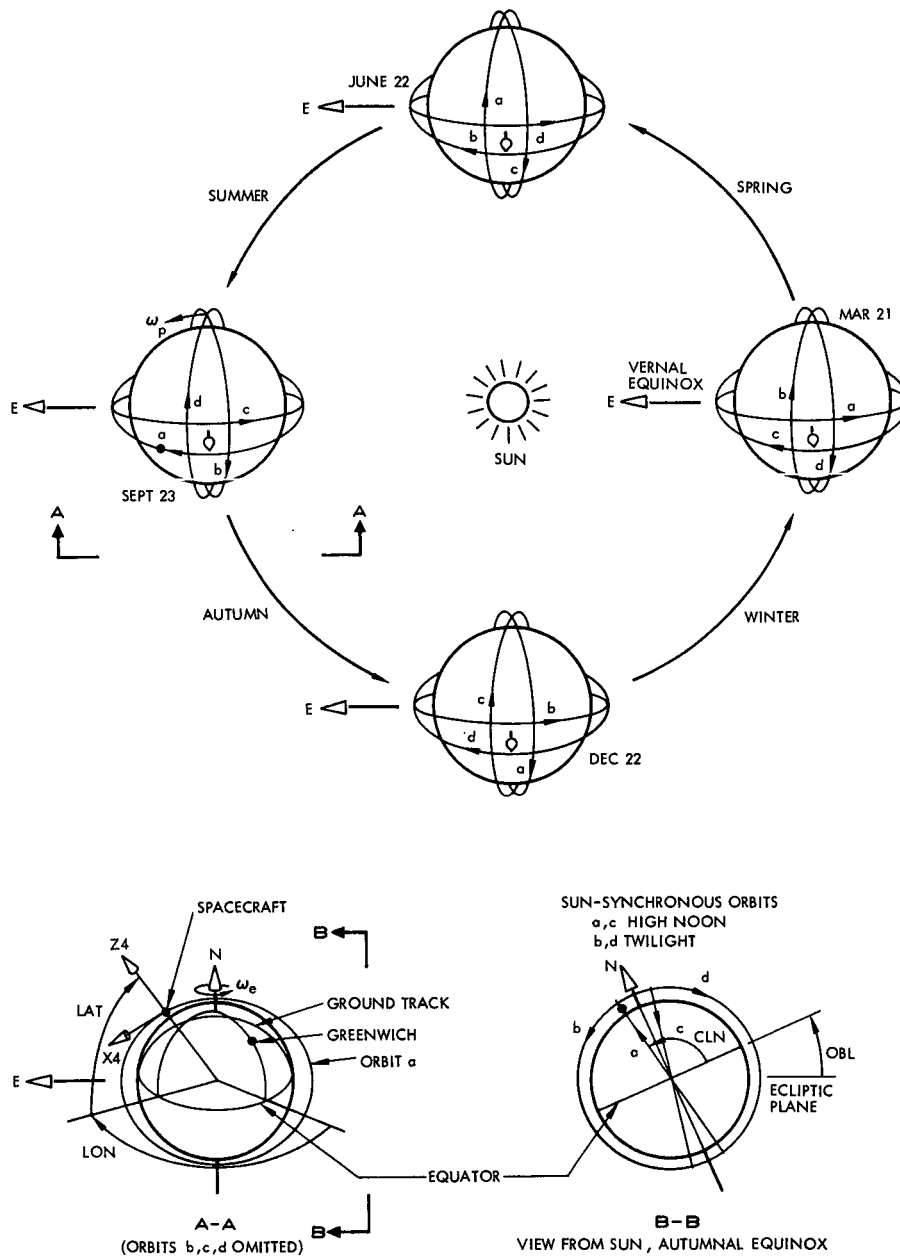face of the STARS as it has been depicted in the layouts.

Figure 5.2-1. Sun-Synchronous Spacecraft Orbits

Figure 5.2-2 shows the spacecraft orbit with respect to the ecliptic plane. Sets of coordinates have been assigned starting with a sun-centered reference plane. The X-axis points to the vernal equinox and the Z-axis is perpendicular to the ecliptic plane. This is assumed to be an inertial reference frame and deviations, such as precession of the equinox, may be handled as perturbations.

All the coordinate sets used herein are orthogonal X, Y, Z sets where rotation of the X-axis towards the Y-axis defines the Z-axis per the right-hand rule. Each set is assigned a subscript which is written on the same line as the axis to facilitate printing and use in computer programs. Thus the sun-centered coordinate set is X0, Y0, Z0, called set 0.

Coordinate set 1 has its origin at the center of mass of the earth and the moon. The orientation of this frame is assumed to be constant and the same as set 0. The parallax of any star to be used by the STARS system will either be too small to cause a significant error or the parallax can be included in the ephemeris data along with such effects as the aberration in apparent star position due to earth's velocity versus the speed of the light from the star.

Coordinate set 2 is an earth-centered frame of reference which is rotated about the vernal equinox from set 1 by the amount of the obliquity of the earth's axis to the ecliptic plane, PBL, so that the Z2 axis is coincident with the earth's spin axis. The earth's spin axis and the vernal equinox are common to many of the frames of reference and are denoted as N (for north) and E (for equinox) respectively.

At the top in **Figure 5.2-2 are shown the earth-centered coordinates, set 2,** the precessing frame, set 3, and the orbiting coordinates, set 4. The origin of the precessing frame coincides with the center of the earth and the Z3 axis is tilted from Z2 (the earth's axis) by the inclination, CLN, of the spacecraft orbit. Because we are interested in sun-synchronous orbits the spacecraft rotation will be retrograde and the inclination angle will be $\pi/2 <$ CLN $< \pi$. For a 500-mile altitude sun-synchronous orbit CLN is about 98 degrees. Axis Z3 will precess about N, as shown by the dashed line, at a rate ω_p of 1 revolution per year.
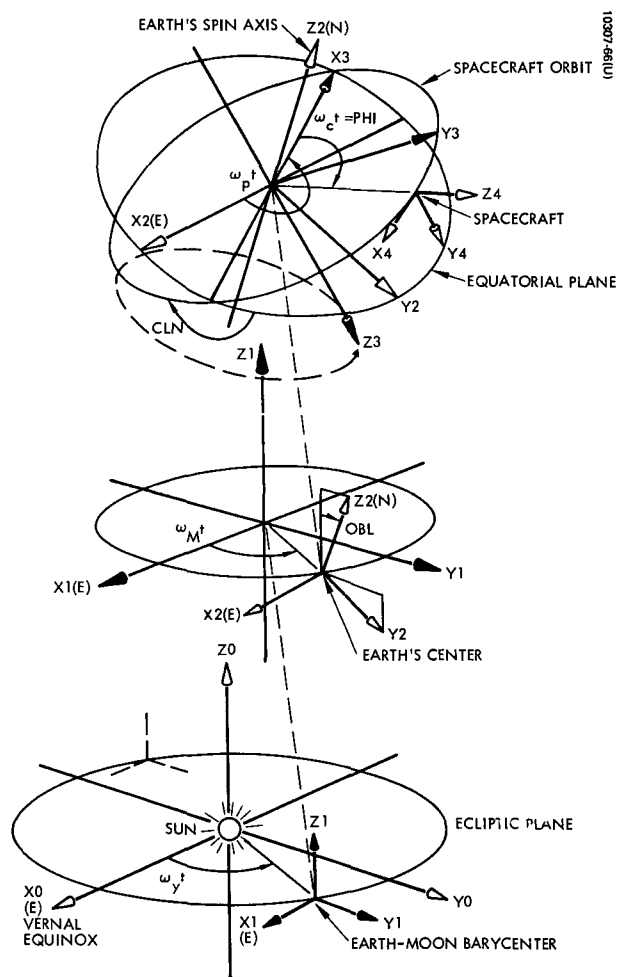
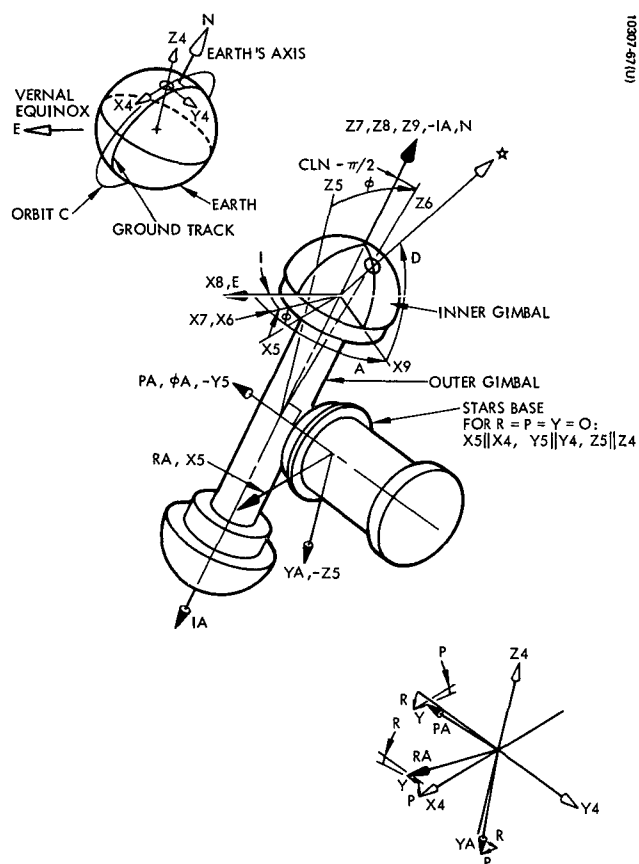Figure 5.2-2. Spacecraft Coordinates With Respect to Earth's Orbit

Figure 5.2-3. STARS Coordinate

Coordinate set 4 is the "perfect" frame of reference for the space-craft in its actual orbit such that Z4 is the "perfect" vertical, X4 and Y4 are in the local horizontal plane, and X4 is in the orbit plane and points in the direction of motion in the orbit. The projection of X4 on the surface of the earth approximates the ground track but must be corrected for the relative rotational velocity of the earth, ω_e, the precession of the spacecraft orbit, ω_p, and the spacecraft rotation, ω_c.

For the purposes of the error analysis the "perfect" vertical direction will be assumed to pass through the earth's center. The perfect vertical could also point along the local perpendicular to: the best-fitting mathematical ellipsoid, the dynamic geoid or the niveau ellipsoid, or it could point along the local gravity vector which takes into account the earth's local gravitational anomalies. The specific vertical direction is to be accounted for by the ephemeris data and included in the commands for inner gimbal angle, outer gimbal angle, and the offset tracking angle for each star.

5.2.4.2   Spacecraft and STARS Coordinates

Figure 5.2-3 shows the relationship of the spacecraft roll, pitch and yaw axes, set 5, to the set 4 reference frame. For all cases to be con-sidered, the "perfect" roll, pitch and yaw angles R0, P0, and Y0 will be zero, thus the error in roll, ER = R - R0, reduces to ER = R. This means that any resultant roll, pitch or yaw angle other than zero is an error.

Rotation about an axis is considered positive per the right-hand rule. Thus:

- roll to the right is positive
- pitch up is positive
- yaw right is positive

Rotation will be considered in the order X,Y,Z (or R, P, Y) so that the pointing of the yaw axis is affected only by roll and pitch deflections as shown at the lower right in Figure 5.2-3.
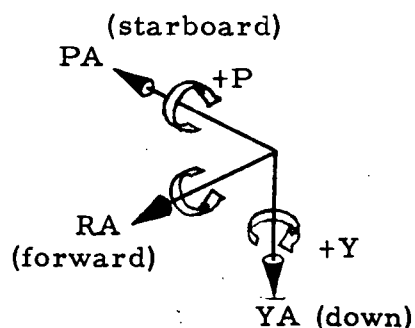
The relationship of the various axes and angles in Figure 5.2-3 may be better understood by referring to Figure 5.2-4. Coordinate set 5 is for the mount-ing base of the STARS and is considered to define the spacecraft axes. It differs
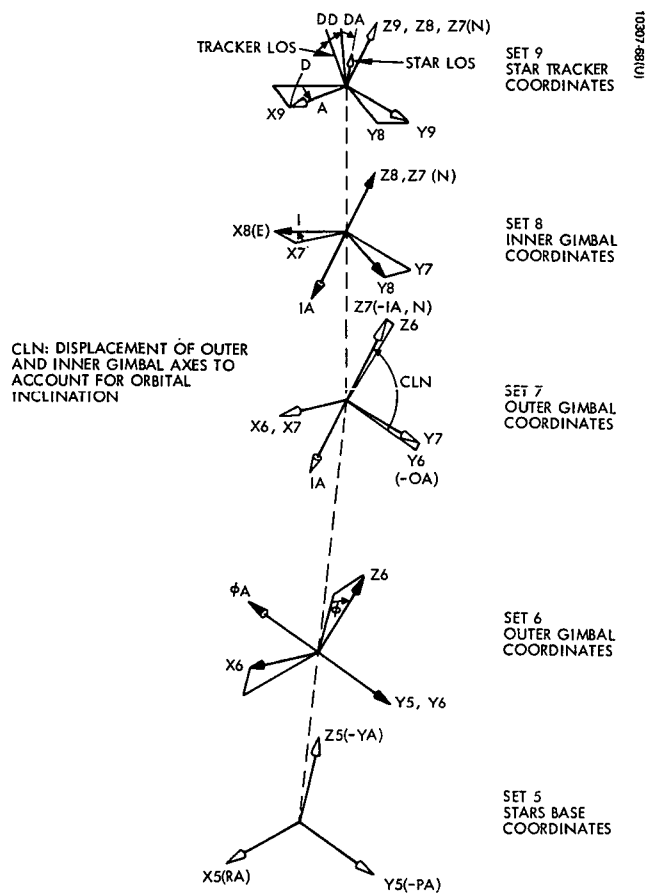
Figure 5.2-4.   STARS Gimbal Coordinates

from the "perfect" reference axes, set 4, only by the small error angles, ER, EP and EY. Coordinate set 6 represents the outer gimbal and is rotated by the outer gimbal ϕ from set 5. The outer gimbal axis ϕA is parallel to the pitch axis within the dimensional accuracy of the base and the outer gimbal bearings. The choice of coordinate directions permits the outer gimbal angle ϕ to be positively increasing during orbital operations, although the pitch rate is negative. The "perfect" angle ϕ0 equals in value the orbital central angle PHI minus 90 degrees. ϕ is zero at sunrise as the spacecraft passes the North Pole.

The nominal orbital inclination is accounted for by introducing a second set of outer gimbal coordinates, X7, Y7 and Z7 with the angle CLN between the outer and inner gimbal axes, OA and IA, on the outer gimbal cross piece.

The outer gimbal axis may be referred to as the pitch axis and the inner gimbal axis may be referred to as the polar axis in other sections of this report.

The inner gimbal coordinates are set 8 and are rotated from set 7 by the inner gimbal angle I. The direction of IA was chosen such that the inner gimbal angle I will be constantly increasing at the rate of 1 revolution per year in orbital operation. I is zero at the vernal equinox.

The right ascension angle A for a given star tracker is measured in set 8. There is a set 9 for each star tracker in which the declination angle D and offset tracking angle DD are measured in the XZ plane. See Figure 5.2-4. The star trackers are assigned numbers, Table 5.2-1, which will be used as subscripts to denote the coordinates of the individual star tracker lines of sight. Thus for star tracker No. 6, the star is Rigel and $A6 = 78.25^{\circ}$, $D6 = -8.24^{\circ}$. Star trackers No. 1, 2, 3 and 4 are on the north polar sensor cluster assembly and star trackers 5, 6, 7 and 8 are on the south polar sensor cluster assembly. The north and south polar sensor cluster assemblies are both on coordinate set 8.

The errors for the STARS system are collected in the several frames of reference and transformed to the roll, pitch and yaw axes of the spacecraft.

5.2.4.3   Ground Track

The projection of the spacecraft axes on a horizontal plane at the surface of the earth is shown in Figure 5.2-5.

It will be noted in Figure 5.2-5 that the primary effect of a roll error is a lateral displacement of the ground track. The primary effect of a pitch error is equivalent to an error in time. A yaw error causes a rotation about the vertical axis of any facsimile of ground features.
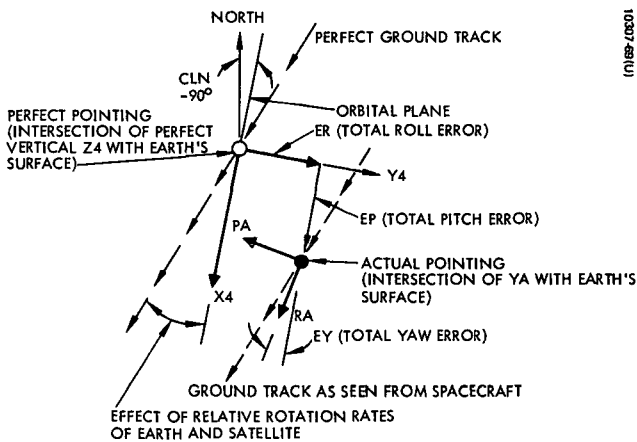
Figure 5.2-5.   Ground Track
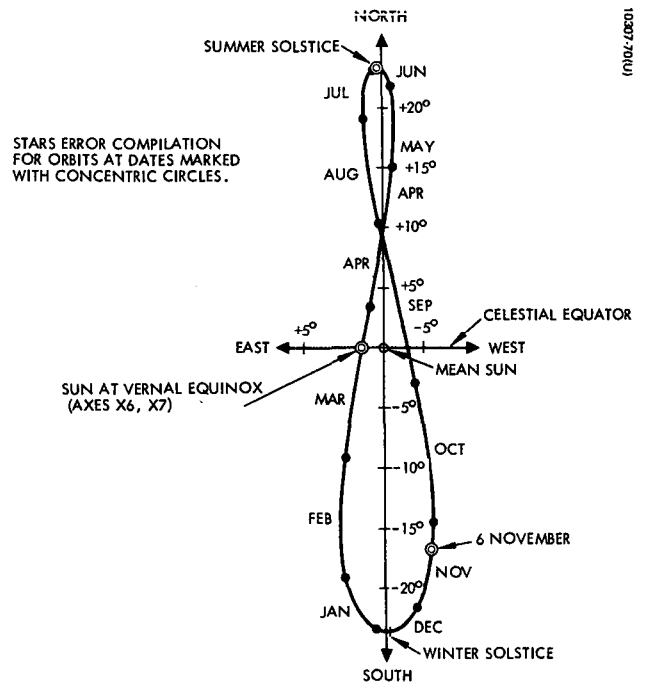
Figure 5.2-6.   Position of Sun on Celestial Sphere With Respect to Mean Sun

5.2.5   Orbital Conditions for Error Analysis

The orbit specified for the STARS feasibility study is a 500 statute mile altitude, high noon, sun-synchronous orbit. An inclination of CLN = 98.3° is required to provide a precession rate ω_p equal to the mean rate of rotation of the earth about the sun, ω_y, at an altitude of 500 miles above the earth's surface. See Reference 3, Figure 4, Page 166. The period for a circular 500-mile orbit is approximately 101 minutes.

The error analysis will assume a 500 sm circular orbit with a period of 100 minutes, an inclination of 98°, and a precession rate equal to that of the mean sun. These numbers are not perfectly consistent but result in adequate accuracy and numerical simplicity. The STARS orientation is assumed to be such that axes X6 and X7 on the outer gimbal are pointed at the vernal equinox, E, at the time of the vernal equinox. Orbit c, which travels southbound in the sun, is assumed.

The above assumptions make the "perfect" coordinate set 8 on the inner gimbal, see Figure 5.2-4, the same as coordinate set 2 in Figure 5.2-2 except that the origin of coordinates is in the spacecraft instead of at the center of the earth. The orbital precession rate ω_p serves to "unwind" the inner gimbal rotation and the orbital rate ω_c unwinds the outer gimbal so that axes X6 and X7 remain pointed in the general direction of the sun. The sun's radiation falls on the outer gimbal from the restricted aspect shown in Figure 5.2-6.

For the purposes of the error compilation the three orbital conditions are:

		Sun Position re Axis X7	Inner Gimbal Angle
1.	Vernal Equinox	0° North 0° West	0°
2.	Summer Solstice	23.5° North 1.4° West	30°
3.	6 November	16.6° South 5.8° West	225°

5.3   Sources of Error

5.3.1   Star Trackers

5.3.1.1   Optics

A basic error source in the STARS system is the effective irradiance of light scattered from bright sources and its effect on the signal-to-noise ratio of the optical system including the photomultiplier tube. The following expression has been shown to approximate the one sigma jitter in the tracking loop error signal due primarily to scattered light in the sunshade.

$$\Psi = 7.9 \times 10^{-8} \; \frac{\sqrt{W(H_{eff} + H_s) \, 4\pi \, f_t}}{H_{eff} \, \sqrt{A_{eff}}}$$

where, for the baseline design:

$$W = 60 \text{ arcsec slit width}$$

$$H_{eff} = \text{W/cm star effective irradiance}$$

$$H_s = 1.1 \times 10^{-13} \text{ W/cm scattered light}$$

$$f_t = 0.1 \; H_z \text{ track loop bandwidth}$$

$$A_{eff} = 6.4 \text{ cm}^2 \text{ effective aperture}$$

This expression then becomes:

$$\Psi = 1.31 \times 10^6 \; \sqrt{H_{eff} + 1.1 \times 10^{-13})/H_{eff}} \quad \text{microradians}$$

This noise appears in both error channels from a given star tracker. Table 5.3-1 begins with a listing of the loop noise due to scattered light for the baseline star set. These values tend to be conservative because of the high value for effective irradiance of scattered light which is used. $H_s = 1.1 \times 10^{-13}$ W/cm^2 implies that the sun is at 30° to the line-of-sight of the sun shield. The weakest star, Phecda ($H_{eff} = 1.1 \times 10^{-13}$ W/cm^2), is 54° from the ecliptic and the sun only moves to this close an approach once a year near the autumnal equinox. Scattering from the earth or spacecraft at displacements as close as 15° occurs twice per orbit but again the high value for H_s is periodic rather than continuous. Thus the value of H_s might have been made an orbit variable and its average much reduced.

TABLE 5.3-1. STAR TRACKER ERRORS

SYMBOL	MICRORADIANS	DESCRIPTION
		OPTICS
EDA1SU	3.43	Tracking loop noise due to scattered light: random error in angle DA of tracker No. 1, star Cih
EDD1SU	3.43	random error in angle DD of tracker No. 1, star Cih
EDA2SU	5.51	Phecda
EDD2SU	5.51	Phecda
EDA3SU	1.99	Arcturus
EDD3SU	1.99	Arcturus
EDA4SU	2.25	Altair
EDD4SU	2.25	Altair
EDA5SU	1.57	Achernar
EDD5SU	1.57	Achernar
EDA6SU	1.47	Rigel
EDD6SU	1.47	Rigel
EDA7SU	3.93	Delta Vela
EDD7SU	3.93	Delta Vela
EDA8SU	3.66	Peacock
EDD8SU	3.66	Peacock
EDAeSB	2.43	Residual misalignment in telescopes after calibration. "e" represents star tracker Nos. 1 thru 8
EDDeSB	2.43	
EDAeSB	1.70	Edge tolerance of reticle slit
EDDeSB	1.70	
EDAeSB	145 DA	Misalignment of arms of reticle slit and non-perpendicularity of arms of reticle slit. Units of angles DA and DD are radians.
EDDeSB	145 DD	
EDAeSB	145 DD	
EDDeSB	145 DA	

TABLE 5.3-1. (Continued)

SYMBOL	MICRORADIANS	DESCRIPTION
		SIGNAL PROCESSING
EDAeSU EDDeSU	2.43 2.43	Wedge position
EDAeSU EDDeSU	2.43 2.43	Wedge position pickoff
EDAeSU EDDeSU	4.85 4.85	Filter delay variation
EDAeSB EDDeSB	4.85 4.85	Image asymmetry
EDAeSU EDDeSU	.49 .49	Threshold accuracy
EDAeSU EDDeSU	0.66 cos (90DA) 0.66 cos (90DD)	Quantization error
EY7SR	(see 5.3.5.4)	Thermal Distortion

The optics for each telescope is to be aligned to the sensor cluster within 30 arc seconds but calibrated to within one arcsecond. The assumption in this error analysis is that a tolerance represents two standard deviations. This is because the difficulty of the work does not permit a normal Gaussian distribution. Thus the figure for EDDeSB in Table 5.3-1 is 2.43 microradian or 0.5 arcseconds one sigma for each telescope.

The tolerance on the edges of the slits in the reticle is $\pm$ .00012 inch. This also is considered two sigma. The error in blur position detection is one-half of the position error of one side of the slit. The focal length is 2.5 inches. Thus the one sigma error due to one edge is $1/2 \ (1/2) \ \frac{12\mu inch}{2.5 \ inch} =$ 1.2 μrad. Assuming the errors on each side of the slit are independent

$$\sqrt{1.2^2 + 1.2^2} = 1.70 \ \mu rad$$

is the expected error from this source.

The alignment of the legs of the L-shaped slit in the reticle can be adjusted mechanically by rotating the reticle in the telescope. The accuracy of adjustment is limited by the straightness of the slits, the perpendicularity of one slit to the other, the quantization in the signal processing, tracking loop noise and calibration errors. Assume that system noise is made small by use of a simulated star of adequate irradiance and that calibration errors are small. The quantization interval at the edges ($\pm$ 0.5^o) of the field of view is 1.67 μrad. It would be possible to adjust the slit so that the quantization jump did not occur in DA while the simulated source was moved over the field of view in DD except for the straightness tolerances on the slit edges. The number of positive jumps might be made equal to the number of negative jumps. The quantization interval could thus be used in the determination of the minimum cross-coupling:

$$EDA = \frac{1.67 \ \mu rad}{1.0 \ degree} \ DD \qquad (DD \ in \ degrees)$$

$$= 96 \ DD \ \mu \ rad/rad \qquad (DD \ in \ radians)$$

The perpendicularity of one slit to the other is specified as $\pm$ 1.0 minute of arc or 290 μrad/rad. The reticle adjustment tolerance must accommodate the above errors. With a tolerance (two sigma) of $\pm$ 1.0 minute of arc on each arm:

$$EDA = \pm \ 145 \ DA + 145 \ DD$$

5.3.1.2 Signal Processing

The errors listed under signal processing in Table 5.3-1 are estimated to be attributable to the STARS signal processing up to the point where output registers store counts representing angles DA and DD from each star being viewed. The quantization error decreases at the edge of the field of view due to the geometry of the reticle slit and the nutation circle.

5.3.2 Gimbal Errors

5.3.2.1 Ball Bearings

The maximum errors for the ball bearings of each gimbal axis were presented in Table 3.4-4. For the purposes of the error analysis these data were summed as described below; the results are listed in Table 5.3-2. The values in Table 3.4-4 are maximum, or specified, so they are considered tolerances at two-sigma. Item numbers are from Table 3.4-4.

Item 2 is the residual error in one inner race after mechanical compensation. The one-sigma value is 0.75 microradians. The bearing at the other end has the same residual error but it is assumed to be independent so the misalignment about the two axes perpendicular to the shaft axis is 0.75 microradians each. This same mechanism is presumed to act on the outer raceways.

Items 3, 4, 5, 12, 13 and 14 similarly cause misalignments with a one-sigma summation of

$$\frac{1}{2} \sqrt{(1.5)^2 +(1.5)^2 +(1.0)^2 +(0.5)^2 +(0.5)^2+(0.5)^2} = 1.25$$

microradians rss. These errors are also assumed to cause both inner and outer race misalignment.

Items 6 and 15 are difficult to evaluate. Again we will consider that the "worst case" figures given in Table 3.4-4 for contamination and Brinnelling are two-sigma, but rather than causing simple eccentricity they will be considered to be rms noise. Thus

$$1/2 \sqrt{(4.5)^2 + (3.0)^2} = 2.70 \text{ micro-}$$

radians. This figure is assumed to be independent for inner and outer races.

The remaining items of Table 3.4-4 are either combinations herein accounted for (10 and 11) or they are not applicable (1, 7, 8, 9).

TABLE 5.3-2. GIMBAL ERROR SOURCES

SYMBOL	MICRORADIANS	DESCRIPTION
		Ball Bearings
EX8GB EY8GB EX7GB EY7GB	0.75 0.75 0.75 0.75	Residual misalignment after mechanical compensation, inner gimbal axis
EX6GB EZ6GB EX5GB EZ5GB	0.75 0.75 0.75 0.75	Residual misalignment after mechanical compensation, outer gimbal axis
EX8GU EY8GU EX7GU EY7GU	1.25 1.25 1.25 1.25	Uncertainty in alignment, inner gimbal axis
EX6GU EZ6GU EX5GU EZ5GU	1.25 1.25 1.25 1.25	Uncertainty in alignment, outer gimbal axis
EX8GU EY8GU EX7GU EY7GU	2.70 2.70 2.70 2.70	Uncertainty due to contamination and Brinelling of races, inner gimbal axis
EX6GU EZ6GU EX5GU EZ5GU	2.70 2.70 2.70 2.70	Uncertainty due to contamination and Brinelling or races, outer gimbal axis

TABLE 5.3-2. (Continued)

SYMBOL	MICRORADIANS	DESCRIPTION
		Gimbal Machining
EX5GB EZ5GB	2.72 2.72	Runout of STARS mounting flange
EY5GB	3.84	Pin locations in STARS mounting flange
EX7GB	2.42	Residual error of inclination angle between gimbal axes after compensation
EX8GB EY8GB	2.69 2.69	Runout of mounting flanges for star sensor clusters.
EZ8GB	3.81	Pin locations in cluster mounting flanges
		Dimensional Creep
EX8GU EY8GU	5.16 5.16	Warping of inner gimbal shaft
EZ8GU EZ8GU EZ7GU	0.48 3.90 1.67	twisting of inner gimbal shaft, north cluster twisting of inner gimbal shaft, south cluster twisting of inner axis housing
EX6GU EX6GU	4.06 4.06	warping of outer gimbal shaft
EX5GU EZ5GU	3.00 3.00	warping of base
EY6GU EY5GU	3.68 3.23	twisting of outer gimbal shaft twisting of base
		Acceleration-Sensitive Error
EX6GB	2.60	Residual error after compensation for bending and bearing compliance

5.3.2.2   Gimbal Tolerances

Five tolerances of the gimbals must be considered. These errors are fixed biases which can be measured and compensated. They are:

1. Runout of STARS base mounting flange with respect to the outer gimbal axis.

2. Pin or notch locations in STARS base mounting flange.

3. Accuracy of machining of inclination angle between inner and outer gimbal axes.

4. Runout of mountings for the north and south polar star sensor clusters.

5. Pin locations in mounting for the north and south polar star sensor clusters.

We will assume that the runout can be controlled to 50 microinches two-sigma on the 6.5 inch diameter mounting base. The error is thus $1/2 \left(\frac{50}{6.5}\right) = 3.84$ microradians, 0.707 of which will be assigned to each axis perpendicular to the outer gimbal axis. The pins which establish rotation about the pitch axis are given a 50 microinch location tolerance, all of which occurs about the outer gimbal axis.

The machining of the inclination angle need only be held closely enough to not use a significant part of the offset tracking capability. The uncompensated value might be as much as one minute of arc. The residual after measurement and compensation is 0.5 second of arc or 2.42 microradians.

The runout in the mounting for the star sensor clusters is more critical due to the smaller diameter. If the tolerance on this runout is held to 20 microinches on the 2.625 inch mounting bolt circle, the one-sigma error is $1/2 \left(\frac{20}{2.625}\right) = 3.81$ microradians. Again, 0.707 of this will be assigned to each perpendicular axis. The pin locations must be held to the same magnitude of tolerance.

5.3.2.3   Dimensional Stability

The warping which may occur in a symmetrical, thermally stabilized beryllium structure is next to impossible to predict. The STARS operates in a stable temperature environment because of its layer of insulation but it is continuously subjected to thermal cycling with a period of 100 minutes and a peak-to-peak amplitude of about $1^\circ F$. As an allowance for creep due to relief of internal stresses and bearing preload, and to account for launch stresses, a one-sigma figure of 1 microinch per inch uncertainty in bending and 0.3 microinch per in twisting is introduced in the gimbal structural members.

The inner gimbal shaft has a total length between sensor cluster mounting flanges of 14.6 inches. Thus a warpage of 14.6 microradians is introduced, half on each end, so $1/2$ (0.707) $(14.6) = 5.16$ μrad on each of axes X8 and Y8. Warping of the inner axis housing has negligible effect. Twisting along the inner gimbal axis is 3.9μrad for the south star sensor cluster and 0.48 for the north star sensor cluster due to the location of the pickoff at the north end. The same twisting allowance applied to the housing about the shaft results in a dislocation of the encoder stator and resultant errors for both clusters. The same reasoning applied to the outer axis produces the values shown under dimensional creep in Table 5.3-2.

5.3.2.4   Acceleration Sensitive Errors

Pointing errors due to compliance in the gimbals may be extremely difficult to measure because of the unavailability of a precise star field which can be "tumbled" during test. It will probably be necessary to correct for the displacements due to gravity during test by measuring the weights and compliances of structural elements of STARS and making the compensation "open loop".

As an example, consider that the STARS is being tested in the laboratory with the polar axis vertical. The outer gimbal shaft will deflect due to the overhung weight of the inner axis components and the sensor cluster assemblies. The base cylinder will also bend slightly but the major source of compliance will be the ball bearings.

The outer gimbal shaft is sketched below. For simplicity it is assumed that the shaft is horizontal.
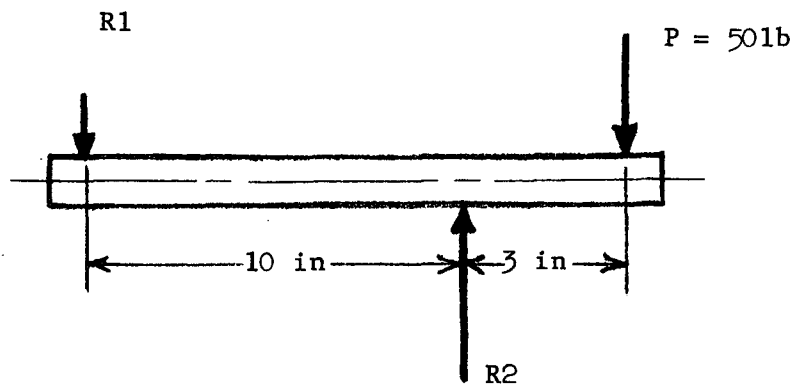
The load P is approximately 50 lb and the resultant bearing reactions are R1 = 15 lb, R2 = 65 lb. Bearing R1 is one of the smaller bearings and is mounted on a compliant member. A compliance of K1 = 5 microinches/lb is reasonable at this point. Bearing R2 is a larger bearing and is solidly mounted into the base structure. K2 is approximately 1 microinch per lb. The total deflection, assuming shaft and base are perfectly stiff, is:

$$EX6 = \frac{R1 \times K1 + R2 \times K2}{10}$$

$$= \frac{15\ (5) + 65\ (1)}{10}$$

$$EX6 = 14 \text{ microradians}$$

The question becomes "what is the accuracy of compensation". We will assume that the calculated compensation can remove 80% of the error, leaving a residual bias of 2.8 microradians, one-sigma.

TABLE 5.3-3.   ERRORS OF GIMBAL ANGLE ENCODERS

SYMBOL	MICRORADIANS	DESCRIPTION
EϕEB EIEB	$3.30 \sin (\phi + \theta_1)$ $3.30 \sin (I + \theta_2)$	Centering of Inductosyn discs (θ_n are random phase angles)
EϕEB EIEB	$2.42 \sin (\phi + \theta_3)$ $2.42 \sin (I + \theta_4)$	Effect of bearing bias
EϕEB EIEB	$4.85 \sin (\phi + \theta_5)$ $4.85 \sin (I + \theta_6)$	Rotor to housing alignment
EϕEB EIEB	$4.85 \sin (\phi + \theta_7)$ $4.85 \sin (I + \theta_8)$	Stator to shaft alignment
EϕEB EIEB	$.97 \sin (\phi + \theta_9)$ $.97 \sin (I + \theta_{10})$	Wobble
EϕEB EIEB	$8.05 \sin (\phi + \theta_{11})$ $8.05 \sin (\phi + \theta_{12})$	Root-sum-squared total bias errors. θ_{11} and θ_{12} are random phase angles 0 to 360°.
EϕEU EIEU	1.54 1.54	Electronic error systematic with poles of Inductosyn. rms of 2.14 $\sin (512\,\phi + \theta)$
EϕEU EIEU	.49 .49	Uncertainty due to bearings
EϕEU EIEU	3.47 3.47	Quantization
EϕEU EIEU	3.83 3.83	Root-sum-squared total of uncertainties

5.3.3 Gimbal Position Encoders

The errors given in Table 5.3-3 are derived from Table 3.4-5. The errors which are due to alignment and centering adjustments are systematic and have the form of sinusoids of one gimbal revolution where the value given in 3.4-5 is the one-sigma amplitude. Each of items B1 through B5 in Table 3.4-5 has an independent phase angle. Their rss total, expressed in microradians, is the 8.05 amplitude seen in Table 5.3-3 for the bias errors. The bias error from the encoders has been characterized as a "typical" error in order to demonstrate the propagation of error through the system.

The errors which are systematic with the poles have an amplitude of 2.18 microradians and a rms value of 1.54 microradians. This has been classified as an uncertainty error but could be considered as a compensatable bias. The quantization error due to utilization of a 19 bit register is calculated as follows. The step is 12 microradians so the peak error is 6 microradians. The rms error of a saw tooth is $1/\sqrt{3}$ times the peak or 3.47 microradians.

5.3.4 STARS Control System

The errors listed for the STARS control system in Table 5.3-4 are taken from Section 3.5 and are explained in detail there.

TABLE 5.3-4.   ERRORS OF STARS CONTROL SYSTEM

SYMBOL	MICRORADIANS	DESCRIPTION
EØCB EICB	-5.00 -5.00	Mean droop of servo positioning error
EØCU EICU	3.50 7.70	Uncertainty and diurnal variation in servo positioning error

A) BASE VIEWED FROM SUN   B) BASE VIEWED FROM NORTH

C) OUTER GIMBAL VIEWED FROM EAST   D) INNER GIMBAL VIEWED FROM EAST
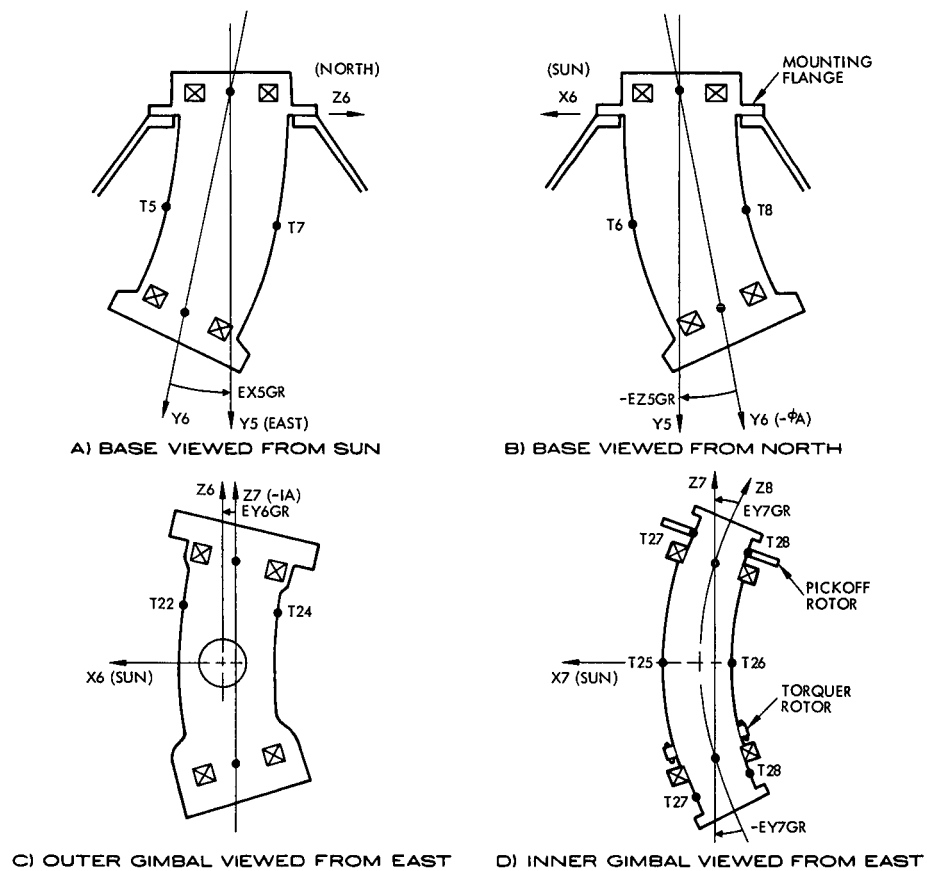
Figure 5.3-1.   Thermal Distortion of Base and Gimbals

5.3.5 Thermal Distortion

5.3.5.1 Definition

Thermal distortion is herein defined as the angular errors of the STARS axes which are the result of the in-orbit operating thermal environment (vacuum, spacecraft heat sink, radiation to deep space, direct sun load, eclipse) compared to a condition wherein the STARS is assembled with all parts at 25°C (77°F, 298.15K).

A less conservative definition would compare the in-orbit operating thermal environment with the laboratory thermal environment in which the STARS is calibrated. For use in the error analysis, this definition would require that the laboratory thermal environment be defined and calculated, and that temperature mapping and the resultant distortions be obtained for this environment for subtraction from the in-orbit distortions. The improvement available from use of this definition is considered to be small unless the sun load and vacuum conditions could be simulated during the calibration.

5.3.5.2 Mechanisms

The following source of thermal distortion are evaluated in this study:

1. Base - The temperature difference between the "sun" side and the shade side, temperatures T6 and T8 respectively in Figure 5.3-1), will bow the cylinder as shown, carrying the centerline of the bearings out of line with the mounting flange. Each bearing is presumed to act as a self aligning bearing. At the vernal equinox the radiation received at T5 and T7 is equal. During the summer the sun moves north with respect to the celestial equator and T7 becomes warmer causing a distortion as sketched in Figure 5.3-1). The analysis assumed that the base was covered with the same insulation blanket as was applied to the gimbals and that the spacecraft structure provided no thermal shielding.

2. Outer Gimbal - Bowing of the shaft of the outer gimbal (pitch) axis is considered as is bowing of the housing for the inner gimbal (polar) axis as shown in Figure 5.3-1). Symmetrical bowing of a member may not cause a net angular error as will be seen by study of Figure 5.3-1).

3. Inner Gimbal - Bowing of the inner gimbal due to differences between the "hot" side and the "cold" side of the shaft, temperatures T25 and T26 in Figure 5.3-1) directly influence the alignment of the sensor cluster assemblies on both ends of the inner gimbal axes.

4. Sensor Cluster - A difference between temperatures 29 and 30 due to sun load on the adaptor and mirror mount will further displace axis Z9 of the sensor cluster with respect to the IA as seen in Figure 5.3-2 Unsymmetrical dissipation of the wedge motor would affect this warping, but the dissipation of the motor is so low and the precision with which it must be wound is so high that the effect will be considered negligible compared to sun load. Warping of the mirror cluster is considered to be too complex to consider at this time. The spacer that supports the telescope objective cluster is subject to warping due to differences in temperatures 31 and 33.

5.3.5.3 Thermal Analysis

5.3.5.3.1 Objectives and Design

The objective of the thermal analysis was to investigate the feasibility of maintaining STARS temperatures and temperature gradients within acceptable levels. An operational bulk temperature of $90 \pm 10^{\circ}F$ is specified for the system, while the acceptability of temperature gradients is determined from the magnitude of the induced angular position errors.

An assumed baseline design directed towards minimizing temperature gradients was employed for the feasibility study. The entire unit is super-insulated (except for the sunshade apertures), and conductively isolated from the spacecraft. The insulation blanket, with an effective emittance (ϵ) of 0.03, is encased in an aluminum kapton cover. Since the same surface of STARS is always illuminated, the back (shadowed) surface can be black to provide a total effective $\epsilon = 0.76$ while maintaining the solar absorptance of the kapton ($\alpha^* = 0.16$) on the illuminated surface.

A bulk thermal analysis was performed on the cantilever configuration shown in HAC Drawing L3006211. Internal heat dissipation was assumed to be constant and distributed in the following manner:

Unit	q, Watts
Gimbals	
Pitch Motor	.2
Polar Motor	.2
Inductosyn (2)	.5
Slip Rings (2)	.2
Sensor Head	
Wedge Motor (2)	8.0
High Voltage P.S. (2)	.5
Electronics (2)	1.5
TOTAL	11.1

The nominal orbit for STARS application has been defined as a sun synchronous, 500 mile, circular, high noon orbit with a 100 minute period. In this orbit, the sun vector is always normal to the pitch axis, and within $\pm$ 23 1/2° of perpendicular to the polar axis.

Since spacecraft configuration and temperatures are not defined, a parametric study was performed to determine the compatability of the baseline thermal design with various spacecraft and orbital conditions. The results show that adequate temperature control (90 $\pm$ 10°F) can be provided over a reasonable range of typical environments.

5.3.5.3.2 Bulk Analysis

A simplified nodal model was employed to determine the suitability of the baseline design for several orbital conditions, spacecraft temperatures and viewability. Four nodes representing STARS, the outer cover of the insulation blanket, the spacecraft and space are shown with the radiation coupling terms in Figure 5.3-3. The latter two nodes were treated as boundary conditions thereby requiring two heat balance equations to describe the network:

Node 1, STARS:
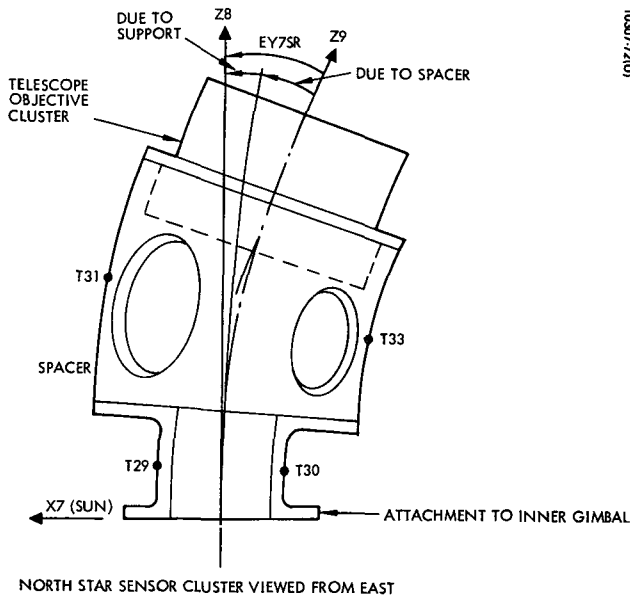
North Star Sensor Cluster Viewed From East

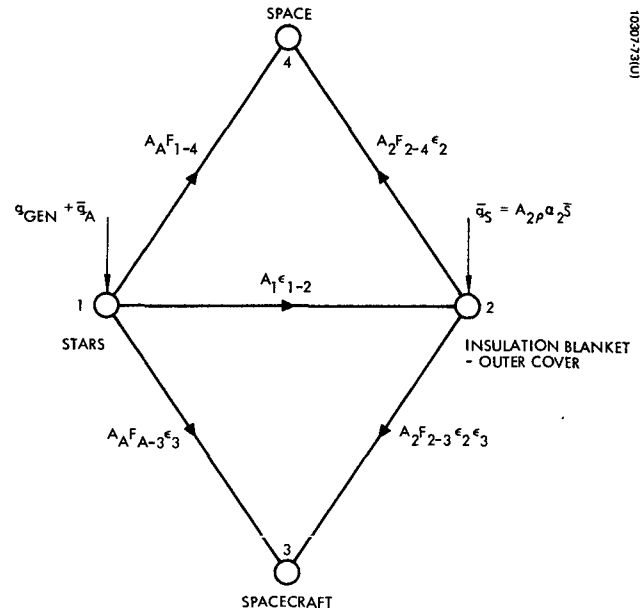Figure 5.3-2. Thermal Distortion
of Star Sensor Cluster

Figure 5.3-3. Bulk Thermal Model
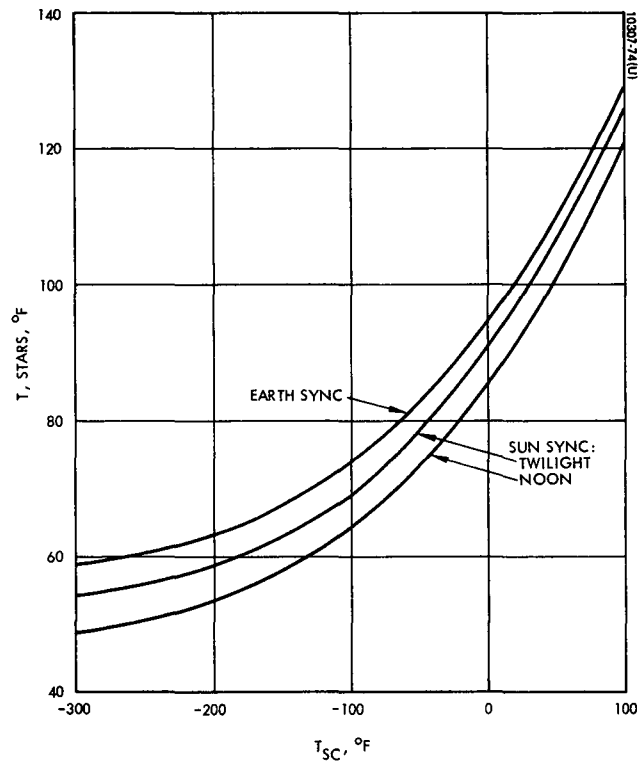

Figure 5.3-4. STARS Bulk Temperature Versus Spacecraft
Bulk Temperature

$$q_{gen} + \bar{q}_a = A_1 \epsilon_{1-2} (\sigma T_1^4 - \sigma T_2^4) + A_A F_{A-3} \epsilon_3 (\sigma T_1^2 - \sigma T_3^4) +$$

$$A_A F_{A-4} (\sigma T_1^4) \tag{1}$$

Node 2, Insulation Blanket Cover:

$$\bar{q}_S = A_2 F_{2-3} \epsilon_2 \epsilon_3 (\sigma T_2^4 - \sigma T_3^4) + A_2 F_{2-4} \epsilon_2 \sigma T_2^4 - A_2 \epsilon_{1-2} (\sigma T_1^4 - \sigma T_2^4) \tag{2}$$

Nomenclature and nominal values are contained in Table 5.3-5. The nominal values were used to compute the orbital average bulk temperature of STARS as a function of spacecraft temperature for sun synchronous noon and twilight orbits, and for an earth synchronous orbit; results are shown in Figure 5.3-4. For the sun synchronous noon orbit the sun vector was assumed to be normal to the plane of the pitch and polar axis; the twilight orbit analysis was based upon a sun vector normal to the polar axis and pointing at the pitch axis. The earth synchronous orbit was considered to provide the same illumination angle as the noon orbit.

Seasonal temperature variation of STARS for the nominal 500 mile, circular, sun synchronous noon orbit was computed to be on the order of $1^{\circ}F$ higher than during equinox. The small temperature increase results from the STARS symmetry; the projected area is 2.13 ft^2 at both summer and winter solstice and 2.06 ft^2 at equinox.

The above analysis assumed a view factor of 0.5 to the spacecraft and no earth view. Figure 5.3-5, generated for the nominal noon orbit, illustrates the range of orbital average spacecraft temperatures as a function of spacecraft view factor which will provide acceptable bulk temperature levels for STARS. It was assumed that the sum of the view factors from STARS to spacecraft and earth was 0.5. Earth loads were computed from a $0^{\circ}F$ IR black body, with a diffuse solar reflectance of 0.34. It is seen that if STARS has a view factor of 0.5 to the spacecraft it can be maintained within the $80-100^{\circ}F$ range if the orbital average spacecraft temperature is within -25 to $+42^{\circ}F$. The divergence of the band results from the earth loads, since the equilibrium temperature of STARS with the earth environment (no spacecraft) is $88^{\circ}F$.

A similar set of data is constructed in Figure 5.3-6 for a typical earth synchronous orbit. Both bounding curves increase with decreasing view factor since earth loads were assumed to be negligible at earth synchronous altitude. Comparison with Figure 5.3-4 shows that lower spacecraft temperatures are required to maintain STARS at $100^{\circ}F$ for the earth synchronous orbit when the view factor exceeds .38 (approximately). This is due to higher orbital average sun loads
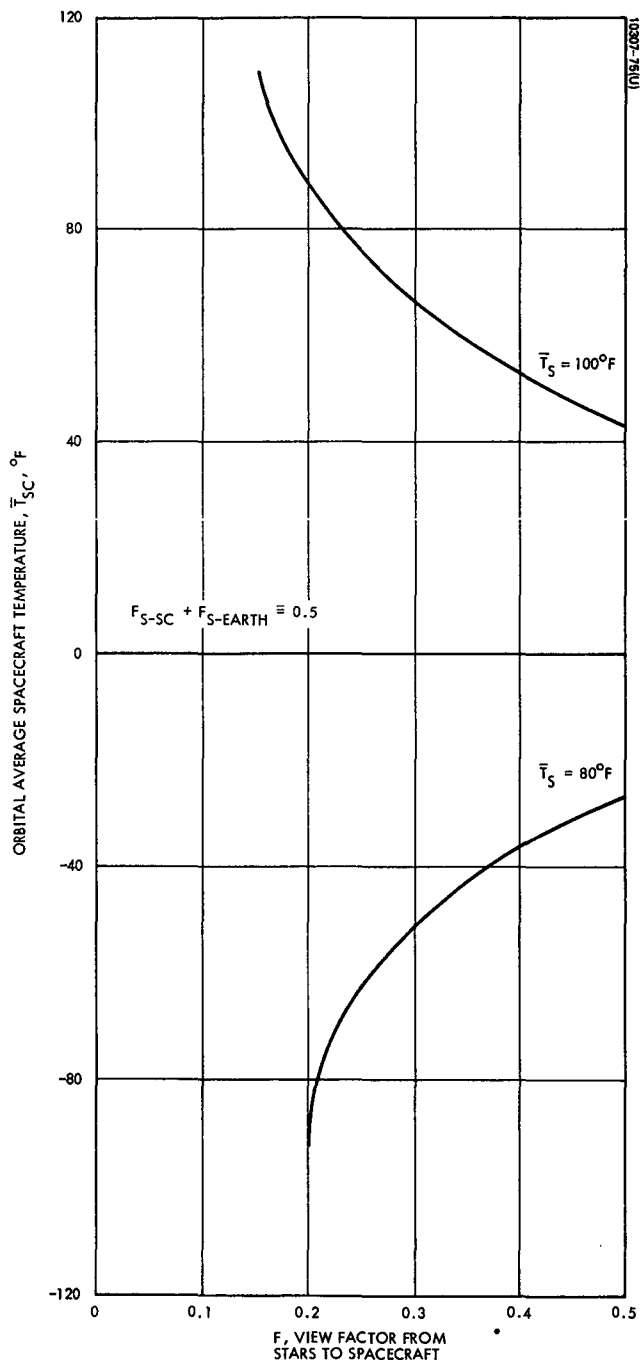
Figure 5.3-5. Orbital Average Spacecraft Temperature Versus View Factor - Sun-Synchronous Orbit
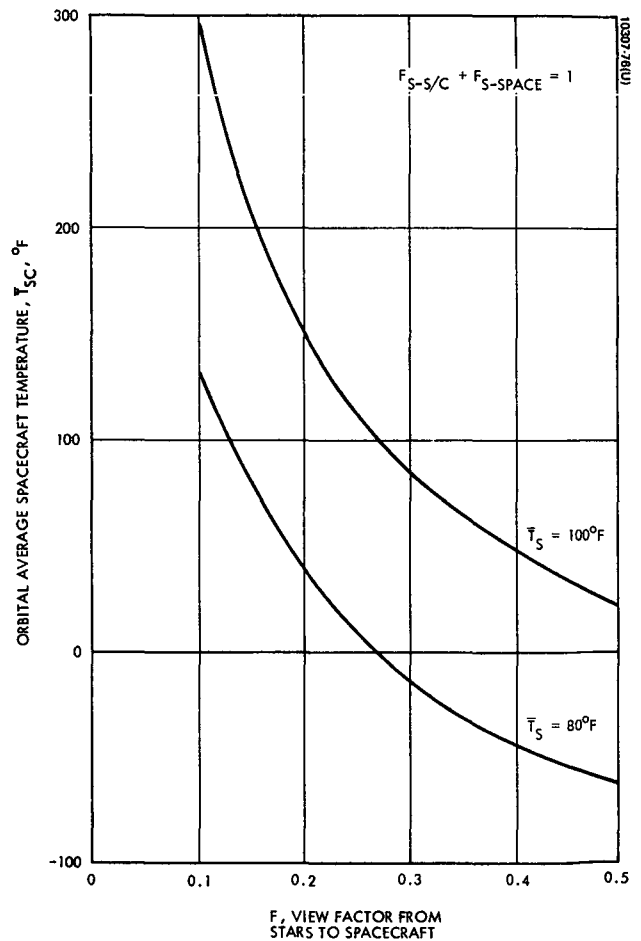
Figure 5.3-6. Orbital Average Spacecraft Temperature Versus View Factor - Earth-Synchronous Orbit

TABLE 5.3-5. NOMENCLATURE AND NOMINAL VALUES

Parameter	Definition	Value (Nominal)
q_{gen}	Internal Dissipation	11.1^W
$\bar{q}_A$	Maximum Orbital Average Solar Load thru Sunshade Aperture	1.0^W
$\bar{q}_s$	Absorbed Orbital Average Solar Load on Exterior of Blanket	21.0^W
A_p	Projected area of STARS: Equinox Solstice	 2.06 ft^2 2.13 ft^2
A_1	Surface Area of STARS	7.6 ft^2
A_2	Surface Area of Blanket	7.6 ft^2 (blanket thickness $\sim .25"$)
A_A	Sunshade Area	1.1 in^2 and 2.3 in^2
$\bar{S}$	Orbital Average Solar Intensity	221 BTU/Hr-Ft^2
ϵ_{1-2}	Effective emittance through Insulation Blanket	$.03$
ϵ_2	Emittance of Blanket Cover	0.76
ϵ_3	Emittance of Spacecraft	0.8
α^*_2	Solar Absorptance of Blanket Cover	$.16$
F_{A-3} F_{A-5}	View Factor through Sunshade to: Spacecraft Space	 $.5$ $.5$
F_{2-3} F_{2-5}	View Factor from Blanket cover to: Spacecraft Space	 $.5$ $.5$
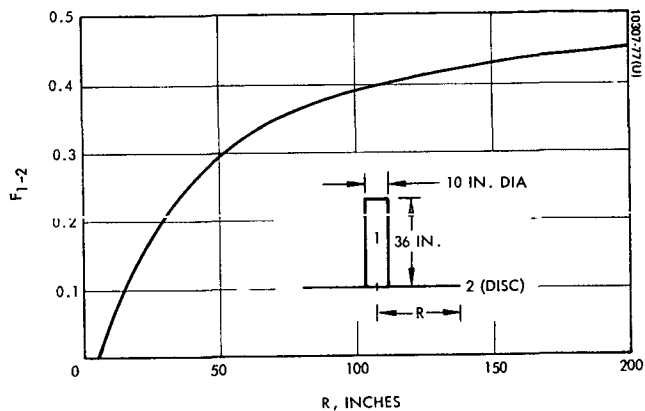
Figure 5.3-7. View Factor From
Cylinder (STARS) to Disk (Spacecraft)
Versus Disc Radius
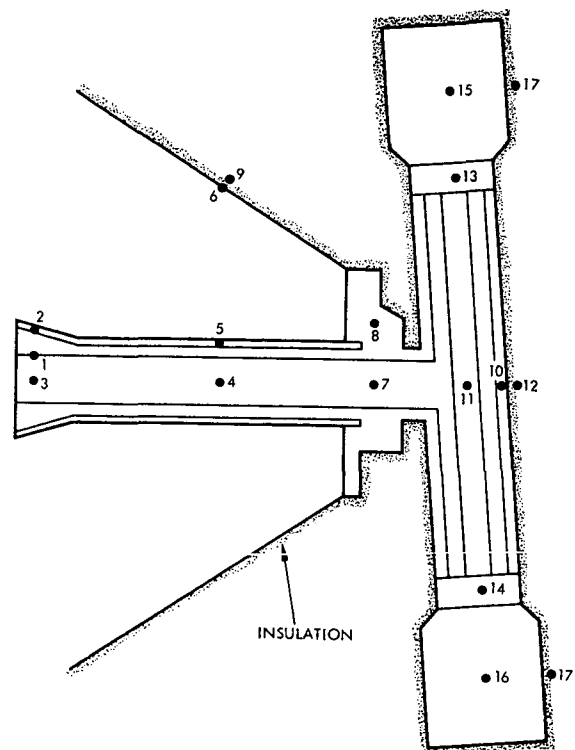
Figure 5.3-8. Nodal Model of STARS
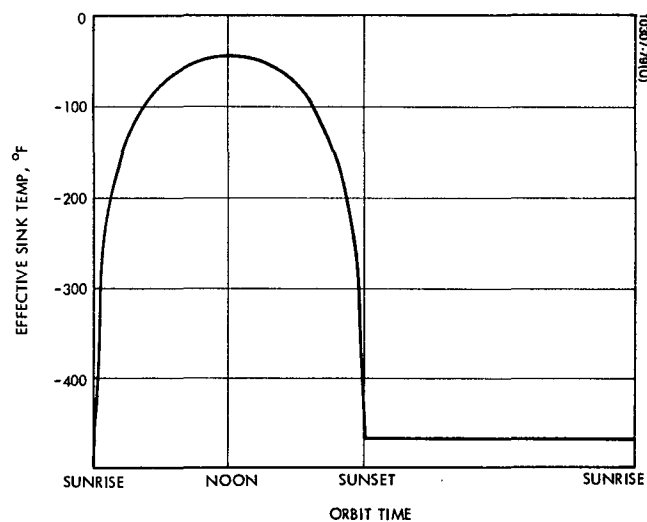
Figure 5.3-9. Effective Sink Temperature Versus Orbit Time

over the 24 hour orbit ($\bar{S} \approx 442 \times (23/24)$ versus $\bar{S} = 442 \times (50/100)$ for 500 mile sun synchronous orbit).

Figure 5.3-7 was generated to provide some insight into the effect of vehicle size on the form factor from STARS to the spacecraft. Approximating STARS with the outside of a 10 inch diameter, 3 foot high cylinder, and the spacecraft by a disc shaped area centered at the base of the cylinder, the form factor to the spacecraft was found as a function of disc diameter. The geometry is illustrated in the figure.

The results of this analysis indicates that the baseline thermal design concept for STARS can provide adequate temperature control when exposed to a reasonably wide spectrum of spacecraft temperatures and orbital conditions. A specific final design must be developed in conjunction with the detailed definition of spacecraft configuration, temperature and orientation. The foregoing analysis has shown feasibility which was its intent.

The final phase of the bulk analysis is devoted to determining the transient response characteristics of STARS throughout an orbit. This analyses was limited to the nominal 500 mile, noon orbit with a 100 minute period. It was assumed that the spacecraft shadowed STARS for half of the 100 minute orbit, and obscured earth at all times.

STARS and its insulation blanket were discretized into 17 nodes shown in Figure 5.3-8. One boundary condition, the effective sink temperature, was employed, which represented a conservative equivalent space/spacecraft temperature as shown in Figure 5.3-9. The variation of effective sink temperature from -460° to $-40^{\circ}F$ is unrealistic and will induce larger temperature variations than will occur under actual conditions. If the view factor to the spacecraft is 0.5 the effective sink temperature of $-40^{\circ}F$ corresponds to a spacecraft temperature of $+40^{\circ}F$. The network was solved with a time sharing program for transient thermal analysis from the HAC library. Initial conditions are at sunrise with the vehicle moving towards noon.

The solar loads used in the analysis are those occurring during equinox. Solstice conditions were not simulated in view of their similarity to equinox as shown in the orbital average analysis. Apertures in the sensor head were treated as black surfaces lumped in the sensor head node. These surfaces were subjected to direct solar loads and radiated directly to the equivalent sink temperature.

TABLE 5.3-6. SUMMARY OF BULK TRANSIENT ANALYSIS

NODE	LOCATION	TEMPERATURES, °F		
		SUNRISE	NOON	SUNSET
1	Pitch Motor	87	87	88
2	Pitch Motor Housing	87	87	87
3	Pitch Motor Shaft	87	87	88
4	Shaft, Pitch Arm	87	87	88
5	Housing, Pitch Arm	87	87	87
6	S/C Mounting Surface	86	87	86
7	Shaft, Pitch Arm	87	88	88
8	Housing, Pitch Arm	86	87	87
9	Insulation Cover	-63	24	-63
10	Housing, Polar Arm	88	88	88
11	Shaft, Polar Arm	89	89	89
12	Insulation Cover	-94	7	-94
13	Sensor Head Mounting Plate	89	89	90
14	Sensor Head Mounting Plate	89	89	89
15	Sensor Head	91	92	92
16	Sensor Head	91	91	92
17	Insulation Cover	-88	10	-88
18	Effective Sink	-460	-40	-460

Table 5.3-6 contains a summary of the results showing nodal temperatures at sunrise, noon, and sunset. The data shows orbital temperature variations on the order of $1^{\circ}F$ per node, and a maximum differential of $5^{\circ}F$ between nodes. These results demonstrate the feasibility of maintaining STARS within $\pm 10^{\circ}F$ of a nominal operating temperature.

5.3.5.3.3 Gradient Analysis

The objective of this phase of the analysis was to obtain circumferential temperature gradients around the sensor head, and the pitch and polar axes as a function of orbit time. Simplified conservative nodal models were synthesized to provide the desired data. Orbital parameters used for this study correspond to the nominal 500 mile, high noon orbit during equinox. Solstice conditions were not simulated in light of the results of the bulk analysis which showed a seasonal variation of $1^{\circ}F$ in bulk temperature. In addition, the extreme conservatism employed in the definition of boundary conditions should result in larger predicted gradients than will actually occur. The temperature response data was obtained with the HAC transient thermal analysis program. Since the results are felt to provide an upper bound on temperature gradients, no attempt was made to determine their accuracy. The two primary sources of error are truncation, which is inherent in finite difference approximations, and roundoff associated with numerical solutions. Another influence on the results is the approximation required to simulate time dependent boundary conditions. The computer program limits such functions to five points, linearly interpolating to obtain data between these points.

The use of uniform nominal property values in model development is another source of difference between predicted and actual performance. The nominal properties of beryllium used for the analysis are:

Thermal Conductivity = 104 BTU/Hr-Ft-$^{\circ}F$

Heat Capacity = .45 BTU/lb-$^{\circ}F$

Density = 0.067 LB_m/Ft^3

Lower than nominal thermal conductivity would result in larger temperature gradients and tend to decrease the response rates of the actual system. Heat capacities and densities below nominal would tend to increase the systems response rate over that predicted.
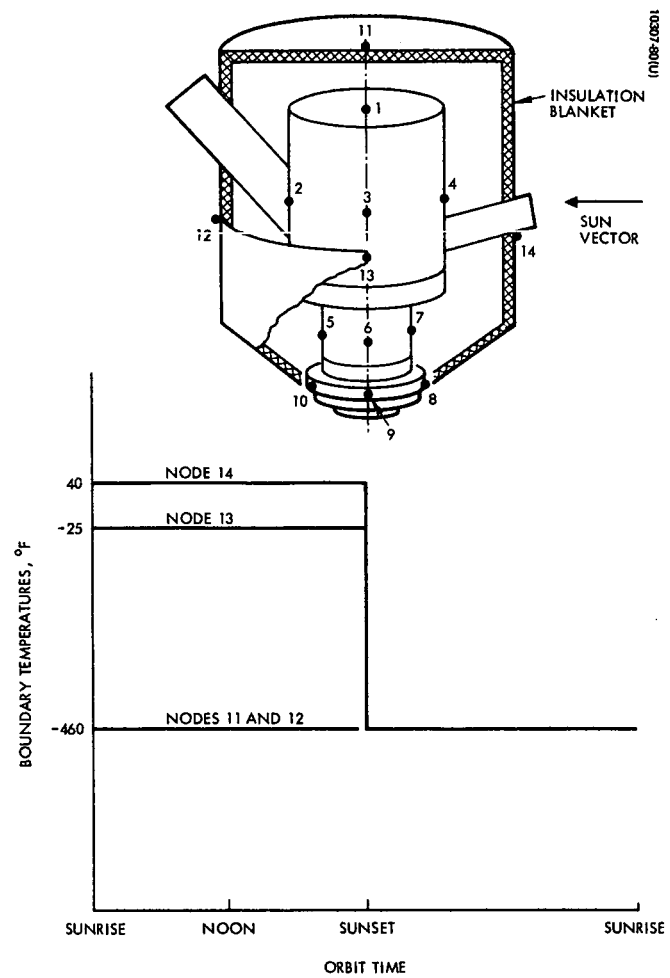
Figure 5.3-10. Sensor Head Model and Boundary Conditions

Temperature variations per node and differences between nodes were typically less than 1°F. In order to obtain observable circumferential temperature differences around the sections, the computer results were used to the fourth decimal place. Roundoff of the data to the nearest degree (or even 0.1°F) showed the circumferential sections to be isothermal.

5.3.5.3.3.1   Star Sensor Cluster

A star sensor cluster assembly was simulated with 10 nodes as shown in Figure 5.3-10. . Heat dissipation from the wedge motor (4 watts), high voltage power supply (.25 watts) and electronics (.75 watts) were assumed to be constant throughout the orbit. Radiation coupling between the sensor head nodes was not included to provide some analytical conservatism. Heat rejection from the sensor head occurs via parallel paths through the insulation blanket and through the sun shades. The temperature profiles applied at the outer skin of the insulation blanket are shown in Figure 5.3-10. These values are unrealistic, but provide extreme conservatism in terms of the resulting gradients and transient temperature variations. Regions of the blankets not illuminated are maintained at -460°F. Temperature profiles on the illuminated regions of the blanket were computed as equilibrium values based on radiation of the solar load to space. During the half orbit when STARS is shadowed by the spacecraft, all blanket temperatures are set to -460°F.

The orbital temperature history of Nodes 1 through 4, which were employed in the distortion analysis, are shown in Figure 5.3-11. The rapid temperature change evidenced by the sun side of the cluster support (Node 4) at sunrise and sunset is its response to the step function boundary temperature applied to the blanket cover (Node 13).

5.3.5.3.3.2   Gimbals

Analysis of the orbital temperature gradients which occur in both pitch and polar axes was performed on the original baseline configuration where the polar shaft was located at the center of the pitch axis. The models employed for this study are felt to be representative of the cantilever concept also. The cantilever design contains a shaft inside of the pitch housing whereas the original design which was analyzed did not. The presence of the shaft would dampen the response characteristics of the housing, thus the pitch axis analysis should be conservative.

TELESCOPE OBJECTIVE CLUSTER

TEMPERATURE, °F

0.4
0.2
92.0
0.8
0.6
0.4
0.2
91.0
0.8
0.6
0.4
0.2
90.0

CLUSTER
SUPPORT:
SUN SIDE
EAST/WEST
SHADE

←— SUNRISE   ←— SUNSET

0   3000   6000
SECONDS FROM SUNRISE

0   180°   360°

10307-81(U)
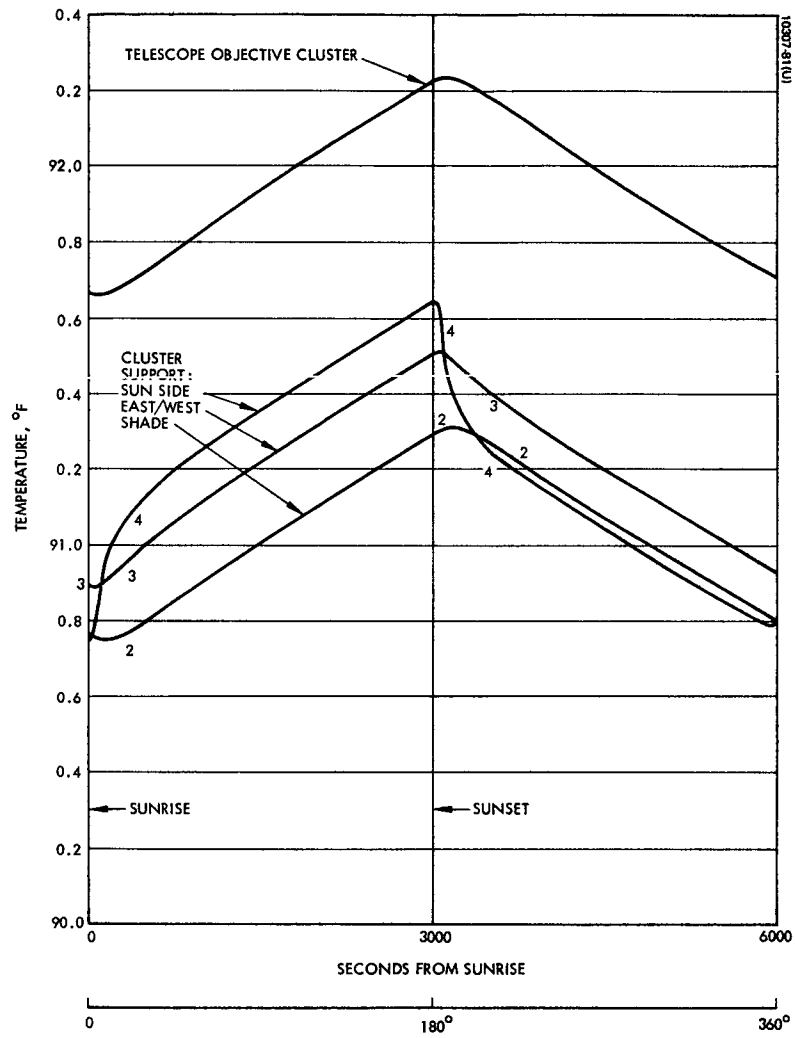
Figure 5.3-11.   Orbital Temperature Variation of Star
Sensor Cluster

Figure 5.3-12 shows the configuration and nodal locations used in this analysis. Boundary conditions are similar to those employed for the sensor head analysis. Conduction boundary conditions were determined from the bulk orbital analyses.

The orbital temperature histories of the circumferential sections through the east and west arms of the pitch axis are presented in Figure 5.3-13. In the original baseline configuration, the pitch axis gimbal motor (dissipating $.5^W$) was located at the end of the east arm and the inductosyn ($.1^W$) at the end of the west arm. The difference in heat dissipation levels associated with this design accounts for the east arm running warmer than the west arm (on the order of 1^oF). Detectable circumferential gradients require temperature resolution to hundreths of a degree as shown. The difference in amplitude and shape of the temperature responses is attributed to the conductive boundary conditions applied. The west arm is more sensitive to the solar load than the east arm because of its lower dissipation level. Bulk analysis showed the pitch motor to have a total temperature variation of 2^oF versus 1^oF for the inductosyn; these amplitudes are reflected in the data of Figure 5.3-13. The difference in the shape of the curves are probably due to the fact that the rate of temperature change for the west pitch axis is about twice that of the east pitch axis.

Figures 5.3-14 and 5.3-15 present the orbital temperature histories of the polar axis housing and inner gimbal respectively. Thermal modeling of the housing simulated conductive coupling to the pitch axis only from the east (node 21) and west (23) nodes. The temperature differential between these two nodes is attributed to the east arm of the pitch axis being warmer than the west arm as previously discussed. The shaded node (24) is shown to run warmer than both east and west nodes. All four nodes (21-24) were conductively coupled to the sensor head which was treated as a boundary condition. Since the system exhibits high conductance relative to the superinsulation blanket, heat flows from the sensor head to node 24, some of which is radiated, and the remainder conducted via nodes 21 and 23 to the pitch axis arm. It would be anticipated that node 24 should be the coolest, suggesting the modeling approach could be improved.
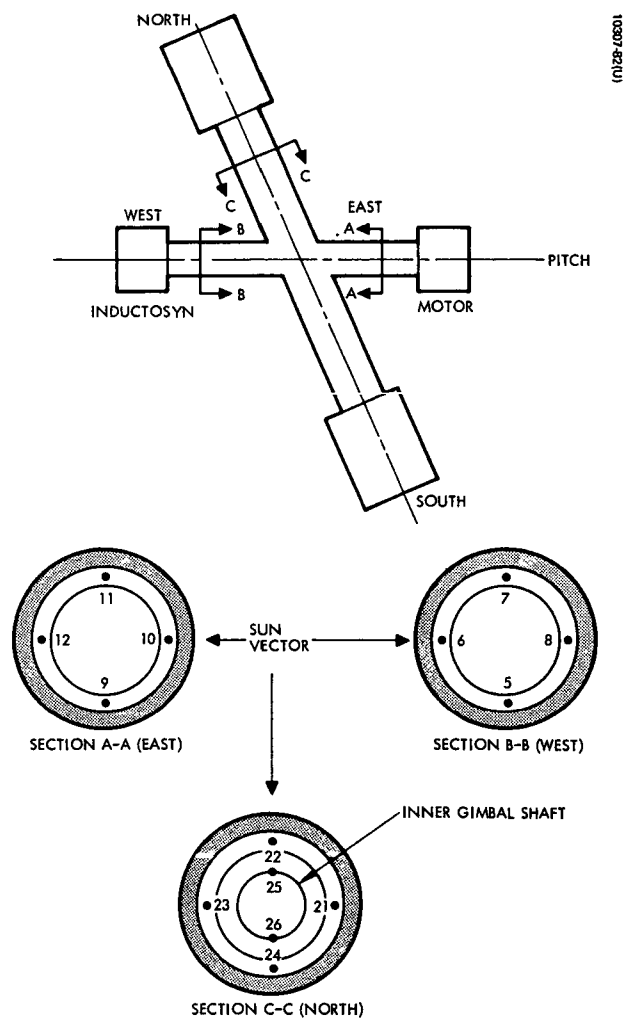
Figure 5.3-12.   Pitch and Polar Axes - Nodal Models
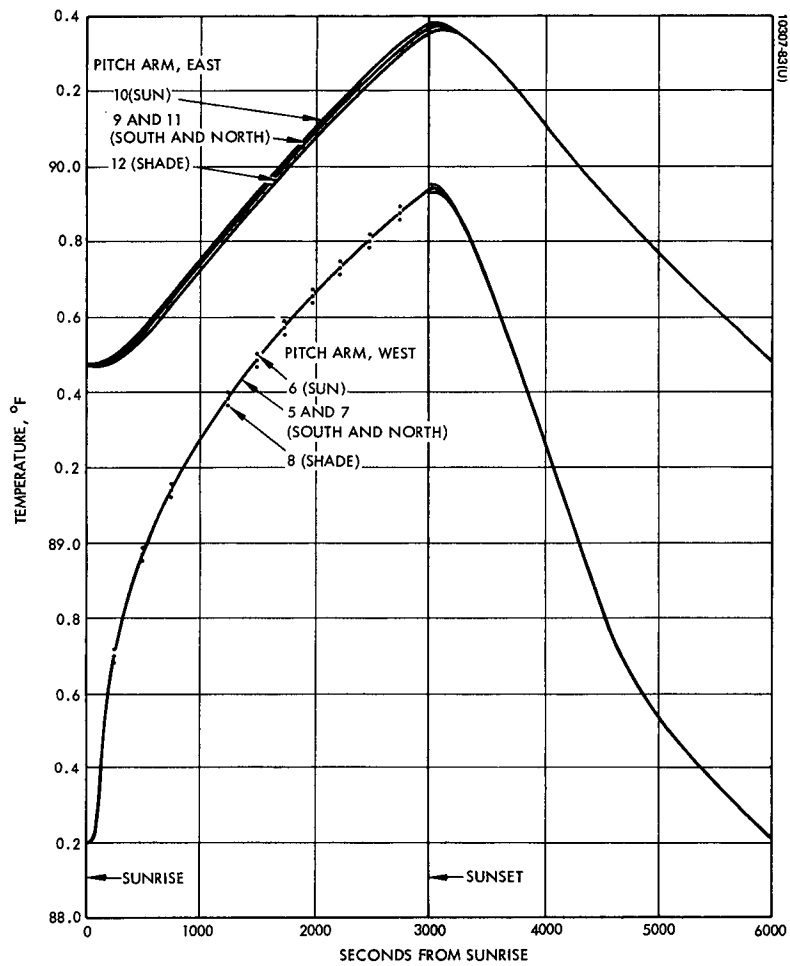
Figure 5.3-13. Temperatures on Pitch Arms of Outer Gimbal
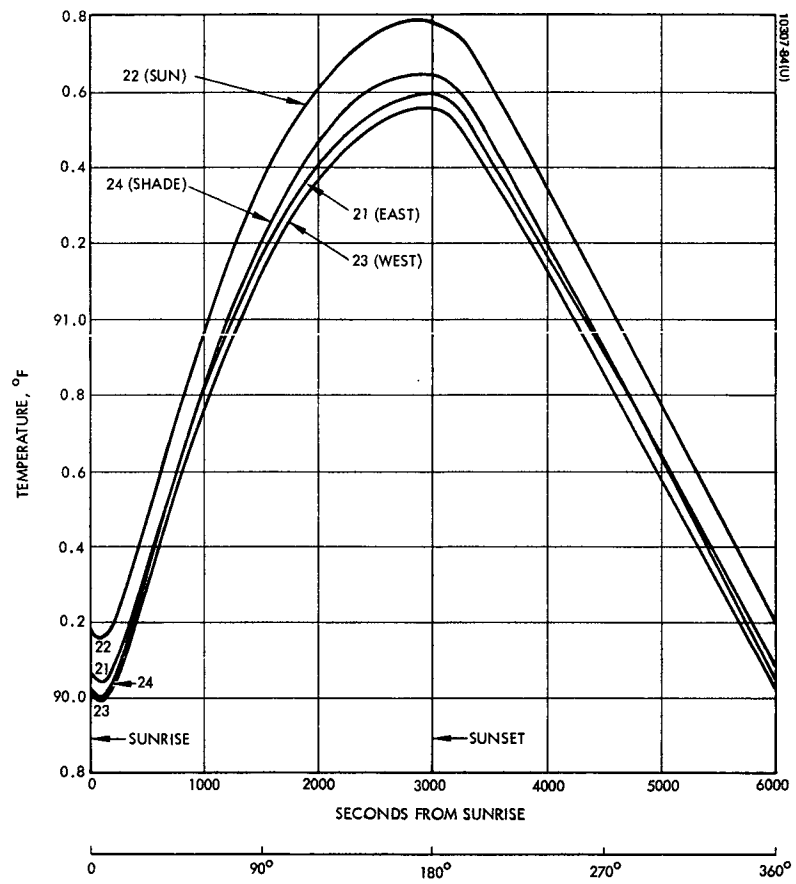
Figure 5.3-14. Temperatures on Polar Arm of Outer Gimbal

5-54
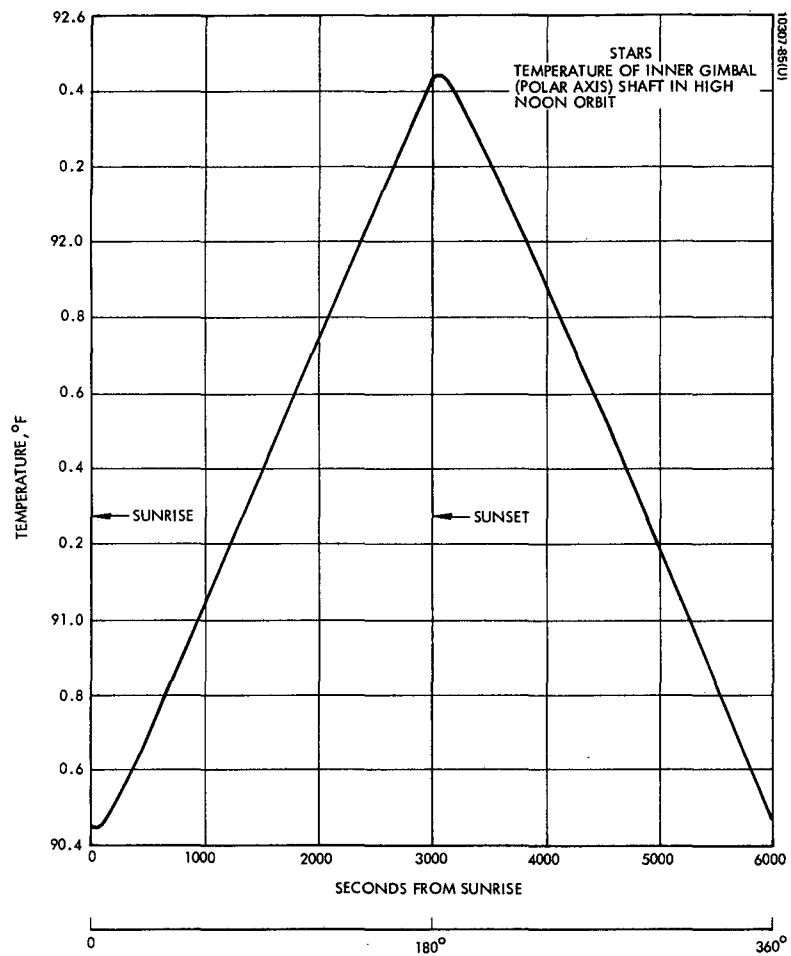
Figure 5.3-15. Temperature of Polar Axis Shaft

5.3.5.3.5 Conclusions

The thermal analysis has demonstrated the feasibility of maintaining adequate thermal control ($90 \pm 10°F$) of STARS under a reasonably wide spectrum of spacecraft and orbital environments. An assumed baseline design, directed towards minimizing circumferential temperature gradients, was employed for this study. Definition and implementation of a flight design will require specification of vehicle configuration temperatures and orbital parameters. If the flight design employs a superinsulation blanket, developmental testing should be performed to insure the desired effective emittance is attained.

Circumferential temperature gradients around the sensor head, and the pitch and polar axes were determined and found to induce angular position errors within the allocated budget. The computed temperature profiles required definition to hundreths of a degree to detect temperature differences. The accuracy of this level of definition is unknown; typically, such data is rounded off to the nearest degree for interpretation and evaluation. The conservatism of the nodal models employed should have produced worst case results, use of the data assumed this to be true.

The magnitude of the allowable gradients (less than $0.1°F$ per inch) precludes direct test verification. In addition to measurement inaccuracies, precise simulation of environmental conditions would be difficult. A possible approach to determining the magnitude of thermally induced pointing errors would be to compare measured errors exhibited under two different thermal conditions. The desired data might be provided by comparison of the pointing error when STARS is subjected to a uniform thermal environment with that occurring in a simulated solar radiation environment. Definition of such a program would require additional analysis and considerable planning and pretesting.

5.3.5.4 Distortion Determination

The temperature gradients obtained from the STARS nodal simulation were applied to the geometries of the appropriate STARS components. The computed gradient was assumed to act over the entire length of each nodal component; conservative analytical approximations to the actual geometries were made, and all components were assumed to be made from beryllium. The respective internal and external gradients were not available for all nodes, but conservative approximations of the gradient values were assigned.

The results of the thermal distortion analysis are given in Tables 5.3-7 and 5.3-8 for the north star sensor cluster. For the south star sensor cluster the errors EY7GR, EY7SR (support) and EY7SR (spacer) are the opposite polarity to those listed.

Errors EX5GR and EZ5GR are distortions of the base. The calculations of temperature were based on the section being one leg of the outer gimbal of the original baseline configuration as shown in Figure 5.3-12. The outer gimbal does not rotate at orbital rate as does the base. The thermal lag in the base will cause some error in the use of outer gimbal temperatures for the base. As seen in Figure 5.3-13, the thermal lag is small. The difference in EX5GR and EZ5GR with the seasons will be essentially as in Table 5.3-8.

The change in relative ascension of the sun with respect to the outer gimbal is less than 6° for the three orbits considered. See Figure 5.2-6. This slight offset about the Z7 axis was not taken into account.

The error due to thermal distortion of the outer gimbal (pitch axis) shaft EZ6GR, was taken to be twice that of the inner gimbal (polar axis) shaft EY7GR because of the cantilever design. Both are insignificant because of the thick-walled beryllium construction and the thermal shielding provided by the surrounding housings and thermal insulation blankets. It will be necessary to use care in the design of the slip rings and other features to avoid non-symmetries in shaft cross-sections which may cause greater thermal non-symmetry than the sun load.

Note in Table 5.3-7 that the error due to thermal distortion of the spacer in the star sensor cluster is of opposite sign to the thermal distortion error of the support. This is because the mirrors mount on the support and the objectives mount on the other side of the spacer. See Figure 5.3-2. The potential for self-compensation is evident.

TABLE 5.3-7. THERMAL DISTORTION, VERNAL EQUINOX

Angle ∅ deg	ERROR ANGLES IN MICRORADIANS						
	EX5GR	EZ5GR	EZ6GR	EY6GR	EY7GR	EY7SR Support	EY7SR Spacer
15	<.001	-.101	.006	<.001	.003	.205	-1.709
30	<.001	-.102	.004	<.001	.002	.225	-2.053
45	<.001	-.102	.004	<.001	.002	.230	-2.120
60	<.001	-.102	.004	<.001	.002	.230	-2.133
75	<.001	-.102	.004	<.001	.002	.230	-2.135
90	<.001	-.102	.004	<.001	.002	.230	-2.136
105	<.001	-.102	.004	<.001	.002	.230	-2.135
120	<.001	-.102	.004	<.001	.002	.230	-2.135
135	<.001	-.102	.004	<.001	.002	.230	-2.136
150	<.001	-.102	.004	<.001	.002	.230	-2.135
165	<.001	-.102	.004	<.001	.002	.231	-2.135
180	<.001	-.102	.006	<.001	.003	.230	-2.135
195	<.001	-<.001	.004	<.001	.002	.017	-.264
210	<.001	-<.001	.006	<.001	.003	-.006	.111
225	<.001	-<.001	.004	<.001	.002	-.011	.184
240	<.001	-<.001	.004	<.001	.002	-.011	.198
255	<.001	-<.001	.004	<.001	.002	-.011	.201
270	<.001	-<.001	.004	<.001	.002	-.011	.199
285	<.001	-<.001	.004	<.001	.002	-.012	.201
300	<.001	-<.001	.004	<.001	.002	-.012	.201
315	<.001	-<.001	.004	<.001	.002	-.011	.201
330	<.001	-<.001	.004	<.001	.002	-.012	.201
345	<.001	-<.001	.004	<.001	.002	-.011	.201
360	<.001	-.012	.004	<.001	.002	.066	.072

TABLE 5.3-8. THERMAL DISTORTION OF BASE

FOR THREE ORBITS

Angle ϕ deg	ERROR ANGLES IN MICRORADIANS					
	EX5GR			EX5GR		
	Equinox	Summer	Nov 6	Equinox	Summer	Nov 6
15	<.001	.040	-.029	-.101	-.093	-.097
30	<.001	.041	-.029	-.102	-.093	-.098
45	<.001	.041	-.029	-.102	-.093	-.098
60	<.001	.041	-.029	-.102	-.093	-.098
75	<.001	.041	-.029	-.102	-.093	-.098
90	<.001	.041	-.029	-.102	-.093	-.098
105	<.001	.041	-.029	-.102	-.093	-.098
120	<.001	.041	-.029	-.102	-.093	-.098
135	<.001	.041	-.029	-.102	-.093	-.098
150	<.001	.041	-.029	-.102	-.093	-.098
165	<.001	.041	-.029	-.102	-.093	-.098
180	<.001	.041	-.029	-.102	-.093	-.098
195	<.001	<.001	<.001	-.001	-.001	-.001
210	<.001	<.001	<.001	-<.001	-<.001	-<.001
225	<.001	<.001	<.001	-<.001	-<.001	-<.001
240	<.001	<.001	<.001	-<.001	-<.001	-<.001
255	<.001	<.001	<.001	-<.001	-<.001	-<.001
270	<.001	<.001	<.001	-<.001	-<.001	-<.001
285	<.001	<.001	<.001	-<.001	-<.001	-<.001
300	<.001	<.001	<.001	-<.001	-<.001	-<.001
315	<.001	<.001	<.001	-<.001	-<.001	-<.001
330	<.001	<.001	<.001	-<.001	-<.001	-<.001
345	<.001	<.001	<.001	-<.001	-<.001	-<.001
360	<.001	.005	.003	-.012	-.011	-.011

TABLE 5.3-9

STELLAR PARALLAX AND PROPER MOTION

Tracker No.	Star Name	Distance parsec	Parallax Semimajor Axis, arc seconds	Proper Motion sec/year
1	Cih			
2	Phecda			
3	Arcturus	11	0.09	2.28
4	Altair	5.1	0.20	0.66
5	Achernar	20	0.50	0.10
6	Rigel	250	0.004	0.00
7	Delta Vela			
8	Peacock			

5.3.6 Error Sources Outside the STARS System

Following are some errors which will affect the accuracy of the STARS system in use but which are not accounted for in the error analysis.

1. Ephemeris data of spacecraft:

   orbital coordinates, time, anomalies, variation in latitude

2. Ephemeris data of stars (data in seconds of arc):

   - precession of the equinoxes (general precession):

     - Lunisolar (precession of the celestial pole):

       - mean: 50" per year

       - nutation: 9.2" semimajor axis, 18.6 year period

     - planetary (precession of the ecliptic pole): about 1.2" per year

   - stellar aberration: 20.5" for stars perpendicular to earth's velocity in orbit

   - stellar parallax due to earth's position in orbit: See Table 5.3-9.

   - proper motion of a star with respect to the local standard of rest: See Table 5.3-9.

   - variation in latitude (movement of the earth with respect to its poles):

     - 12 month period: 0.2" diameter

     - 14 month period: 0.1" to 0.5" diameter

     - secular: 0.003" per year

   - accuracy of known position: 0.1" to 0.01"

3. Time: One second of time is equivalent to 15 arc seconds of rotation of the earth. Ephemeris time progresses at a precisely uniform rate and is based on gravitational theory and the length of the tropical year in 1900. Mean solar time is based on the earth's current tropical year. The two kinds of time have an accumulated difference in 1970 of more than 30 seconds.

TABLE 5.4-1. TRANSFORMATION OF ERROR ANGLES INTO ROLL, PITCH AND YAW

COORDINATE SET	TRANSFORMATION FROM HIGHER-NUMBERED SET
9 Star Tracker	$EX9 = -EDA \sin(D + DD)$ $EY9 = -ED - EDD$ $EZ9 = EDA \cos(D + DD)$
8 Inner Gimbal	$EX8 = EX9 \cos A - EY9 \sin A$ $EY8 = EY9 \cos A + EX9 \sin A$ $EZ8 = EZ9$
7 Outer Gimbal	$EX7 = EX8 \cos I + EY8 \sin I$ $EY7 = EY8 \cos I - EX8 \sin I$ $EZ7 = EZ8$
6 Outer Gimbal	$EX6 = EX7$ $EY6 = EY7 \sin CLN + EZ7 \cos CLN$ $EZ6 = EZ7 \sin CLN - EY7 \cos CLN$
5 STARS Base	$EX5 = EY6 \cos \phi - EZ6 \sin \phi$ $EY5 = EY6$ $EZ5 = EZ6 \cos \phi + EX6 \sin \phi$
4 True Spacecraft	$ER = EX5$ $EP = -EY5$ $\Big\}$ using small angle approximations $EY = -EZ5$

5.4   Solution of Error Model

5.4.1   Transformations

The errors gathered in the various coordinate sets were transformed into roll, pitch and yaw errors using the expressions in Table 5.4-1. The errors of each of the three types (bias, thermal distortion, uncertainty) and of each of the four subsystems (star sensors, gimbals, encoders, control system) were transformed into errors about the roll, pitch and yaw axes. It was assumed that the vehicle control system acts so as to reduce the attitude error signals generated by the STARS to a mean value of zero.

5.4.2   Stars in Use

An important factor in determining errors vs position in orbit is the choice of which two stars are being used to generate spacecraft attitude error signals at that time. Tables 5.4-2, 5.4-3 and 5.4-4 show the stars that are visible at the 45° increments around the three chosen orbits. These stars were determined by an overlay of orbit C (southbound in the sun) on the star visibility chart. The two brightest stars visible at any point were used in the error analysis.

5.4.3   Offset Tracking

The error in the inclination angle of the orbit is likely to be more influenced by the launch and injection parameters than by the accuracy with which the inclination angle is machined into the gimbals. The offsets required between the tracker line of sight and the star line of sight for 0, $.25^{\circ}$ and $.5^{\circ}$ errors in inclination at the vernal equinox are shown in Table 5.4-5   along with the errors which are sensitive to this offset. The offset tracking angles and the errors at the star tracker are not influenced by the outer gimbal angle. The expressions used to calculate the offset tracking angles are:

$$DA = -ECLN \cos (A - I) \sin D$$
$$DD = ECLN \sin (A - I)$$

TABLE 5.4-2. ANGLE NOISE VS POSITION IN ORBIT, VERNAL EQUINOX

OUTER GIMBAL ANGLE, DEG	STARS VISIBLE TO TRACKER NO.		BRIGHTEST STAR			NEXT BRIGHTEST STAR		
	NORTH CLUSTER	SOUTH CLUSTER	NAME	TRACKER NO.	NOISE, μrad	NAME	TRACKER NO.	NOISE, μrad
45	1,4	-	Altair	4	2.25	Cih	1	3.43
90	1,4	5,8	Achernar	5	1.57	Altair	4	2.25
135	4	5,8	Achernar	5	1.57	Altair	4	2.25
180	-	5,7,8	Achernar	5	1.57	Peacock	8	3.66
225	3	7,8	Arcturus	3	1.99	Peacock	8	3.66
270	2,3	7	Arcturus	3	1.99	Delta Vela	7	3.93
315	1,2,3	-	Arcturus	3	1.99	Cih	1	3.43
360	1,2	-	Cih	1	3.43	Phecda	2	5.51

TABLE 5.4-3. ANGLE NOISE VS POSITION IN ORBIT, SUMMER SOLSTICE

OUTER GIMBAL ANGLE, DEG	STARS VISIBLE TO TRACKER NO.		BRIGHTEST STAR			NEXT BRIGHTEST STAR		
	NORTH CLUSTER	SOUTH CLUSTER	NAME	TRACKER NO.	NOISE, μ rad	NAME	TRACKER NO.	NOISE, μrad
45	1,2	6	Rigel	6	1.47	Cih	1	3.43
90	-	5,6,7	Rigel	6	1.47	Achernar	5	1.57
135	-	5,6,7,8	Rigel	6	1.47	Achernar	5	1.57
180	-	5,7,8	Achernar	5	1.57	Peacock	8	3.66
225	4	5,8	Achernar	5	1.57	Altair	4	2.25
270	3,4	8	Arcturus	3	1.99	Altair	4	2.25
315	1,2,3,4	-	Arcturus	3	1.99	Altair	4	2.25
360	1,2,3	-	Arcturus	3	1.99	Cih	1	3.43

TABLE 5.4-4. ANGLE NOISE VS POSITION IN ORBIT, NOVEMBER 6

| OUTER GIMBAL ANGLE, DEG | STARS VISIBLE TO TRACKER NO. | | BRIGHTEST STAR | | | NEXT BRIGHTEST STAR | | |
	NORTH CLUSTER	SOUTH CLUSTER	NAME	TRACKER NO.	NOISE μrad	NAME	TRACKER NO.	NOISE, μrad
45		-	Arcturus	3	1.99	Altair	4	2.25
90	2,3	-	Arcturus	3	1.99	Phecda	2	5.51
135	3	7,8	Arcturus	3	1.99	Peacock	8	3.66
180	-	5,6,7,8	Rigel	6	1.47	Achernar	5	1.57
225	-	5,6,7,7	Rigel	6	1.47	Achernar	5	1.57
270	1	5,6	Rigel	6	1.47	Achernar	5	1.57
315	1	6	Rigel	6	1.47	Cih	1	3.43
360	1,2,3,4	-	Arcturus	3	1.99	Altair	4	2.25

TABLE 5.4-5.   OFFSET TRACKING ANGLES AND ERRORS AT VERNAL EQUINOX

| Tracker No. | ECLN deg. | DA deg. | DD deg. | ERRORS IN MICRORADIANS | | | | | |
| | | | | EDAS | | | EDDS | | |
				Misalign.	Quant.	RSS	Misalign.	Quant.	RSS
All	0	0	0	0	.66	.66	0	.66	.66
1	.25	-.21	.06	.56	.62	.84	.56	.66	.86
2		.20	.01	.51	.63	.81	.51	.66	.84
3		.07	-.14	.39	.66	.76	.39	.65	.75
4		-.02	-.22	.56	.66	.87	.56	.62	.84
5		.19	.10	.55	.63	.84	.55	.65	.85
6		.01	.24	.62	.66	.91	.62	.61	.87
7		-.13	.19	.58	.65	.97	.58	.63	.86
8		.12	-.20	.60	.65	.88	.60	.63	.87
1	.50	-.42	.12	1.11	.52	1.23	1.11	.65	1.29
2		.40	.02	1.02	.53	1.15	1.02	.66	1.22
3		.14	-.28	.78	.65	1.01	.78	.60	.99
4		-.04	-.44	1.13	.66	1.31	1.13	.51	1.24
5		.38	.21	1.10	.54	1.23	1.10	.63	1.27
6		.01	.49	1.24	.66	1.40	1.24	.47	1.33
7		-.27	.38	1.17	.60	1.32	1.17	.55	1.29
8		.24	-.41	1.20	.61	1.35	1.20	.53	1.31

The expressions for the offset tracking errors are:

$$EDAS = \left[(145 \text{ DA})^2 + (145 \text{ DD})^2 + (.66 \cos 90 \text{ DA})^2 \right]^{1/2}$$

$$EDDS = \left[(145 \text{ DD})^2 + (145 \text{ DA})^2 + (.66 \cos 90 \text{DA})^2 \right]^{1/2}$$

The first two terms in each expression are due to misalignment of the reticle slits and the third term will be recognized as the quantization error.

5.4.4   Thermal Distortion

The thermal distortion errors listed in the following tables of errors for the star sensor, gimbal, encoder and control system, subsystems of the STARS were kept separate from the bias and random errors because the thermal distortion errors have specific predicted magnitudes and polarities and are thus transformed and summed algebraically.

The equations used to transform the errors to the roll, pitch and yaw axes are:

$$EZ6 = -EY7 \cos CLN + EZ6$$
$$ER = -EZ6 \sin \phi + EX5$$
$$EP = -Y7 \sin CLN$$
$$EY = -EZ6 \cos \phi - EZ5$$

These expressions are derived from the basic transformations in Table 5.4-1. The terms on the right in three of the four equations are terms which originate on the indicated axis and add to those terms which originate on higher numbered axes and are transformed into the indicated axis.

The polarity of the EY7 error was reversed for star trackers in the south polar sensor cluster to account for the fact that both clusters warp away from the sun. Thus, the thermal distortion errors tend to cancel for the positions in orbit where a star from the north cluster is being used with a star from the south cluster.

Generally it will be noted that the thermal distortion errors are not a significant part of the total error.

5.4.5   Star Sensors

The errors originating in the north and south star sensor cluster assemblies are listed in Tables 5.4-6, 5.4-7 and 5.4-8 for the three orbits considered. The error coefficients from Section 5.4-1 were transformed to the vehicle (STARS base) roll, pitch and yaw axes using the expressions of Table 5.4-1. The bias, thermal distortion and random errors have been separately compiled.

The bias errors are considered to be compensatable if adequate computer capability were available. The thermal distortion errors might also be largely compensated if suitable test techniques could be developed. The errors would then be dominated by the random errors. The random error is dominated by signal processing errors, see Table 5.3-1, but with appreciable error in the tracking loop noise for the weaker stars.

The data in Tables 5.4-6, 5.4-7 and 5.4-8 varies considerably with the outer gimbal angle ϕ for a given star. This is because polarities were observed in the use of the transformations for set 5 in Table 5.4-1. The terms might have been root-sum-squared. The rms value for a complete orbit would not be significantly different. The use of the specific polarities accounts for the sinusoidal variation in roll and yaw data for bias and random which is apparent for tracker No. 4 in Table 5.4-6. Note that the bias and random pitch errors for a given star tracker do not vary with pitch rotation ϕ.

The polarity of the thermal distortion is indicated in the tables because the thermal distortion errors have a specific predicted polarity.

The bias, thermal distortion and random errors were root-sum-squared to obtain the summations shown. At $\phi = 45^{\circ}$ the roll error due to the star sensor assemblies using tracker No. 1 (star Cih) is 6.33 microradians. Due to the relative angles, the error for tracker No. 4 is 11.87 microradians even though Altair is brighter than Cih. If these were the only system errors, wer might average 6.33 and 11.87 to obtain the roll error. The rms of such averages for a complete orbit at the vernal equinox is 7.36 μrad in roll, 8.86 μrad in pitch and 4.97 μrad in yaw.

TABLE 5.4-6. ERRORS IN STAR SENSORS, VERNAL EQUINOX

OUTER GIMBAL DEG	STAR TRACKER NO.	BIAS Microradians			THERMAL DISTORTION Microradians			RANDOM Microradians			Summation (RSS) Microradians		
		ERSB	EPSB	EYSB	ERSR	EPSR	EYSR	ERSU	EPSU	SYSU	ERS	EPS	EYS
45	1	4.39	8.23	1.35	.19	1.67	.19	4.55	8.53	1.40	6.3?	12.00	1.95
	4	6.21	2.83	.10	.19	1.87	.19	3.57	2.?5	.10	11.87	4.50	.24
90	4	5.73	2.83	5.87	.27	1.89	.00	5.98	2.95	6.13	8.29	4.50	8.49
	5	2.70	3.76	6.98	-.33	-2.34	.00	2.83	3.93	7.31	3.93	5.92	10.11
135	4	.10	2.83	8.21	.19	1.89	-.19	.10	2.95	5.57	.24	4.50	11.87
	5	6.85	3.76	3.02	-.25	-2.34	.23	7.17	3.93	3.17	9.92	5.92	4.38
180 Sunset	5	6.98	3.76	2.70	.00	-2.34	.33	7.31	3.93	2.83	10.11	5.92	3.93
	8	2.18	9.02	2.46	.00	-2.34	.33	2.25	9.34	2.55	3.13	13.19	3.56
225	3	5.78	5.28	3.41	.02	-.17	-.02	6.06	5.52	3.57	8.38	7.64	4.94
	8	3.28	9.02	.29	-.02	.19	-.02	3.40	9.34	.21	4.72	12.99	.29
270	3	6.50	5.28	1.68	.03	-.19	.00	6.80	5.52	1.76	9.41	7.64	2.43
	7	5.22	8.16	1.54	-.03	.21	.00	5.40	8.44	1.59	7.51	11.74	2.21
315	1	1.35	8.23	4.39	.02	-.19	-.02	1.40	8.53	4.55	1.95	11.86	6.32
	3	3.41	5.28	5.78	.02	-.19	-.02	3.57	5.52	6.06	4.94	7.64	8.38
360 Sunrise	1	4.06	3.23	2.15	.00	-.14	-.02	4.21	8.53	2.23	5.85	11.85	3.10
	2	6.68	6.98	5.70	.00	-.14	-.02	6.85	7.17	5.86	9.57	10.01	0.18

TABLE 5.4-7. ERRORS IN STAR SENSORS, SUMMER SOLSTICE

OUTER GIMBAL DEG	STAR TRACKER NO.	BIAS Microradians			THERMAL DISTORTION Microradians			RANDOM Microradians			Summation (RSS) Microradians		
		ERSB	EPSB	EYSB	ERSR	EPSR	EYSR	ERSU	EPSU	EYSU	ERS	EPS	EYS
45	1	8.26	3.55	3.84	.19	1.87	.19	3.56	3.68	2.94	11.90	5.44	4.09
	6	3.75	6.67	3.23	-.23	-2.33	-.23	3.94	7.02	3.39	5.44	9.96	4.69
90	5	2.17	7.38	3.34	-.33	-2.34	.00	2.27	7.72	3.50	3.16	10.93	4.84
	6	4.93	6.67	.37	-.33	-2.34	.00	5.19	7.02	.39	7.17	9.96	.54
135	5	.83	7.38	3.90	-.23	-2.34	.23	.87	7.72	4.08	1.22	10.93	5.65
	6	3.23	6.67	3.75	-.23	-2.34	.23	3.39	7.02	3.94	4.69	9.96	5.44
180 Sunset	5	3.34	7.38	2.17	.00	-2.34	.33	3.50	7.72	2.27	4.84	10.93	3.16
	8	8.58	1.64	3.96	.00	-2.34	.33	3.89	1.70	4.11	12.36	3.33	5.72
225	4	6.22	4.96	3.41	.02	-.17	.02	6.51	5.20	3.57	9.00	7.19	4.94
	5	3.90	7.38	.83	-.02	.19	-.02	4.08	7.72	.87	5.64	10.68	1.20
270	3	5.87	.85	6.16	.03	-.19	.00	6.14	.88	6.44	8.50	1.24	8.91
	4	6.81	4.96	1.99	.03	-.19	.00	7.13	5.20	2.08	9.86	7.19	2.88
315	3	8.51	.85	.20	.02	-.19	-.02	3.59	.88	.21	12.31	1.24	.24
	4	3.41	4.96	6.22	.02	-.10	-.02	3.57	5.20	6.51	4.94	7.19	9.00
360 Sunrise	1	7.85	3.55	3.84	.00	-.14	-.02	8.14	3.68	3.98	11.31	5.12	5.53
	3	6.16	.85	5.87	.00	-.14	-.02	6.44	.88	6.14	8.91	1.23	8.50

TABLE 5.4-8. ERRORS IN STAR SENSORS, NOVEMBER 6

OUTER GIMBAL DEG	STAR TRACKER NO.	BIAS Microradians			THERMAL DISTORTION Microradians			RANDOM Microradians			Summation (RSS) Microradians		
		ERSB	EPSB	EYSB	ERSR	EPSR	EYSR	ERSU	EPSU	EYSU	ERS	EPS	EYS
45	3	5.67	6.25	1.21	.19	1.87	.19	5.94	6.55	1.27	8.21	9.25	1.76
	4	.04	3.60	7.91	.19	1.87	.19	.04	3.76	8.25	.20	5.53	11.43
90	2	4.55	1.39	10.17	.27	1.89	.00	4.67	1.43	10.43	6.53	2.75	14.57
	3	4.87	6.25	3.15	.27	1.89	.00	5.10	6.55	3.30	7.06	9.25	4.56
135	3	1.21	6.25	5.67	.19	1.89	-.19	1.27	6.55	5.94	1.76	9.25	8.21
	8	8.44	3.94	2.32	-.23	-2.34	.23	8.74	4.08	2.40	12.15	6.14	3.35
180 Sunset	5	2.57	6.79	4.18	.00	-2.34	.33	2.69	7.10	4.38	3.72	10.10	6.06
	6	3.94	3.60	6.38	.00	-2.34	.33	4.14	3.78	6.70	5.72	5.72	9.26
225	5	4.78	6.79	1.14	-.02	.19	-.02	5.00	7.10	1.19	6.92	9.83	1.65
	6	7.30	3.60	1.73	-.02	.19	-.02	7.67	3.78	1.81	10.59	5.22	2.50
270	5	4.18	6.79	2.57	-.03	.21	.00	4.38	7.10	2.69	6.06	9.83	3.72
	6	6.38	3.60	3.94	-.03	.21	.00	6.70	3.78	4.14	9.25	5.22	5.72
315	1	8.51	2.19	3.41	.02	-.19	-.02	8.82	2.27	3.54	12.26	3.16	4.92
	6	1.73	3.60	7.30	-.02	.21	.02	1.81	3.78	7.67	2.50	5.22	10.59
360 Sunrise	3	3.15	6.25	4.87	.00	-.14	-.02	3.30	6.55	5.10	4.56	9.06	7.05
	4	5.56	3.60	5.62	.00	-.14	-.02	5.80	3.76	5.86	8.04	5.21	8.12

5-72

6

The star sensors are thus generally within the preliminary allocation of 8.72 μrad per axis to a subsystem.

5.4.6   Gimbals

The errors originating in the gimbals are listed in Tables 5.4-9, 5.4-10 and 5.4-11. For the bias and random errors in these tables the terms of the expressions in Table 5.4-1 were root-sum-squared with the errors which originated about a given axis.
For example:

$$ER = EX5 = \sqrt{(EX6 \cos \phi)^2 + (EZ6 \sin \phi)^2 + EX5^2}$$

where the term EX5 under the radical sign might be a thermal distortion such as seen in Figure 5.3-1 a) and the other two terms are components of other errors transformed from coordinate sets 6, 7, 8 and 9. This formulation does not so clearly show the propagation of errors through the system but it avoids the pile-up of errors which occurs at certain angles when positive polarity is arbitrarily assigned to errors with random polarity.

The gimbal errors tend to be larger than the preliminary allocation of 8.72 μrad. The primary cause of this error is the estimate for dimensional stability in 5.3.2.3. This indicates that dimensional stability must indeed be a prime subject for further investigation.

5.4.7   Encoders

Table 5.4-12 shows the errors due to the encoders at the vernal equinox and the summer solstice. The errors at these dates are the same because a phase angle of 45° was arbitrarily chosen for the "typical" bias errors. The rms value of the inner gimbal error is used at these dates as seen in the expressions used to calculate bias errors.

TABLE 5.4-9. ERRORS IN GIMBALS, VERNAL EQUINOX

Outer Gimbal deg	Star Tracker No.	Bias Microradians			Thermal Distortion Microradians			Random Microradians			Summation (RSS) Microradians		
		ERGB	EPGB	EYGB	ERGR	EPGR	EYGR	ERGU	EPGU	EYGU	ERG	EPG	EYG
45	1	5.17	4.82	5.17	.00	.00	.10	8.20	8.22	8.20	9.69	9.53	9.69
	4	5.17	4.82	5.17	.00	.00	.10	8.20	8.22	8.20	9.69	9.53	9.69
90	4	4.79	4.82	5.53	.00	.00	.10	6.86	8.22	9.36	8.37	9.53	10.87
	5	4.79	4.82	5.53	.00	.00	.10	7.85	8.23	9.36	9.20	9.54	10.87
135	5	5.17	4.82	5.17	.00	.00	.11	8.64	8.23	8.64	10.07	9.54	10.07
	8	5.17	4.82	5.17	.00	.00	.11	8.64	8.23	8.64	10.07	9.54	10.07
180 Sunset	5	5.53	4.82	5.17	.00	.00	.11	9.36	8.23	7.85	10.87	9.54	9.20
	8	5.53	4.82	5.17	.00	.00	.11	9.36	8.23	7.85	10.87	9.54	9.20
225	3	5.17	4.82	5.17	.00	.00	.00	8.20	8.22	8.20	9.69	9.53	9.69
	8	5.17	4.82	5.17	.00	.00	.00	8.64	8.23	8.64	10.07	9.54	10.07
270	3	4.79	4.82	5.53	.00	.00	.00	6.86	8.22	9.36	8.37	9.53	10.87
	7	4.79	4.82	5.53	.00	.00	.00	7.85	8.23	9.36	9.20	9.54	10.87
315	2	5.17	4.82	5.17	.00	.00	.00	8.20	8.22	8.20	9.69	9.53	9.69
	3	5.17	4.82	5.17	.00	.00	.00	8.20	8.22	8.20	9.69	9.53	9.69
360 Sunrise	1	5.53	4.82	4.79	.00	.00	.01	9.36	8.22	6.86	10.87	9.53	8.37
	3	5.53	4.82	4.79	.00	.00	.01	9.36	8.22	6.86	10.87	9.53	8.37

TABLE 5.4-10. ERRORS IN GIMBALS, SUMMER SOLSTICE

Outer Gimbal deg	Star Tracker No.	Bias Microradians			Thermal Distortion Microradians			Random Microradians			Summation (RSS) Microradians		
		ERGB	EPGB	EYGB	ERGB	EPGR	EYGR	ERGU	EPGU	EYGU	ERG	EPG	EYG
45	1	5.17	4.82	5.17	.04	.00	.09	8.20	8.22	8.20	9.69	9.53	9.69
	6	5.17	4.82	5.17	.04	.00	.09	8.64	8.23	8.64	10.07	9.54	10.07
90	5	4.79	4.82	5.53	.04	.00	.09	7.85	8.23	9.36	9.20	9.54	10.87
	6	4.79	4.82	5.53	.04	.00	.09	7.85	8.23	9.36	9.20	9.54	10.87
135	5	5.17	4.82	5.17	.04	.00	.10	8.64	8.23	8.64	10.07	9.54	10.07
	6	5.17	4.82	5.17	.04	.00	.10	8.64	8.23	8.64	10.07	9.54	10.07
180 Sunset	5	5.53	4.82	4.79	.04	.00	.10	9.36	8.23	7.85	10.87	9.54	9.20
	8	5.53	4.82	4.79	.04	.00	.10	9.36	8.23	7.85	0.87	9.54	9.20
225	4	5.17	4.82	5.17	.00	.00	.00	8.20	8.22	8.20	9.69	9.53	9.71
	5	5.17	4.82	5.17	.00	.00	.00	8.64	8.23	8.64	10.07	9.54	10.07
270	3	4.79	4.82	5.53	.00	.00	.00	6.86	8.22	9.36	8.37	9.53	10.87
	4	4.79	4.82	5.53	.00	.00	.00	6.86	8.22	9.36	8.37	9.53	10.87
315	3	5.17	4.82	5.17	.00	.00	.00	8.20	8.22	8.20	9.69	9.53	9.69
	4	5.17	4.82	5.17	.00	.00	.00	8.20	8.22	8.20	9.69	9.53	9.69
360 Sunrise	1	5.53	4.82	4.79	.01	.00	.01	9.36	8.22	6.86	10.87	9.53	8.37
	3	5.53	4.82	4.79	.01	.00	.01	9.36	8.22	6.86	10.87	9.53	8.37

TABLE 5.4-11. ERRORS IN GIMBALS, NOVEMBER 6

Outer Gimbal deg	Star Tracker No.	Bias Microradians			Thermal Distortion Microradians			Random Microradians			Summation (RSS) Microradians		
		ERGB	EPGB	EYGB	ERGR	EPGR	EYGR	ERGU	EPGU	EYGU	ERG	EPG	EYG
45	3	5.17	4.82	5.17	-.03	.00	.09	8.20	8.22	8.20	9.69	9.53	9.69
	4	5.17	4.82	5.17	-.03	.00	.09	8.20	8.22	8.20	9.69	9.53	9.69
90	2	4.79	4.82	5.53	-.03	.00	.10	6.86	8.22	9.36	8.37	9.53	10.87
	3	4.79	4.82	5.53	-.03	.00	.10	6.86	8.22	9.36	8.37	9.53	10.87
135	3	5.17	4.82	5.17	-.03	.00	.10	8.20	8.22	8.20	9.69	9.53	9.69
	8	5.17	4.82	5.17	-.03	.00	.10	8.64	8.23	8.64	10.07	9.54	10.07
180 Sunset	5	5.53	4.82	4.79	-.03	.00	.10	9.36	8.23	7.85	10.87	9.54	9.20
	6	5.53	4.82	4.79	-.03	.00	.10	9.36	8.23	7.85	10.87	9.54	9.20
225	5	5.17	4.82	5.17	.00	.00	.00	8.64	8.23	8.64	10.07	9.54	10.07
	6	5.17	4.82	5.17	.00	.00	.00	8.64	8.23	8.64	10.07	9.54	10.07
270	5	4.79	4.82	5.53	.00	.00	.00	7.85	8.23	9.36	9.20	9.54	10.87
	6	4.79	4.82	5.53	.00	.00	.00	7.85	8.23	9.36	9.20	9.54	10.87
315	1	5.17	4.82	5.17	.00	.00	.00	8.20	8.22	8.20	9.69	9.53	9.69
	6	5.17	4.82	5.17	.00	.00	.00	8.64	8.23	8.64	10.07	9.54	10.07
360	3	5.53	4.82	4.79	.00	.00	.01	9.36	8.22	6.86	10.87	9.53	8.37
Sunrise	4	5.53	4.82	4.79	.00	.00	.01	9.36	8.22	6.86	10.87	9.53	8.37

TABLE 5.4-12. ERRORS IN ENCODERS, VERNAL EQUINOX AND SUMMER SOLSTICE

Outer Gimbal deg	Bias Microradians			Random Microradians			Summation (RSS) Microradians		
	EREB	EPEB	EYEB	EREU	EPEU	EYEU	ERE	EPE	EYE
45	3.99	7.26	3.99	2.68	3.87	2.68	4.80	8.97	4.80
90	5.64	4.90	.00	3.79	3.87	.00	6.79	6.93	.00
135	3.99	-.79	-3.99	2.68	3.87	2.68	4.80	3.95	4.80
180 Sunset	.00	-6.48	-5.64	.00	3.87	3.79	.00	6.93	6.79
225	-3.99	-8.84	-3.99	2.68	3.87	2.68	4.80	8.97	4.80
270	-5.64	-6.48	.00	3.79	3.87	.00	6.79	6.93	.00
315	-3.99	-.79	3.99	2.68	3.87	2.68	4.80	3.95	4.80
360 Sunrise	.00	4.90	5.64	.00	3.87	3.79	.00	6.93	6.79

TABLE 5.4-13.   ERRORS IN ENCODERS, NOVEMBER 6

Outer Gimbal deg	Bias Microradians			Random Microradians			Summation (RSS) Microradians		
	EREB	EPEB	EYEB	EREU	EPEU	EYEU	ERE	EPE	EYE
45	-5.64	9.17	-5.54	2.68	3.87	2.68	6.24	9.00	6.24
90	-7.97	6.81	00	3.79	3.87	00	8.83	6.97	00
135	-5.64	1.12	5.64	2.68	3.87	2.68	6.24	4.03	6.24
180 Sunset	00	-4.57	7.97	00	3.87	3.79	00	6.97	8.83
225	5.64	-6.93	5.64	2.68	3.87	2.68	6.24	9.00	6.24
270	7.97	-4.57	00	3.79	3.87	00	8.83	6.97	00
315	5.64	1.12	-5.64	2.68	3.87	2.68	6.24	4.03	6.24
360 Sunrise	00	6.81	-7.97	00	3.87	3.79	00	6.97	8.83

$$E\phi EB = 8.05 \sin(\phi + 45^\circ) \qquad \text{outer gimbal}$$
$$EIEB = 8.05 \sin(I + 45^\circ) \qquad \text{inner gimbal}$$
$$EREB = EIEB \sin CLN \sin \phi \qquad \text{roll}$$
$$EPEB = EIEB \cos CLN + E\phi EB \qquad \text{pitch}$$
$$EYEB = EIEB \sin CLN \cos \phi \qquad \text{yaw}$$

The November 6 orbit picks up the peak inner gimbal error as seen in Table 5.4-13 The propagation of the bias errors in the system is easily seen and the opportunity for their compensation by the computer is clear.

For the random and rss summation columns the two terms of EPE were root-sum-squared instead of algebraically summed, accounting for the higher peak of pitch error in the bias column on November 6.

5.4.8   STARS Control System

Servo positioning errors are gimbal axis errors and the following expressions are used to transform them to spacecraft errors.

$$ERC = EIC \sin CLN \sin \phi$$
$$EPC = EIC \cos CLN + E\phi C$$
$$EYC = EIC \sin CLN \cos \phi$$

Note that the bias error, being a position "droop" has a fixed negative polarity on the gimbal angles ϕ and I, but the outer gimbal angle causes the roll and yaw errors to be alternated. Since the servo positioning errors are not a function of the gross inner gimbal angle, Table 5.4-14 shows the error for each of the three orbits.

5.4.9   Summation of Errors for STARS Subsystems

The errors listed in Tables 5.4-15, 5.4-16 and 5.4-17 were obtained for the previous listings for the subsystems as follows:

TABLE 5.4-14.   ERRORS IN STARS CONTROL SYSTEM

Outer Gimbal deg	Bias Microradians			Random Microradians			Summation (RSS) Microradians		
	ERCB	EPCB	EYCB	ERCU	EPCU	EYCU	ERC	EPC	EYC
45	-3.50	-4.30	-3.50	2.45	3.54	2.45	4.27	5.57	4.27
90	-4.95	-4.30	00	3.46	3.54	.00	6.04	5.57	.00
135	-3.50	-4.30	3.50	2.45	3.54	2.45	4.27	5.57	4.27
180 Sunset	.00	-4.30	4.95	.00	3.54	3.46	.00	5.57	6.04
225	3.50	-4.30	3.50	2.45	3.54	2.45	4.27	5.57	4.27
270	4.95	-4.30	.00	3.46	3.54	.00	6.04	5.57	.00
315	3.50	-4.30	-3.50	2.45	3.54	2.45	4.27	5.57	4.27
360 Sunrise	.00	-4.30	-4.95	.00	3.54	3.46	.00	5.57	6.04

5-80

TABLE 5.4-15. TOTAL STARS ERRORS, VERNAL EQUINOX

Outer Gimbal deg	Star Tracker No.	Bias Microradians			Thermal Distortion Microradians			Random Microradians			Summation (RSS) Microradians		
		ERTB	EPTB	EYTB	ERTR	EPTR	EYTR	ERTU	EPTU	EYTU	ERT	EPT	EYT
45	1	8.61	12.73	7.53	.18	1.87	.28	10.06	12.96	9.08	13.24	18.26	11.80
	4	11.06	10.12	7.41	.18	1.87	.28	12.40	10.19	8.97	16.62	14.48	11.64
90	4	10.59	8.59	8.06	.26	1.89	.10	10.45	10.19	11.19	14.88	13.46	13.79
	5	9.30	8.94	8.91	-.33	-2.34	.10	9.80	10.52	11.88	13.51	14.00	14.85
135	5	7.41	7.10	11.06	.18	1.89	-.08	9.37	10.20	12.70	11.95	12.57	16.84
	8	10.09	7.52	8.00	-.24	-2.34	.34	11.80	10.52	9.89	15.53	13.14	12.73
180 Sunset	5	8.91	9.89	9.30	.00	-2.34	.44	11.88	10.52	9.80	14.85	14.63	13.52
	8	5.94	12.85	9.24	.00	-2.34	.44	9.63	13.51	9.72	11.31	18.79	13.42
225	3	9.40	12.16	8.16	.02	-.17	.02	10.82	11.20	9.65	14.33	16.53	12.64
	8	8.10	14.19	7.41	-.02	.19	-.02	9.87	13.51	9.37	12.85	19.59	11.95
270	3	11.02	10.56	5.78	.03	-.19	.00	10.94	11.20	9.52	15.53	15.39	11.14
	7	10.32	12.26	5.74	-.02	.21	.00	10.82	12.90	9.49	14.95	17.80	11.09
315	2	7.53	10.49	8.61	.02	-.19	-.02	9.08	12.96	10.06	11.80	16.67	13.24
	3	8.16	8.38	9.40	.02	-.19	-.02	9.65	11.20	10.82	12.64	13.99	14.33
360 Sunrise	1	6.86	11.55	9.16	.00	-.14	-.01	10.26	12.96	8.85	12.34	17.36	12.74
	3	8.67	10.70	10.57	.00	-.14	-.01	11.60	12.10	10.38	14.48	16.15	14.81

TABLE 5.4-16. TOTAL STARS ERRORS, SUMMER SOLSTICE

Outer Gimbal deg	Star Tracker No.	Bias Microradians			Thermal Distortion Microradians			Random Microradians			Summation (RSS) Microradians		
		ERTB	EPTB	EYTB	ERTR	EPTR	EYTR	ERTU	EPTU	EYTU	ERT	EPT	EYT
45	1	11.79	11.76	9.25	.22	1.87	.28	12.40	10.42	9.44	17.11	15.82	13.22
	6	9.21	13.05	9.01	-.19	-2.33	-.14	10.17	12.02	9.97	13.72	17.89	13.44
90	5	10.76	11.94	6.46	-.29	-2.34	.09	9.65	12.44	9.99	14.46	17.40	11.90
	6	11.63	11.51	5.54	-.29	-2.34	.09	10.72	12.02	9.37	15.82	16.81	10.89
135	5	8.45	9.87	9.27	-.19	-2.34	.33	9.41	12.44	10.22	12.65	16.05	13.80
	6	9.01	9.35	9.21	-.19	-2.34	.33	9.97	12.02	10.17	13.44	15.41	13.72
180	5	6.46	10.82	10.76	.04	-2.34	.43	9.99	12.44	9.65	11.90	16.65	14.46
Sunset	8	10.21	8.08	11.25	.04	-2.34	.43	12.91	9.91	10.24	16.46	13.00	15.22
225	4	10.46	10.69	9.08	.02	-.17	.02	11.08	11.05	9.65	15.24	15.38	13.25
	5	9.27	12.01	8.45	-.02	.19	-.02	10.22	12.44	9.41	13.80	17.29	12.65
270	3	12.06	7.96	8.28	.03	-.19	.00	10.54	9.79	11.36	16.02	12.62	14.06
	4	12.54	9.34	5.88	.03	-.19	.00	11.15	11.05	9.59	16.78	14.47	11.25
315	3	11.97	6.61	8.42	.02	-.19	-.02	12.63	9.79	8.97	17.40	11.81	12.30
	4	9.08	8.22	10.46	.02	-.19	-.02	9.65	11.05	11.08	13.25	13.77	15.24
360	1	9.60	10.03	11.21	.01	-.14	-.01	12.40	10.42	9.45	15.68	14.46	14.66
Sunrise	3	8.28	9.42	12.06	.01	-.14	-.01	11.36	9.79	10.54	14.06	13.59	16.02

TABLE 5.4-17. TOTAL STARS ERRORS, NOVEMBER 6

Outer Gimbal deg	Star Tracker No.	Bias Microradians			Thermal Distortion Microradians			Random Microradians			Summation (RSS) Microradians		
		ERTB	EPTB	EYTB	ERGR	EPRX	EYRR	ERTU	EPTU	EYTU	ERT	EPT	EYT
45	3	10.15	12.84	8.50	.15	1.87	.28	10.76	11.75	9.06	14.79	17.50	12.43
	4	8.41	11.78	11.55	.15	1.87	.28	8.97	10.45	12.19	12.30	15.86	16.80
90	2	11.47	9.49	11.58	.23	1.89	.10	9.76	9.86	14.01	15.06	13.81	18.18
	3	11.61	11.28	6.36	.23	1.89	.10	9.97	11.75	9.92	15.31	16.40	11.78
135	3	8.50	9.06	10.15	.16	1.89	-.09	9.06	11.75	10.76	12.42	14.96	14.79
	8	11.92	7.65	8.73	-.26	-2.34	.33	12.81	10.58	9.67	17.50	13.26	13.03
180 Sunset	5	6.10	10.43	11.33	-.03	-2.34	.43	9.74	12.07	10.35	11.49	16.12	15.35
	6	6.79	8.69	12.32	-.03	-2.34	.43	10.23	10.47	11.53	12.28	13.81	16.88
225	5	9.68	11.66	8.49	-.02	.19	-.02	10.62	12.07	9.45	14.37	16.78	12.70
	6	11.14	10.13	8.59	-.02	.19	-.02	12.11	10.47	9.55	16.45	14.57	12.84
270	5	11.33	10.43	6.10	-.02	.21	.00	10.35	12.07	9.74	15.35	15.95	11.49
	6	12.32	8.69	6.79	-.02	.21	.00	11.53	10.47	10.23	16.87	13.61	12.28
315	1	11.97	6.91	9.08	.02	-.19	-.02	12.58	10.01	9.64	17.36	12.16	13.24
	6	8.59	7.48	11.14	-.02	.21	.02	9.55	10.47	12.11	12.84	12.87	16.45
360 Sunrise	3	6.36	11.28	11.61	.00	-.14	-.01	9.92	11.75	9.97	11.78	16.29	15.30
	4	7.84	10.05	11.94	.00	-.14	-.01	11.01	10.45	10.38	13.52	14.50	15.82

Bias and random errors for a given date, outer gimbal angle, star tracker number and axis were root-sum-squared from the data from the star sensors, gimbals, encoders and control system per the error model in Section 5.2.1.

The thermal distortion errors were obtained from the separate program which included distortions in the star sensor assemblies and gimbals. The magnitudes and polarities of these predicted errors were preserved. See Section 5.4.4.

Bias, thermal distortion and random errors at a given point in the orbit were then root-sum-squared to provide the total predicted system errors for each date, outer gimbal angle, star tracker number and axis.

To provide the system error for a given data and angle in orbit it is necessary to make an assumption of how the system will combine the errors from two star trackers in use. If the error about roll using either of the trackers is +10 microradians, the resultant error using both will be +10 μrad, not +20 μrad. If one is +10 μrad and the other is -10 μrad the errors cancel each other for a net system error of zero. For errors with random polarity the net error will never exceed the average of the absolute values. We have utilized the conservative approach of averaging the absolute values of the errors from the two trackers to arrive at the errors used in the summary, Tables 5.1-1, 5.1-2 and 5.1-3 in Section 5.1.

5.5 Calibration

5.5.1 Introduction

It is evident that the testing and calibration of a system designed to demonstrate pointing accuracies of less than 4 arc seconds is a challenging task, considering that laboratory secondary standards related to optical alignment procedures and equipment are typically restricted to resolution levels of 0.1 arc sec and calibration accuracies of 0.6 arc sec under closely controlled ambient conditions. It is clear that considerable care must be exercised in conceiving the test procedures and in the design of the facilities and special test equipment that must be employed. Large quantities of test data must be obtained and processed with statistical filtering techniques in order to arrive at a measure of the attainable STARS system performance with an acceptable level of confidence.

To enable meaningful calibration and test accuracy, assessment of the STARS system in a ground environment requires that precision fractional arc second alignment must be established and maintained between the STARS gimbal assembly and a simulated celestial star reference field. Achieving arc second alignment with optical tooling techniques requires that effective mechanical vibration isolation and close thermal environmental control be exercised. It is therefore necessary that the STARS gimbal assembly, the star field simulator, all optical alignment telescopes, reference reflecting surfaces, and precision positioning tables be mounted on the same horizontal seismic pad and operated within a temperature controlled clean room environment. Establishing and maintaining thermal equilibrium among all elements of the system is a practical necessity to precision alignment and measurement.

Closed loop dynamic system testing can be accomplished by moving either the star field simulator, or the STARS gimbal assembly with respect to one another on a precision rate table while the relative angular motion is nullified through STARS gimbal movements commanded by the STARS computer (See Figure 3.6-5). The pointing errors so determined are comprised of both STARS system errors as well as errors in the rate table drive which must maintain a fractional arc second control over only a few arc seconds of table motion.

Although separation of rate table jitter and wobble errors from the test data is not deemed practical and therefore use of a precision rate table during system alignment and calibration is not considered a feasible approach, dynamic testing of the star trackers and STARS gimbal drive can be performed at a subsystem level to fully assess their dynamic error contribution to overall system pointing accuracy.

5.5.2 Testing Methodology and Equipment

5.5.2.1 Facility Requirements

As previously discussed, the entire STARS system, test and calibration equipment must be mounted on the same seismic pad which is maintained horizontal to within a few arc minutes. It is necessary that such a physical reference be provided in order to stabilize the optical lines of sight among autocollimators, star simulator sources, STARS tracking telescopes and reference reflecting surfaces. The seismic pad serves as a reference point from which all elements of the simulated celestial star field can be related both to one another and to the telescopes of the STARS tracking cluster, as well as ultimately to the support of the STARS gimbal assembly.

The seismic pad itself must be located within a temperature controlled clean room environment. The temperature control is necessary to maintain mechanical alignments and preclude thermal gradients in structural elements which lead to thermal angular distortions. General test procedures dictate that adequate time must be provided both before and after alignment adjustments to any equipment are accomplished in order that thermal equilibrium be established and actual alignment changes verified.

Due to the close temperature control and vibration isolation required, a minimum number of test personnel would be permitted within the actual test area. Remote error readout equipment would be utilized extensively.

The filtered air supply of the clean room environment minimizes the possibility
of a tracker intermittently breaking lock with a simulated star source in
order to track a dust particle. Light reflections within the test area are
minimized by use of low reflectance surfaces on all equipment and walls, and
eliminating all light sources other than the star simulators during actual
test sequences.

5.5.2.2 Special Test Equipment

1. Master Alignment Wedge Assemblies (Northern and
   Southern celestial hemisphere required).

   A master alignment wedge assembly is fabricated in order to allow
accurate optical alignment of the simulated celestial star field to be
established within the test laboratory relative to the seismic pad surface.
The master alignment wedge assembly is composed of four optical flats which
have been ground and lapped from either a solid block of optical glass
or beryllium in order to establish fixed lines of sight from the star
simulators with respect to the STARS sensor cluster. The basic accuracy of
simulating the star field hinge upon the fabricated accuracy
and stability of the master alignment wedge assembly and consequently great care must
be exercised in their fabrication and calibration. It is unlikely that
the surface normals to the respective optical flats will be aligned with
respect to one another as well as with respect to the mounting surface
coordinates to within greater accuracy than two (2) arc seconds. However,
it is anticipated that the wedge assembly can be calibrated and the systematic
alignment errors of the wedge assembly be determined to within
six tenths (.6) of an arc second. Both the Northern and Southern celestial
sphere master alignment wedge assemblies are designed to mount directly to
the stars gimbal polar axis in place of the star sensor clusters and thus
simulate the cluster tracking telescope lines of sight.
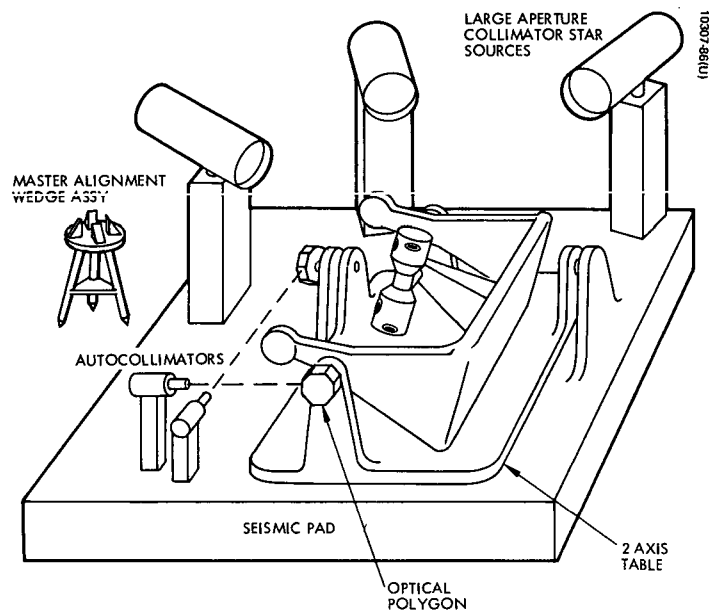
Figure 5.5-1. STARS Ground Test Calibration

The wedge assemblies can also be mounted directly on a separate
alignment jig fixture which will be used to position the reference wedges in the
test set-up in the identical angular orientation that the star sensor clusters
will occupy when the STARS system is under test.

2. Optical Flats/Mirrors

All reference optical flat surfaces to be used for alignment must be flat
to less than two micro-inches per inch in order to minimize angular alignment
errors due to offset between autocollimators, boresight and the center of
the optical flat.

3. Two Axis Positioning Table

A precision two axis positioning table must be fabricated which will support
and be aligned to the STARS gimbal assembly (Figure 5.5-1). The axis of rotation of
the precision table must be orthogonal to one another and can be considered to be
aligned with reference axes of rotation which would normally be those of
a space vehicle to which the STARS gimbal assembly would be attached. The
table does not require a precision divided circle read out for testing
purposes other than for convenience of roughly establishing its orientation,
since alignment of the table relative to the seismic pad will be accomplished
using reference reflecting surfaces on the precision table and autocollimators
which are firmly attached to and aligned with respect to one another on the
seismic pad. The precision two axis table must be designed so that over
its range of angular motion both axes of rotation intersect within the nominal
optical centroid of the star sensor cluster.   Since the bore-
sight axes of the STARS telescopes do not intersect the STARS polar gimbal
axis at the same point it will be impossible to provide a pure rotation of
the STARS cluster with respect to the base without some translation of the
gimbal assembly relative to the star sources. It is for this reason that
such a high degree of flatness is required on the master alignment assembly,
thus allowing the translational motion of a few tenths of inches without
introducing unacceptable angular alignment errors in the measuring process.

5-89

Positioning of the table in the presence of stick-slip friction to .05 arc seconds will be required in a manual mode of operation.

4.   Star Simulators

Each collimated star simulator must be fabricated with a large objective lens such that translation of the telescope boresight with respect to star simulator optical boresight of one inch will not introduce more than a tenth of an arc second uncertainty in pointing alignment. A large collimated field of view is necessary and operation should be maintained as close to the star simulator optical axis as is practical. Integral with the star source, is a two-axis automatic autocollimator that shares the basic optics and allows precise alignment to the master optical wedge assembly. Each tracker telescope will be dedicated to a fixed star simulator and the star magnitude and spectral distribution characteristics will be adequately reproduced with filters and illumination control. Accurate generation of star image size as focused on the tracker reticle is necessary although deviations in size produce deterministic errors and can be accounted for in the testing and data reduction procedures.

5.5.2.3 Testing Sequence (Methodology)

Step 1

A master coordinate reference frame is established with respect to the seismic pad using orthogonally mounted autocollimators, ninety degree reference wedges and levels thus establishing a horizontal plane and master optical reference relative to the seismic pad.

Step 2

A Northern celestial master alignment wedge assembly is mounted on its jig fixture and attached and aligned to the precision two axis table. Reference mirrors on the wedge assembly and on the precision table allow this alignment to be accomplished. The precision two axis table is then aligned with the master reference autocollimators and therefore establishes the table rotation axes with respect to the seismic pad reference.

The basic master optical alignment coordinate reference frame on the seismic pad is initially established with targets which can be removed or inserted at any time during the testing procedure in order to verify alignment of the basic system. Each axis of the precision positioning table has an optical polygon rigidly attached which will allow the table to be positioned with great accuracy to discrete angular position as determined from the seismic pad autocollimators. Following attachment of the master alignment wedge assembly to the positioning table and alignment of the table to the seismic pad, the positioning table surface is rotated to a pre-selected angular orientation with respect to the seismic pad. Essentially the alignment reference frame for the celestial coordinate set is being positioned with respect to the pad and also with respect to the local gravity vector.

Step 3

Each of the star simulators is now aligned to the appropriate reflecting surfaces of the master wedge assembly. In addition to establishing the proper angular relationship, the boresight of the star simulator is brought into coincidence with the center of the master alignment wedge assembly by using targets on each wedge surface. Minimizing off-axis translation will minimize alignment errors due to imperfect collimation of the star source and will minimize errors due to non flat reference wedge assemblies. Each star simulator is attached to a rigid mechanical structure which must allow angular freedom as well as a limited range of translation in order to establish both optical alignment to the appropriate reference wedge and as well as bore-sighting with respect to the center of the reference wedge. The northern celestial reference sphere is now established in alignment with the seismic pad base and indirectly with respect therefore to the local gravity vector.

Step 4

The precision table is returned to its zero reference position with respect to the seismic pad. The master alignment wedge assembly and jig fixture is removed and the STARS gimbal assembly with a north sensor cluster is mounted to the precision table surface and aligned with the table surface, using reflecting surfaces on the STARS gimbal support and on the table itself. With the STARS gimbal assembly fixed and aligned to the table, the table is then returned to the previous angular position from which the celestial references were aligned.

Step 5

The STARS polar and pitch gimbal drives are now commanded to the appropriate
angles which will align the star sensor cluster to the reference
celestial star set. Basically, therefore all of the star source simulators
will lie within each STARS telescope field of view.

Step 6

The star trackers on the cluster are activated in pairs and the STARS
computer determines the precision table platform errors with respect to the
simulated celestial star set and resolves these errors into the table
coordinate axes. The resolved errors which are recorded are the normal
command errors that would be fed to the space vehicle attitude control
system to be nullified. The electrical boresight of each of the optical
telescopes has been previously aligned to the mechanical optical axis
by both adjusting positions of the tracker reticle and establishing bias
voltages within the tracker processing electronics. The remaining systematic
alignment errors within the system will be minimized by incorporating the
bias errors into the STARS computer processing circuitry.

Step 7

The precision table is now perturbed sequentially in small angular increments
which vary up to ± one degree about both table axes. The STARS computer error
signals are recorded at each of these positions, and the recorded error
signals are essentially identical to those attitude correction commands which would
result if the space vehicle to which the STARS gimbal assembly were attached slowly
changed its attitude with respect to inertial space. As a part of this
test sequence, the table angular positions that precisely null the
STARS computer error signals will also be determined. The data determined in
test Steps 6 and 7 will allow an initial evaluation of the system error
coefficients which will be inserted into the STARS computer in order to
minimize the platform pointing errors with respect to the simulated star reference
set.

Step 8

The precision table is now oriented to a new angular relationship with respect to the seismic pad and also to a new angular relationship with respect to the simulated star celestial reference frame. Test sequence 5, 6, and 7 are then repeated. This test sequence establishes the performance of the STARS system over the entire gimbal travel range. Also an evaluation of the one G gravity effects upon the distortions within the STARS gimbal assembly are determined by aligning the gimbal assembly to various orientations with respect the the local gravity vector while carrying out an end to end system test. The systematic error due to the one G field effect can be estimated and incorporated into the calibration sequence.

Step 9

The entire sequence from steps 1 through 8 inclusive is now to be repeated for the Southern celestial hemisphere star set. As a consequence, the Southern hemisphere master alignement wedge assembly is employed to establish a new star reference frame.

5.5.2.4 Data Processing

The large quantitities of redundant measurements obtained by following the previously described test sequence is useful in terms of improving the estimate of the pointing measurements errors. The effect of the errors can be further reduced by making redundant measurements and then by applying statistical data reduction techniques to the celestial reference sphere. In terms of the data reduction concepts, consideration will be given to the use of arithmetic mean, least square angular regression, least square solution error regression, and the normal sequential estimation (Kalman filtering). The first three methods do not make use of the statistical properties of the errors and each of them is about as good as the others when the error statistics are not known. However, when the statistics of the errors are given, the Kalman filtering or sequential estimation technique will give better results .

The calibration of each of the celestial master wedge alignment wedge assemblies must be incorporated into the data reduction process. The systematic alignment errors and the computational position errors of the STARS system as determined in the lab, allow the system error coefficients to be estimated and inserted into the STARS computer to yield best fit alignment of the STARS gimbal assembly support with respect to the simulated star field.

5.5.3   In-Orbit Calibration Considerations

It is desirable to review the in-orbit operation of the STARS celestial reference system in conjunction with the satellite attitude control system so as to achieve a better understanding of just what parameters must be measured and evaluated in order to establish in-orbit performance capabilities. The sensor clusters are continuously oriented to the celestial hemisphere by the spacecraft attitude control system in response to error signals generated by computer processed star tracker signals. Isolation of the STARS tracking cluster from space vehicle small amplitude (0.5 degree) angular motion is provided by off axis tracking capabilities of the STARS telescopes in conjunction with the real time computational capabilities of the STARS on-board computer. Articulation of the tracker cluster with respect to the space vehicle through the STARS two-axis gimbal assembly permits the required precision orientation of the space vehicle with respect to the celestial coordinate system.

From a satellite attitude control system point of view, the STARS system provides a precise narrow field of view sensor. The sensor boresight axis can be accurately oriented in 1.8 arc second increments with respect to the satellite, so that consequently the attitude control system indirectly positions the vehicle in sensor coordinates by simply nulling the sensor error signals presented to it.

Verification of the in orbit pointing performance will consist principally of comparing the satellite reference control axes when operating with the STARS celestial reference system to an alternate precise inertial reference. This alternate inertial reference can be obtained indirectly or directly. The indirect method consists of establishing the satellite attitude with respect to an earth oriented line of sight and by utilizing the known orbital characteristics of the satellite to subsequently relate the earth referenced line of sight to an inertial celestial reference. The alternate technique is a direct establishment of an inertial line of sight between the satellite and the celestial star field. The latter approach is a more desirable approach since no accuracy is lost in transferring between coordinate sets.

Establishment of the in orbit orientation of the satellite with respect to an earth oriented line of sight depends largely on orbit determination accuracy.

Optical alignment techniques are subject to atmospheric disturbance limitations, and preclude fractional arc second pointing capabilities. Direct use of conventional earth radiation balance and edge tracking horizon detectors will not permit determination of the local vertical as defined by the earth limbs to better than .05 degrees under the most favorable of circumstances after calibrating out all systematic errors. Such a random error already exceeds the desired measurement level of the STARS system by 50 times, so that earth horizon sensing techniques are not a practical approach.

A possible technique, however, to establish an earth subsatellite position is through the use of earth photography and subsequent photogrammetric processing. Since in-orbit processing and interpretation present a formidable problem, TM techniques and ground processing may be a practical alternative.

Although application of laser techniques will permit ranging and position determination of the satellite, attitude determination with such a system requires that autocollimation techniques be used. To enable alignment to be achieved requires that both the autocollimator and the space vehicle-borne reflecting surfaces be articulated with respect to their mounting surfaces. Here one is attempting to establish an optical line of sight over great distances to the same arc second level of accuracy that is achieved with difficulty within the carefully controlled laboratory environment without atmospheric degradation.

The use of RF interferometry, though less susceptible to atmospheric disturbances, requires antenna apertures of such large dimension that it becomes impractical to obtain the clear field of view necessary for the STARS tracking clusters as well as achieve mechanical alignment between the antenna boresight references and the STARS gimbal base. Arc second pointing levels are not deemed achievable with such a system.

Direct establishment of a reference orientation can be achieved at least two ways. The optical boresight of a precision long focal length camera may be aligned to the base of the STARS gimbal assembly and pointed away from the earth. By photographing the star field background at discrete times in the orbit, and comparing the position of the camera optical axis with respect to the star field, one can accurately establish the orientation of the satellite with respect to the celestial field. The principal difficulty again becomes one of either in orbit processing and interpretation, or the recovery from orbit of the film for ground processing. In either case only a limited number of calibration measurements could be obtained and the ability to reset the STARS systematic error coefficient correction factors in the on-board computer and subsequently evaluate the pointing performance is greatly curtailed. Holding the STARS gimbal assembly fixed with respect to the satellite would allow time exposures to be utilized and the resultant increase in star image blur size becomes a direct measure of the residual vehicle motion.

A separate long focal length narrow field of view calibration sensor assembly can be aligned such that its boresight axis is diametrically opposed to the satellite earth line of sight and hard mounted adjacent to the STARS gimbal assembly.

As the satellite maintains its earth orientation, the calibration star sensor scans the celestial sphere along the satellite orbit plane. An angular position fix can be achieved each time that a known star of sufficient magnitude passes through the reference telescope field of view. The calibration star sensor could either operate as a star transit detector with reticle slits, or it could track within a narrow field of view. The alignment to the STARS gimbal base coupled with the precision and repeatibility to which reference stars can be measured with respect to the reference telescope optical axis will limit the accuracy to which the STARS system can be calibrated. It appears reasonable that the celestial references which the STARS system uses for its basic pointing reference should also be used as the best means of evaluating the pointing capabilities. Use of the redundant calibration star sensor as outlined will permit long term in orbit calibration test sequences to be performed. The procurement of large numbers of redundant datum points will improve the basic accuracy of the measurement procedure and allow use of the same statistical data reduction techniques that are employed in the ground test calibration phase. If a redundant tracking calibration star sensor is used, the STARS gimbals can be held fixed with respect to the satellite and by monitoring the outputs of the reference tracker via telemetry, the level of space vehicle residual attitude motions can be established. Figure 5.5-2 illustrates the recommended in orbit test concept to evaluate the STARS system.

FOV SCANNED BY
ORBITAL MOTION

CALIBRATION
STAR
SENSOR

$\bar{V}$

PAYLOAD

EARTH

CALIBRATE
STAR
LOS

| CALIBRATE SUN SENSOR | → | SIGNAL PROCESSING | → TM |

STARS MECHANISM   TM   **COMPUTER**

| GIMBAL DRIVES AND PICKOFFS | ← | GIMBAL DRIVE ELECTRONICS | ← | GIMBAL ANGLE COMPUTATIONS | ← | MEMORY, TIMING AND CONTROL | ← EPHEMERIS UPDATE |

TM

STAR
LOS

| STAR SENSORS | → | SENSOR SIGNAL PROCESSING ELECTRONICS | → | COORDINATE TRANS- FORMATIONS | → | CORRECTIONS AND COMPENSATIONS |

| SPACECRAFT DYNAMICS | ← | ATTITUDE CONTROL SYSTEM | ← TM |

Figure 5.5-2. In-Orbit Test Configuration

5.6 REFERENCES

1. Abell, George, "Exploration of the Universe", Second Edition, Holt, Rinehart and Winston, New York, 1969.

2. Mechtly, E. A., "The International System of Units", Revised, NASA SP-7012, 1969.

3. Jensen, J., Townsend, G., Kork, J. and Kraft, D, "Design Guide to Orbital Flight," McGraw-Hill, New York 1962.

6. Comprehensive Summary and Recommendations

6.1 System Analysis

The major system level feasibility questions associated with the STARS concept are concerned with the availability of a suitable set of reference stars which will provide a reliable inertial reference throughout the projected satellite lifetime. A set of eight such stars was found, having adequate irradiance and coordinate locations which avoid sun, moon, and planet interference problems. It was found that the inertial reference can be acquired from an arbitrary attitude with the use of a spacecraft mounted two axis sun sensor, and without any problems of false acqusition. The linear offset tracking range of $\pm$ 0.5 degree required to account for orbit injection errors, perturbations, and star aberration, was found to be adequate for initial acquisition. It was determined that the selected star set provides complete reference redundancy more than 78 per cent of the time (on the average) for the 500 mile baseline orbit. Increasing the number of stars used to 10 raises this value to over 95 per cent. The computations required to be performed by the onboard computer were determined and no associated mechanization problems are forseen. As a result, at the system level the STARS concept was found to be entirely feasible.

As a prelude to development of a STARS prototype, additional system studies and preliminary design efforts should concentrate on analysis, design, and simulation of the entire spacecraft attitude control system. This must be accomplished once a suitable spacecraft has been selected since the successful integration of the STARS into the spacecraft is essential to the successful accomplishment of the precision pointing objective. As part of this major task, the computer/electronics portions of the STARS must be analyzed in more detail and the detailed mechanization diagrams must be developed. Subsequent to this step, the more critical component sections of the electronics unit should be developed.

6.2 Gimbal Mechanism

The STARS gimbal configuration which in its original concept involved a conventional yoke support for the outer (pitch) axis, was analyzed in detail, with a resultant change to a cantilevered approach. The principal advantages of this configuration are the considerably improved thermal distortion characteristics and lower weight. Beryllium shafts and housings, with single pairs of angular contact bearings, are used for each axis and direct drive servos are used for angular positioning. The shaft angle transducer for each axis is an Inductosyn which provides a resolution of 2^{19} bits per revolution. The entire gimbal system is wrapped with an insulating blanket, thus reducing temperature gradients and fluctuations to a level where thermal distortions are within the assigned error budgets. The two gimbal axes are driven by a digital servo, controlled by the onboard digital computer. In investigating the angular positioning characteristics of the polar gimbal axis (the slow axis), they were found to depend critically on the detailed stiction characteristic hypothesized for this design. Computer simulation showed that momentary sharp transient overshoots in position could occur if elasticity were present in the stiction characteristic at the one revolution per year velocity of the polar axis. Although such sharp transients are not expected to significantly affect the pointing accuracy of the payload, a more detailed investigation of the entire phenomenon, integrated with an assessment of attitude control system interactions, appears in order.

To permit straightforward development of the STARS as a flight system, the polar axis gimbal system and drive should receive preliminary development emphasis. In particular, the stiction characteristics and variable torque effects, under the microscopic motions required in such a precision drive system, should receive analytical and experimental attention. A two pronged approach is therefore recommended, involving a general investigation of stiction at creep speeds on the one hand, and the rather specific development of the STARS polar axis gimbal system and drive on the other.

6.3   Star Tracker

Analysis and preliminary design of the star trackers has resulted in a configuration and design details which promise to meet all essential STARS requirements.   System considerations of star irradiance, interference effects, data rate and off axis tracking requirements, missed pulse and false alarm situations, and the various mechanical design constraints imposed by star visibiltty and gimbal system comsiderations have all contributed to the evolution of the baseline design.   The principal tracker parameters, as determined by the design study include an effective aperture of 6.4 cm^2, a scan rate of 4 revolutions/sec, a minimum signal to noise ratio of 9, and a tracking loop angle noise of 1.15 arc sec (1σ). The scanning function is accomplished by a rotating optical wedge which nutates the target star image across an L shaped reticle, with the time between a reference position on the wedge and the reticle slit crossing determining the star location.   A linear offset tracking range of 1/2 degree is provided for.   The optical path for each tracker consists of a first reflecting surface (one of four facets on a single beryllium block) which reflects light from a selected star through an optical wedge into the lens system (a pair of doublets) and then onto the reticle.   The light from the reticle is then relayed through condensing optics to a photomultiplier tube.   A common optical wedge, used for all four trackers in a STARS sensor cluster, automatically provides the synchronization required for multiplexing pairs of trackers onto single PMT's.   The basic structure of each sensor cluster is made of beryllium to provide mechanical stability and minimize thermal distortion effects.   The wedge drive motor is located at the base of the cluster, so that its heat may be conducted away easily. An insulating blanket surrounds each cluster, broken only by the four sunshades, one for each of the four star trackers per cluster.

Although the baseline tracker design evolved in the study essentially satisfies the performance requirements, several potential problems areas require further exploration.   Although theoretically adequate, the quality of the imagery on the focal plane, based on the use of two optical doublets requires further verification.   The tradeoffs between multiplexing and not multiplexing of PMT's must be investigated in more detail.

A more thorough study and evaluation of thermal effects within the sensor cluster
should be undertaken. Sunshade design, particularly with respect to
attentuation of light from distributed interference sources, should be
evaluated and analyzed in more depth. Finally, alignment and calibration of
the sensor cluster must be studied in detail, so that a logical program
for performing these functions as part of a **development** effort can be constructed.
The above described problem areas - all involving development problems -
can be attacked and resolved most efficiently by undertaking the development
of an engineering model sensor cluster, which is the recommended course of
action at the conclusion of this feasibility study.

6.4 Error Analysis

The objectives of the error analysis were to establish a basic framework
for defining and compiling the principal errors which contribute to pointing
precision, establish reasonable baseline values for the primary sources of
error, calculate the resultant probable pointing errors for orbital operation, and
study laboratory and in-orbit calibration techniques.

The system pointing errors were computed for three different times of
the year (for the baseline, noon-midnight sun-synchronous orbit). It
was found that, with one exception (the pitch axis at 225° at vernal equinox),
the error is less than 0.001 degree about each axis at each of the 24 orbital
conditions for which the error was calculated. The rms error for all axes
and all orbits considered is less than 0.001 degree, thus confirming that the
design objective pointing accuracy is indeed within the state of the art.
It was concluded that the accuracy potential of STARS might be even further
improved by the use of extensive in orbit calibration using a method such
as is described in Section 5.5.

7. Appendices

7.1 Computer Programs

The principal time share computer programs developed especially for the STARS feasibility study, are given in the following pages. They may be briefly described as follows:

*LIST B -   This program takes as its input the names, irradiances, equatorial and ecliptic coordinates of the 100 brightest stars out of computer files, applies a selected irradiance versus ecliptic declination criterion to each star in succession, and prints out a list of only those stars which meet this criterion.

*VIS-1 -   Using data on eight preselected stars as its input, this program scans the celestial sphere in 2.7 degree declination increments along right ascension coordinates, every 6.4 degrees right ascension, and prints out the number (of the eight stars) visible above a specified elevation angle at each point. The digit "3" is suppressed to reduce the density of the printout. The entire printout is scaled to overlay on the chart of the 100 brightest stars issued by the US Hydrographic Office. Following this printout, the program prints the number of times each digit has been printed (or should have been in the case of the digit "3") and the percentage of the celestial sphere covered by each digit. Subsequent to this printout, the program lists those locations where only one star is visible above the specified minimum elevation angle, and then gives details (star number, irradiance, and elevation angle) on the three highest stars at that point.

ACQ-5* - Using the various possible included angles that exist between any pair of the eight reference stars as input data, this program examines all possible pairs of the first 100 stars and records all those cases where a match within 2 degrees is found. The results are printed and written into computer files.

ACQ-7* - This program uses the information written into the computer files by program ACQ-5* and, for each star pair so listed, determines if a line exists in the ecliptic plane (a sun line), about which the appropriate STARS trackers could be rotated to bring them from alignment with the correct star pair into alignment with the pair under investigation. If such a rotation is possible in a particular case, and the alignment is possible within a specified tolerance, the details on the particular rotation are recorded.

PDDSS* - This program simulates the performance of a direct drive servo such as is planned for the STARS gimbal drive. It models in detail the digital nature of the shaft position transducer and permits performance evaluation in the presence of two possible static friction characteristics.

```
100 FILE RITASC,DECLIN,*NAME,ECL*RA,ECL*DC,*MAG
110 DIM A(100),B(100),CC(100),D(100),G(100),E(100),H(100)
180 PRINT "                        IRRAD.      EQUATORIAL COORD.     ":
190 "    ECLIPTIC COORD."
200 PRINT "                                        R.A.     DEC.     ":
210 "       R.A.     DEC."
220 PRINT
230 SET I=3,S
240 SET A=5.2,S
250 SET B=G=4.2
260 SET F=6.2,S
270 SET H=Z=V=2.2,S
290 FOR I=1 TO 100
300 READ FILE 1,A(I)
301 Z1=15\Z2=20\Z3=24\Z4=27\Z5=32.5\Z6=42.5
302 V1=90\V2=25\V3=10\V4=6.25\V5=2.75\V6=.8
310 READ FILE 2,B(I)
320 READ BINARY 3,CC(I)
330 READ FILE 4,D(I)
340 READ FILE 5,G(I)
350 E(I)=ABS(G(I))
360 READ FILE 6,H(I)
370 F=INT(100*D(I)+.5)/100
380 G=INT(100*G(I)+.5)/100
410 B9=Z2*V1-Z1*V2\B1=(Z2-Z1)/B9\A1=(V1-V2)/B9
420 B8=Z3*V2-Z2*V3\B2=(Z3-Z2)/B8\A2=(V2-V3)/B8
430 B7=Z4*V3-Z3*V4\B3=(Z4-Z3)/B7\A3=(V3-V4)/B7
432 B6=Z5*V4-Z4*V5\B4=(Z5-Z4)/B6\A4=(V4-V5)/B6
434 B5=Z6*V5-Z5*V6\B0=(Z6-Z5)/B5\A5=(V5-V6)/B5
440 IF E(I)<Z1 THEN 530
450 IF A1*E(I)+B1*H(I)<1 THEN 530
460 IF A2*E(I)+B2*H(I)<1 THEN 530
470 IF A3*E(I)+B3*H(I)<1 THEN 530
472 IF A4*E(I)+B4*H(I)<1 THEN 530
474 IF A5*E(I)+B0*H(I)<1 THEN 530
480 PRINT I;TAB(5);CC(I);TAB(24);H(I);TAB(35);A(I);B(I);TAB(56);F;G
530 NEXT I
540 PRINT\PRINT\PRINT
550 PRINT "THE ABOVE LISTED STARS SATISFY THE IRRADIANCE VS. ECLIPTIC"
560 PRINT "DECLINATION CRITERION DEFINED BY THE FOLLOWING COORDINATES:"
570 PRINT
580 PRINT "IRRADIANCE >"V6"E-13 W/SQ CM"
590 PRINT "ECLIPTIC DECLINATION >"Z1" DEGREES"
600 PRINT
610 PRINT "DECL.";TAB(10);Z1;TAB(20);Z2;TAB(30);Z3;TAB(40);Z4;
620 PRINT TAB(50);Z5;TAB(60);Z6
630 PRINT "IRRAD.";TAB(10);V1;TAB(20);V2;TAB(30);V3;TAB(40);V4;
640 PRINT TAB(50);V5;TAB(60);V6
650 END
```

```
100 FILE NE1,NE2,NE3,NE4,NE5
110 DIM A(8),B(8),C(8),D(8),T(9,2),R(60,3),Y(8)
120 DIM S(65),Q(65)
130 FOR I=1 TO 8
140 READ A(I),B(I),C(I),D(I)
150 NEXT I
160 DATA 78.25,-8.24,9,4
170 DATA 24.13,-57.40,8,5
180 DATA 305.78,-56.84,2,38
190 DATA 130.96,-54.59,1.8,41
200 DATA 297.31,8.78,4.3,13
210 DATA 213.55,19.35,5.3,10
220 DATA 13.69,60.54,2.2,32
230 DATA 178.04,53.87,1.1,69
240 Z0=15
250 LET Z1=SIN(Z0/57.3)
260 SET D=2.0,S
270 PRINT "THE STAR NUMBERS USED ARE -";
280 FOR W=1 TO 7\PRINT D(W)",";\NEXT W\PRINT D(8)
290 PRINT
300 FOR I=56 TO 0 STEP -1
310 FOR J=-32 TO 32
320 LET R=6.4*I/57.3
330 LET S(J+32)=.97
340 LET D=2.7*J/57.3
350 LET E=0
360 DEF FNA(S)=SIN(D)*SIN(B(S)/57.3)+COS(D)*COS(B(S)/57.3)*COS(A(S)/57.3-R)
370 LET X1=(COS(D))^2*COS(6.4/57.3)+(SIN(D))^2
380 LET X2=(ATN((SQR(1-X1^2))/X1))/2.68
390 FOR L=1 TO 8
400 LET T(L,1)=FNA(L)
410 NEXT L
420 GOSUB 1400
430 LET S(J+32)=T(2,1)
440 IF T(2,1)<Z1 THEN 460
450 GO TO 600
460 DEF FNC(S)=57.3*ATN(S/SQR(1-S^2))
470 FOR L=1 TO 4
480 LET V(L)=FNC(T(L,1))\WRITE FILE 1,V(L),\NEXT L
490 FOR L=1 TO 8\FOR O=1 TO 4
500 IF T(O,1)=FNA(L) THEN 520
510 GO TO 540
520 LET Q(O)=D(L)
530 LET P(O)=C(L)
540 NEXT O\NEXT L
550 FOR L=1 TO 4
560 WRITE FILE 2,Q(L),\WRITE FILE 5,P(L),
570 NEXT L
580 LET A1=A1+1
590 WRITE FILE 3,I,\WRITE FILE 4,J,
```

```
600 FOR L=1 TO 8
610 IF T(L,1)<Z1 THEN 630
620 LET E=E+1
630 NEXT L
640 FOR L=1 TO 8
650 IF T(2,1)=FNA(L) THEN 670
660 GO TO 680
670 LET Q(J+32)=L
680 NEXT L
690 LET P9=S(0)
700 FOR H=0 TO 63
710 IF S(H+1)>P9 THEN 750
720 LET P9=S(H+1)
730 LET P8=Q(H+1)
740 LET R(I,2)=2.7*(H-31)
750 NEXT H
760 LET R(I,1)=57.3*ATN(P9/SQR(1-P9^2))
770 LET R(I,3)=P8
780 IF J=0 THEN 1110
790 IF E=3 THEN 1170
800 IF E=2 THEN 870
810 IF E=4 THEN 910
820 IF E=1 THEN 950
830 IF E=5 THEN 990
840 IF E=6 THEN 1030
850 IF E=7 THEN 1070
860 GO TO 1500
870 PRINT TAB(J+32);"2";
880 LET Y(2)=Y(2)+1
890 LET X(2)=X(2)+X2
900 GO TO 1220
910 PRINT TAB(J+32);"4";
920 LET Y(4)=Y(4)+1
930 LET X(4)=X(4)+X2
940 GO TO 1220
950 PRINT TAB(J+32);"1";
960 LET Y(1)=Y(1)+1
970 LET X(1)=X(1)+X2
980 GO TO 1220
990 PRINT TAB(J+32);"5";
1000 LET Y(5)=Y(5)+1
1010 LET X(5)=X(5)+X2
1020 GO TO 1220
1030 PRINT TAB(J+32);"6";
1040 LET Y(6)=Y(6)+1
1050 LET X(6)=X(6)+X2
1060 GO TO 1220
1070 PRINT TAB(J+32);"7";
1080 LET Y(7)=Y(7)+1
1090 LET X(7)=X(7)+X2
```

```
1100 GØ TØ 1220
1110 IF E=3 THEN 1130
1120 GØ TØ 800
1130 PRINT TAB(32);"I";
1140 LET Y(3)=Y(3)+1
1150 LET X(3)=X(3)+X2
1160 GØ TØ 1220
1170 IF I=0 THEN 1190
1180 GØ TØ 1200
1190 PRINT TAB(J+32);"-";
1200 LET Y(3)=Y(3)+1
1210 LET X(3)=X(3)+X2
1220 NEXT J
1230 LET V=(INT(10*R(I,I)+.5))/10
1240 PRINT TAB(66);V
1250 NEXT I
1260 PRINT
1270 PRINT
1280 PRINT
1290 SET X=4.2
1300 PRINT "THE NUMBER ØF TIMES EACH DIGIT APPEARS AND THE CØRRESPØNDING"
1310 PRINT "PERCENT CØVERAGE ØF THE CELESTIAL SPHERE IS AS FØLLØWS:"
1320 PRINT "DIGIT","FREQUENCY","PERCENT CØVERAGE"
1330 FØR L=1 TØ 7
1340 PRINT L,Y(L),X(L)
1350 NEXT L
1360 PRINT
1370 PRINT
1380 GØ TØ 1500
1390 REM ØRDERING SUBRØUTINE
1400 FØR L=1 TØ 8
1410 FØR K=1 TØ 7
1420 IF T(K+1,1)<T(K,1) THEN 1470
1430 LET T(K,2)=T(K+1,1)
1440 LET T(K+1,2)=T(K,1)
1450 LET T(K,1)=T(K,2)
1460 LET T(K+1,1)=T(K+1,2)
1470 NEXT K
1480 NEXT L
1490 RETURN
1500 PRINT\PRINT
1510 RESTØRE FILE 1
1520 RESTØRE FILE 2
1530 RESTØRE FILE 3
1540 RESTØRE FILE 4
1550 RESTØRE FILE 5
1560 SET Z=2.0,S
1570 PRINT "AT THE LØCATIØNS WHERE ØNLY ØNE STAR IS VISIBLE ABØVE "ZO" DEGRĔ
1580 PRINT "THE FØUR HIGHEST STARS - 'STAR NØ.(IRRAD.)ELEV.ANG. - ARE";
1590 " AS FØLLØWS:"
```

```
1600 SET Q=I=2.0,S
1610 SET P=1.1,S
1620 SET V=2.2,S
1630 SET J=2.0
1640 PRINT "LØCATIØN (I-J)","          1","          2","          3","          4"
1650 PRINT
1660 FØR K=1 TØ A1
1670 READ FILE 3,I
1680 READ FILE 4,J
1690 PRINT I"      J,
1700 FØR L=1 TØ 4
1710 READ FILE 2,Q
1720 READ FILE 1,V
1730 READ FILE 5,P
1740 PRINT Q" ("P")"V,
1750 NEXT L\PRINT
1760 NEXT K
1770 END
```

```
100 FILE RITASC,DECLIN,*NAME,*FI3,*FI4,*FI5,*FI6
110 DIM B(100),C(100),D(28),
112 SET D=3.2,S
115 SET I=J=2.0,S
116 SET X=3.2,S
120 FOR I=1 TO 99
130 READ FILE 1,B(I)
140 READ FILE 2,C(I)
160 NEXT I
170 DEF FNA(S)=1.5708-.2146*S+.089*S^2-.0507*S^3+.0331*S^4:
180 -.022*S^5+.0126*S^6-.005*S^7+.001*S^8
190 FOR K=1 TO 26
200 READ D(K)
210 PRINT "TRACKER ANGLE = "D(K)" DEGREES"
220 FOR I=1 TO 99
230 FOR J=I+1 TO 99
250 R1=(B(I)-B(J))/57.3
260 D1=(C(I))/57.3
270 D2=(C(J))/57.3
280 X1=SIN(D1)*SIN(D2)+COS(D1)*COS(D2)*COS(R1)
290 IF X1<-1 THEN 390
300 IF X1<0 THEN 340
310 IF X1>1 THEN 360
320 X2=FNA(X1)*SQR(1-X1)
330 GO TO 370
340 X2=3.14159-FNA(ABS(X1))*SQR(1-ABS(X1))
350 GO TO 370
360 X2=0
370 X3=57.3*X2
380 GO TO 400
390 X3=180.00
400 IF ABS(ABS(X3)-ABS(D(K)))<=2 THEN 420
410 GO TO 470
420 GO TO 431
431 IF M=1 THEN 446
432 IF ENDFILE 4 THEN 444
440 WRITE FILE 4,I,\WRITE FILE 5,J,
442 GO TO 447
444 M=1
446 WRITE FILE 6,I,\WRITE FILE 7,J,
447 P=P+1
448 IF P<13 THEN 455
449 PRINT\P=1\Z=Z+1
450 IF Z<50 THEN 455
452 FOR Z1=1 TO 5\PRINT\NEXT Z1
453 Z=0\GO TO 484
455 PRINT I"-"J",";
470 NEXT J
480 NEXT I
482 IF Z<47 THEN 488
```

```
483 FOR Z1=Z TO 55\PRINT\NEXT Z1
484 PRINT"------------------------------------------------------
 485 FOR Z1=1 TO 7\PRINT\NEXT Z1
486 PRINT "ACQ-5* CONTINUED"
487 PRINT\IF Z=0 THEN 455\Z=0\GO TO 490
488 PRINT\PRINT\P=0\Z=Z+3
490 P=0\NEXT K
500 DATA    64.3274
510 DATA   104.2308
520 DATA    62.3408
530 DATA   141.4102
540 DATA   135.3346
550 DATA    85.1662
560 DATA   102.4170
570 DATA    40.1304
580 DATA    53.4060
590 DATA    95.7012
600 DATA   141.3325
610 DATA   118.2249
620 DATA    68.5031
630 DATA    65.9903
640 DATA   107.3073
650 DATA   123.8932
660 DATA   132.9224
670 DATA   101.5117
680 DATA   147.1658
690 DATA   115.1912
700 DATA    81.2621
710 DATA    75.6944
720 DATA    99.3057
730 DATA    98.5225
740 DATA    43.9077
750 DATA    64.9237
760 FOR Z=Z1 TO 60\PRINT\NEXT Z
770 END
```

```
100  FILE ECL*RA,ECL*DC,*FI3,*FI4,*FI5,*FI6
110  SET S=2.0,S\SET Z=1.0,S
120  SET T=1.2,S\SET E=2.0,S
130  SET R=3.2\SET D=2.0,S
140  PRINT "MISS(DEG)";TAB(12);"TRACKER PAIR";TAB(27);"ØBSERVED PAIR";
150  PRINT TAB(43);"ECL-RA ØF SUN";TAB(59);"APPRØX. DATE"
160  IF Z8=50 THEN 1890
170  DIM A(100),B(100)
180  FØR I=1 TØ 99
190  READ FILE 1,A
200  A(I)=A/57.3
210  READ FILE 2,B
220  B(I)=B/57.3
230  NEXT I
240  FØR I=1 TØ 8
250  READ E(I)
260  C(I)=A(E(I))
270  D(I)=B(E(I))
280  NEXT I
290  REM DEFINITIØN ØF ARCCØSINE AND ARCSINE FUNCTIØNS
300  DEF FNA(X)=1.57079633-.21460184*X+.08904567*X^2-.05072733*X^3:
310  +.03313246*X^4-.02199838*X^5+.01261235*X^6-.00499706*X^7+.0009513*X^8
320  DEF FNS(X)=(1.5709-(SQR(1-ABS(X)))*FNA(ABS(X)))*SGN(X)
330  DEF FNC(X)=(SQR(1-X))*FNA(X)
340  DEF FND(X)=3.14159-(SQR(1-ABS(X)))*FNA(ABS(X))
350  FØR I=1 TØ 8
360  FØR J=I+1 TØ 8
370  IF J=8 THEN 380\GØ TØ 390
380  IF I=2 THEN 610\IF I=3 THEN 610
390  READ X1
400  FØR K=1 TØ X1
410  IF ENDFILE 3 THEN 440
420  READ FILE 3,S1\READ FILE 4,S2
430  GØ TØ 460
440  READ FILE 5,S1\READ FILE 6,S2
450  REM PAIRING ØF STAR SETS
460  R1=C(I)\D1=D(I)
470  R3=C(J)\D3=D(J)
480  R2=A(S1)\D2=B(S1)
490  R4=A(S2)\D4=B(S2)
500  Z=1\GØSUB 690
510  R2=A(S2)\D2=B(S2)
520  R4=A(S1)\D4=B(S1)
530  Z=2\GØSUB 690
540  R1=C(J)\D1=D(J)
550  R3=C(I)\D3=D(I)
560  Z=3\GØSUB 690
570  R2=A(S1)\D2=B(S1)
580  R4=A(S2)\D4=B(S2)
590  Z=4\GØSUB 690
```

```
600  NEXT K
610  NEXT J
620  NEXT I
630  DATA 4,5,38,41,13,10,32,69
640  DATA 142,149,138,103,98,133,141,124,125,141,102,142,147,141,164,129
650  DATA 114,135,97,162,143,153,143,146,122,131
660  GO TO 1910
670  REM ANGLE COMPUTATIONS
680  REM STARS 1 AND 3 ARE TRACKER STARS; STARS 2 AND 4 ARE TO BE CHECKED
690  IF R1<>R2 THEN 720
700  IF D1=D2 THEN 1900
710  REM ANGLE BETWEEN STARS 1 AND 2 (T1)
720  U1=(SIN(D1)*SIN(D2)+COS(D1)*COS(D2)*COS(R2-R1))
730  IF U1<0 THEN 750
740  T1=FNC(U1)\GO TO 770
750  T1=FND(U1)
760  REM ANGLE BETWEEN MERIDIAN THROUGH STAR 2 AND PLANE THRU 1,2 (T2)
770  U2=((COS(D1)*COS(R2-R1)-COS(D2)*COS(T1))/(SIN(D2)*SIN(T1)))
780  IF U2<0 THEN 800
790  T2=FNC(U2)\GO TO 820
800  T2=FND(U2)
810  REM INCLINATION OF PLANE THROUGH 1 AND 2 (T3)
820  S3=(SIN(T2)*COS(D2))
830  IF S3<0 THEN 850
840  T3=FNC(S3)\GO TO 870
850  T3=FND(S3)
860  REM DECLINATION OF MIDPOINT (Q) BETWEEN STARS 1 AND 2 (V2)
870  W1=SIN(D2)/SIN(T3)
880  IF ABS(W1)<.00001 THEN 900
890  V1=FNS(W1)\GO TO 910
900  V1=W1
910  W2=SIN(T3)*SIN(V1-T1/2)
920  IF ABS(W2)<.00001 THEN 940
930  V2=FNS(W2)\GO TO 960
940  V2=W2
950  REM ANGLE BETWEEN MERIDIAN OF Q AND PLANE THROUGH 1 AND 2 (T4)
960  S4=COS(T3)/COS(V2)
970  IF ABS(S4)>1 THEN 1000
980  IF ABS(S4)<.00001 THEN 1010
990  T4=FNS(S4)\GO TO 1030
1000 T4=FNS(SGN(S4))\GO TO 1030
1010 T4=S4
1020 REM R.A. OF SUN LINE USED FOR ROTATION OF 1 INTO 2 (R6)
1030 IF T4=0 THEN 1060
1040 R9=ATN(SIN(V2)/TAN(T4))
1050 GO TO 1070
1060 R9=(SGN(SIN(V2)))*1.5709
1070 U6=TAN(V2)/TAN(T3)
1080 IF ABS(U6)>1 THEN 1110
1090 IF ABS(U6)>.00001 THEN 1120
```

```
1100 R8=U6\GØ TØ 1130
1110 R8=FNS(SGN(U6))\GØ TØ 1130
1120 R8=FNS(U6)
1130 Y1=TAN(D1)/TAN(T3)
1140 IF ABS(Y1)>1 THEN 1170
1150 IF ABS(Y1)>.00001 THEN 1180
1160 Y2=Y1\GØ TØ 1190
1170 Y2=FNS(SGN(Y1))\GØ TØ 1190
1180 Y2=FNS(Y1)
1190 Y3=SGN(V2)*SGN(D2-D1)
1200 Y4=Y3*ABS(R9)
1210 R6=R1+R8+Y4-Y2
1220 REM ANGLE ABØUT SUN LINE FØR RØTATIØN ØF 1 INTØ 2 (2*T6)
1230 S5=(TAN(D1)/SIN(R6-R1))
1240 T5=ATN(S5)
1250 T6=ATN(TAN(V2)/SIN(R9))-T5
1260 REM INCLINATIØN ØF STAR 3 WITH RESPECT TØ SUNLINE (T7)
1270 S7=TAN(D3)/SIN(R6-R3)
1280 T7=ATN(S7)
1290 REM RØTATIØN ØF STAR 3 ABØUT SUN LINE, DECLINATIØN ØF STAR 3 (D5)
1300 U5=(SIN(2*T6+T7)*SIN(D3)/SIN(T7))
1310 IF ABS(U5)<.00001 THEN 1330
1320 D5=FNS(U5)\GØ TØ 1350
1330 D5=U5
1340 REM R.A. ØF RØTATED STAR 3 (R5)
1350 U3=TAN(D5)/TAN(2*T6+T7)
1360 IF ABS(U3)>1 THEN1390
1370 IF ABS(U3)>.00001 THEN 1400
1380 U4=U3\GØ TØ 1410
1390 U4=FNS(SGN(U3))\GØ TØ 1410
1400 U4=FNS(U3)
1410 R5=R6-U4
1420 REM ANGLE BETWEEN STAR 4 AND RØTATED STAR 3 (T9)
1430 S8=(SIN(D4)*SIN(D5)+CØS(D4)*CØS(D5)*CØS(R4-R5))
1440 IF S8>0 THEN 1460
1450 T8=FND(S8)\GØ TØ 1470
1460 T8=FNC(S8)
1470 T9=57.3*T8\IF R6>6.28318 THEN 1510
1480 IF R6<0 THEN 1500
1490 R7=57.3*R6\GØ TØ 1520
1500 R7=57.3*R6+360\GØ TØ 1520
1510 R7=57.3*R6-360
1520 IF ABS(T9)>10 THEN 1900
1530 PRINT Z")";TAB(4);T9;
1540 PRINT TAB(13);E(I)"-"E(J);TAB(29);S1"-"S2;TAB(43);R7;
1550 REM DETERMINATIØN ØF APPRØXIMATE DATE
1560 D6=R7*365/360\D7=D6+80
1570 IF D7>365 THEN 1580\GØ TØ 1590
1580 D8=D7-365\GØ TØ 1600
1590 D8=D7
```

ACQ-7* CØNTINUED

```
1600 IF D8<31.5 THEN 1720
1610 IF D8<59.5 THEN 1730
1620 IF D8<90.5 THEN 1740
1630 IF D8<120.5 THEN 1750
1640 IF D8<151.5 THEN 1760
1650 IF D8<181.5 THEN 1770
1660 IF D8<212.5 THEN 1780
1670 IF D8<243.5 THEN 1790
1680 IF D8<273.5 THEN 1800
1690 IF D8<304.5 THEN 1810
1700 IF D8<334.5 THEN 1820
1710 D9=D8-334\AA="DECEMBER"\GØ TØ 1830
1720 D9=D8\AA="JANUARY"\GØ TØ 1830
1730 D9=D8-31\AA="FEBRUARY"\GØ TØ 1830
1740 D9=D8-59\AA="MARCH"\GØ TØ 1830
1750 D9=D8-90\AA="APRIL"\GØ TØ 1830
1760 D9=D8-120\AA="MAY"\GØ TØ 1830
1770 D9=D8-151\AA="JUNE"\GØ TØ 1830
1780 D9=D8-181\AA="JULY"\GØ TØ 1830
1790 D9=D8-212\AA="AUGUST"\GØ TØ 1830
1800 D9=D8-243\AA="SEPTEMBER"\GØ TØ 1830
1810 D9=D8-273\AA="ØCTØBER"\GØ TØ 1830
1820 D9=D8-304\AA="NØVEMBER"\GØ TØ 1830
1830 PRINT TAB(60);AA" "D9
1840 Z8=Z8+1\IF Z8<50 THEN 1900
1850 FØR Z7=1 TØ 5\PRINT\NEXT Z7
1860 PRINT"-----------------------------------------------------------------o
1870 FØR Z7=1 TØ 7\PRINT\NEXT Z7
1880 PRINT"ACQ-7* CØNTINUED"\PRINT\GØ TØ 140
1890 Z8=0
1900 RETURN
1910 IF Z8=50 THEN 1930
1920 FØR Ø1=Z8 TØ 50\PRINT\NEXT Ø1
1930 FØR Ø1=1 TØ 4\PRINT\NEXT Ø1
1940 PRINT"-----------------------------------------------------------------o
```

```
100 REM   **PRECISION DIRECT DRIVE SERVO SIMULATION**
110 REM   R = INPUT STEP SIZE, RADIANS
120 R = .02
130 REM   R1 = INPUT RATE, RAD/SEC
140 R1 = 0
150 REM   Q = INPUT AND FEEDBACK QUANTIZATION, RADIANS
160 Q = 8.8E-6
170 REM   EO = ERROR SIGNAL LIMIT, RADIANS
180 EO = .002253
190 REM   X0 = RATE LIMIT, RAD/SEC
200 X0 = .05
210 REM   LO = CONTROL TORQUE LIMIT, FT-LB
220 L0 = .5
230 REM   L1 = FRICTION TORQUE, FT-LB
240 L1 = .05
250 REM   L2 = STICTION TORQUE, FT-LB
260 L2 = 2*L1
270 REM   L5 = DITHER TORQUE AMPLITUDE, FT-LB
280 L5 = 0
290 REM   F5 = DITHER FREQUENCY, HERTZ
300 F5 = 650
310 REM   J = LOAD INERTIA, SLUG-FT SQUARED
320 J = .05
330 REM   K = DC TORQUE GAIN, FT-LB/RAD
340 K = 15000
350 REM   T1, T3 = LEAD TIME CONSTANTS, SEC
360 T1 = .02
370 T3 = .015
380 REM   T0, T2, T4 = LAG TIME CONSTANTS, SEC
385 T0 = .25
390 T2 = .0015
400 T4 = .001
410 REM   D = LOOP ITERATION PERIOD, SEC
420 D = .0002
430 REM   P = PRINTOUT INTERVAL, SEC
440 P = .025
470 REM   B = BEARING INITIAL CONDITION: 0 = STUCK, 1 = FREE
480 B = 0
490 REM   C2 = BREAKAWAY ANGLE OF STICTION, RADIANS
500 C2 = .0002
502 SET I = 1.4,S,Z
503 SET R = 6.1,S
504 SET E = 6.1
505 SET X = 6.1
506 SET L = 1.4,,Z
507 SET C = 6.1,S
510 PRINT "T0 ="T0, "T1 ="T1, "T2 ="T2, "T3 ="T3, "T4 ="T4
520 PRINT "R ="1E6*R,"R1 ="1E6*R1,"EO ="1E6*EO,"X0 ="1E6*X0,"Q ="1E6*Q
530 PRINT "LO ="L0, "L1 ="L1, "L2 ="L2, "L5 ="L5, "F5 ="F5*SGN(L5)
540 PRINT "K ="K, "J ="J, "D ="D, "B ="B, "C2 ="1E6*C2*SGN(L2)
```

```
550 PRINT
560 R9 = R
570 D5 = 1/(2*D*F5)
580 S = P/D-D
590 M = S
595 N9 = 5/D
600 RO = R1*D
602 IF C2 = 0 THEN 610
605 K2 = 12/C2
610 PRINT " TIME   Q-INPUT   Q-ERRØR   T-ERRØR   RATE   TØRQUE"
620 FØR N = 0 TØ N9
630 E9 = R9-C9
640 REM  ERRØR SIGNAL LIMITER
650 IF ABS(E9) < EO THEN 710
660 IF E9 > 0 THEN 690
670 E9 = -EO
680 GØ TØ 710
690 E9 = EO
700 REM  PRINTØUT CØNTRØL
710 M = M + 1
720 IF M < S THEN 810
725 GØSUB 1250
790 M = 0
800 REM  SHAPING NETWØRK
810 Y5 = (K*E9-X5)/T4
815 Y4 = (X5-X4)/T2
820 Y3 = (T3*Y4+X4-X3)/TO
822 X5 = X5+D*Y5
825 X4 = X4+D*Y4
830 X3 = X3+D*Y3
835 L = T1*Y3+X3
840 REM  TØRQUE LIMITER
845 IF ABS(X3) < LO THEN 870
850 IF X3 > 0 THEN 865
855 X3 = -LO
860 GØ TØ 870
865 X3 = LO
870 IF ABS(L) < LO THEN 892
875 IF L > 0 THEN 890
880 L = -LO
885 GØ TØ 892
890 L = LO
891 REM  RATE LIMITER
892 IF ABS(X2) < XO THEN 910
894 IF X2 < 0 THEN 898
896 L = -LO
897 GØ TØ 910
898 L = LO
900 REM  TØRQUE DITHER
910 IF L5 = 0 THEN 1010
```

```
920  N1 = INT(N/D5)
930  L = L+L5*SGN((-1)+N1)
1000 REM  FRICTION-STICTION MODEL
1010 IF L1 = 0 THEN 1140
1015 IF C2 = 0 THEN 1095
1017 REM-ELASTIC STICTION
1020 IF B = 1 THEN 1055
1025 L9 = L - K2*(C-C0)
1030 X2 = X2+D*L9/J
1035 C = C+D*X2
1040 IF ABS(C-C0) < C2 THEN 1150
1042 GOSUB 1250
1045 B = 1
1050 GO TO 1150
1055 L9 = L - L1*SGN(X2)
1060 X2 = X2+D*L9/J
1065 IF SGN(X2) = SGN(X9) THEN 1145
1067 GOSUB 1250
1070 B = 0
1075 C = C+D*X2
1080 C0 = C
1085 GO TO 1150
1090 REM-INELASTIC STICTION
1095 IF X2 = 0 THEN 1130
1100 L9 = L - L1*SGN(X2)
1105 X2 = X2+D*L9/J
1110 IF SGN(X2) = SGN(X9) THEN 1145
1115 IF ABS(L) > L2 THEN 1145
1120 X2 = 0
1125 GO TO 1150
1130 IF ABS(L) < L2 THEN 1170
1135 REM-NO FRICTION
1140 X2 = X2+D*L/J
1145 C = C+D*X2
1150 X9 = X2
1169 REM  QUANTIZATION
1170 IF Q = 0 THEN 1220
1180 C9 = Q*INT(C/Q+.5)
1190 R = R+R0
1200 R9 = Q*INT(R/Q+.5)
1210 GO TO 1240
1220 C9 = C
1230 R = R + R0
1235 R9 = R
1240 NEXT N
1245 GO TO 1320
1250 I = N*D
1260 R6 = 1E6*R9
1270 E6 = 1E6*(R-C)
1280 E7 = 1E6*E9
```

```
1290 X6 = 1E6*X2
1300 PRINT I;TAB(7);R6;TAB(15);E7;TAB(25);E6;TAB(35);X6;TAB(46);L
1310 RETURN
1320 END
```

7.2   Computer Printout

In the following pages the computer printout of program ACQ-5*
is given. It lists, for each of the useful included angles between
pairs of the eight star trackers, those stars pairs (in the list
of the first 100 stars) which have the same included angle (within
2 degrees).

ACQ-5*   16:57   THURS. 10/22/70

TRACKER ANGLE = 64.33 DEGREES
 1- 9, 1-44, 1-78, 2-93, 3-35, 3-64, 3-69, 3-70, 4- 5, 4-41, 4-49, 5-14,
 5-27, 5-48, 5-60, 5-61, 5-91, 5-97, 6-40, 8-89, 8-93, 9-26, 9-27,10-71,
10-87,11-54,11-55,11-62,12-47,12-50,12-51,12-54,12-65,12-91,13-38,13-40,
13-43,13-46,13-58,13-63,13-79,13-83,13-91,13-96,14-16,14-59,14-61,14-80,
14-88,15-27,15-31,15-33,15-34,16-57,16-60,17-23,17-26,17-49,17-51,17-58,
18-41,19-21,19-30,20-31,21-47,21-50,21-65,21-91,22-51,22-98,23-94,24-41,
24-55,25-48,25-62,25-64,25-89,26-32,26-35,27-44,27-81,28-79,28-85,29-51,
30-40,30-47,30-72,30-96,31-53,32-51,32-69,34-67,35-52,37-62,37-64,37-90,
38-55,38-59,38-75,39-65,40-70,40-73,40-87,41-37,42-81,44-51,44-95,46-81,
49-70,50-67,51-74,51-85,51-94,54-91,55-87,55-91,56-57,56-75,57-61,57-80,
58-66,58-86,58-95,59-60,59-86,60-61,60-80,61-77,62-82,62-85,64-82,65-86,
71-74,73-81,74-91,74-95,75-98,78-95,81-92,86-96,89-97,97-98,

TRACKER ANGLE = 104.23 DEGREES
 1-21, 1-26, 1-32, 1-38, 1-43, 2-79, 3-77, 3-86, 3-99, 4- 7, 4-38, 4-52,
 4-65, 4-69, 5-59, 5-86, 6-18, 6-24, 8-20, 8-37, 9-10, 9-58,10-30,10-31,
10-39,10-55,10-77,11-53,11-63,11-99,12-37,12-89,13-14,13-62,14-80,14-33,
14-37,14-99,15-65,15-85,15-95,15-96,16-50,16-64,16-69,17-29,17-90,17-91,
18-40,18-51,18-95,19-90,20-60,20-86,21-33,22-30,22-57,22-81,23-28,23-36,
23-47,23-50,23-52,23-70,23-75,23-38,24-40,24-51,24-52,26-57,26-68,26-70,
26-71,26-87,26-93,27-71,28-56,28-81,28-94,29-60,29-97,31-35,31-59,31-80,
31-82,32-56,33-57,34-38,34-70,34-93,36-43,36-56,36-95,37-57,37-60,38-58,
39-62,39-69,40-45,41-44,42-70,42-95,43-58,44-86,45-51,45-95,46-64,46-95,
47-79,48-50,48-83,48-96,49-58,50-89,51-57,51-68,51-70,51-72,51-93,51-96,
56-78,56-85,57-69,58-70,60-99,62-30,62-33,62-92,62-98,63-95,64-70,64-80,
64-83,65-70,69-71,69-75,69-87,69-93,70-73,70-89,70-92,72-90,77-86,80-99,
81-84,84-86,87-94,92-95,97-99,

TRACKER ANGLE = 62.34 DEGREES
 1-44, 1-78, 1-81, 2-20, 2-33, 3-70, 4- 5, 4-41, 4-49, 4-55, 5- 6, 5- 7,
 5-14, 5-18, 5-39, 5-48, 5-61, 5-91, 5-97, 6-40, 8-16, 8-61, 8-76, 8-97,
 9-26, 9-43, 9-95,10-53,10-71,10-87,11-41,11-54,11-56,11-82,12-19,12-23,
12-47,12-50,12-54,12-72,12-91,13-40,13-43,13-58,13-63,13-79,13-92,13-96,
14-16,14-48,14-80,15-18,15-27,15-33,15-44,15-77,16-22,16-25,16-60,17-49,
17-51,17-58,19-81,21-43,21-47,21-50,21-65,21-91,22-48,22-51,23-76,25-62,
25-64,25-66,25-85,25-89,26-32,26-44,27-44,27-78,27-81,28-43,28-48,28-79,
28-85,29-66,29-98,30-40,30-50,30-96,31-33,31-53,31-68,32-51,32-62,32-84,
34-54,34-67,35-52,35-93,36-57,36-60,36-97,37-62,38-55,38-57,38-59,38-67,
38-75,38-99,39-93,40-70,41-87,47-81,48-57,48-60,49-70,51-74,52-83,55-87,
57-59,57-80,58-66,59-86,60-61,61-75,61-97,62-85,64-82,65-76,72-81,73-81,
74-87,74-91,74-95,81-83,86-96,97-98,

TRACKER ANGLE = 141.41 DEGREES
 1-17, 1-80, 2-66, 3-18, 3-24, 3-30, 4-13, 4-73, 4-83, 5-10, 5-58, 6-43,
 6-44, 7-43, 7-77, 8-32,11-80,12-78,13-15,13-20,13-29,13-31,13-89,14-17,
15-99,16-95,17-27,17-57,17-60,18-19,18-36,18-47,18-58,18-72,18-88,18-96,
19-24,19-45,20-50,21-23,22-49,22-73,24-36,24-58,24-72,24-76,24-83,24-78,
25-53,25-63,26-29,27-58,27-59,27-80,28-63,29-30,29-96,32-91,33-76,34-35,
34-63,35-72,35-82,37-46,37-83,38-51,40-56,43-54,43-71,46-81,44-59,45-47,
45-58,45-72,45-96,48-95,49-76,49-80,49-81,51-99,53-77,57-65,57-70,57-78,

7-19

ACQ-5* CONTINUED

58-99,60-82,62-65,65-78,65-95,66-75,66-91,68-77,69-99,70-75,71-84,75-94,
78-88,79-90,79-93,82-88,82-97,93-95,94-97,

TRACKER ANGLE = 135.33 DEGREES
  1-35, 1-58, 2-26, 2-85, 3-11, 3-81, 4-10, 4-19, 4-36, 4-72, 4-88, 4-96,
  5-90, 5-25, 6-77, 8-78, 9-57, 9-60, 9-76, 9-97,10-21,10-79,11-19,11-47,
 11-50,11-59,11-72,11-94,12-28,12-49,12-82,13-84,14-79,14-94,15-88,16-53,
 18-50,20-91,21-22,22-59,22-65,23-38,23-89,24-50,25-93,27-35,28-58,28-93,
 29-42,29-92,30-49,31-66,32-50,32-83,32-86,33-87,33-91,34-36,34-83,34-88,
 34-94,35-49,37-38,37-87,38-49,38-82,39-70,40-66,40-77,41-43,43-56,43-67,
 43-87,49-88,50-66,52-77,53-84,54-70,57-94,60-70,62-99,64-91,65-69,66-71,
 68-79,68-84,68-95,70-97,71-79,75-78,76-77,76-79,77-93,78-97,79-97,85-91,
 89-95,95-98,

TRACKER ANGLE = 85.17 DEGREES
  1- 6, 1-52, 1-99, 2-22, 2-50, 2-96, 4-32, 5-73, 6-15, 6-27, 6-74, 8-10,
  8-11, 8-21, 8-34, 8-90, 9-56, 9-94,10-88,11-51,11-57,11-60,11-66,11-97,
 12-48,13-23,13-51,13-65,13-71,15-68,15-71,15-78,15-82,16-53,16-68,16-99,
 17-36,17-99,18-43,18-62,18-81,18-85,18-90,19-94,20-30,20-90,21-55,21-67,
 21-81,21-87,21-92,22-36,22-95,23-42,23-73,23-82,24-43,24-62,24-90,25-31,
 26-63,26-78,27-52,27-56,28-95,29-41,29-54,30-33,30-59,30-80,30-99,31-50,
 31-96,32-58,33-43,33-56,33-69,33-79,34-75,34-79,34-90,34-97,36-41,36-99,
 37-67,38-79,39-91,40-74,41-63,41-76,41-84,42-94,45-62,45-64,45-81,45-85,
 45-90,45-51,48-71,48-82,51-80,51-84,52-58,53-61,55-56,55-63,55-99,56-74,
 56-80,57-58,58-85,59-90,61-68,62-74,62-76,63-94,64-76,67-88,67-90,72-94,
 73-94,74-85,74-86,76-94,78-94,81-90,83-90,84-95,87-90,89-93,90-98,92-94,
 94-99,

TRACKER ANGLE = 102.42 DEGREES
  1-21, 1-32, 1-38, 1-40, 1-71, 1-79, 2-35, 2-63, 2-79, 3-68, 3-77, 3-99,
  4- 6, 4-38, 4-52, 4-65, 4-69, 4-86, 5-59, 5-82, 5-86, 7-11, 7-34, 8-20,
  8-37, 9-10, 9-31, 9-58,10-30,10-41,10-67,10-77,11-53,12-27,12-37,12-66,
 13-62,14-33,14-99,15-73,16-64,16-69,17-22,17-38,17-84,17-91,18-26,18-40,
 20-51,20-60,20-75,20-86,20-97,21-48,21-61,22-30,22-75,22-81,23-28,23-33,
 23-35,23-36,23-47,23-52,23-75,24-26,24-40,25-67,26-45,26-53,26-71,26-87,
 26-93,27-32,27-38,27-43,27-71,28-56,28-94,29-57,29-60,29-79,29-97,31-82,
 31-88,32-56,33-57,33-60,34-65,34-70,34-93,36-39,36-43,36-95,37-57,37-60,
 37-97,38-58,38-62,40-45,43-89,44-53,45-57,45-86,45-95,46-62,46-64,48-50,
 48-64,48-69,48-96,49-58,50-89,51-57,51-63,51-70,51-93,51-96,53-69,54-77,
 55-77,56-82,57-89,58-70,59-66,61-89,61-91,62-80,62-83,63-64,63-95,64-70,
 64-79,69-73,69-93,70-73,70-96,77-86,81-84,87-94,97-99,

TRACKER ANGLE = 40.13 DEGREES
  1-84, 2- 5, 3-58, 4-11, 5-21, 5-38, 5-99, 6-19, 6-41, 6-42, 6-47, 6-55,
  6-72, 6-73, 6-83, 6-92, 7-38, 7-42, 7-46, 7-54, 7-92, 8-81, 9-20, 9-32,
  9-33,10-26,11-25,11-77,11-98,12-46,12-57,12-63,12-68,12-83,12-87,13-38,
 14-31,14-91,15-22,16-20,16-33,16-67,17-32,18-77,18-78,19-76,19-93,20-22,
 20-29,20-44,20-61,20-82,20-89,20-98,23-66,23-90,24-77,25-34,26-58,26-90,
 27-84,30-93,31-60,31-75,32-78,33-61,33-82,33-89,35-46,35-63,35-83,36-71,
 37-78,37-82,38-96,40-83,41-52,42-52,42-74,45-48,45-78,46-52,46-74,46-88,

7-20

47-93,49-66,49-84,50-52,50-93,52-55,52-73,52-86,52-92,53-59,53-81,53-86,
54-93,54-98,56-69,58-59,59-71,59-88,59-91,60-86,61-67,63-74,63-88,64-90,
65-67,65-73,67-93,68-76,70-99,71-80,71-81,72-76,72-93,74-76,76-93,82-85,
83-88,85-94,86-90,86-97,

TRACKER ANGLE = 53.41 DEGREES
1-67, 1-77, 2-18, 2-24, 2-45, 2-57, 3-51, 3-66, 3-85, 4- 9, 4-22, 4-31,
4-44, 5-41, 5-81, 5-98, 6-76, 7-12, 7-31, 7-35, 7-59, 7-76, 7-80, 7-88,
8-12, 8-19, 8-38, 8-42, 8-46, 8-73, 8-92,10-62,10-64,10-80,10-83,10-92,
11-31,11-90,12-15,12-80,12-96,13-59,14-38,14-63,15-26,16-84,17-79,19-57,
19-60,19-97,21-35,22-27,25-32,26-95,27-67,28-89,28-93,29-49,29-61,29-69,
30-38,30-87,30-91,31-93,32-77,33-49,34-44,35-53,35-68,35-76,36-52,37-89,
38-52,38-53,38-80,38-92,39-45,41-68,41-86,42-58,42-60,42-75,42-97,44-69,
44-85,46-75,46-86,46-97,47-57,47-60,47-74,47-97,49-79,50-75,51-95,53-88,
54-71,55-63,56-53,57-72,58-83,58-92,60-63,60-72,61-84,62-77,63-86,64-95,
65-80,66-77,67-86,68-88,72-97,73-75,73-97,74-96,75-92,78-79,79-82,81-89,
81-98,83-86,84-89,84-93,92-97,

TRACKER ANGLE = 95.70 DEGREES
1-12, 1-68, 1-69, 2-42, 2-56, 2-73, 2-83, 2-88, 2-90, 2-92, 3-44, 3-71,
4-14, 4-40, 4-57, 4-62, 4-64, 4-66, 4-70, 5-11, 5-13, 5-37, 5-46, 5-63,
5-80, 6-11, 6-13, 6-34, 8-18, 8-45, 8-58, 8-74, 9-39,10-11,10-54,10-85,
11-52,11-85,11-93,12-22,13-93,14-24,16-87,17-25,17-28,17-40,17-50,17-83,
18-60,18-75,18-97,19-39,19-56,20-26,20-56,21-31,21-34,21-45,21-95,22-67,
23-68,23-71,23-78,23-93,23-96,24-60,25-54,25-55,26-28,26-42,26-43,26-73,
27-62,27-64,27-79,28-67,29-43,31-36,31-44,31-76,32-90,33-51,33-86,34-85,
35-41,36-79,37-95,38-61,38-94,39-42,39-46,39-47,39-72,39-73,39-76,39-82,
39-92,40-48,40-61,41-59,41-80,43-51,43-62,43-88,44-99,45-56,45-70,45-75,
45-97,48-49,48-62,48-91,50-70,54-99,55-59,55-80,56-72,56-95,58-65,58-97,
59-62,59-64,61-62,61-87,69-80,69-83,70-72,70-91,71-89,74-75,74-79,74-97,
77-94,78-90,80-90,81-99,88-95,89-90,89-91,90-95,91-94,

TRACKER ANGLE = 141.33 DEGREES
1-17, 1-80, 2-66, 3-18, 3-24, 3-30, 4-13, 4-73, 4-83, 5-10, 5-58, 6-43,
6-44, 7-43, 7-77, 8-82,11-80,12-78,13-15,13-20,13-29,13-31,13-89,14-17,
15-93,16-95,17-27,17-57,18-19,18-36,18-47,18-58,18-72,18-88,18-96,19-24,
19-45,20-50,21-23,22-42,22-73,24-36,24-58,24-72,24-76,24-83,24-88,25-53,
25-68,26-99,27-58,27-59,27-80,28-68,29-80,29-95,32-91,33-76,34-35,34-63,
35-78,35-92,37-46,37-83,38-51,40-56,43-54,43-81,44-59,45-47,45-58,45-72,
45-96,48-95,49-76,49-80,49-81,51-93,53-77,57-66,57-70,57-78,58-99,60-82,
62-65,65-73,65-95,66-75,66-91,63-77,69-99,70-75,71-84,75-82,75-94,78-88,
79-90,79-93,82-88,82-97,93-95,94-97,

TRACKER ANGLE = 118.22 DEGREES
1-10, 1-50, 1-70, 1-96, 3-28, 3-57, 3-84, 4-12, 4-53, 4-71, 5-15, 5-17,
5-32, 5-74, 5-85, 5-94, 6-26, 6-29, 6-69, 7-20, 7-26, 7-37, 7-51, 7-69,
8-26, 8-28, 8-51, 8-69, 9-12, 9-67,10-33,10-84,12-18,12-45,12-84,13-30,
13-56,13-81,14-62,14-84,15-17,16-23,16-51,16-66,17-18,17-45,17-53,17-71,
18-68,19-69,20-33,20-65,20-93,20-94,21-37,21-58,21-66,21-77,22-75,23-27,
23-34,23-39,23-54,23-81,24-53,24-68,25-58,25-75,26-31,26-54,26-98,27-50,

ACQ-5* CONTINUED

27-96,28-60,28-75,28-36,28-97,29-53,29-68,30-44,30-58,30-78,30-79,32-48,
32-80,33-65,35-66,35-69,35-89,36-61,36-85,37-58,37-94,38-95,39-51,40-49,
40-82,41-58,41-64,42-66,42-79,42-89,42-93,43-48,43-91,46-89,46-98,46-99,
47-69,48-86,51-91,52-64,54-64,54-74,54-82,55-62,55-79,60-64,61-85,62-96,
63-99,64-68,64-87,66-73,66-83,66-88,66-92,66-98,67-74,67-82,69-81,69-89,
70-76,70-87,73-79,73-98,75-77,76-85,85-93,88-98,89-92,92-98,

TRACKER ANGLE = 68.50 DEGREES
 1- 5, 1-82, 2-37, 2-38, 2-40, 2-68, 3-43, 3-62, 3-63, 3-76, 3-88, 4-54,
 4-67, 5-34, 5-50, 5-52, 5-75, 5-88, 6-48, 8-35, 8-40, 8-59, 8-80, 8-88,
 9-15, 9-51, 9-79,10-68,10-93,10-96,11-49,11-64,11-67,11-89,12-26,12-30,
12-41,12-67,12-69,13-85,14-35,14-40,14-89,14-98,15-18,15-20,15-24,15-25,
15-34,15-41,15-45,15-54,15-57,15-75,15-98,16-77,17-64,18-54,18-55,19-58,
22-23,22-32,23-29,23-32,23-59,23-85,23-86,24-54,25-43,26-49,26-74,26-77,
26-94,27-82,28-99,29-39,29-88,30-34,30-73,30-83,31-37,31-71,34-49,35-94,
36-81,37-69,38-41,38-54,39-53,39-68,39-84,40-42,40-52,40-67,40-68,40-71,
40-79,40-80,40-81,40-92,41-45,41-91,43-44,44-90,45-55,47-67,48-52,48-77,
48-86,49-69,49-94,51-76,53-56,53-58,53-74,56-93,58-71,58-72,58-87,58-96,
59-75,59-97,60-88,60-89,60-98,62-84,63-81,64-78,64-84,65-84,66-90,67-96,
69-85,70-78,70-82,75-80,75-89,76-90,77-90,77-93,78-89,78-99,80-86,80-97,
84-85,86-91,89-99,

TRACKER ANGLE = 65.99 DEGREES
 1- 9, 2-38, 2-93, 3-35, 3-43, 3-64, 3-69, 3-76, 4- 5, 4-54, 4-99, 5-27,
 5-34, 5-60, 5-61, 8-40, 8-80, 8-88, 8-89, 8-98, 9-26, 9-27, 9-51,10-68,
10-93,10-96,11-55,11-62,11-64,12-26,12-51,12-54,12-65,12-67,12-69,12-74,
13-38,13-46,13-79,13-83,13-91,14-59,14-61,14-80,14-88,14-98,15-24,15-25,
15-31,15-54,15-75,15-84,16-57,16-77,17-23,17-26,18-41,18-55,19-21,19-30,
20-31,21-72,22-32,22-98,23-94,24-41,24-55,25-48,26-77,26-85,26-94,27-72,
28-85,28-99,29-51,30-47,30-72,31-37,31-53,31-71,32-51,32-69,34-49,34-67,
35-75,37-64,37-90,38-54,39-65,39-68,40-42,40-73,40-87,41-45,41-91,42-81,
44-51,44-90,44-95,46-81,48-86,49-69,50-67,51-74,51-85,51-94,54-91,55-91,
56-57,56-75,57-61,58-66,58-86,58-87,58-95,58-96,59-60,59-75,60-80,60-98,
61-77,62-82,62-84,64-84,65-86,67-96,69-85,70-78,70-82,71-74,73-81,75-98,
76-90,77-98,78-95,78-99,81-92,84-85,89-97,89-99,97-98,

TRACKER ANGLE = 107.31 DEGREES
 1-43, 1-51, 1-66, 1-85, 1-87, 2-76, 3-15, 3-22, 3-93, 4-93, 5-77, 6-18,
 6-45, 7-24, 8-15, 8-29,10-37,10-38,10-49,10-55,11-43,11-71,11-79,12-40,
12-94,13-14,13-57,13-60,13-82,14-20,14-29,14-37,15-74,15-80,15-96,16-50,
16-79,16-96,17-29,17-56,17-90,18-51,18-52,18-95,19-48,19-51,19-79,19-89,
19-90,20-23,20-40,20-57,21-33,21-76,21-84,22-57,22-60,22-94,22-97,23-60,
23-70,23-88,24-51,24-52,24-65,24-95,25-30,25-86,26-27,26-34,26-68,26-75,
26-79,26-96,27-66,27-85,27-87,28-40,28-81,31-59,34-38,35-51,35-85,37-70,
39-49,39-64,39-69,39-98,40-85,41-44,41-78,42-62,42-64,42-95,43-58,43-98,
44-54,44-55,45-51,45-52,46-48,46-95,47-48,47-51,47-79,47-89,47-90,48-72,
48-76,48-83,50-61,50-79,50-90,50-98,51-52,51-72,51-75,51-79,52-99,53-62,
55-73,55-85,56-94,57-62,58-77,58-81,61-79,61-96,62-70,62-75,62-79,62-92,
63-70,64-83,64-92,64-93,65-70,65-90,66-80,66-86,66-99,67-77,68-69,69-87,
70-89,70-92,72-79,72-80,72-90,73-95,73-99,74-81,79-80,79-91,80-99,83-95,

ACQ-5* CONTINUED

84-94,85-88,87-99,89-96,90-91,90-94,92-95,96-98,

TRACKER ANGLE = 128.89 DEGREES
 1-36, 1-95, 2-32, 2-64, 3- 5, 4-50, 4-94, 5-95, 6-28, 6-64, 6-79, 7-17,
 7-64, 7-79, 7-84, 8-70, 9-81,10-18,10-24,10-28,10-34,10-45,11-17,11-21,
11-38,11-40,11-42,11-73,11-91,11-92,11-96,12-32,12-85,13-25,13-54,13-55,
13-77,14-77,15-43,16-59,16-80,17-34,17-86,17-93,18-37,18-91,19-66,20-53,
21-86,22-74,23-30,23-55,24-87,24-91,24-94,26-55,26-89,27-36,27-42,27-63,
27-73,27-92,28-52,28-65,29-46,29-63,29-74,29-83,29-87,30-62,32-38,32-42,
32-46,32-63,32-92,33-71,34-50,34-95,35-61,35-82,36-62,36-64,37-40,37-76,
38-73,39-43,39-66,43-46,43-83,43-90,44-57,44-60,44-76,44-97,45-91,47-62,
47-64,47-66,48-58,48-70,49-54,49-86,50-62,50-64,50-85,51-55,51-65,51-67,
52-94,53-70,54-79,59-61,61-80,64-88,66-72,66-96,67-70,70-81,71-95,74-77,
74-78,78-86,79-81,79-87,80-89,81-82,82-86,83-85,84-93,

TRACKER ANGLE = 132.92 DEGREES
 1-58, 1-88, 2-13, 2-26, 2-85, 3-11, 3-20, 3-33, 4-19, 4-36, 4-47, 4-72,
 4-88, 4-96, 5-56, 5-90, 6-17, 6-25, 7-23, 8-44, 8-79, 9-40, 9-75, 9-97,
10-21,10-79,10-89,11-50,11-59,11-94,12-28,12-49,13-41,14-44,14-70,15-35,
15-38,15-88,17-52,19-32,19-34,20-71,22-46,22-59,22-63,22-83,22-87,23-38,
25-52,26-30,26-65,27-88,28-58,29-59,29-85,29-92,30-43,30-51,30-64,31-43,
31-70,31-74,32-39,32-47,32-72,32-73,32-83,33-58,33-87,34-47,34-72,34-94,
35-49,37-38,37-87,38-82,38-84,38-90,39-70,40-77,41-70,43-55,43-76,45-87,
49-67,49-88,50-66,51-89,52-70,52-77,53-66,53-95,57-94,58-61,59-89,59-93,
62-88,62-91,64-99,65-69,65-84,66-71,66-87,68-95,70-93,70-97,75-78,76-77,
76-79,76-99,77-93,78-97,80-98,85-96,

TRACKER ANGLE = 101.51 DEGREES
 1-32, 1-40, 1-71, 1-79, 2- 9, 2-35, 2-63, 3-68, 3-78, 3-99, 4- 6, 4-56,
 4-65, 4-69, 4-86, 5-59, 5-82, 5-86, 6-99, 7-11, 7-34, 8-20, 8-33, 8-37,
 9-10, 9-31,10-30,10-41,10-67,10-77,12-27,12-66,13-64,14-33,14-45,14-99,
15-32,15-42,15-73,16-62,16-64,17-22,17-38,17-84,18-26,18-57,19-23,20-51,
20-75,20-97,21-39,21-48,21-61,22-30,22-75,22-81,23-33,23-35,23-47,23-52,
23-72,23-75,24-26,25-67,25-94,26-45,26-53,26-71,26-87,27-32,27-38,27-43,
27-53,27-69,27-71,28-56,28-94,29-57,29-79,29-97,31-88,33-57,33-60,33-70,
33-95,34-65,34-70,34-93,36-39,36-43,36-95,37-57,37-60,37-97,38-58,39-62,
42-69,43-89,44-53,45-57,45-86,46-62,46-64,48-64,48-69,49-56,49-58,50-89,
51-71,51-87,51-93,51-96,53-69,54-77,55-77,56-82,56-89,57-69,58-70,59-66,
61-64,61-89,61-91,62-83,63-84,63-95,64-70,64-79,66-76,69-73,70-73,70-96,
81-84,85-90,97-99,

TRACKER ANGLE = 147.17 DEGREES
 1-94, 3-34, 3-54, 3-67, 4-63, 4-76, 5-66, 6- 9, 6-78, 6-95, 7-44, 7-78,
 8-43, 9-93,11-36,12-70,12-99,13-18,13-24,13-33,13-37,13-39,14-43,17-75,
17-97,17-98,18-35,18-42,18-46,18-73,18-92,20-36,20-47,20-72,20-76,20-88,
20-95,21-26,21-64,22-40,22-96,23-99,24-35,24-42,24-46,24-63,24-73,24-92,
25-71,27-94,28-35,28-71,28-74,29-40,29-91,32-41,32-55,32-87,33-46,33-47,
33-83,33-95,35-45,36-72,37-42,37-74,37-92,37-96,38-66,38-77,40-51,43-53,
43-68,44-46,44-53,44-68,44-71,44-80,45-46,45-73,45-76,45-83,49-63,52-78,
52-95,54-66,56-70,57-79,59-77,60-66,65-77,71-77,74-84,76-82,81-94,84-87,

ACQ-5* CONTINUED

89-94,

TRACKER ANGLE = 115.19 DEGREES
 1-10, 2-43, 2-70, 3- 6, 4-68, 4-68, 5-22, 5-29, 5-44, 5-74, 6-20, 6-26,
 6-29, 6-37, 6-51, 6-69, 7-33, 7-51, 8-23, 8-28, 8-69, 8-84, 9-13, 9-21,
 9-54,10-16,10-25,10-82,10-84,11-76,11-87,12-18,12-24,12-33,12-77,13-56,
13-81,13-86,14-26,14-51,14-69,14-84,15-19,15-47,15-50,15-72,16-32,16-36,
16-42,16-43,16-51,16-63,16-73,16-76,16-92,17-33,17-71,19-43,19-69,20-52,
20-65,22-52,22-76,22-93,23-34,23-39,23-48,23-61,24-68,26-36,26-39,26-50,
26-88,26-97,27-51,28-97,29-70,29-76,30-58,30-74,30-78,31-49,31-64,32-59,
32-61,32-80,32-88,33-40,33-93,34-71,34-95,35-66,35-89,36-48,36-90,36-98,
37-93,38-45,39-51,40-58,40-82,41-62,41-69,42-61,42-66,43-50,43-59,43-61,
43-72,44-57,45-93,46-66,46-99,48-51,50-95,51-61,51-91,51-97,52-62,53-94,
53-99,54-58,54-62,55-82,57-84,58-67,58-79,59-79,59-99,60-62,60-84,61-63,
61-66,61-73,61-76,61-92,62-68,62-87,62-97,64-71,64-75,64-87,64-89,64-93,
65-94,66-83,66-92,67-78,68-94,69-72,70-87,70-98,73-89,73-98,77-81,79-96,
83-89,83-93,83-99,85-89,85-93,95-96,

TRACKER ANGLE = 81.26 DEGREES
 1-49, 1-56, 2-15, 2-25, 2-29, 2-87, 3-49, 3-50, 3-96, 4-43, 5-28, 5-33,
 5-53, 6-10, 6-21, 6-56, 7-10, 7-56, 7-74, 8-15, 9-48, 9-70, 9-89,10-13,
10-14,10-17,10-35,10-36,10-60,10-91,10-95,10-97,11-26,11-75,12-88,13-66,
14-90,15-28,15-30,15-52,15-53,15-76,16-56,16-82,17-21,17-44,18-32,18-79,
18-81,19-41,20-62,20-64,20-66,20-67,21-42,21-73,21-80,21-89,22-31,23-83,
23-92,24-32,24-79,24-81,25-51,25-99,26-59,26-84,27-57,27-86,27-90,27-99,
28-31,28-62,29-86,30-35,30-76,31-40,31-90,32-45,33-66,33-85,33-99,35-99,
36-54,36-55,36-70,36-86,36-94,37-51,37-54,37-85,38-39,38-89,39-77,40-43,
41-42,41-46,41-56,41-73,41-90,41-92,42-55,42-56,43-45,45-79,46-55,46-90,
48-53,48-68,51-63,51-82,52-74,52-90,54-63,54-76,55-73,55-92,56-61,56-67,
56-73,56-81,58-91,59-81,60-90,61-65,61-82,63-90,64-74,64-86,65-74,65-93,
65-99,67-76,68-90,69-78,70-74,71-90,82-94,84-99,86-93,90-97,93-98,

TRACKER ANGLE = 75.69 DEGREES
 1-14, 1-57, 1-60, 1-90, 2-71, 2-84, 2-86, 2-91, 3-19, 3-72, 3-79, 3-83,
 4-15, 5-45, 5-63, 5-79, 5-93, 5-96, 6-61, 6-89, 6-98, 7-16, 7-61, 8-27,
 9-23, 9-61, 9-90, 9-93,10-47,10-50,10-75,11-30,11-81,12-31,12-39,12-62,
13-32,13-87,13-99,14-27,14-56,15-55,15-58,15-60,15-67,15-81,15-97,16-44,
16-78,17-35,17-62,17-80,17-82,18-30,19-54,19-55,20-41,20-43,20-55,20-79,
23-63,23-77,24-30,24-99,26-82,26-86,27-60,27-75,27-97,28-39,29-31,29-85,
30-63,30-88,31-33,31-84,31-91,32-33,33-54,33-62,33-64,34-81,34-99,35-75,
36-67,37-41,37-56,38-76,38-86,39-90,40-41,40-46,40-54,40-59,40-63,41-50,
41-96,42-54,42-67,44-48,44-79,44-93,45-67,46-54,46-67,47-54,47-55,48-56,
48-65,48-90,48-93,49-99,50-58,51-59,51-86,52-98,54-56,54-72,54-73,54-83,
54-92,55-72,56-59,56-66,56-87,56-92,57-89,58-68,58-88,58-93,61-78,61-90,
62-86,62-94,65-89,66-70,66-79,67-73,67-92,69-74,69-76,69-84,69-94,74-93,
75-87,79-84,81-83,82-95,84-90,85-99,88-99,90-93,98-99,

TRACKER ANGLE = 99.31 DEGREES
 1-53, 1-71, 2- 9, 2-35, 2-44, 2-46, 2-82, 3-38, 3-40, 3-53, 3-63, 3-78,
 4-56, 4-57, 4-66, 5-25, 6-11, 6-99, 7-34, 7-99, 8-33, 8-99, 9-31,10-32,

ACQ-5* CONTINUED

10-44,10-67,10-85,12-13,12-27,12-98,13-49,13-52,13-64,13-69,14-18,14-45,
15-32,15-42,15-59,15-92,16-21,16-62,16-91,17-50,17-96,18-21,18-57,18-70,
18-86,19-23,20-21,20-51,20-95,21-24,21-27,21-39,21-45,21-49,21-57,21-75,
21-82,22-58,22-79,23-43,23-57,23-68,23-72,24-57,24-70,24-86,25-54,25-94,
26-45,26-53,27-38,27-40,27-53,27-68,27-69,28-30,28-51,29-30,29-57,29-58,
29-75,29-81,30-84,31-78,33-60,33-70,33-75,33-95,33-97,34-40,34-52,34-65,
34-66,34-69,37-75,37-97,38-43,39-63,39-76,39-82,41-77,42-69,43-89,44-58,
45-60,45-86,46-62,47-56,48-64,49-56,50-56,51-53,51-71,51-87,55-77,56-65,
56-82,56-89,56-91,56-95,59-66,59-70,61-64,61-69,61-91,62-63,63-64,66-76,
69-92,70-91,76-95,79-98,85-90,87-89,87-93,90-96,91-94,91-98,96-99,

TRACKER ANGLE = 98.52 DEGREES
1-53, 2- 9, 2-42, 2-44, 2-45, 2-82, 2-88, 2-92, 3-38, 3-40, 3-53, 3-78,
4-56, 4-57, 4-66, 5-25, 5-63, 6-11, 6-34, 6-99, 7-34, 7-99, 8-33, 8-58,
8-99,10-11,10-32,10-44,10-54,10-85,11-85,11-93,12-13,12-98,13-49,13-52,
13-64,13-69,14-18,14-24,14-45,15-32,15-42,15-59,15-92,16-21,16-62,16-91,
17-28,17-50,17-96,18-21,18-57,18-70,18-86,19-23,20-21,20-26,20-95,21-24,
21-27,21-39,21-45,21-49,21-57,21-75,21-82,22-58,22-79,23-43,23-57,23-68,
23-72,23-93,24-57,24-70,24-86,25-54,25-94,26-53,27-40,27-53,27-64,27-68,
27-69,27-79,28-30,28-51,29-30,29-58,29-75,29-81,30-84,31-44,31-78,33-70,
33-75,33-86,33-95,33-97,34-40,34-52,34-66,34-69,37-75,38-43,38-94,39-42,
39-63,39-76,39-82,41-59,41-77,42-69,43-69,43-89,45-60,47-56,48-62,48-91,
49-56,50-56,51-53,51-71,51-87,55-59,56-65,56-89,56-91,56-95,58-65,59-70,
61-64,62-63,66-76,69-92,70-91,76-95,79-93,85-90,87-89,87-93,90-96,91-94,
91-98,96-99,

TRACKER ANGLE = 43.91 DEGREES
1-41, 2- 9, 2-34, 4-73, 5-30, 6-38, 6-42, 6-46, 6-92, 7-36, 7-41, 7-55,
7-63, 8-39, 8-86, 9-45, 9-66, 9-85,10-59,10-89,10-90,11-39,11-44,12-42,
12-52,12-75,12-90,12-92,14-50,14-86,14-96,15-62,15-86,16-30,16-37,17-43,
17-66,17-70,18-22,18-29,19-52,20-48,21-70,22-24,22-28,22-45,22-62,22-64,
22-82,23-56,24-29,24-78,26-56,27-28,27-41,28-29,29-45,29-62,30-48,30-68,
30-89,31-57,32-44,32-94,33-48,34-39,35-40,35-74,35-87,36-40,36-53,36-68,
37-61,39-60,39-75,39-97,40-65,40-91,40-99,42-65,42-74,43-49,43-95,44-45,
44-64,44-66,45-82,46-74,47-52,47-76,50-78,51-56,51-90,52-63,52-72,53-80,
54-89,55-65,56-62,57-83,57-91,57-96,59-68,60-91,60-96,65-83,65-88,65-92,
67-89,67-98,68-80,68-86,70-85,70-94,71-86,73-74,74-83,74-92,76-86,79-85,
87-88,91-97,

TRACKER ANGLE = 64.92 DEGREES
1- 9, 1-78, 2-93, 3-35, 3-64, 3-69, 3-76, 4- 5, 4-99, 5-27, 5-48, 5-60,
5-61, 8-40, 8-89, 8-93, 9-26, 9-27,10-68,10-71,10-87,10-93,11-54,11-55,
11-62,12-47,12-51,12-54,12-65,12-74,12-91,13-38,13-40,13-43,13-46,13-79,
13-83,13-91,14-16,14-59,14-61,14-80,14-88,15-27,15-31,15-84,16-57,17-23,
17-26,17-51,18-41,18-55,19-21,19-30,20-31,21-47,21-50,21-65,21-72,22-32,
22-51,22-93,23-94,24-41,24-55,25-48,25-62,26-32,26-77,26-85,27-44,27-81,
28-85,28-99,29-51,30-47,30-72,31-53,31-71,32-51,32-69,34-67,36-75,37-62,
37-64,37-90,38-55,38-59,38-75,39-65,40-70,40-73,40-87,41-87,42-81,44-51,
44-95,46-81,50-67,51-74,51-85,51-94,54-91,55-87,55-91,56-57,56-75,57-81,
57-90,57-66,58-86,58-95,59-60,59-86,60-51,60-80,60-93,61-77,62-82,62-85,

ACQ-5* CONTINUED

65-86,71-74,73-81,74-95,75-98,76-90,78-95,81-92,86-96,89-97,97-98,

7.3   Sunshade Design and Testing

Critical to meeting the STARS Star Tracker goals is the successful achievement of the sunshade performance requirements. The design and manufacture of sunshades has historically proven to be a difficult task and the manufactured hardware has often not matched theoretical prediction. Hughes Aircraft has, and is doing, a considerable amount of work in the area of sunshade design in numerous visible and IR sensor systems. Sunshade analysis, material evaluation, and testing approaches are receiving on-going efforts.

Proper evaluation of sunshade designs is as important as their design and analysis. During the development of the sunshade for the LORS (Lunar Optical Rendezvous Subsystem) Star Tracker, it was necessary to evolve methods for evaluation of sunshade performance. At that time, (April 1966), the technique of testing in a helium atmosphere was first utilized at Hughes Aircraft Company. Sunshade testing previously was always done in vacuum to eliminate the Rayleigh and Mie scattering effects of air and the aerosol particles suspended in it. The problems associated with vacuum chambers were the large volume required to reduce wall radiances to acceptable levels and their relative inflexibilities. Tests in vacuum are consequently expensive.

The use of helium, which does not support most aerosol particles, and has a scattering coefficient that is one thirty-sixth that of air provides a medium that approximates vacuum well enough to simulate space. The helium tent can be relatively large, reducing wall radiances, and black, because baffling can be used that would not be allowable in vacuum chambers. Modifications to handle special test requirements are easily and quickly achieved.

Figure 7.3-1 provides a photograph of the helium tent used for the LORS sunshade evaluation. Using this facility, extensive evaluation was done and the tracker was shown to meet design performance.

More recently, another helium tent was constructed to evaluate another star sensor and is pictured in Figure 7.3-2. During this particular test series, a method of independently measuring the radiance of the tent walls in the FOV of the test specimen was developed which allows these sources of error to be corrected out. This tent had wall radiances of 6×10^{-10} w/cm^2 steradian which approaches the average radiance of the celestial sphere
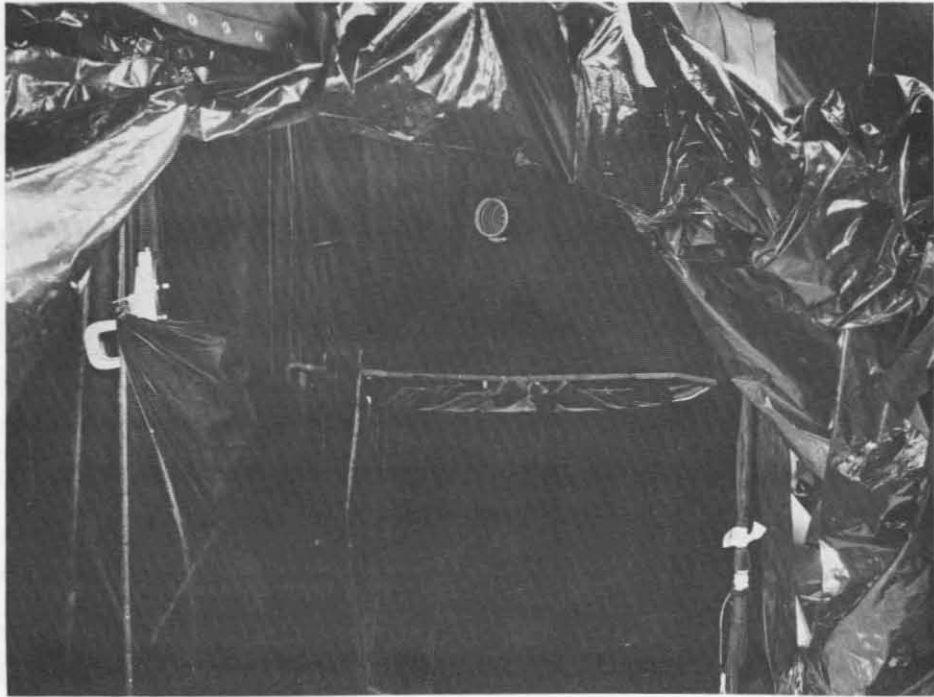
Figure 7.3-1. LORS Sunshade Evaluation Helium Chamber
(Photo R108654)

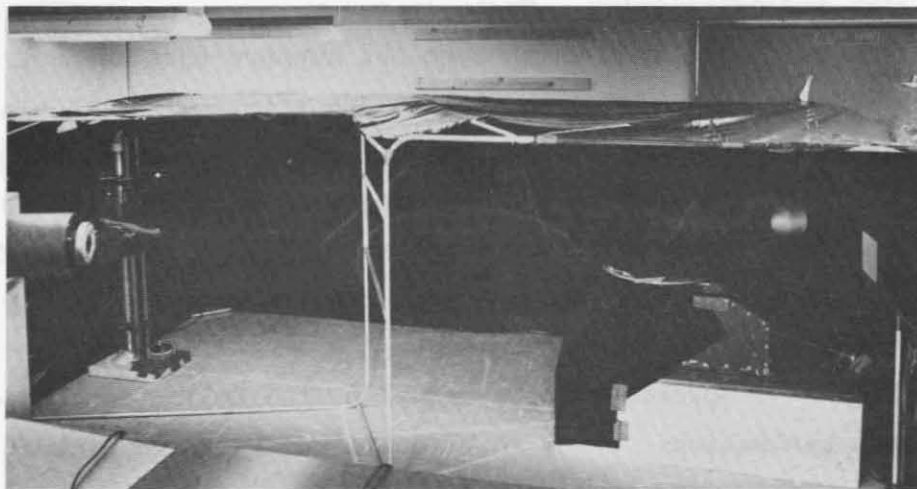Figure 7.3-2. Star Sensor Sunshade Evaluation Helium
Tent (Photo 4R11243)

$(2.3 \times 10^{-11} \text{ w/cm}^2 \text{ steradian})$. As part of this test effort, an extensive material and process evaluation was performed. Various paints (3-M and Parson's black) and coatings (black anodized aluminum and a proprietary coating manufactured by Optical Coating Lab., Inc.) were investigated.